REPORT 239

BARNICARNDY 1 INTERPRETATIVE WELL COMPLETION REPORT

LS Normore, PW Haines, Y Zhan, MTD Wingate, DS Edwards, Y Lu, SK Martin, E Grosjean, CJ Boreham, L Wang, D Dewhurst, A Bailey, CB Foster, DE Kelsey, HJ Allen, IOH Fielding, M Wawryk, EA Hancock, N De Souza Kovacs, LK Carr and P Henson

Government of Western Australia
Department of Mines, Industry Regulation and Safety

Geological Survey of Western Australia

Government of **Western Australia**
Department of **Mines, Industry Regulation and Safety**

REPORT 239

BARNICARNDY 1 INTERPRETATIVE WELL COMPLETION REPORT

LS Normore, PW Haines, Y Zhan, MTD Wingate, DS Edwards[1], Y Lu, SK Martin, E Grosjean[1], CJ Boreham[1], L Wang[1], D Dewhurst[2], A Bailey[1], CB Foster[3], DE Kelsey, HJ Allen, IOH Fielding, M Wawryk, EA Hancock, N De Souza Kovacs, LK Carr[1] and P Henson[1]

1 Geoscience Australia, GPO Box 378, Canberra ACT 2601, Australia
2 CSIRO Energy, Kensington, Perth WA 6155, Australia
3 The Australian National University, Canberra ACT 2600, Australia

PERTH 2023

Geological Survey of Western Australia

MINISTER FOR MINES AND PETROLEUM
Hon Bill Johnston MLA

DIRECTOR GENERAL, DEPARTMENT OF MINES, INDUSTRY REGULATION AND SAFETY
Richard Sellers

EXECUTIVE DIRECTOR, GEOLOGICAL SURVEY AND RESOURCE STRATEGY
Michele Spencer

DEPARTMENT OF INDUSTRY, SCIENCE, ENERGY AND RESOURCES
MINISTER FOR RESOURCES AND WATER
Hon Madeleine King MP

CHIEF EXECUTIVE OFFICER, GEOSCIENCE AUSTRALIA
Dr James Johnson

REFERENCE
The recommended reference for this publication is:
Normore, LS, Haines, PW, Zhan, Y, Wingate, MTD, Edwards, DS, Lu, Y, Martin, SK, Grosjean, E, Boreham, CJ, Wang, L, Dewhurst, D, Bailey, A, CFoster, B, Kelsey, DE, Allen, HJ, Fielding, IOH, Wawryk, M, Hancock, EA, De Souza Kovacs, N, Carr, LK and Henson, P 2023, Barnicarndy 1 interpretative well completion report: Geological Survey of Western Australia, Report 239, 113p.

ISBN 978-1-74168-997-6
ISSN 1834-2280

A catalogue record for this book is available from the National Library of Australia

Funding provided by Geoscience Australia's Exploring for the Future 2016-20 Program and the Geological Survey of Western Australia's Exploration Incentive Scheme.

U–Pb measurements were conducted using the sensitive high resolution ion microprobe (SHRIMP) II ion microprobes at the John de Laeter Centre, Curtin University, with the financial support of the Australian Research Council and AuScope NCRIS. Additional U–Pb analyses by Chemical Abrasion Isotope Dilution Thermal Ionization Mass Spectrometry were conducted at the Boise State University Isotope Geology Laboratory, Boise, Idaho.

Grid references in this publication refer to the Geocentric Datum of Australia 1994 (GDA94). Locations mentioned in the text are referenced using Map Grid Australia (MGA) coordinates, Zone 51. All locations are quoted to at least the nearest 100 m.

Disclaimer
This product uses information from various sources. The Department of Mines, Industry Regulation and Safety (DMIRS) and the State cannot guarantee the accuracy, currency or completeness of the information. Neither the department nor the State of Western Australia nor any employee or agent of the department shall be responsible or liable for any loss, damage or injury arising from the use of or reliance on any information, data or advice (including incomplete, out of date, incorrect, inaccurate or misleading information, data or advice) expressed or implied in, or coming from, this publication or incorporated into it by reference, by any person whosoever.

Published 2023 by the Geological Survey of Western Australia
This Report is published in digital format (PDF) and is available online at <www.dmirs.wa.gov.au/GSWApublications>.

© State of Western Australia (Department of Mines, Industry Regulation and Safety) 2023

With the exception of the Western Australian Coat of Arms and other logos, and where otherwise noted, these data are provided under a Creative Commons Attribution 4.0 International Licence. (https://creativecommons.org/licenses/by/4.0/legalcode)

Further details of geoscience products are available from:
First Floor Counter
Department of Mines, Industry Regulation and Safety
100 Plain Street
EAST PERTH WESTERN AUSTRALIA 6004
Telephone: +61 8 9222 3459 Email: publications@dmirs.wa.gov.au
www.dmirs.wa.gov.au/GSWApublications

Cover photograph: Evening light surrounds DDH1 Drilling's ER01 rig during the drilling of Barnicarndy 1

Contents

Figures

Tables

Appendices

Available as an accompanying digital resource

Plate

Barnicarndy 1 interpretative well completion report

LS Normore, PW Haines, Y Zhan, MTD Wingate, DS Edwards[1], Y Lu, SK Martin, E Grosjean[1], CJ Boreham[1], L Wang[1], D Dewhurst[2], A Bailey[1], CB Foster[3], DE Kelsey, HJ Allen, IOH Fielding, M Wawryk, EA Hancock, N De Souza Kovacs, LK Carr[1] and P Henson[1]

Abstract

Barnicarndy 1 is a deep, vertical stratigraphic well drilled as a joint project between the Geological Survey of Western Australia (GSWA) and Geoscience Australia (GA). The fundamental objective of this stratigraphic well was to continuously core through the entire Canning Basin stratigraphy and obtain approximately 100 m of core from the pre-Canning Basin basement. The continuous core and acquisition of downhole geophysical surveys, including a standard suite of wireline logs and a vertical seismic profile, allows correlation of seismic reflectors on the Kidson seismic survey to their corresponding stratigraphic horizons in the well. To achieve these principal objectives, budgetary and access controls necessitated the selection of the well location in the undrilled Barnicarndy Graben (previously Waukarlycarly Embayment) near Common Depth Point (CDP) 65970 on the Kidson Seismic Line (18GA-KB1). The Basic Data Well Completion Report released in June 2020 covers the well summary, formation evaluation, and drilling and completions data (Normore and Rapaic, 2020) whereas this Interpretative Well Completion Report includes seismic interpretation, well stratigraphy, petrophysical evaluation, multiple varieties of geoscience analysis and contributions to geological knowledge.

Barnicarndy 1 was the first deep stratigraphic well within the Barnicarndy Graben, defining a unique depositional architecture for this part of the Canning Basin. Key geological insights into this underexplored sedimentary sequence, many of which corroborate consistent outcomes from multiple analytical sources, are listed below:

- anomalous seismic velocity of Permian and Ordovician intervals
- Barnicarndy and Yapukarninjarra formations type sections
- diverse macro- and microfossil assemblages
    - identified three spore-pollen biozones in the Carboniferous–Permian section
    - identified three conodont biozones in the Ordovician section
    - described a new conodont species *Juanognathus*? *denticulatus*
    - identified the biostratigraphic potential of Ordovician palynology
    - identified the presence of Ordovician cryptospores of paleobotanical significance
- chemical abrasion isotope dilution thermal ionization mass spectrometry (CA-IDTIMS) provides a maximum depositional age of 477.24 ± 0.33 Ma in the Samphire Marsh Member
- detrital zircon stacked probability plots for each stratigraphic interval
- thermochronology indicates 2–3 km of post-Permian uplift and erosion
- chemostratigraphy defined six major chemostratigraphic boundaries and nine distinct packages
- unique organic matter contributions to the Samphire Marsh and Fly Flat members as compared to other Ordovician-sourced oils of the Canning Basin
- vitrinite reflectance equivalence indicate an oil window depth of about 500 m (i.e. Rv >0.55%) in the Grant Group
- fluid inclusion studies indicate paleo-hydrogen and -helium systems in the pre-Permian section
- two distinctive reservoir-seal pairs that have potential for future sequestration and storage of CO_2 or other gases
- integrated sequence stratigraphic assessment provides eight third order sequences through Barnicarndy Graben
- structural and mineralizing impacts of major reactivation of the Rudall Internal major crustal boundary with 2–3 km of post-Permian uplift in the Barnicarndy Graben.

These geoscientific outcomes apply to the Barnicarndy Graben and potentially directly north along the trend to the Samphire Graben. Information obtained in this stratigraphic well can be applied to stratigraphic horizons across the entire Canning Basin.

KEYWORDS: Barnicarndy Graben, biostratigraphy, Canning Basin, chemostratigraphy, geochronology, organic geochemistry, petrophysics, sedimentology, stratigraphic drilling, thermochronology, well completion report, Yeneena Basin

1 Geoscience Australia, GPO Box 378, Canberra ACT 2601

2 CSIRO Energy, Kensington, Perth WA 6155

3 The Australian National University, Canberra ACT 2600

Introduction

Overview

Barnicarndy 1 is a 2680.5 m deep, vertical stratigraphic well drilled between 1 September and 30 November 2019 as a joint project between the Geological Survey of Western Australia (GSWA) and Geoscience Australia (GA). Funding for the project was primarily from GA's Exploring for the Future Program with assistance from GSWA's Exploration Incentive Scheme. The well is located in the Barnicarndy Graben, the most southwesterly tectonic subdivision of the Canning Basin, which adjoins the Samphire Graben to the north, Anketell Shelf to the northeast and Wallal Platform to the northwest (Fig. 1). The Neoproterozoic Yeneena Basin, a component of the Paterson Orogen and the Centralian Superbasin, is exposed to the southeast, south and southwest of the graben. The drill site was located on Newcrest Ltd's miscellaneous road licence (L45/00110), on a previously cleared area including existing water bores. The drill site is approximately 360 km southeast of Port Hedland, 215 km east of Marble Bar and 60 km west of the Telfer Mine. Access to the site was either via the Marble Bar–Telfer road or through the Nifty Mine airport, 30 km to the southwest. The Nifty Mine airport was used during the drilling stage for crew changes.

Barnicarndy 1 was originally named Waukarlycarly 1. In consultation with the Western Desert Lands Aboriginal Corporation (WDLAC) and due to the culturally significant nature of the original name, Waukarlycarly, both the well and the tectonic subdivision it was drilled in required the following name changes: Waukarlycarly 1 to Barnicarndy 1, Waukarlycarly Embayment to Barnicarndy Graben and West Waukarlycarly Fault to Barnicarndy Fault (Normore et al., 2021).

Barnicarndy 1 is named after the Barnicarndy Hills located 28 km north-northwest of the drill site in the northwest corner of the Paterson Range 1:250 000 map sheet (Fig. 1). The existence of a narrow fault-bounded graben-type structure in the area was first identified by Geopeko geologists during exploration for the Barnicarndy coal project in 1978 (Kitto, 1978). The company referred to the structure as the Barnicarndy Embayment, but it was independently named the Waukarlycarly Embayment after Lake Waukarlycarly by GSWA (Hocking et al., 1994).

Barnicarndy 1 was the first deep stratigraphic well within the Barnicarndy Graben. It defined a unique depositional architecture for this part of the Canning Basin and is the type section for the recently defined Barnicarndy and Yapukarninjarra formations. Numerous geological insights into this distinctive sedimentary sequence are validated from different scientific methodologies. For example, anomalously high seismic velocities in the upper stratigraphy of Barnicarndy 1 indicate post Permian uplift and erosion of a thick sedimentary interval, which is supported by organic thermal maturity analysis from vitrinite and vitrinite equivalence, in addition to the thermal evolution provided by thermochronology analysis.

A detailed sequence of depositional environments has been provided over this distinctive tectonic unit using image logs, which also detail the structural zonation, stress regime and sediment dispersal for the upper stratigraphy in Barnicarndy 1. Beyond the successful application of palynology and conodont biostratigraphy to constrain the age of the Permian and Lower Ordovician sections of the well, significant biostratigraphic and paleontological outcomes include the documentation of a new conodont species and the identification of cryptospores with the potential to contribute to the global understanding of plant evolution during the Early Ordovician. Enormous potential also exists in the future biostratigraphic correlation of numerous Lower Ordovician fossil groups, including but not limited to, conodonts, acritarchs, trilobites, graptolites, brachiopods and bivalves.

Geochemical analysis is broadly subdivided into inorganic and organic sections. The inorganic geochemistry analysis provided a unique Ordovician chemostratigraphic signature with a distinctive sediment provenance. Chemostratigraphy also defined nine distinct packages and six major chemostratigraphic boundaries. Carbon isotope curves from Barnicarndy 1 have potential for global correlation with data from Argentina and China, with the prospective of extending the Yapukarninjarra Formation into the Cambrian. Multi-element geochemistry of the Yeneena Basin section indicates anomalous copper mineralization while the portable X-ray diffraction (pXRD) provided a useful tool for rapid validation and quantification of mineralogy identified from infrared hyperspectral analysis.

Organic geochemistry has concluded there is no present-day hydrocarbon source potential for the Barnicarndy 1 sedimentary succession; however, petroleum inclusions identified in the Barnicarndy Formation indicate previous hydrocarbon migration. The Barnicarndy 1 drill location was chosen due to a lack of structural trapping, with this data suggesting the potential for hydrocarbon accumulations elsewhere in the Barnicarndy Graben that may have a closure. Molecular and isotopic characterization of organic matter provides insights into the redox conditions and type of organic matter preserved but also indicated the potential for hydrocarbon contamination in Barnicarndy 1 samples. Compound specific isotope analysis (CSIA) discriminates a different source of organic matter in the rock extracts from both the Samphire Marsh and Fly Flat Members and also distinct from previously analysed Ordovician-sourced oils of the Canning Basin.

A fluid inclusion stratigraphy (FIS) study of Barnicarndy 1 detected traces of hydrocarbons and also identifies two main intervals of enhanced hydrogen and one interval of enhanced helium. The co-variance of anomalous hydrogen and helium in fluid inclusions near the bottom of the well suggests a common source, possibly related to radioactive decay (He) and associated radiolysis of water (to produce H_2). The absence of significant helium in the upper anomalous hydrogen zone suggests a redox process of iron oxidation and reduction of water to produce only hydrogen in this shallower interval.

With large-scale mining and renewable energy projects in the region, and existing pipeline infrastructure and fairways, the Barnicarndy Graben is a potential target for both carbon capture and underground storage or hydrogen storage. The primary reservoir is the Barnicarndy Formation, which is below the critical CO_2 storage depth of 800 m with over 500 m of porous and permeable sandstone. This reservoir interval is sealed by the Grant Group diamictite with up to a 940 m CO_2 column sealing capacity.

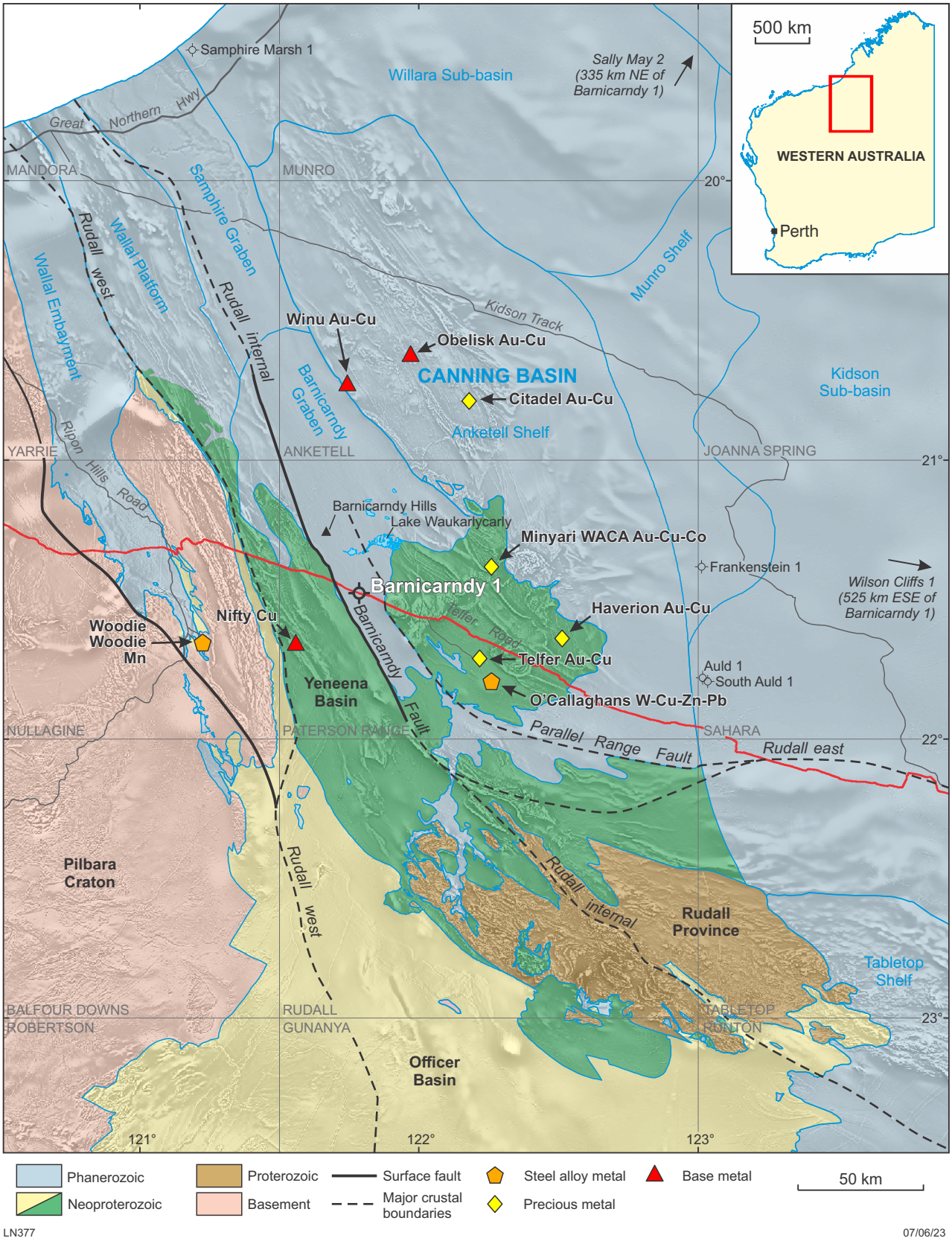

Figure 1. Regional map of the south-western Canning Basin, showing the location of deep stratigraphic well Barnicarndy 1, Kidson deep crustal seismic line 18GA-KB1 (red), first vertical derivative magnetic anomalies, tectonic subdivisions, major crustal boundaries, local surface faults, nearby mineral deposits and relevant petroleum exploration wells

Drill cuttings were collected at 3 m intervals from surface to 580.0 m; below this continuous core was recovered to total depth at 2680.5 m. All depths are measured from rotary table (RT). Figure 2 illustrates the drill cuttings (Fig. 2a) and examples of the individual units throughout the cored section (Figs 2b–m). A detailed geological description core log was compiled on site for the entire cored interval (580.0 – 2680.5 m) by the following GSWA geologists: Sarah Martin, Leon Normore, Josh Guilliamse, Sidy Morin-Ka, Charmaine Thomas, Peter Haines and Chris Phillips, with assistance from wellsite geologists Phil Rose, Dave Thornton and Paul Elliott from InGauge Energy. This log was reviewed and consolidated by Iain Copp and is available as Appendix 1.

The multi-disciplinary nature of this interpretative well completion report has resulted in numerous co-authors, primarily from GSWA and GA but also from CSIRO and ANU. The introduction and regional geology was authored by Leon Normore, Peter Haines and David Kelsey. Seismic interpretation was written by Yijie (Alex) Zhan. Well stratigraphy sections were covered by the following: Cenozoic (Nadir De Souza Kovacs), Grant Group (Sarah Martin and Leon Normore), Barnicarndy, Nambeet and Yapukarninjarra formations (Leon Normore and Peter Haines), and the Yeneena Basin (Peter Haines and David Kelsey). The petrophysical evaluation was written by Leon Normore and Peter Haines. Paleontology and biostratigraphy sections were covered by the following: Permian palynology (Sarah Martin), Ordovician palynology (Clinton Foster and Diane Edwards), conodonts and fish microfossils (Heidi Allen), macrofossils (Sarah Martin, Heidi Allen and Peter Haines), and ichnology was summarized by Leon Normore from Appendix 4. The geochronology section was written by Michael Wingate, Yongjun Lu and Imogen Fielding. Thermochronology was summarized by Leon Normore and Peter Haines based on Danišík (2021). Inorganic geochemistry and multi-element geochemistry was written by Leon Normore. Chemostratigraphy was summarized by Leon Normore from Forbes et al. (2020). The XRD section was authored by Michael Wawryk and Elena Hancock. Diane Edwards, Chris Boreham and Emmanuelle Grosjean provided the text for the organic geochemistry section. Routine core analysis was written by Leon Normore. Rock properties analysis was provided mainly by David Dewhurst and Alan Bailey with bulk density and magnetic susceptibility written by Emmanuelle Grosjean.

Exploration history

The Barnicarndy Graben is a frontier region with minimal previous mineral or petroleum exploration. Mineral exploration began with a coal exploration project in the late 1970s by Geopeko Division of Peko-Wallsend Operations Limited, targeting the Grant Group (Kitto, 1978). This was followed by the exploration of sediment hosted targets by Western Mining Corporation in the 1980s (Brooke, 1987) and more recently by Metallicity from 2017 to 2019 (Wilson, 2016). A potash exploration project in surficial lacustrine deposits was completed by Reward Minerals in 2010 (Percival, 2015).

Geopeko's Barnicarndy Coal Project used earlier field mapping which identified Permian sedimentary rocks in the area (Traves et al., 1956) along with Bureau of Mineral Resources gravity data to suggest a potential sedimentary basin in this area (Kitto, 1978). A stratigraphic drilling program was completed, including four drillholes to a maximum depth of 150 m that terminated within diamictite of the Grant Group. Although three thin carbonaceous horizons were identified, the economic value of these horizons was limited. The sedimentary sub-basin was later included as one of the structural elements of the Canning Basin with an estimated depth of 2 km and, based on palynology, the Permian stratigraphic units identified were correlated with Permian strata on the eastern side of the Canning Basin (Guppy et al., 1958). The Lake Waukarlycarly potash exploration project targeted potash saturated brines within a paleo-valley system. Twenty reverse circulation drillholes and one development bore were completed totalling 2909 m, with the maximum depth of 192 m also ending within the Grant Group (Percival, 2015).

The Yeneena Basin of the Paterson Orogen is host to a diverse range of mineral deposits, prospects and occurrences (Maidment et al., 2017). The Telfer gold–copper deposit, one of Australia's largest gold mines, was the earliest discovery in the region during the early 1970s (Porter, 2017b) and is located 60 km to the southeast of Barnicarndy 1. This spurred additional regional exploration resulting in the discovery of the Nifty sediment-hosted copper deposit in 1981 (Haynes et al., 1993), located 30 km to the southwest and the Maroochydore copper–cobalt deposit (Porter, 2017a) in 1984, located 96 km to the southeast. Other notable mineral deposits in the vicinity of Barnicarndy 1 include the recently discovered Winu copper–gold deposit 83 km to the north, the Haverion gold deposit 93 km southeast, the Obelisk copper–gold prospect 97 km to the north-northeast, the Woodie Woodie manganese mine 57 km to the west-southwest and the Kintyre uranium deposit 100 km south-southeast.

Figure 2. (page 5) Ditch cuttings and core photos: a) ditch cuttings from surface to 580 m (3 m intervals); b) upper Grant Group sandstone reservoir interval, 644.55 – 645.07 m, RCA and TS 644.77 m; c) lower Grant Group diamictite seal interval, 799.14 – 799.54 m, RCA and TS 799.17 m; d) lower Grant Group conglomerate, 847.00 – 847.50 m; e) basal Grant Group unconformity, 854.50 – 855.05 m; f) upper Barnicarndy Formation, 970.50 – 970.90 m; g) lower Barnicarndy Formation, 1268.94 – 1269.38 m; h) Samphire Marsh Member, Nambeet Formation, 1999.80 – 2000.20 m; i) Fly Flat Member, Nambeet Formation, 2346.00 – 2346.50 m; j) Yapukarninjarra Formation, 2563.52 – 2564.00 m; k) basal Canning Basin unconformity, 2585.25 – 2585.75 m; l) Yeneena Basin paleo-regolith horizon (weathered silty dolomite), 2621.75 – 2622.25 m; m) Yeneena Basin fresh slightly metamorphosed dolomite, 2678.70 – 2679.20 m

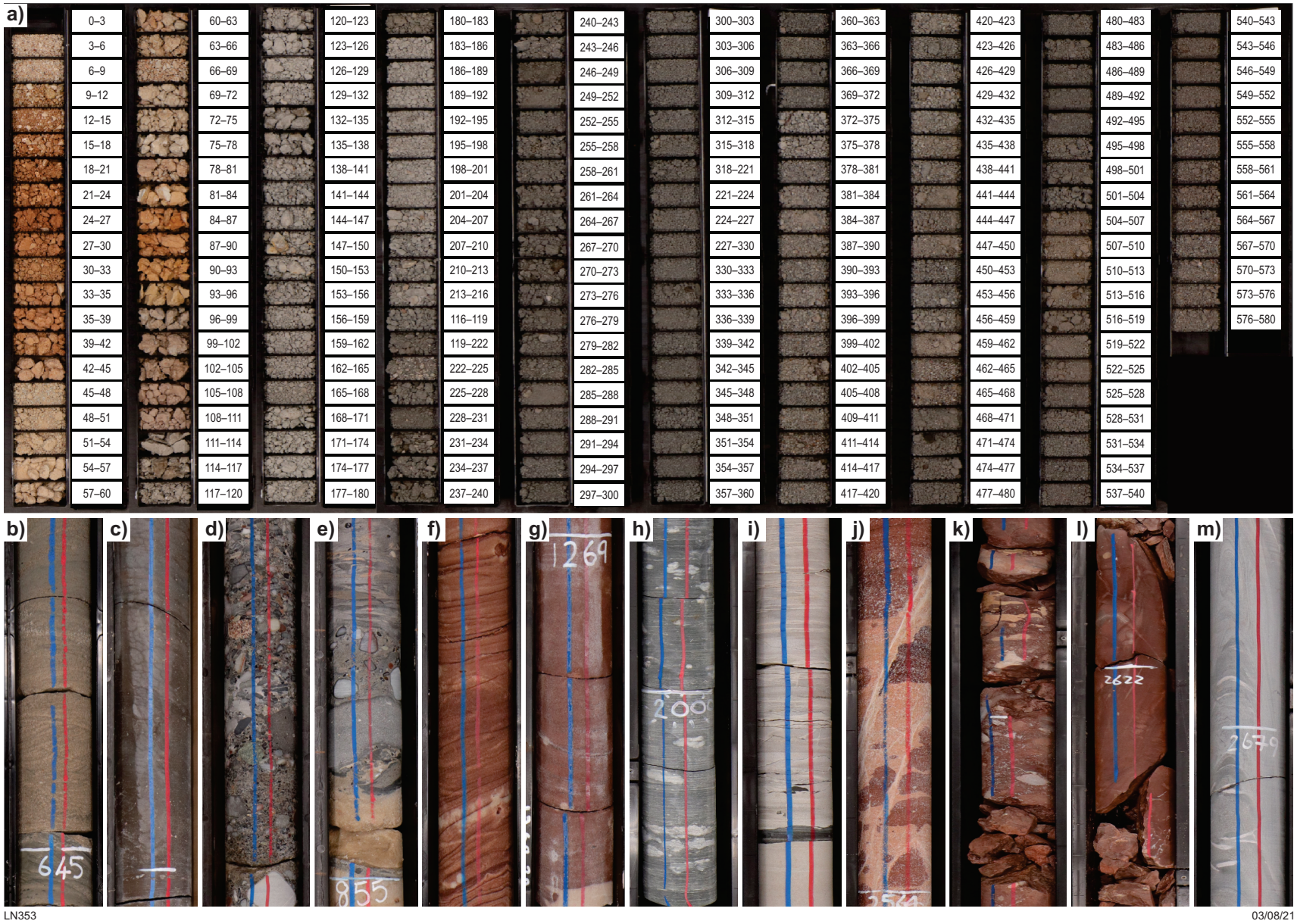

LN353 03/08/21

Regional geology

The Barnicarndy Graben is a fault-bounded block of Paleozoic sedimentary rocks on the southwestern margin of the Canning Basin, overlying and surrounded by Neoproterozoic rocks of the Yeneena Basin. The Barnicarndy Fault defines the western boundary of the graben and coincides with the informally named 'Rudall Internal' major crustal boundary (Martin et al., 2021a). The Rudall Internal boundary transects the entire Paterson Orogen, from the Yeneena Basin in the north, through the Rudall Province to the south. The eastern boundary of the Barnicarndy Graben incorporates the Parallel Range Fault, which is the boundary between distinct lithospheric domains: reworked Pilbara lithosphere to the west and lithosphere younger than, and thus distinct from, the Kimberley and North Australian Craton to the east (Lu et al., 2021).

The Paleoproterozoic to Mesoproterozoic Rudall Province represents the oldest constituents of the Paterson Orogen and has a multiphase history that was shaped by the amalgamation of the West and North Australian Cratons (Maidment, 2017). The Rudall Province is unconformably overlain by siliciclastic and carbonate rocks of the Yeneena Basin, contiguous with the early phase of the Officer Basin to the south, with deposition beginning in the early to middle Tonian (early Neoproterozoic). Neoproterozoic deformation and igneous intrusion during the Miles and Paterson Orogenies produced major folding, faulting and metamorphism up to greenschist facies of this succession (Goellnicht et al., 1991; Bagas, 2004; Czarnota et al., 2009; Gardiner et al., 2018). Deformed and steeply dipping metasedimentary rocks of the Yeneena Basin form the basement beneath the Paleozoic sedimentary rocks that fill the Barnicarndy Graben, but the exact timing of graben initiation is unclear.

Renewed rifting between the West and North Australian Craton began in the middle Cambrian as evidenced by bimodal mafic–felsic magmatism surrounding and beneath the Canning Basin (Haines et al., 2018a). The Kalkarindji Large Igneous Province, including the Antrim Plateau and Table Hill Volcanics to the northeast and south of the Canning Basin, respectively, produced flood basalts and dykes at c. 511 Ma (Maidment, 2005; Jourdan et al., 2014). Monzogranite at the bottom of petroleum exploration well Samphire Marsh 1, within the Samphire Graben of northwest Canning Basin, yielded a magmatic crystallization age of 505 ± 4 Ma (Wingate et al., 2018a). This mid-Cambrian rifting is potentially related to the extensional Larapinta Event in central Australia (Scrimgeour, 2013), followed by the beginning of Canning Basin deposition during the Early Ordovician or potentially late Cambrian. The earliest deposition may have included alluvial fans and plains with braided streams associated with nearby extrusive volcanism, followed by major subsidence and marine incursions as demonstrated in Barnicarndy 1.

Seismic interpretation

Seismic interpretation to support the Barnicarndy 1 well includes pre-drill and post-drill interpretation and analysis, based on integration with gravity, magnetic, well data and basement outcrops in the vicinity of Barnicarndy 1. Zhan (2021) detailed the numerous geophysical analyses supporting the well; this section provides a condensed description of the pre- and post-drilling interpretation.

The shallow formations penetrated in Barnicarndy 1, particularly the interval between 210 and 1392 m has an unexpectedly high seismic velocity (Zhan, 2021). This velocity anomaly was the primary cause of depth discrepancies in the pre-drilling prognosis. The depth difference was 385 m for the top basement pick, from the 2200 m prognosis to the 2585 m actual depth. A secondary cause of the prognosis depth discrepancy of the top basement pick was due to out-of-plane seismic reflections from steep topography on the Canning Basin basal unconformity. Any future seismic acquisition over the Barnicarndy Graben, or possibly the contiguous Samphire Graben, could use the higher seismic velocity modelled in Barnicarndy 1 to provide a more accurate depth prognosis. The high seismic velocities of the Permian strata and Barnicarndy Formation can be explained by earlier deep burial, followed by uplift and erosion of a thick upper sedimentary section from the Barnicarndy Graben.

Historical geophysical interpretation

The Barnicarndy Graben (Fig. 3a) is interpreted as part of the Canning Basin, but is distinctly separated by faults and shallow Precambrian basement from the main depocentres (Willara and Kidson sub-basins) in the southern peripheral area of the basin. The graben was first identified through Bouguer gravity images, which show a localized gravity low within a regional north-northwesterly trending gravity high, the Anketell Regional Gravity Ridge of Fraser (1976) or the Warri Gravity Ridge of Iasky (1990). High-resolution gravity data became available across the Barnicarndy Graben in 2005, with a 2.0 – 2.5 km spacing between gravity stations (Bacchin et al., 2006). The elongated gravity low within the regional gravity high (Fig. 3b) implies the presence of a basinal depression between the Pilbara Craton and the main part of the Canning Basin. The gravity low is about 25– 50 km wide and 150 km long, and subparallel to the nearby Precambrian structural trends in the Paterson Orogen.

The graben configuration was confirmed by four seismic profiles broadly normal to the strike of the graben (Fig. 3b). The oldest in the north was acquired by the West Australian Petroleum Pty Ltd. (Allen et al., 1971) and the remaining three lines by Hunt Oil Company (Hunt Oil Company of Australia, 1997). These seismic lines show that the graben (Fig. 4) is fault-bounded to the nearby tectonic units, including the Paterson Orogen and Anketell Shelf. The thickness of Canning Basin sedimentary rocks within the graben was unknown prior to the drilling of Barnicarndy 1. The Permian and younger cover was interpreted to be widespread (Hocking, 1994) and extended from the main part of the Canning Basin in the north. The thick section interpreted to be beneath the Permian with a highly reflective seismic signature was of uncertain age. This prompted several speculative interpretations, such as a thin Ordovician section overlying a thicker Proterozoic succession, in turn overlying crystalline basement (Hunt Oil Company of Australia, 1997), or a lower Paleozoic succession equivalent to the Ordovician–Silurian section near the southern margin of the Willara and Kidson Sub-basins (Roach et al., 2010; Alavi, 2013).

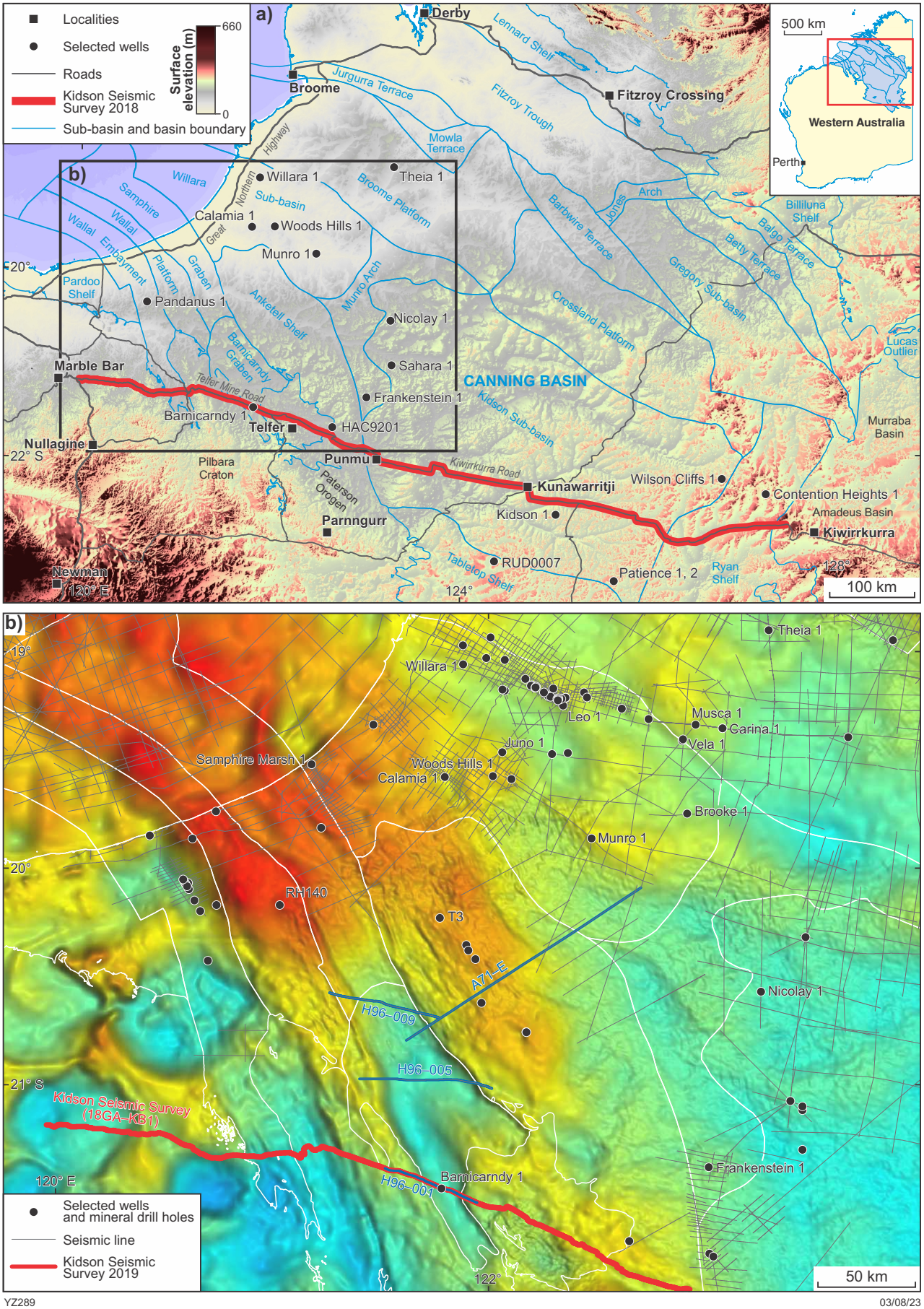

Figure 3. a) location map of Kidson deep crustal seismic line 18GA-KB1, stratigraphic well Barnicarndy 1 and Canning Basin tectonic elements overlying a surface digital elevation model; b) seismic lines and drillholes on Bouguer gravity anomaly

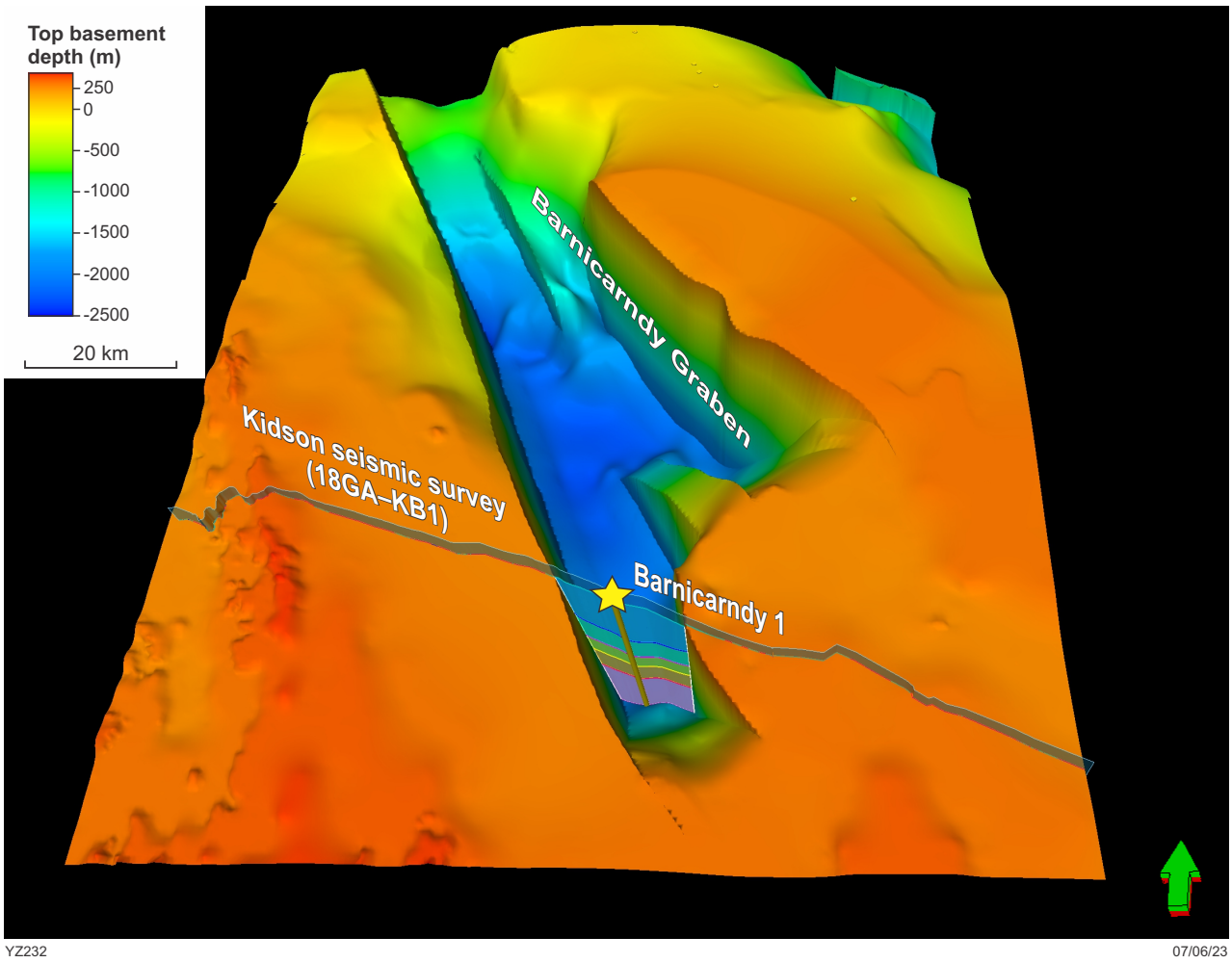

Figure 4. Oblique 3D model of the Barnicarndy Graben showing the Barnicarndy 1 stratigraphic well and the Kidson seismic survey crossing the southern end of the graben

Pre-drill seismic interpretation

The route of the southern-most line of the Hunt Oil seismic survey in the Barnicarndy Graben was re-surveyed as part of the Kidson deep crustal seismic survey (18GA-KB1) in 2018. This survey was designed to investigate the regional architecture of the southern Canning Basin and its underlying and surrounding tectonic domains (Southby et al., 2019; Doublier et al., 2020b; Zhan and Haines, 2021). The Kidson seismic survey was processed with a minimum phase and retained its recording polarity for the final trace polarity (Velseis Processing Pty Ltd, 2019). The final seismic datum was placed at 500 m above mean sea level, which is above the highest surface elevation (480 m) in order to preserve the data in elevated areas. Static corrections were applied to the seismic data to compensate for the effects of variations in elevation, weathering zone thickness and velocity. A replacement velocity of 2500 m/s was used between the near-weathering floating datum and the final datum.

The sedimentary successions in the Barnicarndy Graben were initially difficult to interpret, especially for the thick section below the Permian, due to the lack of deep drilling. Therefore, the seismic interpretation for pre-spud well prognosis (Fig. 5) only included three major horizons: base Mesozoic, base Permian and top basement. This interpretation was based on the hypothesis that the graben was filled with a Lower Paleozoic section, consistent with Roach et al. (2010) and Alavi (2013), and is an alternative hypothesis to a Proterozoic infill interpretation (Hunt Oil Company of Australia, 1997). These horizons were interpreted at prominent angular contacts, as they were formed during tectonic events, the Fitzroy Transpression, Meda Transpression and Samphire Marsh Movement, respectively (Kennard et al., 1994). The pre-Permian section was tentatively interpreted, with horizon picks named as top Nita, Willara, and Nambeet formations based on regional correlation to the widespread Ordovician–Silurian stratigraphy outside of the graben in the southern Canning Basin (Zhan, 2018).

Pre-drill velocity analysis and depth conversion

Due to the lack of previous deep well penetrations, the only velocity information that could be used for depth conversion was from the seismic stacking velocity inside the Barnicarndy Graben and offset wells beyond the graben in the southern Canning Basin. The stacking velocity is picked on the semblance profile to find the best fit on common depth point seismic gathers to improve the signal-to-noise ratio. The velocity can be converted into average or

interval velocities using the Dix equation, but may bear little relation to the actual geological boundaries. The Kidson seismic survey was depth migrated after iterations of the velocity model. However, due to the long distance between the seismic line and pre-existing wells, such as 60 km to Frankenstein 1, 15 km to Kidson 1 and 75 km to Patience 2, the interval velocity model of depth migration derived from stacking velocity was not calibrated to the well velocities throughout the seismic line (Velseis Processing Pty Ltd, 2019).

The interval velocities for the depth migration were considered faster than the actual formation velocities by comparing the results with well velocities from Frankenstein 1, which has the fastest velocity among offset wells (Zhan, 2021). If the velocity model used in the seismic depth migration was correct, then basement at the Barnicarndy 1 location was predicted to be about 2800 m deep. For this reason, the pre-spud prognosis used the time migration data for the seismic interpretation, and applied velocities from offset wells to convert to depth for

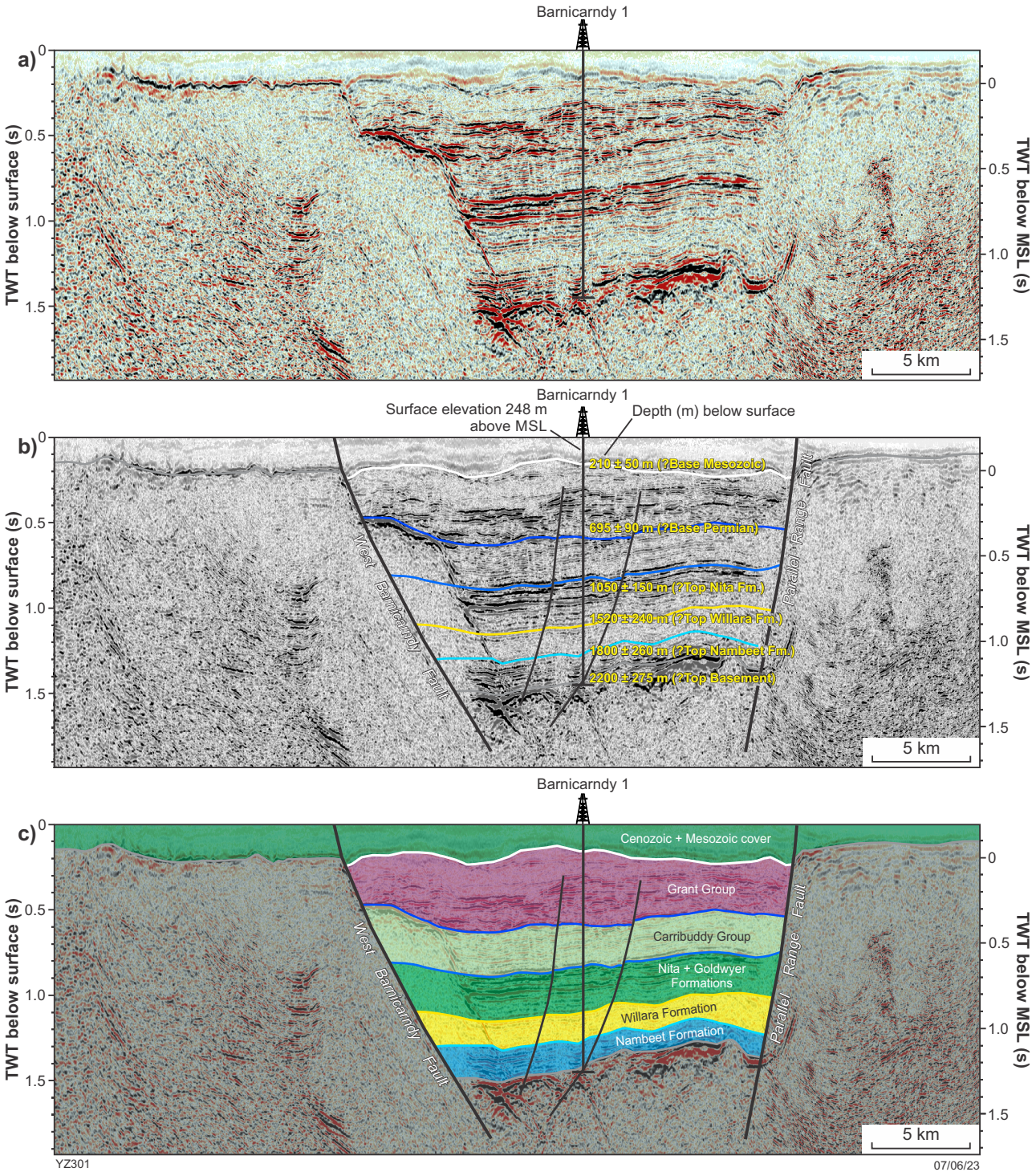

Figure 5. Pre-drilling seismic interpretation and depth prognosis for Barnicarndy 1, with vertical axes marking two-way time (TWT) below surface (left axis; 0 s = ground level at well site) and TWT below mean sea level (right axis; 0 s = mean sea level (MSL) along seismic profile): a) uninterpreted seismic section; b) seismic interpretation with depth prognosis; c) predicted geological section

the predicated formation boundaries. The application of the offset well velocities was based on the assumption that the Barnicarndy Graben is geologically similar to the Willara and Kidson sub-basins.

The time-depth relationships of the offset wells are based on their vertical seismic profile (VSP) and checkshot data, which show a broad range of velocities, such as slow in Munro 1, medium in Willara 1 and fast in Frankenstein 1 (Fig. 6). This widely variable velocity created significant uncertainty in the predicted depth at Barnicarndy 1. For example, the differences from applying the time-depth of Munro 1 versus Frankenstein 1 are about 440 m at two-way time (TWT) 0.8 s, 500 m at 1.0 s, and 550 m at 1.2 s. The broad range of velocity is probably related to the different stratigraphy, density and compaction across different parts of the Canning Basin. It was difficult to apply a specific geological scenario to the Barnicarndy Graben, as there was no prior knowledge of the sedimentary fill within this tectonic unit. The pre-drill depth prognosis used an averaged velocity curve derived from wells in the Kidson and Willara Sub-basins, and the Broome Platform. The seismic interpretation in TWT and velocity prognosis indicated that the Base Mesozoic, Base Permian, and Top basement sit about 210, 695 and 2200 m respectively, below the surface, with increasing uncertainty with depth to around ± 275 m at the interpreted top basement horizon after adding a contingency error margin to allow for the unknown geology (Table 1).

Post-drill well correlation and interpretation

Sonic velocity

Open-hole sonic logs were acquired over three intervals: 216–727 and 726–1603 m by Wireline Service Group using a monopole detector, and 1603–2679 m by Weatherford with a dipole tool. The logs mostly display reasonable changes at lithological boundaries (Fig. 7). The wireline sonic velocity is distinctively different from those of the offset wells that generally increase in velocity with depth (see the velocity comparison in Fig. 8). Barnicarndy 1 reaches high velocity at shallow depths, such as 3000 m/s at 210 m (about 48 m above mean sea level [MSL]), 3500 m/s at 450 m and 4200 m/s at 850 m, which are approximately 500–1000 m/s faster than other wells at equivalent depths. It is likely that the high velocity extends upwards into the unlogged section below the weathering layer at 96 m. The thick claystone from 1392 to 2270 m has a relatively low velocity (3900 m/s; Fig. 8), compared to 4000 m/s in the offset wells, which include a certain percentage of high-velocity halite and carbonate at depth.

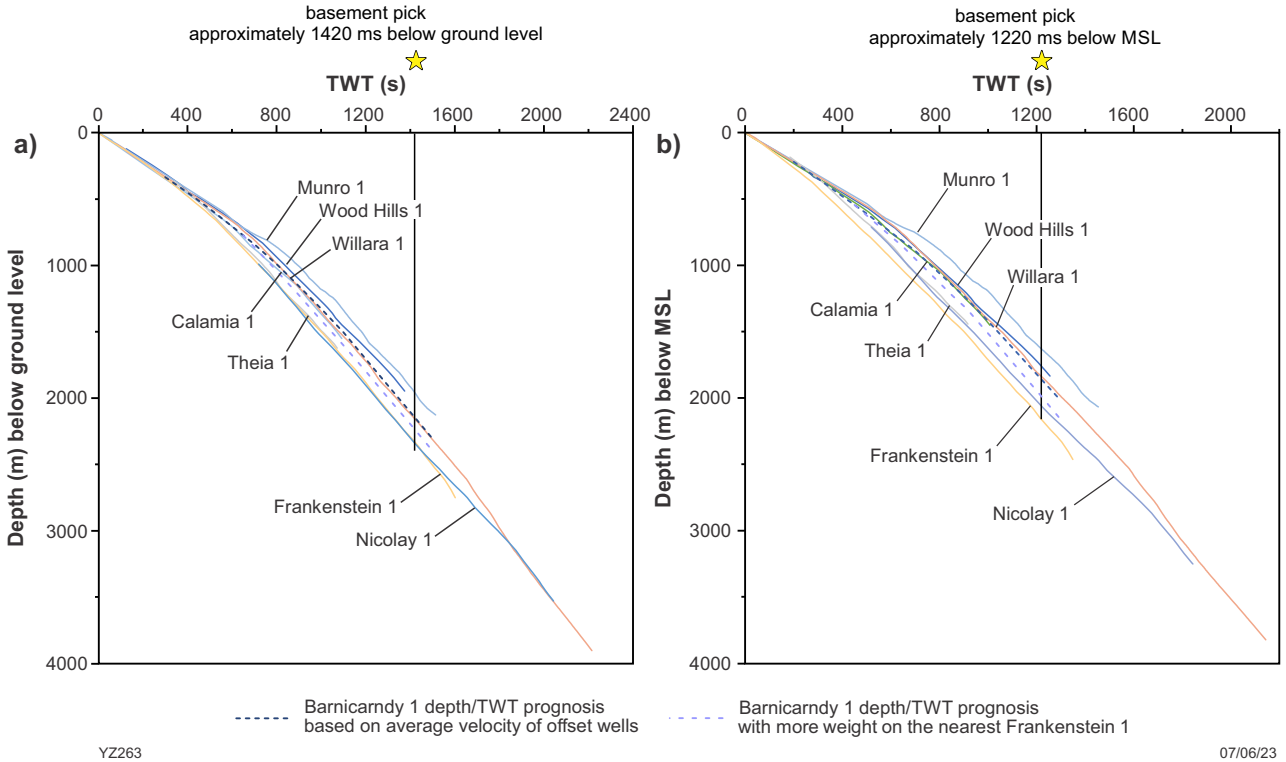

Figure 6. Time-depth pairs of offset wells from vertical seismic profile (VSP) and checkshot surveys: a) true vertical depth (TVD) vs two-way time (TWT) below surface; b) true vertical depth sub sea (TVDSS) vs two-way time sub sea (TWTSS) below mean sea level (MSL). Note the locations of the offset wells are marked in Figure 3b

Table 1. Formation depth prognosis for Barnicarndy 1. Note the uncertainties are only based on the broad range of the velocity and do not include any errors from seismic interpretation that are difficult to quantify prior to the drilling

Stratigraphic pick	*TWT below surface (s)*	*TWT below MSL (s)*	*Depth below surface (m)*	*Uncertainty due to velocity variability (m)*
Base Mesozoic	0.16	-0.04	210	± 50
Base Permian	0.6	0.4	695	± 90
Top Nita Fm	0.84	0.64	1050	± 150
Top Willara Fm	1.15	0.92	1520	± 240
Top Nambeet Fm	1.25	1.05	1800	± 260
Top Basement	1.42	1.22	2200	± 275

Vertical seismic profile and checkshot surveys

A zero-offset VSP (Fig. 9) was acquired by HiSeis using two levels of Sercel slimware system with 10 m spacing (Kopty, 2020). It used one vibroseis truck as the energy source to generate two sweeps for every logging circle and a surface geophone to ensure timing integrity. The VSP data was collected in various borehole conditions, open-hole between 1600 and 2620 m, through PQ casing between 727 and 1600 m, and through PQ and SQ casings between 650 and 727 m. The VSP first arrivals are excellent quality over the open-hole section and show a distinctive arrival event between 0.60 and 0.85 s one-way time (OWT; Fig. 9). The first arrivals measured inside the PQ casing are mostly good quality due to the small annulus between the borewall and casing, except for the upper- and lower-most parts of the measurement (727–825 and 1400–1610 m) where it lacks hard-coupling with rock formations. Between 727 and 650 m, although it was logged through two sets of casing, PQ and SQ, the data show a similarly good quality with OWT between 0.35 and 0.40 s.

Checkshot data were collected (wiggle lines in Fig. 9) when lowering the logging tool, prior to pulling up for VSP measurement. The checkshot points were selected at the boundaries of major lithological zones to measure the OWT as anchor points for well calibration with the seismic line. The checkshot data are good quality below 450 m, with the first break consistent with the VSP profile at each trace record. The data is reasonable quality at 380 and 420 m, but becomes difficult to interpret at 220 and 280 m.

The logging company provided the interpretation of the VSP first arrivals and checkshot data (Fig. 10). The VSP measures one-way travel time in thick formations between the vibroseis source and downhole geophone sensors, compared to thin intervals detected by the sonic wireline tool. The inaccuracies have been reduced by slightly editing the original first break to remove some abnormalities at individual points.

The interval velocity profiles from the VSP and sonic log are parallel to each other, confirming that the shallow section in Barnicarndy 1 does have anomalously high velocities. On the other hand, the velocities also show some difference, particularly in porous sandstones. This is probably caused by drilling mud where solid weighting agents with particles smaller than the sandstone's pore sizes were deposited as a thin mud-cake was formed around the borehole. Thus the flushed/transition zone probed by the sonic tool will record a higher velocity than expected for the formation (Sorensen, 2015). Due to the compromise in sonic velocity by the mud invasion, the VSP, especially its travel time difference (Δt; 510 ms OWT) between the top (650 m) and bottom (2620 m) measurements, is considered more robust than the sonic log. Therefore, the VSP data is used for time-depth correlation between synthetic seismograms and the seismic trace from the Kidson seismic survey. The sonic velocity and density logs are conditioned by the VSP time-depth pairs and used to generate the reflection coefficient.

Well to seismic correlation and interpretation

The absolute time-depth pairs from the original VSP data show that the top of basement at 2582 m corresponds to 1.7 s TWT, which is about 0.3 s below the seismic reflective package. This anomalous calibration is perhaps caused by instrumental delays in the VSP acquisition. The correlation uses the relative time-depth (Δt) of 510 ms OWT between the top and base measured depths of 650–2620 m (Fig. 9). The relative time-depth pairs include good-quality checkshots between 470 and 650 m. The integrated relative pairs have been vertically shifted, without squeezing or stretching to maintain the interval velocity to compensate for the uncertainties from the impact of systematic VSP delay.

An upward shift of 215 ms of the synthetic seismogram creates the best tie to the seismic interpretation (Fig. 10), because the formation tops and wireline logs both match well with the seismic profile for the upper half of the well from 210 to 1500 m. The lower half of the synthetic seismogram requires an extra 55 ms shift compared to the top part of the well in order to match with the seismic line (Fig. 10). The quantitative analyses of the synthetic correlations suggest that the depth discrepancies in the prognosis are not related to the TWT picks for major boundaries, which mostly match what has been penetrated in Barnicarndy 1. The difference in the pre-drill vs actual formation depths is likely due to anomalous velocities measured in the well, and out-of-plane reflections on the seismic line.

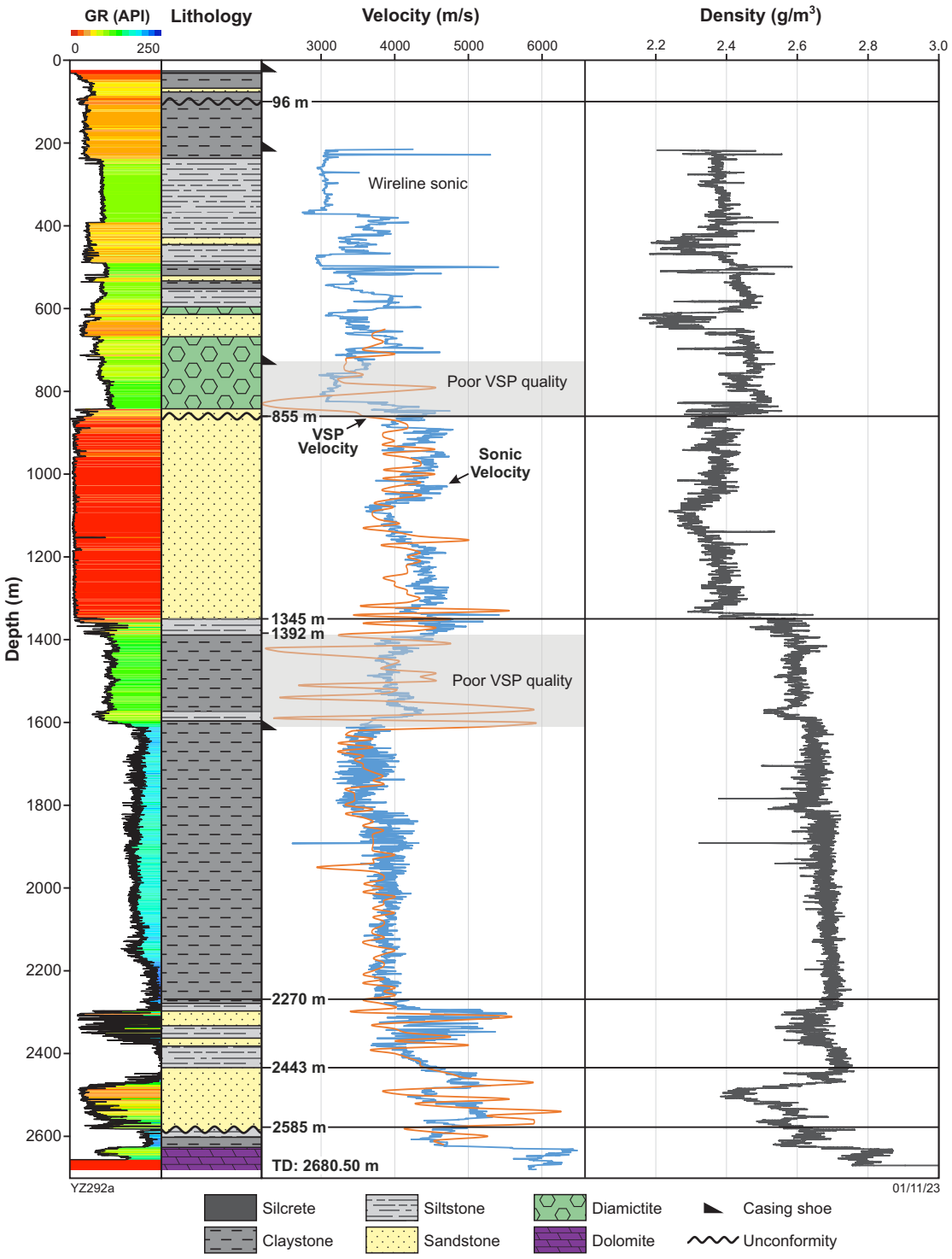

Figure 7. Wireline density (black), sonic velocity (blue; converted from sonic slowness after petrophysical correction in Walker Petrophysics, 2020) and vertical seismic profile (VSP) interval velocity (red) compared with a generalized stratigraphic column for Barnicarndy 1

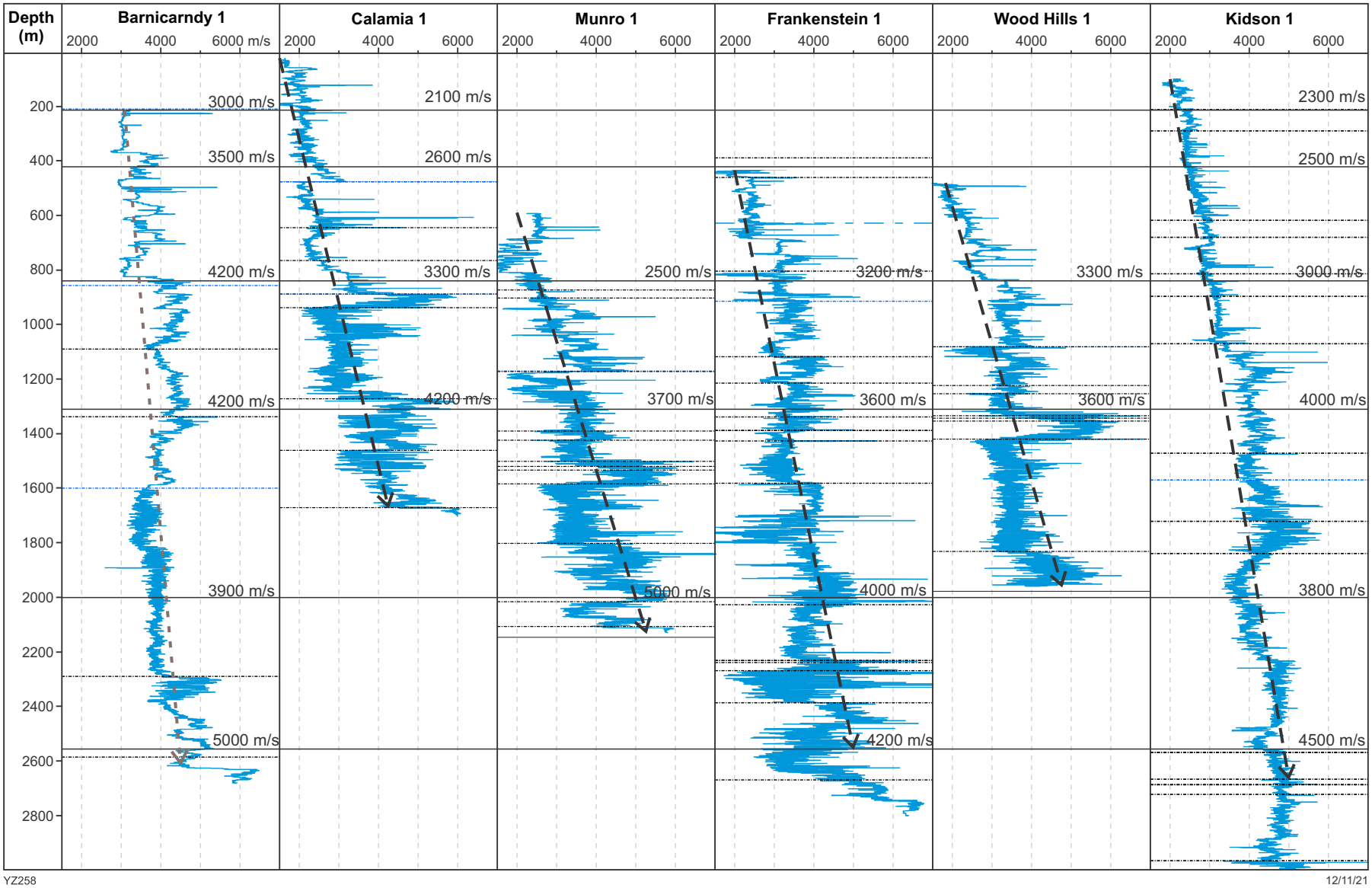

Figure 8. Sonic velocity comparison between Barnicarndy 1 and offset wells. The velocity in Barnicarndy 1 is higher than at comparable depths in offset wells and has a reduced velocity to depth gradient (dashed lines with arrows)

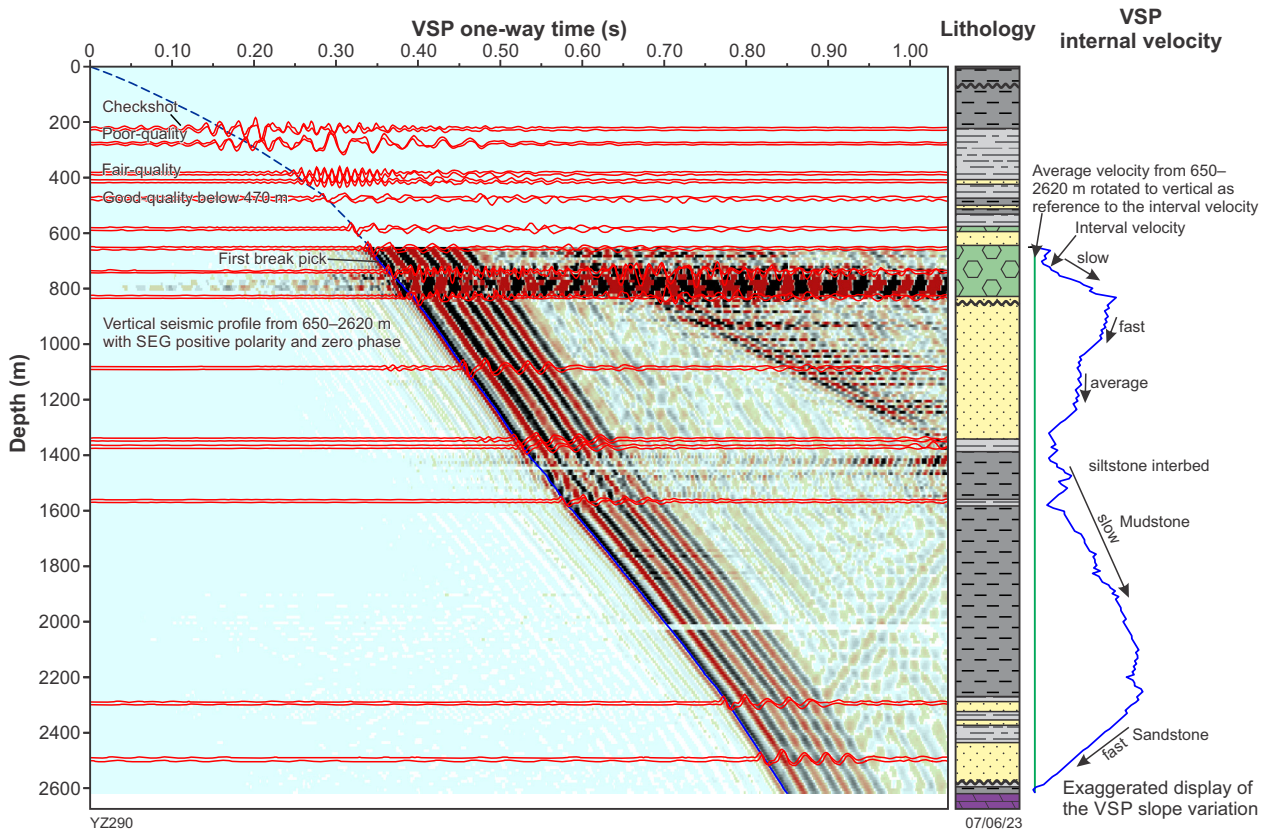

Figure 9. VSP and checkshot records. The first break picks were provided by the logging company HiSeis. The interval velocity is derived from the vertical seismic profile (VSP) slope variation and shows a consistency with lithological packages: fast velocity predominantly in sandstone and slow in mudstone-dominated diamictite and claystone

Two-thirds of the error for the depth prognosis to the top of the basement comes from the unexpected high velocity in the shallow formations. The velocity starts off at 3000 m/s at 210 m (about 48 m above MSL) and increases with depth, for example, 3500 m/s at 450 m and 4200 m/s at 855 m, with the possibility of high velocity immediately below the weathering layer at 96 m. These velocities are approximately 500 m/s to 1000 m/s faster than other Canning Basin wells at equivalent depths. Compared to the same shallow interval in Frankenstein 1, the high velocity of the Permian diamictite alone in Barnicarndy 1 reduces the seismic travel time by about 50 ms, which generates an approximately 120 m difference at the basement. The difference increases further in the high-velocity sandstone between 855 and 1345 m. The velocity reverts back to a normal range in the deep claystone with an average value of 3900 m/s at 2000 m, which slightly narrows the difference in the predrill vs actual depths for the Top basement horizon. The velocity anomalies indicate that the Barnicarndy Graben has a complex structural history and a thick sedimentary section may have been eroded during the Late Triassic.

The remaining discrepancy in depth prognosis for the basement is considered to be related to out-of-plane seismic reflections from the nearby south-southeast end of the Barnicarndy Graben. This impact is calculated to result in 130 m shallower depth difference (Table 2) at the Top basement between the in-plane drilling and out-of-plane seismic section, based on the extra approximately 55 ms shift required for the synthetic seismogram to correlate with the deep section. The steeply dipping basement causes out-of-plane issues for 2D seismic data, such that the Kidson seismic survey images the shallower basement reflected from further south, rather than what is vertically below the survey route.

The base Grant Group unconformity provides a very distinctive reflection surface, which can be traced across the Barnicarndy Graben (Fig. 11). A strong reflector is also present at the base of the Barnicarndy Formation defining the change from sandstone to mudstone. The contacts between the Samphire Marsh and Fly Flat members and the underlying Yapukarninjarra Formation are difficult to interpret on the seismic line. The Canning Basin unconformity at the base of the Yapukarninjarra Formation truncates the basement reflectors at a prominent high-amplitude horizon.

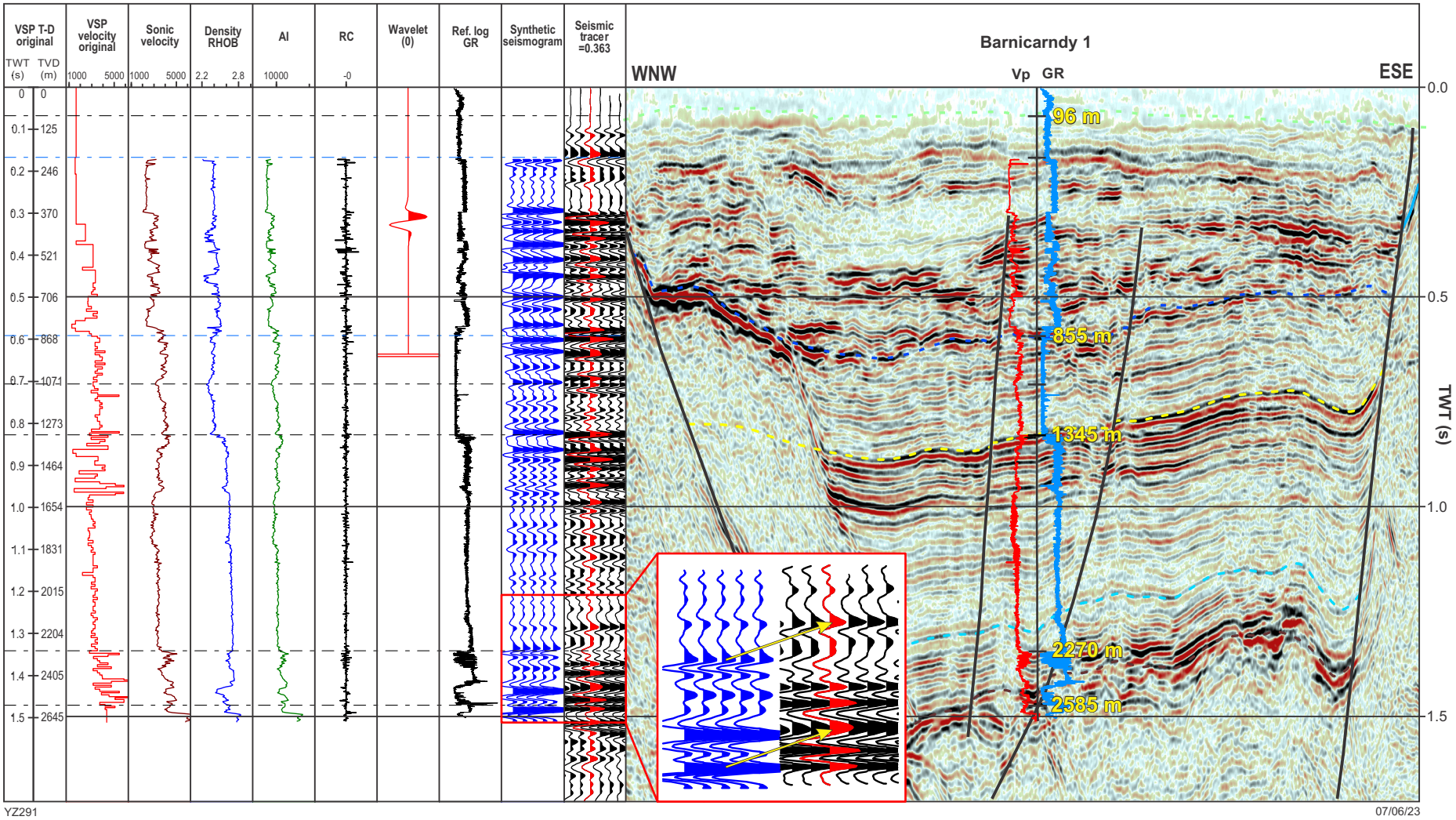

Figure 10. Synthetic seismic correlation and interpretation after shifting vertical seismic profile (VSP) time-depth pairs upwards by 215 ms. The bottom part of the well shows a mismatch and requires an additional 55 ms shift for correlation (see arrows in the enlarged box)

Table 2. Impacts of the velocity and out-of-plane issues in the prognosis of Barnicarndy 1

TWT (ms) datum (0 ms) at surface	*TWT (ms) datum (0 ms) at MSL*	*Depth prognosis (m)*	*Depth on corrected VSP after synthetic correlation (m)*	*Depth difference due to high velocity (m)*	*Depth difference caused by out-of-plane reflection (m)*	*Comments*
180	-20	210	210	0	N/A	*Permian intra-formational boundary
600	400	695	855	160	N/A	**Base Grant Group
840	640	1050	1345	≤295	Unknown	Top Nambeet Formation
1420	1220	2200	2455	255	130	Top basement

* This seismic interface was interpreted as Base Mesozoic in the well prognosis; based on palynology data and HyLogger spectral analysis, it appears to be an intra-formational boundary between claystone and sandstone within the Permian Grant Group, and the weathering layer has a thickness of about 96 m which does not show a reflection event on the seismic section at 0.06 s
** This seismic horizon was originally interpreted as Base Permian, although the base of the mostly Permian Grant Group locally extends into the upper Carboniferous (Backhouse and Mory, 2020)

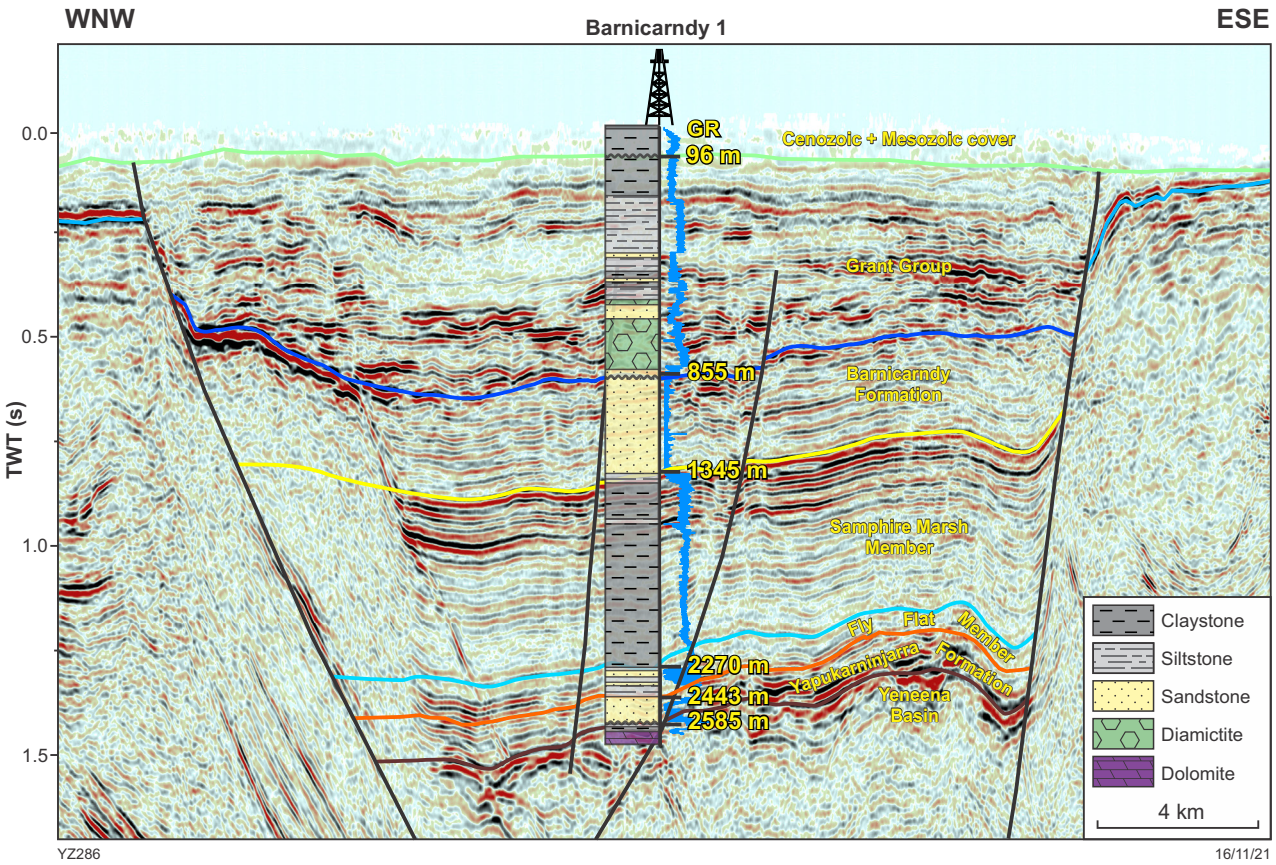

Figure 11. Barnicarndy Graben seismic section with depths to seismic reflectors of Barnicarndy 1 superimposed

Well stratigraphy

The stratigraphy in Barnicarndy 1 is anomalous compared to other wells in the southern Canning Basin, which may be the result of the distinctive tectonic history of the Barnicarndy Graben. The well provides type sections for two recently named new formations within the Canning Basin (Normore et al., 2021). Formation definition cards for the Barnicarndy and Yapukarninjarra formations are found in Appendix 2 and 3 respectively. The predicted vs actual lithology (Fig. 12) demonstrates the uncharacteristic stratigraphy compared with offset wells. Formation boundaries were established using a combination of the lithology, wireline logs, HyLogger data, paleontology, detrital geochronology and correlation with selected wells in other tectonic sub-divisions of the Canning Basin.

A thin Cenozoic section extends from the surface to 96 m depth, followed by 759 m of Carboniferous to Permian Grant Group to 855 m. Below the basin-wide Grant Group unconformity is a 1730 m thick Ordovician section comprising the Barnicarndy, Nambeet and Yapukarninjarra formations, in descending order. The Yapukarninjarra Formation, marking the base of the Canning Basin succession, unconformably overlies 95 m of Yeneena Basin weathered siltstones and dolomite to total depth.

Cenozoic

The Cenozoic section of the Barnicarndy 1 stratigraphic well includes deposits of the Percival or Canning Paleovalley (van der Graaff et al., 1977). The surface expression of the Percival Paleovalley is defined by Quaternary playa systems, whereas the valley is infilled with Cenozoic aeolian, lacustrine and fluvial deposits. The Percival Paleovalley, as with many paleovalleys in semi-arid Australia, was formed as the result of uplift following the late Paleozoic glaciation and the tectonic events associated with the rifting of Gondwana. During the Mesozoic, the erosive power of the Percival Paleoriver cut a valley by removal of weathered bedrock. The Percival Paleovalley extends in a westerly direction from Stansmore Range, northwest of Lake MacKay, to the west coast (Fig. 13). It crosses the Great Sandy Desert, turns 90° northwest following the contact between the Proterozoic Paterson Orogen and the Canning Basin, connecting Lake Dora and Lake Waukarlycarly. The Percival Paleovalley continued northwest to the Oakover River and the De Grey River Paleovalleys north to Port Hedland (Magee, 2009; Mory, 2017).

The Cenozoic section of Barnicarndy 1 can be subdivided into three distinct units from surface down to a depth of 96 m: 1) a localized, 11 m thick surficial silcrete cap, 2) a transported regolith unit from 11 to 71 m depth, and 3) an in situ regolith unit from 71 to 96 m. Although Beard (1973) suggested that the Percival Paleovalley incised the Permian–Cretaceous sequences to 60 m deep, the Barnicarndy 1 stratigraphic well confirms that the transported regolith unit reaches over 70 m deep. No visible macrofossils or fossil debris were noted in the cuttings from this section (Martin et al., 2021b), and the potential for biostratigraphic age control is therefore very low.

Miocene–Holocene (silcrete, sand and sandstone) (0–11 m)

The silcrete is off-white to white, light orange-brown to pale orange, opaque to translucent with minor carbonaceous fragments. This very hard diagenetic crust has a variable thickness of zero to 11 m from water bores in the immediate vicinity of the drill site, becoming interbedded with sandstone and loose sand. Sand grains range from light brown-grey to clear in colour, are fine to medium grained, angular to subangular and moderately sorted. Silcrete occasionally encases the sand grains and gradually gives way to claystone.

Silcrete is a silica-cemented regolith material, mostly composed of secondary silicate minerals such as anatase and amorphous silica (i.e. opal, chalcedony), but may also include iron oxides, clays, quartz, carbonates, sulfates and halite. It is formed in lower parts of the landscape along drainages and lakes by the precipitation of silica from groundwater saturated in dissolved silica. The silica is derived from the weathering of primary silicate minerals dissolved by acid groundwater. Silcretes are formed from many rock types and sediments, and are commonly preserved as topographically inversed highs and mesa cappings over ancient alluvial deposits and saprolite. The age of silcretes in Australia range through most of the Cenozoic (Krapf, 2011; Taylor, 2017).

Eocene–Oligocene (surficial transported regolith/overburden) (11–71 m)

The surficial transported regolith interval consists of light orange, light brown to tan coloured, soft and amorphous clay from 11 to 71 m (Fig. 2a). A distinctive clay mineral assemblage is identified across this interval using HyLogger™ thermal infrared (TIR) and shortwave infrared (SWIR) data from the analysis of drill cuttings within 2.5 x 4.0 cm trays (Fig. 14). Kaolinite is the dominant clay followed by smectite (montmorillonite). The abundance of silica and white mica gradually increase down section as clay, carbonate and oxide contents similarly decrease (Hancock et al., 2020b).

This clay-rich interval represents the transported sediments deposited in a playa lake system, which includes Lake Waukarlycarly and northerly flowing ephemeral rivers. Playa systems are common landforms in the arid and semi-arid regions of Australia, formed from pre-existing rivers and lakes that dried out in the Cenozoic due to climatic changes. Australia's climate has been fluctuating since the Late Cretaceous, following continental breakup between Australia and Antarctica and subsequent northward movement of the Australian Plate. At the end of the Eocene and beginning of the Oligocene, around 33 Ma ago, ocean temperatures cooled quickly causing Australia's climate to shift from warm humid to colder, mostly semi-arid conditions (Zachos et al., 2001; Pillans, 2004).

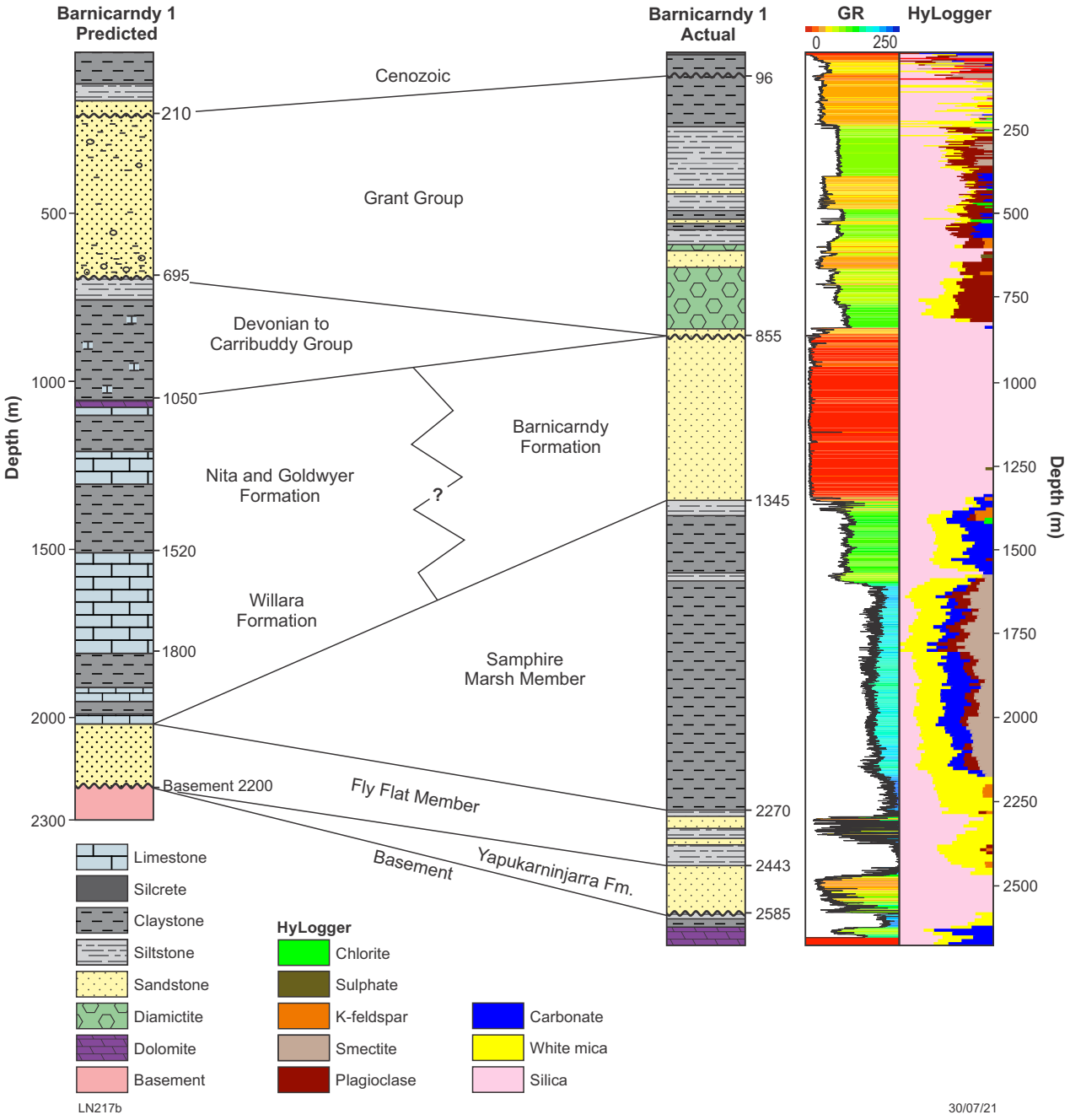

Figure 12. Predicted vs actual stratigraphy with gamma ray log and HyLogger thermal infrared (TIR) log

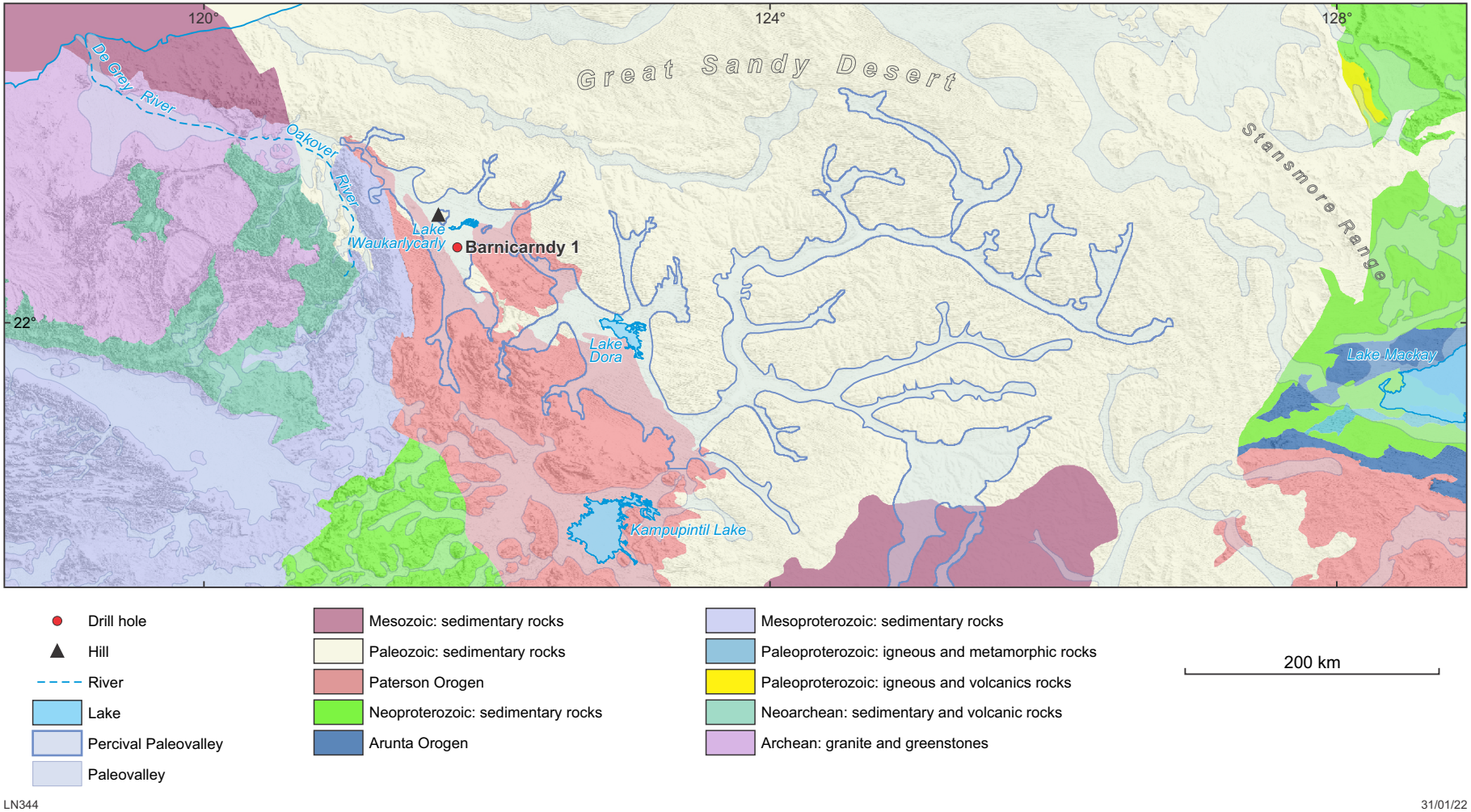

Figure 13. Percival Paleovalley map

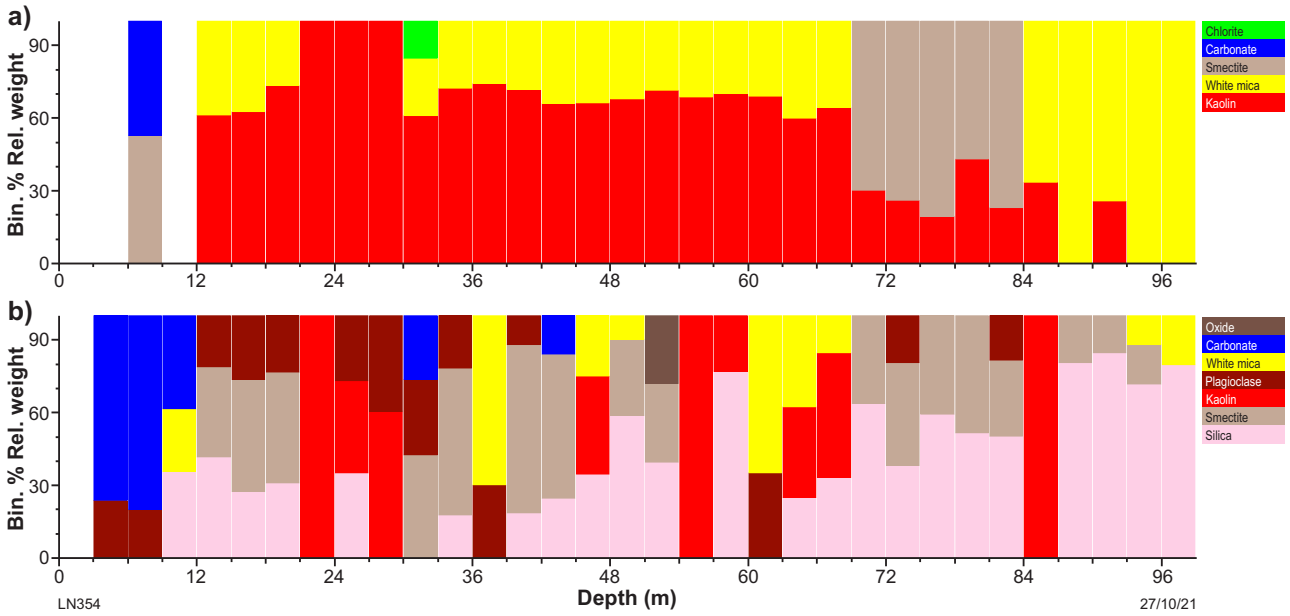

Figure 14. HyLogger data for Cenozoic regolith. Spatial summary of mineral groups in 4 m depth bins and interpreted by: a) The Spectoral Assistant (TSA) shortwave infrared (SWIR); b) TSA thermal infrared (TIR)

Mesozoic–Paleogene (residual/relict regolith) (71–96 m)

Interbedded sandstone and siltstone between 71.0 and 84.0 m followed by mottled clays down to 96.0 m has been interpreted as saprolite or residual/relict regolith (Fig. 2a). HyLogger summary data (Fig. 15) shows a sharp drop in ferric oxide abundance indicating the base of oxidation at 94.5 m, which is also likely to be the base of the regolith layer at the same depth, ± 4 m due to HyLogger sampling interval error. The boundary between the transported and residual in situ regolith is a stratigraphic discontinuity marked by a sharp change in clay mineralogy from kaolinite rich to smectite rich at 71.0 m (± 4 m). The residual regolith is clay-rich, smectite dominated, with secondary kaolinite, phengite and muscovite increasing below 85.0 m. The saprolite in this interval originates from the weathering of the underlying sedimentary unit containing white micas (phengite and muscovite), quartz, and smectite (montmorillonite). The weathering age in this part of Western Australia is Mesozoic to Paleogene (Anand, 2004).

One relatively unoxidized cuttings sample was selected from this section (75–78 m) for palynology, but the sample was lean and its age indeterminate.

Grant Group (96–855 m)

The Carboniferous to lower Permian Grant Group is 759 m thick in Barnicarndy 1, overlying a well-defined unconformity at 855 m (Fig. 2b–e) and extending up to the shallowest occurrence of Permian pollen spores at 96 m (Fig. 2a). Equivalent to the much thinner Paterson Formation, which outcrops over basement to the south of the drilling location, the Grant Group is a subsurface unit identified in all tectonic sub-divisions of the Canning Basin (Backhouse and Mory, 2020). From 96 to 580 m (over 60% of the unit) the upper Grant Group was rotary drilled, with 484 m of ditch cuttings collected at three metre intervals (Fig. 2a). The remainder of the section, covering both the upper and lower Grant Group, was continuously cored at two core sizes: 580–727 m at SQ (156 mm diameter) and 727–855 m at PQ (121 mm diameter).

A total of nine samples from eight depths within the Grant Group were processed for palynology by GSWA (Fig. 16; Martin et al., 2021b), with an additional four samples processed by Geoscience Australia (Foster et al., 2021). The uppermost four ditch cuttings samples, between 96.0 and 580.0 m, returned components of the *Pseudoreticulatispora confluens* Spore–Pollen Zone, which is assigned an Asselian age based on the most recent analysis of Canning Basin Carboniferous–Permian palynology (Backhouse and Mory, 2020). The underlying interval of core from 650.0 to 787.3 m contained elements of the Gzhelian *Microbaculispora tentula* Spore–Pollen Zone, whereas the core sample at 823.2 m is assigned to the Gzhelian to Kazimovian *Vallatisporites arcuatus* Spore–Pollen Zone. This latter assemblage was particularly low yielding, and the core was therefore sampled twice at approximately the same depth to obtain adequate palynomorphs to confirm the initial age interpretation. The deepest Grant Group sample processed, at 841.62 m, was low yielding and could not be assigned to any particular palynomorph zone, but was considered consistent with latest Carboniferous microfloras (Foster et al., 2021). The range of zones interpreted within the sampled interval matches the palynology of the Grant Group elsewhere within the Canning Basin, and can be used to distinguish an upper Carboniferous (Kasimovian to Gzhelian) lower Grant Group from 700.0 to 855.0 m and a lower Permian (Asselian) upper Grant Group from 700.0 to 96.0 m. Finally, the palynological data indicates that the Permian section in Barnicarndy 1 is restricted to the Grant Group, with the absence of the Asselian–Sakmarian *Pseudoreticulatispora pseudoreticulata* and younger spore–pollen zones in the shallowest samples suggesting an absence of the Poole Sandstone that overlies the Grant Group across most of the basin.

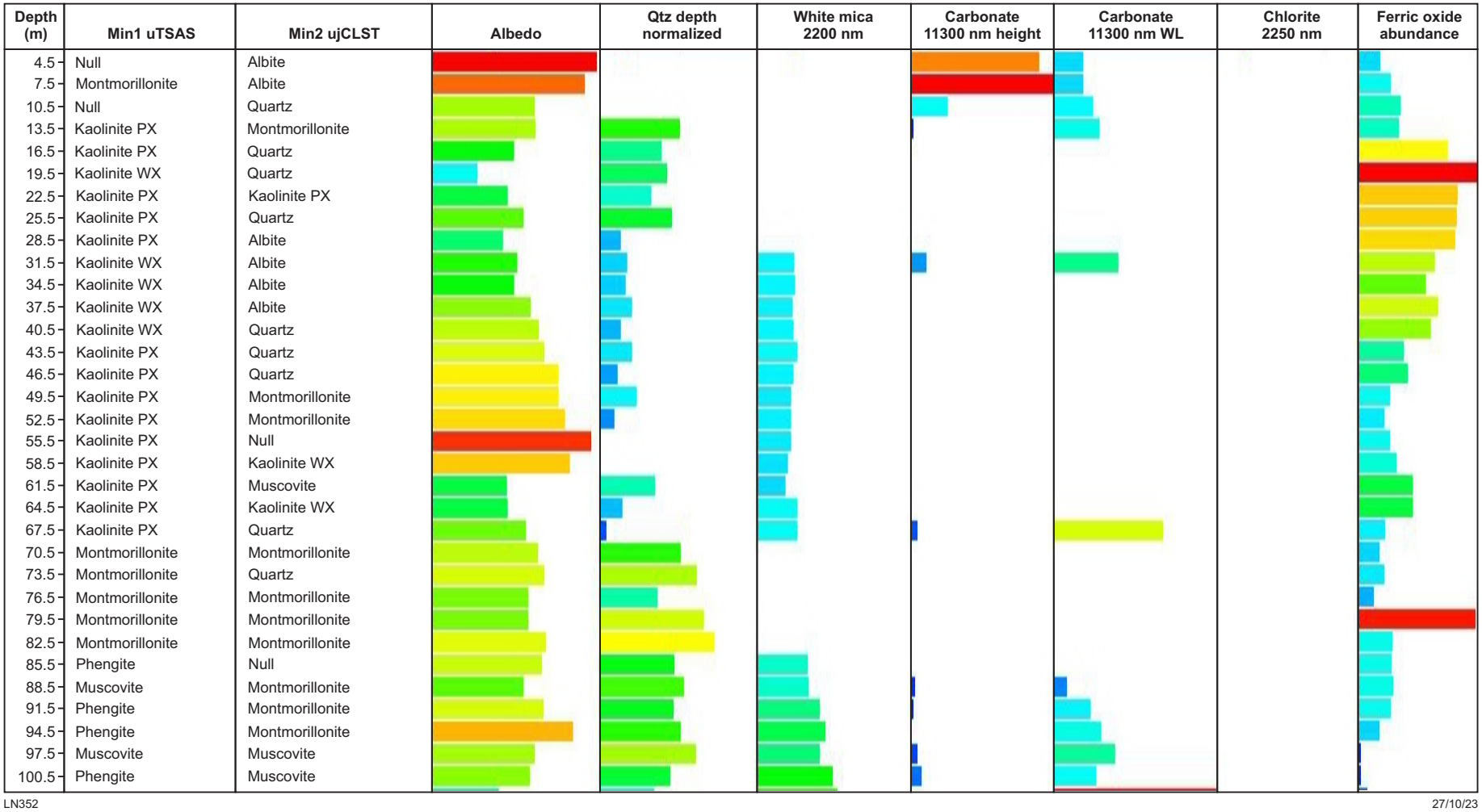

Figure 15. HyLogger log screen spatial summary of major mineralogical composition of cuttings interpreted from spectral data for Cenozoic regolith: Column 1) depth in metres; Column 2) mineral 1 by user The Spectoral Assistant (TSA) shortwave infrared (SWIR); Column 3) mineral 2 by user TSA thermal infrared (TIR); Column 4) albedo of cuttings; Column 5) quartz abundance interpreted from absorption depth of quartz diagnostic feature in TIR; Column 6) white mica–sericite–illite composition interpreted using 2200 nm AlOH absorption feature; Column 7) carbonate abundance interpreted from diagnostic peaks at 11 300 nm; Column 8) carbonate composition interpreted from diagnostic peaks at 11 300 nm; Column 9) chlorite abundance interpreted using 2250 nm absorption feature; Column 10) ferric oxide abundance interpreted from visible and near-infrared (VNIR) spectra. Abbreviations: PX, poorly crystallized; WX, well-crystallized

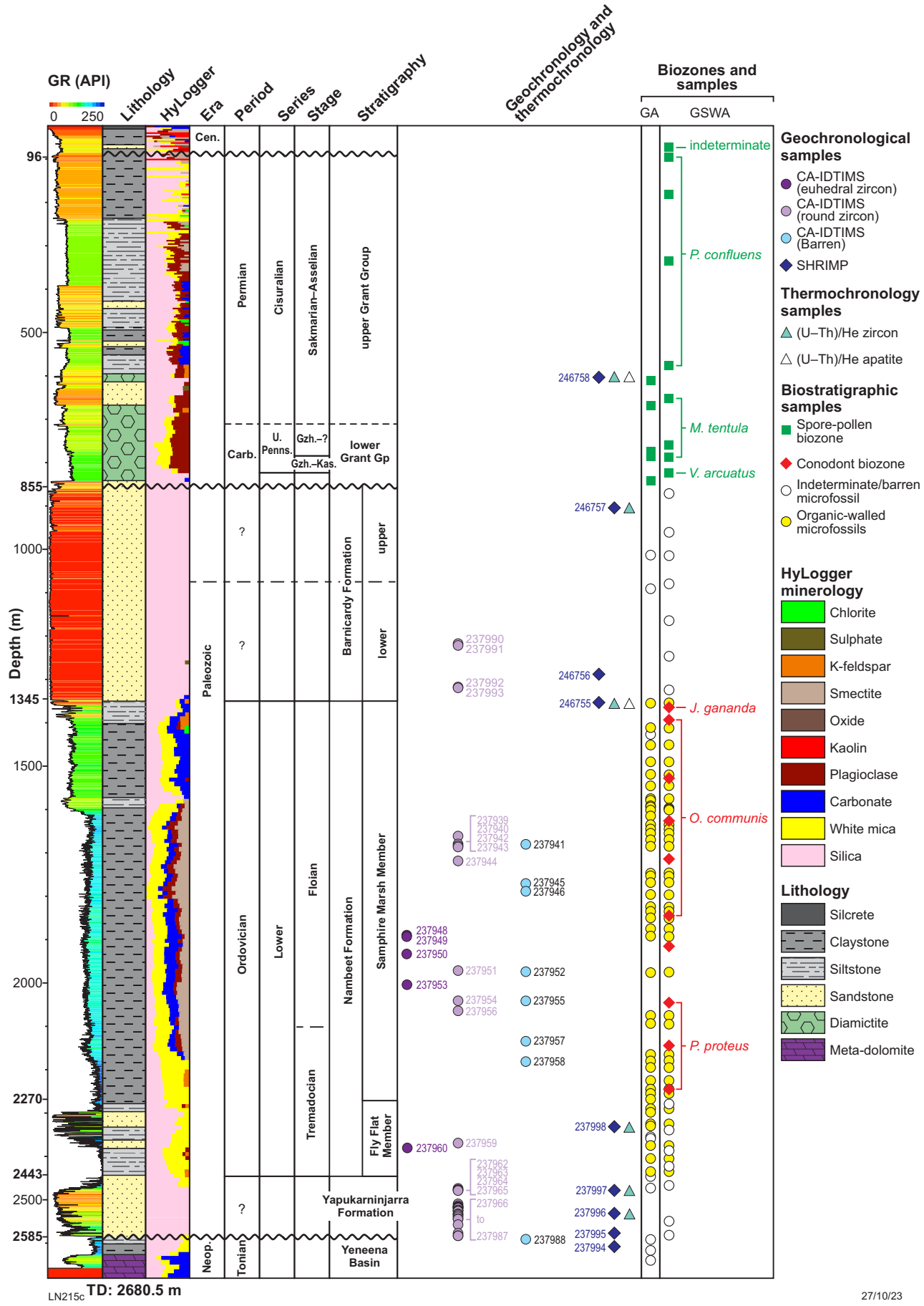

Figure 16. Stratigraphic column showing biostratigraphy, geochronology, and thermochronology sample locations

There is also no evidence of the late Carboniferous *Diatomozonotriletes birkheadensis* or older spore–pollen zones suggesting that the Reeves Formation, which locally underlies the Grant Group, is also absent.

Upper Grant Group (96–700 m)

The upper Grant Group is much more heterogeneous than the lower Grant Group, consisting of interbedded muddy diamictite, siltstone and poorly sorted sandstone (Fig. 2b) with soft-sediment deformation. With only 120 m of core over this interval (580–700 m), the bulk of the upper Grant Group is represented only by ditch cuttings. HyLogger analysis on the ditch cuttings (Hancock et al., 2020b) identified alternating carbonate and chlorite content from 580 to 400 m, with smectite content appearing from 380 to 250 m. Plagioclase content is absent from 230 m to the top of the upper Grant Group at 96 m, with the uppermost interval dominated by quartz and lesser white mica. The upper Grant Group has two reservoir sections identified from 370 to 473 m and 557 to 653 m (see under Wireline logs, below).

Lower Grant Group (700–855 m)

The lower Grant Group consists primarily of glacial diamictite with very low porosity and permeability (Fig. 2c). The diamictite has a mudstone to very fine-grained sandstone matrix and contains clasts ranging from granule to boulder size. This interval has been the focus of routine core analysis and more detailed special core analysis (reported below). The aim was to determine the seal capacity for carbon sequestration and storage within the underlying Barnicarndy Formation reservoir. The basal unconformity of the lower Grant Group (Fig. 2e) is overlain by locally reworked sandstone, eroded directly from the underlying Barnicarndy Formation, which in turn is overlain by a well-rounded, poorly-sorted, pebble to cobble conglomerate (Fig. 2d).

Wilson and Thrane (2020) completed a detailed sedimentological and structural analysis using Acoustic Televiewer (ATV) logs, defining image facies and image facies associations to describe the depositional environment for the Grant Group in Barnicarndy 1. The basal erosional unconformity is overlain by cyclical glacial deposits dating from the upper Carboniferous glacial maximum, succeeded by subaqueous outwash fan deposits produced during glacial retreat, followed by muddy diamictite deposited distal from the glacier front.

Barnicarndy Formation (855–1345 m)

The type section for the Barnicarndy Formation has been defined between depths of 855 and 1345 m in Barnicarndy 1 (Normore et al., 2021). The formation definition card is provided in Appendix 2. This formation is named after the stratigraphic well, which was in turn named after the Barnicarndy Hills 28 km north-northwest of the drill site (Fig. 1). The 490 m thick Barnicarndy Formation is primarily composed of well-sorted quartz arenite (Fig. 2f,g) and can be grossly subdivided into two intervals based on a combination of ATV and wireline log data, and trace fossil interpretations (see appropriate sections below). The upper boundary of the Barnicarndy Formation is the major angular unconformity, overlain by diamictites and sandstones, that marks the base of the Grant Group. The lower boundary is a conformable transition from the underlying siltstone and mudstone of the Samphire Marsh Member of the Nambeet Formation (Dent et al., 2021). Routine core analysis of the Barnicarndy Formation provides details on the reservoir quality of this interval and is discussed in detail under the 'Carbon sequestration and underground hydrogen storage potential' section below. Detrital geochronology results from the Barnicarndy Formation are comparable to other Ordovician formations in the Canning Basin (see Geochronology section below). The Barnicarndy Formation has a similar provenance as the Nambeet Formation and may be a proximal equivalent to the more distal Willara and Goldwyer Formations.

Shelly fossil material is rarely preserved in the Barnicarndy Formation. Martin et al. (2021b) report mostly indeterminate shells and one brachiopod at 871.4 to 871.7 m, highly fragmentary shelly material sporadically between 1090.0 and 1140.0 m, and small inarticulate brachiopods and other fragments at 1336.4 m. These fossils do not provide useful age constraints. Seven samples from this formation were processed for phosphatic microfossils (Fig. 16; Zhen et al., 2021). The primary target was fish microfossils, although the samples were also examined for conodonts. Acid processing at Macquarie University's acid preparation laboratory was completed in April 2021, with no obvious fish or conodont fossils identified (Zhen et al., 2021). As a result, there is presently no biostratigraphic control on the Barnicarndy Formation other than it is early Dapingian and younger, based on the age of the top of the underlying Nambeet Formation. The lithology is not amenable to palynology. Ichnology provides key information on the depositional settings of the Barnicarndy Formation (Appendix 4). Trace fossil abundance, diversity and ichnotaxa size were used in combination with sedimentary structures to divide the formation into seven distinct intervals (Fig. 17). A summary of Allgöwer's detailed ichnological analysis from Appendix 4 is found in the ichnology section below.

Upper Barnicarndy Formation (855–998 m)

The upper Barnicarndy Formation is 143 m thick, from 85 to 998 m. This clean, moderately sorted, fine- to coarse-grained quartz arenite (Fig. 2f) is differentiated from similar lithologies in the lower Barnicarndy Formation based on differences in ichnofacies (Appendix 4), ATV log interpretation (Appendix 5; Wilson and Thrane, 2020) and petrophysical evaluation (Fig. 17; Appendix 6, Walker, 2020; Appendix 7, Walker, 2021). The change in ichnofacies, paleo-flow direction and formation water salinity may indicate a localized change in tectonic setting or a disconformity at the boundary between the upper and lower Barnicarndy Formation.

Calculated formation water salinities were determined by analysing five additional core plugs for special core analysis, using a known salinity saturation to calculate the formation resistivity factor (FRF) and the cementation exponent 'm' (Walker, 2021). This confirmed the original petrophysical interpretation by Walker (2020) that formation water in the upper Barnicarndy Formation (unknown sandstone #1 in Walker (2020) had much higher salinity than the lower Barnicarndy Formation). The subsequent analysis of core electrical properties and re-examination of the wireline log data reveals that the upper Barnicarndy Formation

covers the salinity transition interval with 32 000 ppm NaCl equivalent occurring from 1000 to 950 m, increasing to 80 000 ppm NaCl equivalent from 950 m to the top of the Barnicarndy Formation reservoir section at 855 m.

ATV logs enable evaluation of paleocurrent patterns through the Barnicarndy Formation (Wilson and Thrane, 2020). This data includes all flow-relevant bedding and erosion features picked from the ATV log and is summarized as azimuth rose diagrams for six intervals through the formation (Fig. 17). A consistent northeasterly average paleoflow direction is evident through most of the lower Barnicarndy Formation before changing slightly to the north. At the base of the upper Barnicarndy Formation, the average paleoflow direction changes to the west and finally to the northwest for the top of the upper Barnicarndy Formation.

Lower Barnicarndy Formation (998–1345 m)

The lower Barnicarndy Formation extends from 998 m down to a gradational contact with the underlying Samphire Marsh Member of the Nambeet Formation at 1345 m. As with the upper unit, it is also dominated by well-sorted, fine to medium-grained quartz arenite (Fig. 2g) with excellent reservoir quality. The ATV logs have been used to interpret continuous deposition from the Lower Ordovician Samphire Marsh Member of the Nambeet Formation to the lower Barnicarndy Formation. The cryptic contact with the upper Barnicarndy Formation is defined based on ichnology, wireline and ATV interpretation as discussed above.

Nambeet Formation (1345–2443 m)

Samphire Marsh Member (1345–2270 m)

The Samphire Marsh Member is the mudstone-dominated upper member of the Nambeet Formation. This member was recently formally defined and described based on the cored interval from petroleum exploration well Olympic 1, drilled on the Broome Platform in 2015 by Buru Energy (Dent et al., 2021). The type section in Olympic 1 was defined by facies, biostratigraphy, geochronology and HyLogger spectral signature (Dent et al., 2021). This fine-grained member commonly consists of limestone–marl rhythmites similar to the facies described by Munnecke and Samtleben (1996). The mudstones are generally calcareous and contain carbonate nodules, whereas limestone textures range from grainstone to wackestone.

The presence of a section equivalent to the upper Nambeet Formation in Barnicarndy 1 was initially suggested at the drillsite based on tentative trilobite identifications, and was subsequently confirmed with conodont identifications (see under Conodonts below and Zhen et al., 2021). The facies seen in this well differ from the type section in the lack of well-defined limestone intervals, possibly indicating a more distal setting in this part of the Canning Basin. In Barnicarndy 1, the Samphire Marsh Member is a predominantly calcareous mudstone unit (Fig. 2h) with minor siltstone to very fine-grained sandstone beds in the upper section. It is highly fossiliferous (Martin et al., 2021b), organically leaner (see under Organic geochemistry below) when compared to the type section (Dent and Normore, 2017; Normore and Dent, 2017b), and contains multiple bentonite beds (see under Geochronology below).

The contacts between the Samphire Marsh Member and both the older Fly Flat Member of the Nambeet Formation and overlying Barnicarndy Formation are conformable, with evidence of continuous deposition. The Samphire Marsh Member is 925 m thick, more than four times thicker than the type section in Olympic 1, indicating either a more complete section, or greater subsidence and more rapid deposition in the Barnicarndy Graben than on the Broome Platform.

Ten conodont samples were processed from the Samphire Marsh Member (Fig. 16) as detailed in Zhen et al. (2021). The resulting data provides age constraints for the unit, with the identified assemblage suggesting the late Floian to early Dapingian *Jumodontus gananda* Conodont Biozone from 1354 to 1356 m, the middle Floian *Oepikodus communis* Conodont Biozone from 1394 to 1848 m, and the upper Tremadocian to lower Floian *Paroistodus proteus* Conodont Biozone from 2047 to 2248 m (Zhen et al., 2021). In other Canning Basin wells the *O. communis* and *J. gananda* Biozones are variously recorded in both the Nambeet and overlying Willara formations (Zhen et al., 2020), indicating the time-transgressive nature of the lithostratigraphic formation boundaries, whereas the *P. proteus* Biozone is recorded only in the Nambeet Formation.

The Samphire Marsh Member is densely and diversely fossiliferous (Martin et al., 2021b), with the macrofossils strongly reminiscent of assemblages recorded from Lower to Middle Ordovician units elsewhere in the Canning Basin and more broadly across northern Australia. This suggests that this unit is predominantly Lower Ordovician in age, which agrees well with the conodont biostratigraphic data cited above (Zhen et al., 2021).

Although detailed ichnology studies (Appendix 4) were mostly focused on the Barnicarndy and Yapukarninjarra Formation, a small section of the upper Samphire Marsh Member was also examined. In this section, a combination of ichnological and sedimentological evidence including synaeresis cracks, a decrease in trace fossil diversity and reduction in ichnotaxa indicates an up-section transition from fully marine conditions in the upper Nambeet Formation into more stressed brackish conditions at the start of the Barnicarndy Formation.

A reconnaissance study conducted on organic-walled microfossil assemblages of the Nambeet Formation recovered a diverse assemblage of acritarchs, graptolites, chitinozoans, and scolecodonts from both the Samphire Marsh and Fly Flat Members (Foster et al., 2021). The occurrence of the acritarch *Aryballomorpha grootaertii* in the lower Samphire Marsh Member is significant as known occurrences are from faunally dated upper Tremadocian to lower Floian sections in northeast China and Canada (see Foster and Wicander 2015, p.388). *A. grootaertii* was also recorded from assemblages from the Nambeet Formation in Acacia 2 by Foster and Wicander (2015). Although earlier studies suggested that the enigmatic (possibly cyanobacterial) microfossil *Gloeocapsomorpha prisca* was confined to younger (Middle) Ordovician palynological assemblages in the Canning Basin, and its common abundance used as a biozone marker (Combaz and Peniguel, 1972), many recent studies (mostly unpublished) have shown that this is no longer an applicable correlation (Fowler et al., 2004), and the results from Barnicarndy 1 corroborate those reports (Foster et al., 2021).

Fly Flat Member (2270–2443 m)

The recently formally defined Fly Flat Member is the lower sandstone-dominated interval of the Nambeet Formation, with a cored type section in the Olympic 1 petroleum exploration well (Dent et al., 2021). The Fly Flat Member in Barnicarndy 1 extends from a conformable upper contact with the overlying Samphire Marsh Member at 2270 m to a conformable lower contact with the underlying, recently defined Yapukarninjarra Formation at 2443 m, giving a total thickness of 173 m. This member is characterized by white, very fine to fine-grained sandstone (Fig. 2i) with low permeability and porosity owing to the occurrence of siliceous and carbonate cements. Interbeds of siltstone and mudstone occur throughout the Fly Flat Member, and it also contains common glauconite and trace pyrite. This member in Barnicarndy 1 is nearly three times thicker than the type section in Olympic 1 on the Broome Platform, again suggesting greater subsidence and more rapid deposition in the Barnicarndy Graben.

None of the four samples collected for phosphatic microfossils within the Fly Flat Member (Fig. 16; table 1 of Zhen et al., 2021) yielded any diagnostic conodont elements, although the deepest sample yielded a simple, cone-shaped element. The Fly Flat Member is much less carbonate-rich and less fossiliferous than the overlying Samphire Marsh Member, as also noted in wells elsewhere within the Canning Basin (Dent et al., 2021).

Organic-walled microfossils were common within the Fly Flat Member in Barnicarndy 1 (Foster et al., 2021) and integration with palaeofacies data is required to elucidate the differences in depositional environment between the two members of the Nambeet Formation. Macrofossils are also recorded within this section of the Nambeet Formation (Martin et al., 2021b), although these sediments appear to be less fossiliferous than the overlying Samphire Marsh Member.

Yapukarninjarra Formation (2443–2585 m)

The Yapukarninjarra Formation was named after consultation with the Western Desert Lands Aboriginal Corporation, and is a Martu word translated as 'rock underground' (Normore et al., 2021). The type section for the Yapukarninjarra Formation was defined from 2443 to 2585 m in Barnicarndy 1 with a total thickness of 142 m. The formation definition card is provided in Appendix 2. The Yapukarninjarra Formation consists of red and grey, medium to coarse-grained quartz arenite (Fig. 2j) with rare mottled bioturbation, local argillaceous sandy siltstone interbeds and poorly sorted arkose at the base.

The detrital zircon age signature of the Yapukarninjarra Formation varies from that of the overlying Fly Flat Member (Normore et al., 2021; see under Geochronology below). The base of the Yapukarninjarra Formation is a major angular unconformity with pre-Canning Basin basement (Fig. 2k). The formation is inferred to include some of the oldest sedimentary rocks intersected thus far in the Canning Basin, and a possible late Cambrian age has been suggested based on preliminary chemostratigraphic interpretations, which suggest a distinctive chemical signature for this interval (Appendix 8; Forbes et al., 2020). Further geochronological and biostratigraphic evidence will be required to confirm the age of the Yapukarninjarra Formation.

Three samples from the Yapukarninjarra Formation were processed for conodonts (Fig. 16; table 1 of Zhen et al., 2021), but none yielded age-diagnostic elements; similarly, two samples were processed for acid-soluble microfossils, but both were found to be barren (Foster et al., 2021). Due to these results and the lack of macrofossils identified within this section of the core (Martin et al., 2021b), there is presently no biostratigraphic control on this recently defined formation other than it is older than the upper Tremadocian, based on the oldest age-diagnostic conodont sample from the conformably overlying Nambeet Formation. Ichnological analysis suggest brackish to marine traces grading up from *Skolithos* to *Cruziana* ichnofacies (Appendix 4).

Yeneena Basin unit (2585.0 – 2680.5 m)

The pre-Canning basement consists of an upper paleo-regolith and paleo-weathering horizon of red silty mudstone (Fig. 2l) gradationally overlying fresh rock comprised of weakly metamorphosed grey, thinly laminated, dolomitic siltstone (Fig. 2m). Bedding in both fresh and weathered horizons is very steeply dipping with faulting and folding throughout and distinct near-vertical cleavage, consistent with lowermost greenschist-facies metamorphism. The Kidson seismic line interpretation (Doublier et al., 2020a), and detrital zircon geochronology (Normore et al., 2021) assists in correlation of this interval with the Yeneena Basin, which is exposed adjacent to the Barnicarndy Graben. The cored interval cannot be confidently assigned to a specific stratigraphic unit, although several formations of the Yeneena Basin contain similar carbonate intervals, including the Isdell Formation, which is inferred under cover to the west and south of the graben.

'Paleo-regolith' weathered top to the Yeneena Basin unit (2585–2625 m)

The interval from 2585 to 2625 m represents a 40 m thick paleo-regolith developed on metamorphosed carbonate sedimentary rocks of the lower Neoproterozoic Yeneena Basin (Doublier et al., 2020a). Its relative age is Neoproterozoic, possibly related to a prolonged period of weathering prior to the failed rifting of the Canning Basin.

The first analytical indicator that this interval is a regolith unit is the increase in white mica identified in the shortwave infrared (SWIR) HyLogger data, from 40 to 70% in the fresh basement to 100% white mica (Fig. 18) in the weathered zone (Hancock et al., 2020a). White mica in regolith is generally present in lower saprolite, as it is produced during weathering of surficial deposits, breaking down to clay species (Eggleton, 2008). The second indicator is the calculation of the chemical index of alteration (CIA; Wang et al., 2020), which separates the weathered horizon from the fresh dolomitic siltstones below (see under Multi-element geochemistry below).

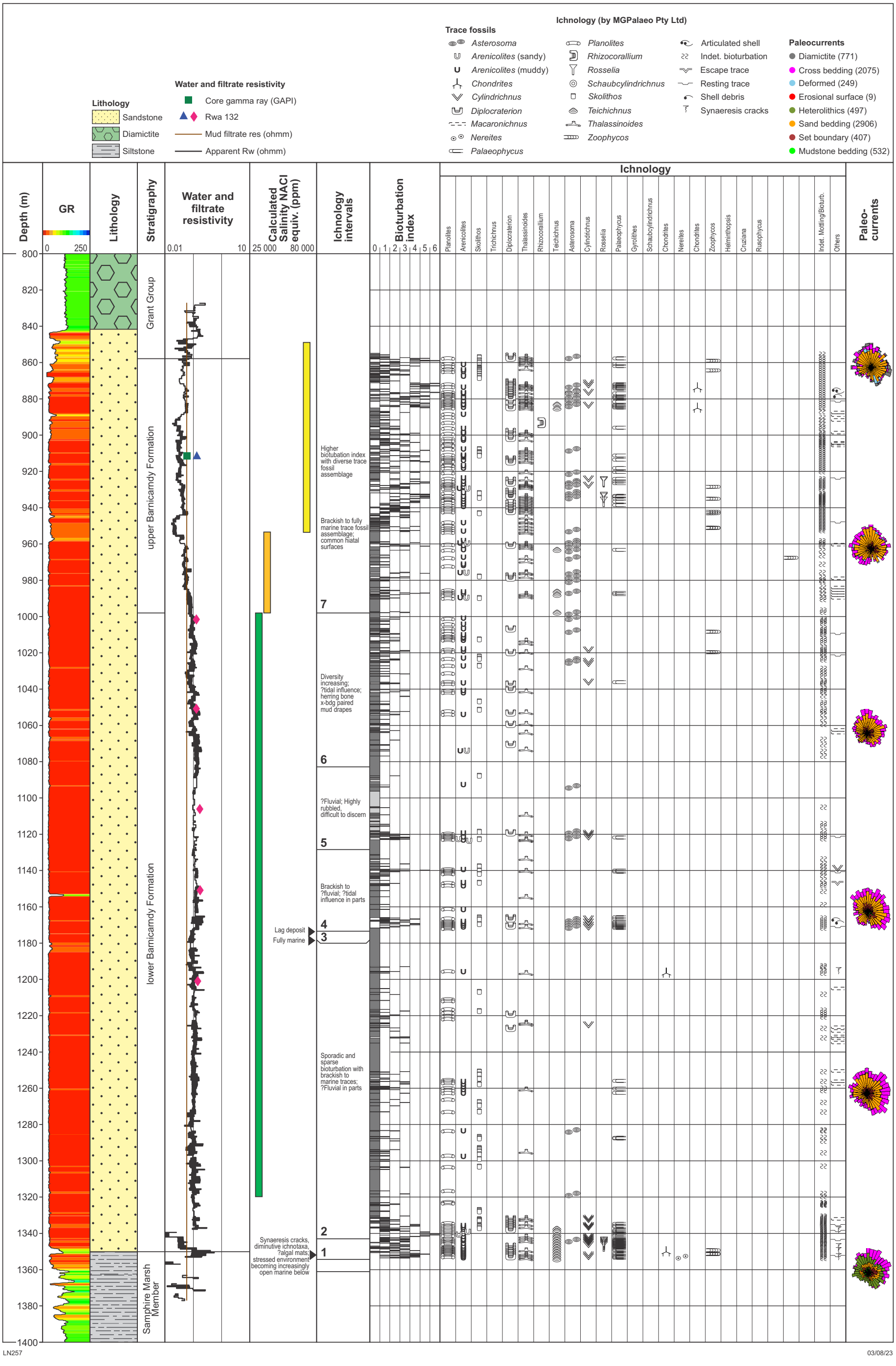

Figure 17. Separation of the upper and lower Barnicarndy Formation based on calculated salinities, ichnology interpretations and acoustic televiewer (ATV) paleocurrent interpretations (data from Appendix 4, 5 and 6)

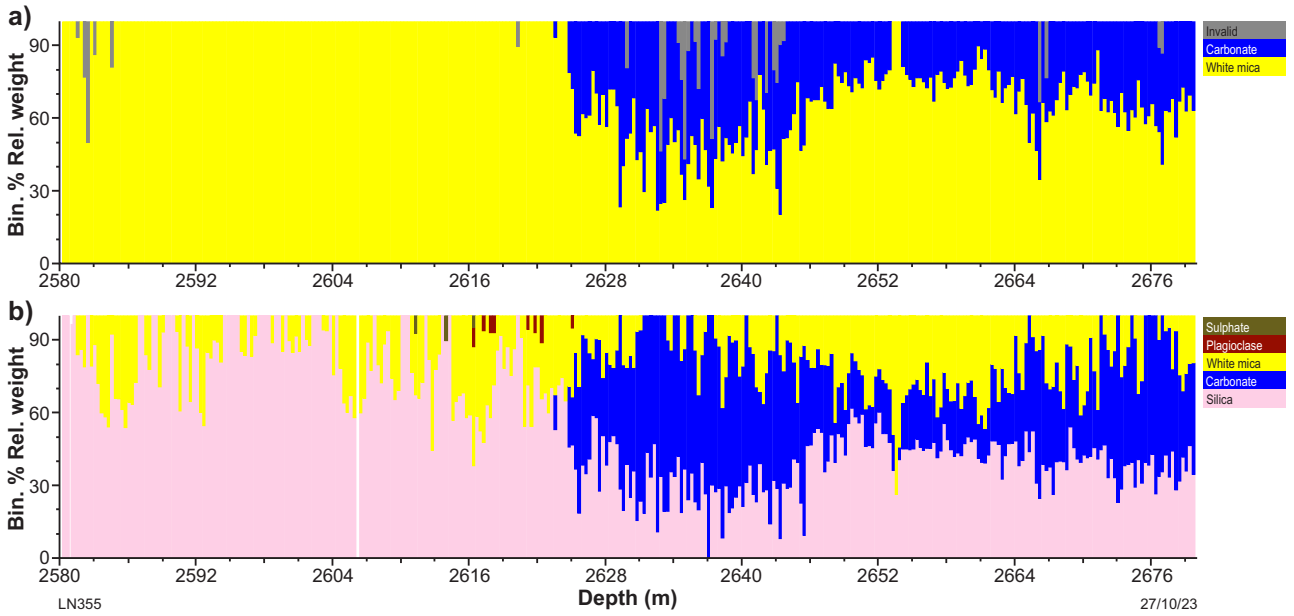

Figure 18. HyLogger data for paleo-regolith, spatial summary of mineral groups binned by 4 m and interpreted by: a) TSA shortwave infrared (SWIR); b) TSA thermal infrared (TIR)

'Fresh' Yeneena Basin unit (2625.0 – 2680.5 m)

The HyLogger data indicates a lithological boundary at 2625 m (Fig. 19), interpreted as the base of the paleo-regolith and transition into fresh pre-Canning basement rocks. The unaltered Yeneena Basin section below this point consists of a highly fractured, light grey, slightly metamorphosed dolomitic siltstone. The cored interval is 49.5 m, but due to the very steep dip of bedding the core intersected a relatively thin true thickness. The HyLogger data indicates abundant dolomite-ankerite below 2625 m. Ankerite is a Fe–Mg–Mn carbonate forming from the hydrothermal alteration or metasomatism of carbonate-rich rocks.

Petrophysical evaluation

A log based petrophysical evaluation includes five separate studies. The interpretation of Acoustic Televiewer (ATV) logs covered the upper two-thirds of Barnicarndy 1, the spectral core gamma focused on geological contacts, while the wireline logging interpretations covered the entire drilled interval.

ATV logs were instrumental in initiating a depositional environment reconstruction for the entire Barnicarndy 1 sedimentary section (Appendix 5; Wilson and Thrane, 2020). ATV logs also subdivided the upper Barnicarndy 1 stratigraphy into three distinct structural zones, provided a maximum horizontal stress orientation and specified sediment dispersal trends.

Spectral core gamma measurements across the formation contacts provided an accurate depth match between the wireline logs and the core. This was particularly important to match logging depth and amalgamate the four separate logging datasets in the initial wireline logging interpretation (Walker, 2020). A standard and artificial neural network (ANN) petrophysical interpretation was completed on the Ordovician section (Wang et al., 2021). A fifth petrophysical study focused on the Barnicarndy Formation, confirming a reverse formation water salinity transition corresponding to the contact between the upper and lower Barnicarndy Formation.

Acoustic Televiewer log analyses

ImageStrat Limited provided a structural and sedimentological analysis of the Barnicarndy 1 Acoustic Televiewer (ATV) logs (Appendix 5; Wilson and Thrane, 2020). These logs cover a 1386 m thick interval (212–1598 m), which includes the uppermost 251 m of the Samphire Marsh Member of the Nambeet Formation, the entire Barnicarndy Formation and most of the Grant Group. ATV logs were acquired by Wireline Services Group, following completion of the intermediate PQ hole section using the borehole Televiewer probe BHTV42 (Normore and Rapaic, 2020). The detailed ATV log interpretation by Imagestrat Limited provided structural zonation, in situ stress regime, sediment dispersal and a depositional history across this depth interval.

Structural zonation

Structural zonation was based on analysis of dip orientation of mudstone bedding which identified three distinct structural zones (Fig. 20). The deepest zone occurs from the base of the ATV log at 1598.0 – 1489.3 m with a mean dip orientation of 02°/240°. The second zonation extends from 1489.3 to 855.0 m with a mean dip orientation of 02°/255°. Structural zone 2 is particularly important, as this suggests continuous deposition from the Samphire Marsh Member of the upper Nambeet Formation into the overlying Barnicarndy Formation. In the absence of biostratigraphic control, the structural continuity implying continuous deposition from

the underlying biostratigraphically and geochronologically constrained Floian Samphire Marsh Member provides additional evidence for an Ordovician age for the Barnicarndy Formation. Structural zone 3 occurs over the Grant Group interval and has a mean dip orientation of 01°/190° indicating a significant 65° shift in dip direction towards the south during the late Paleozoic glaciation.

Stress regime

The identification of borehole breakout within the ATV logs provided a mean orientation of 354° for the minimum horizontal stress in Barnicarndy 1 (Fig. 21). This provides a maximum horizontal stress orientation of 84–264°, filling a previous large data gap in northern Western Australia (Fig. 22). Comparing the sparse dataset in the Canning Basin and adjacent Pilbara Craton to the Australia wide dataset (Rajabi et al., 2017) demonstrates that the Barnicarndy Graben currently resides on a major flexure in the regional stress regime (Fig. 23), possibly reflecting ongoing structural deformation in the crustal boundary between the Pilbara and the pre-Canning Basin basement. Recent updates of the Australian Stress Map emphasize the direct relationship of recent deformation to contemporary stress and the increased significance of intra-plate stress sources (Rajabi et al., 2017; Bailey et al., 2021).

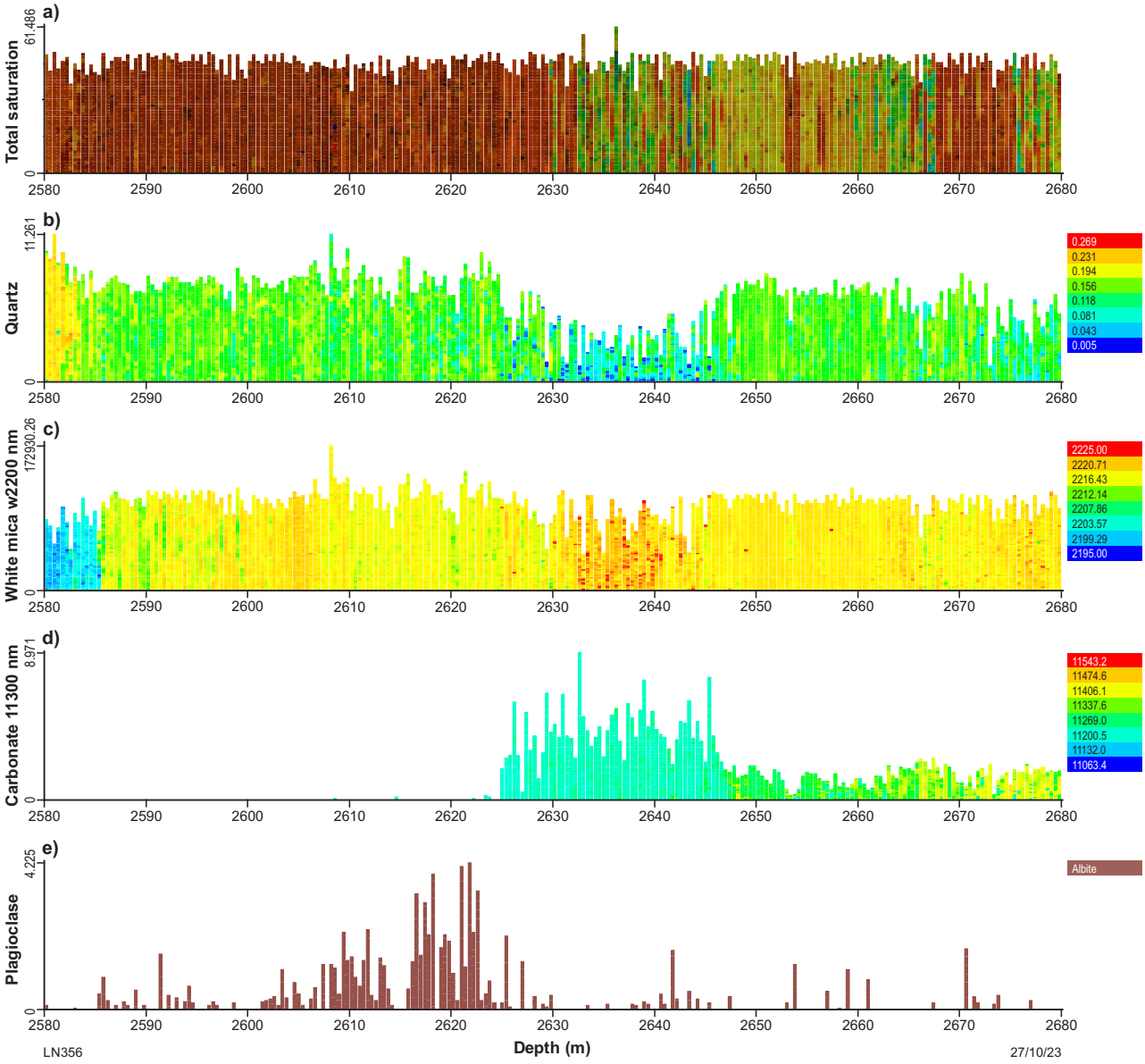

Figure 19. Spatial summary of major mineralogical composition of paleo-regolith drillcore binned by 0.8 m and interpreted from spectral data: a) total saturated RGB colour of core; b) quartz abundance interpreted from absorption depth of quartz diagnostic feature in thermal infrared (TIR); c) white mica–sericite–illite abundance and composition interpreted using 2200 nm AlOH absorption feature on the base of TSA data for white mica; warmer colours – Al-poor, Fe-rich or phengitic mica; cooler colours – Al-rich, Fe-poor or muscovite mica; d) carbonates abundance and composition interpreted from both diagnostic peaks at 6500 nm and 11 300 nm; coloured by variations in wavelength of 11 300 nm peak; warmer colours – Fe-rich carbonates (Fe calcite and possible siderite); cooler colours – Mg-rich carbonates (dolomite in this dataset); green and yellow colours – ankerite and calcite respectively; e) plagioclase abundance from albite

Top (m)	Base (m)	Zone	Azimuth rose	Dip (°)	Azimuth (°)	Origin of change in dip: comments	Formation
214.30	854.87	Zone 3	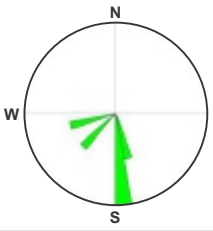	01	190	Boundary at erosion surface. Change in facies. First appearance of diamictite in Zone 3. Change in dip angles indicate an unconformity.	Grant Group
854.87	1494.07	Zone 2	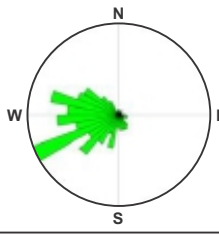	02	255	Boundary at minor change in bedding orientation and close to washout zone possibly reflecting a (non-imaged) fault. Possibly due to a minor change in basin tilt due to tectonic tilting.	Barnicarndy Formation and upper Samphire Marsh Member (boundary at 1345 m)
1494.07	1598.53	Zone 1	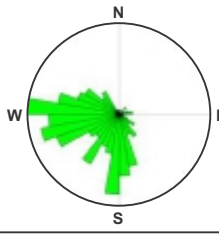	02	240		Samphire Marsh Member

LN349 07/06/23

Figure 20. Structural zones defined from dip orientation of mudstone determined by acoustic televiewer (ATV) log interpretation (Appendix 5; Wilson and Thrane, 2020)

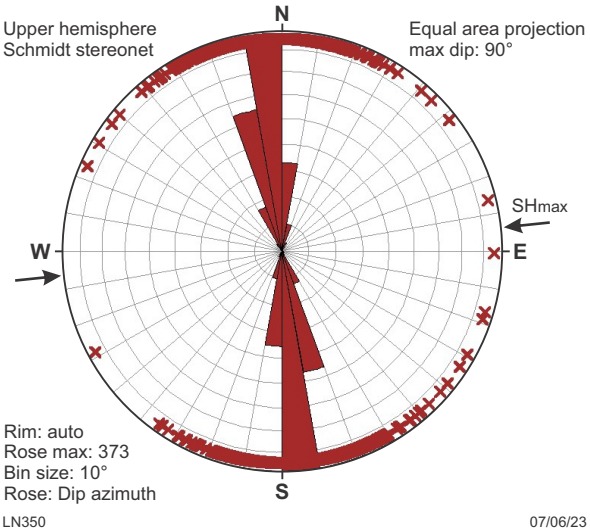

Figure 21. Azimuth orientation of borehole breakouts. The orientation of SHmax is 84°–264°, 90° to the orientation of breakouts or minimum stress (from Appendix 5; Wilson and Thrane, 2020)

Sediment dispersal

Cross-bedding dip directions (with structural dip removed) were measured over the Barnicarndy Formation and Grant Group sections to provide sediment dispersal analysis. Cross-bedding was not observed in the upper Samphire Marsh Member. Dip azimuth vector walkout plots and the accompanying stereonet rose diagram illustrate the north-easterly dip azimuth trend from 1332 to 1072 m (Fig. 24). This is followed by a highly variable paleo-flow direction up to 955 m before a consistent trend to the northwest develops. This 90° change in mean sediment dispersal direction may represent a change in depositional environment from shoreface to tidal. The change in transport direction coincides with a formation water salinity boundary identified through wireline log interpretation (Appendix 6; Walker, 2020; Appendix 7; Walker, 2021) and the boundary between distinctive ichnological units (Appendix 4) separating the Barnicarndy Formation into two distinct sandstone units.

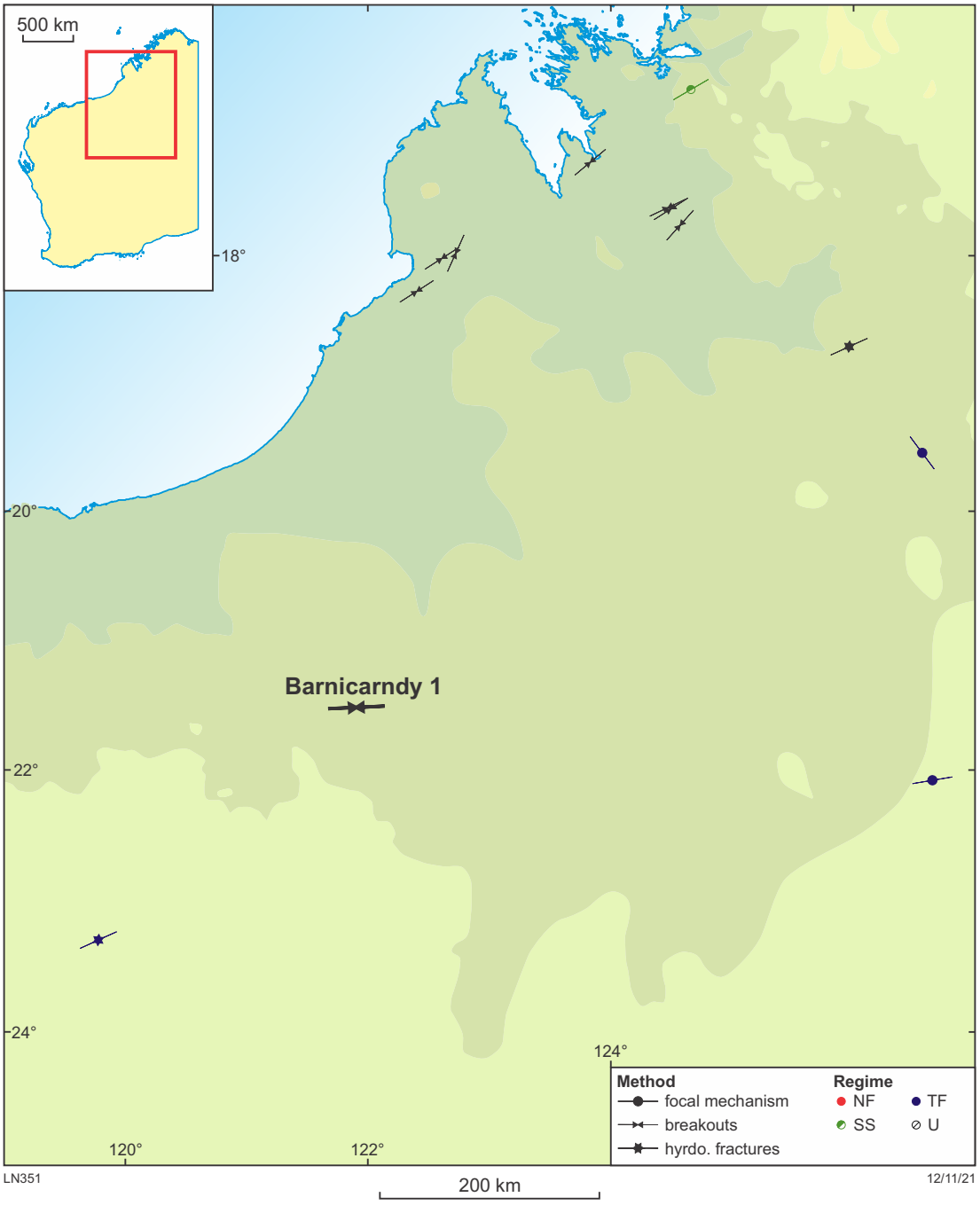

Figure 22. SHmax orientations from the Canning Basin area from the World Stress Map Project <www.world-stress-map.org>. The position of Barnicarndy 1 is shown along with the SHmax orientation derived from breakout orientation (from Appendix 5; Wilson and Thrane, 2020)

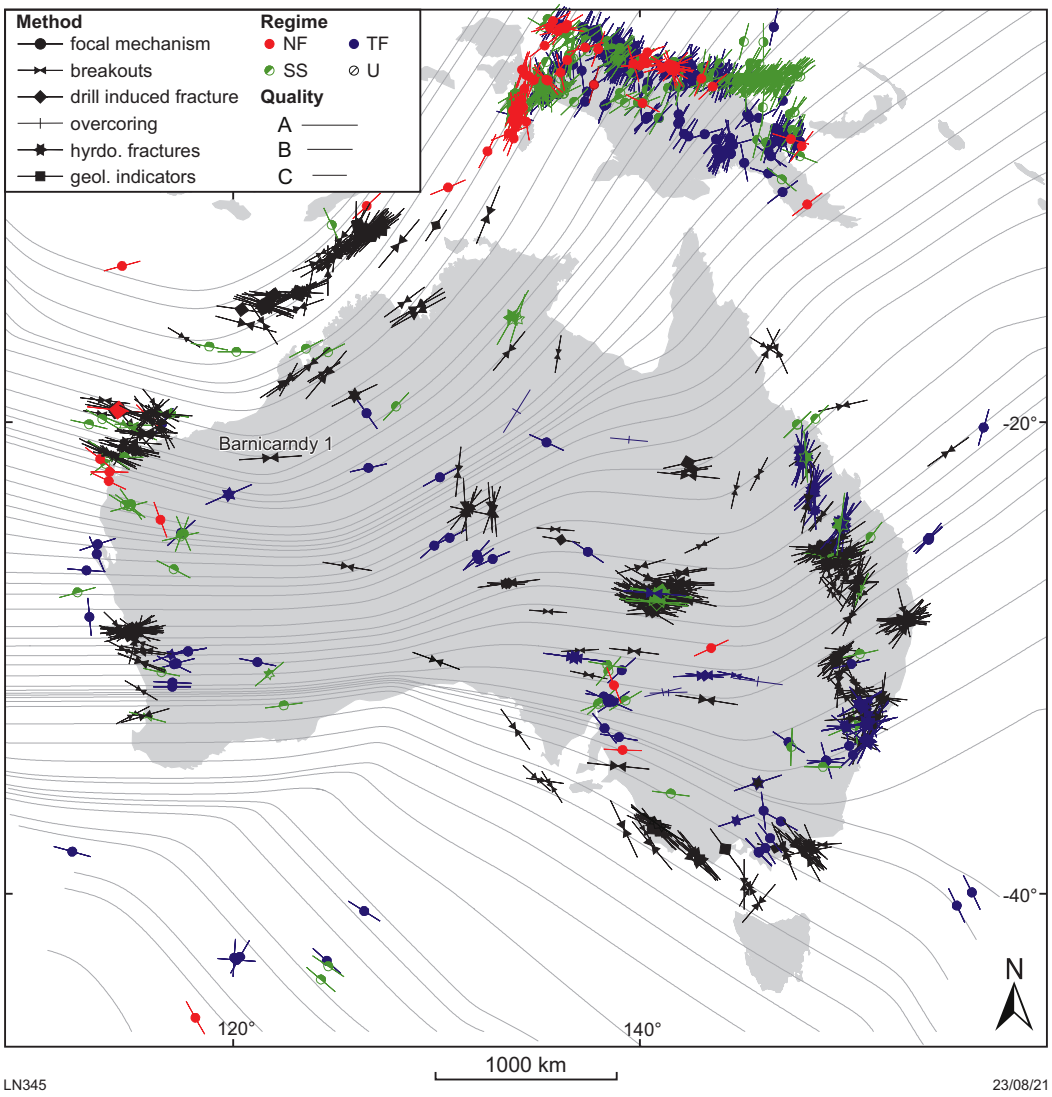

Figure 23. SHmax orientation for Barnicarndy 1 superimposed on the Australian Stress Map database release (Rajabi et al., 2017) with 1147 A–C quality data records showing the SHmax orientations and the complementary stress trajectories (grey lines). Different colours in these maps show different stress regimes (SS: strike-slip, NF: normal, TF: thrust and U: undefined tectonic stress regime). The length of the lines indicates the quality and reliability of the SHmax orientation based on the World Stress Map (WSM) quality ranking scheme. The azimuth of each line shows the orientation of SHmax in each location. Note that only A–C quality SHmax data records are plotted on the maps

Barnicarndy Graben depositional environment development

A detailed interpretation of the Barnicarndy 1 ATV logs covering the depth interval from 214.30 to 1598.53 m was provided in Wilson and Thrane (2020; Appendix 5). This included a synthesis of the depositional history from a combination of facies analysis and associations, sedimentological features and sediment dispersal analysis, and was summarized as a series of 11 depositional box models. An additional 19 depositional box models of similar style, based on a facies and sequence stratigraphic analysis of the core, were subsequently created to cover the remainder of the well (Appendix 9).

The geological history of the full well sequence includes episodic events over more than 800 million years and a wide range of depositional environments. The initial phase of deposition within the Yeneena Basin during the early Neoproterozoic involved a deep water slope to basin muddy carbonate setting. Dolomitization of this interval may have been primary or very early diagenetic in origin, prior to major mountain building events during the Miles and Paterson orogens. These compressional events deformed and slightly metamorphosed the Yeneena Basin succession, exposing this sedimentary sequence on a surface where it was subjected to an extensive period of weathering resulting in a regolith profile up to 40 m thick.

The Canning Basin was initiated by a major extensional event (Samphire Marsh Movement) with attempted rifting of the West and the North Australian Cratons during the late Cambrian–early Ordovician. Deposition initiated by this event includes the Yapukarninjarra Formation in the Barnicarndy Graben. Very coarse sediment with thin planar bedding is consistent with an alluvial fan to braid plain proximal depositional setting for the lower Yapukarninjarra Formation.

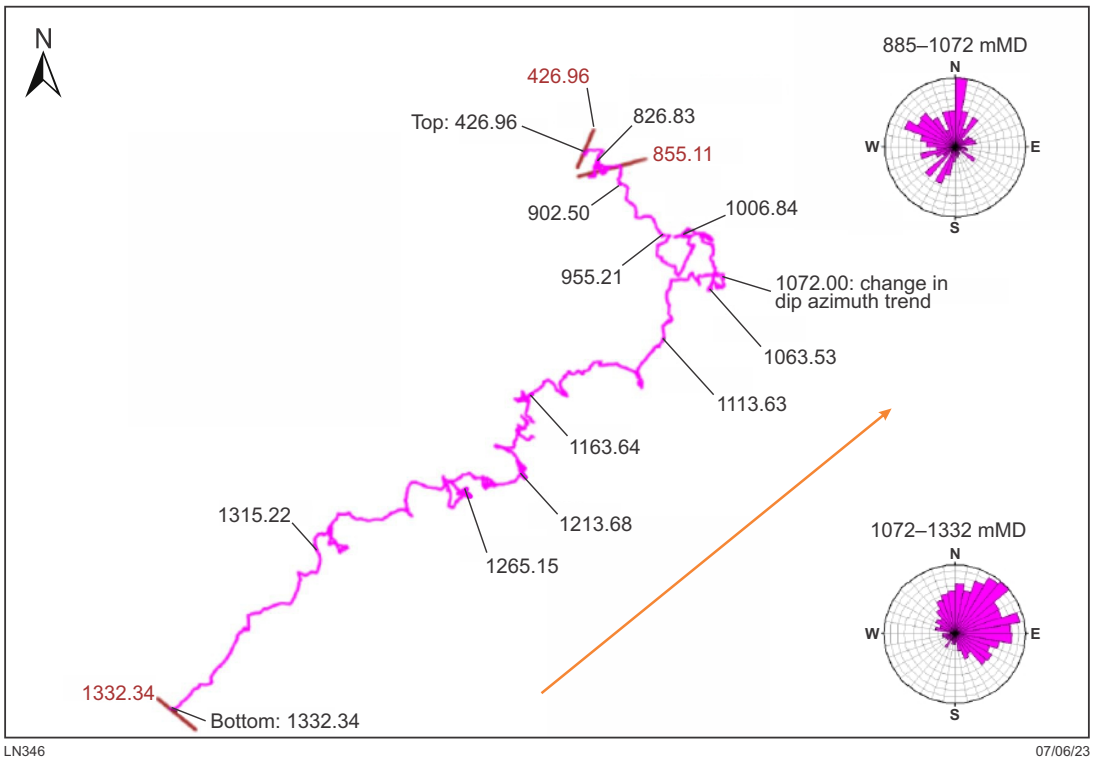

Figure 24. Dip azimuth vector walkout plot of all cross-bedding from the Barnicarndy Formation below 855.11 m and Grant Group above 855.11 m (from Appendix 5; Wilson and Thrane, 2020). Dips were derotated to remove tectonic tilting before plotting. Note the small-scale detail showing NW and SE dip intervals interpreted as due to tidal deposition. Numbers are measured depths in metres

The occurrence of multiple bentonite layers in this interval also attest to the close proximity of active volcanism during the beginning of Canning Basin development. The upper Yapukarninjarra Formation shows a transition into a setting of increasing marine influence, possibly distributary channels, based on the appearance of bioturbation combined with marine sedimentary structures, such as hummocky cross lamination and potential tidal couplets.

The lower Fly Flat Member represents a change to a fully marine, shelf to offshore setting with the deposition of highly bioturbated mudstone. A relative sea-level drop led to an estuarine setting for the upper Fly Flat Member. The lower Samphire Marsh Member represents a return to an offshore setting and the deposition of a thick sequence of bioturbated, fossiliferous mudstone. A minor tidal/estuarine excursion was interpreted in the upper Samphire Marsh Member. Continuous deposition occurs from the fully marine upper Samphire Marsh Member into the distributary channel environment at the base of the lower Barnicarndy Formation. The distributary channel environment is succeeded by sandy tidal flat and following upper shoreface environments, before this depositional pattern is repeated in the upper Barnicarndy Formation. Ichnological analysis corroborates a transition from fully marine in the upper Samphire Marsh Member to a stressed brackish environment in the lower Barnicarndy Formation as well as repeated, relative sea-level rises occurring in both the lower and upper Barnicarndy Formation.

A major erosional unconformity separates the Barnicarndy Formation from the overlying Grant Group. The lower Grant Group diamictites and sandstones were deposited in non-marine environments during a major glacial event, with evidence for glacial retreat in the upper Grant Group. Based on thermochronology, seismic velocity anomalies and maturity data, up to 3 km of section may have been eroded from above the preserved Grant Group. It is thus possible that younger Permian to Mesozoic units, as documented elsewhere in the Canning Basin, were previously present in the Barnicarndy Graben. These could include Permian to Lower Triassic sedimentary units from the Poole Sandstone to the Erskine Sandstone and Middle Jurassic to Lower Cretaceous sedimentary units from the Wallal Sandstone to the Anketell Formation. Outcrops of the Lower Cretaceous Callawa Formation have been identified on the northwestern corner of the PATERSON 1:100 000 map sheet 3354 (Bagas, 2000) indicating renewed deposition in the area following the Fitzroy Transpression and possibly the Jurassic–Cretaceous Breakup Unconformity.

The final phase of deposition includes Mesozoic to Paleogene residual regolith formation, followed by Eocene to Oligocene surficial transported regolith and finally Miocene to Holocene sand dunes and silcrete formation.

Spectral core gamma

Spectral core gamma was acquired at 5 cm intervals and a speed of 12 cm/minute by Core Laboratories (Fig. 25). Eight intervals, focusing on formation contacts, were completed for a total of 364.92 m (Table 3). Barnicarndy 1 was continuously cored with nearly 100% core recovery, hence the spectral core gamma could be used for accurate depth matching of wireline logs to the core, with variable shifts required over each log interval (Appendix 6; Walker, 2020).

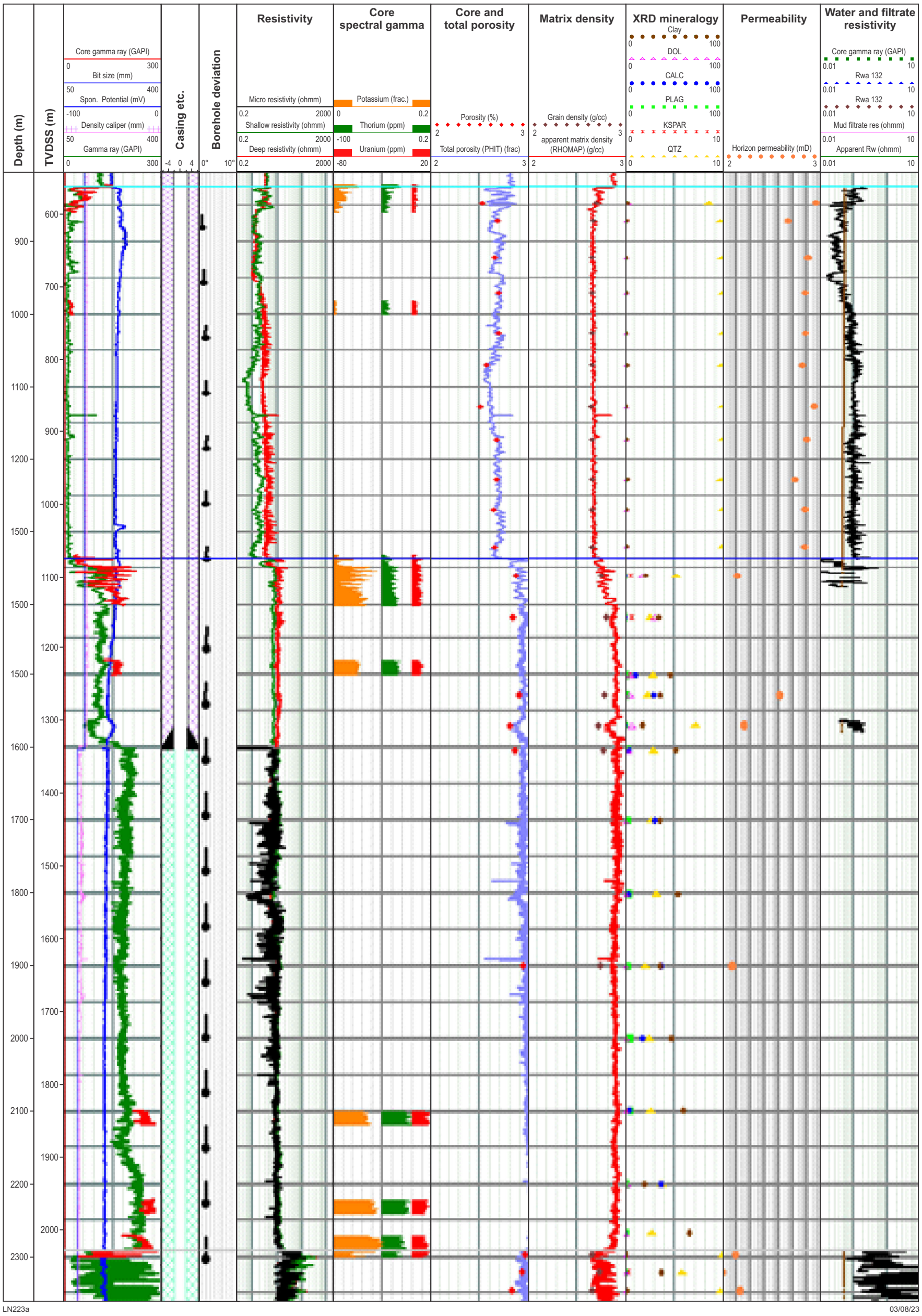

Figure 25. Spectral core gamma over eight major lithological boundaries plotted with other petrophysical data (for full explanation see Appendix 6; Walker, 2020)

Table 3. Spectral core gamma intervals from Barnicarndy 1

Spectral Core Gamma interval	*Stratigraphic unit and/or contact*	*Depth from (m)*	*Depth to (m)*	*Interval thickness (m)*
1	Grant Group/Barnicarndy Fm.	821.92	859.87	37.95
2	Barnicarndy Fm.	981.11	1000.66	19.55
3	Barnicarndy Fm/Samphire Marsh Mbr	1331.70	1401.90	70.20
4	Samphire Marsh Mbr	1481.14	1500.74	19.60
5	Samphire Marsh Mbr	2100.07	2119.37	19.30
6	Samphire Marsh Mbr	2221.65	2240.40	18.75
7	Fly Flat Mbr/Yapukarninjarra Fm.	2270.68	2300.93	30.25
8	Yapukarninjarra Fm/Yeneena Basin	2451.04	2600.36	149.32

Wireline logs

Three studies of the Barnicarndy 1 wireline logs have been completed thus far; an initial petrophysical evaluation of all four wireline datasets (Appendix 6; Walker, 2020); a more detailed petrophysical interpretation by Wang et al. (2021) focused on the Canning Basin section between the base Grant Group and base Canning Basin unconformities; and a third report comprising a review of the Barnicarndy Formation section (Appendix 7; Walker, 2021).

Walker (2020) amalgamated the three suites of wireline logs acquired by Wireline Services Group with the deepest wireline suite acquired by Weatherford, and used the spectral core gamma described above to provide an accurate shift of wireline log depths to match the continuous core depths. This report also provides estimates for reservoir quality and water salinity by integrating petrophysics with selected routine core analysis, XRD and optical and SEM petrography data (Table 4). Using cut-offs of 10% porosity and 50% Vshale, four reservoir units were identified in Barnicarndy 1; two in the Grant Group, a third representing the entire Barnicarndy Formation and the basal part of the Grant Group, and a fourth in the Yapukarninjarra Formation. The Barnicarndy Formation provides the best reservoir quality and this will be discussed in more detail below.

Wang et al. (2021) completed a twofold petrophysical interpretation of the stratigraphy below the Grant Group and above the Yeneena Basin. Established petrophysical techniques used Schlumberger's Techlog platform (Schlumberger Limited, 1991; Wang et al., 2021) to determine the effective porosity, water saturation and elastic properties whereas artificial neural network (ANN) technology estimated permeability, organic geochemical properties and mineral compositions. The three informal subdivisions ('upper sandstone', 'middle interval', 'lower sandstone') based on the petrophysical and ANN interpretation of (Wang et al., 2021; Fig. 26) closely match the formal well stratigraphy of Barnicarndy Formation, Nambeet Formation and Yapukarninjarra Formation, respectively. A further subdivision of the Nambeet Formation into six additional subunits corroborates the elemental package subdivisions provided by chemostratigraphy, indicating the potential for further subdivision of the Fly Flat and Samphire Marsh members of the Nambeet Formation.

The original petrophysical interpretation by Walker (2020) regarding the occurrence of higher salinity formation waters (82 000 ppm) above lower salinity formation waters (25 000 ppm) in the Barnicarndy Formation was investigated by analysing five additional core plugs by special core analysis. A known salinity saturation was used to determine the formation resistivity factor (FRF) and the cementation exponent 'm' (Walker, 2021). This confirmed the transition from lower salinity formation waters in the lower Barnicarndy Formation to higher salinity formation waters in the upper Barnicarndy Formation, with the salinity change occurring at approximately 1050 m.

Sample analysis

A multi-disciplinary approach to post well analysis provided valuable information for stratigraphic subdivision of the Barnicarndy 1 section and numerous additional scientific outcomes. Biostratigraphic sampling and geochronology provided age control for the Carboniferous–Permian Grant Group and the multi-formational Ordovician section overlying Neoproterozoic basement. Paleontological data, including palynology, macrofossil studies and ichnology, also provided invaluable paleoenvironmental and paleoecological information on this previously unstudied Canning Basin succession. Thermochronology analysis built on existing geochronology samples (Appendices 10 and 11) providing modelled maximum burial temperatures throughout the well section, indicating 2–3 km of missing stratigraphy (Appendix 12; Danišík, 2021). Geochemical studies by inorganic and organic techniques providing insights into stratigraphic and source rock correlations, thermal maturity and fluid inclusion stratigraphy. Routine core and rock mechanics analysis provide detailed information on reservoir and seal characterization for the Grant Group/Barnicarndy Formation and Samphire Marsh Member/Fly Flat Member, seal/reservoir pairs.

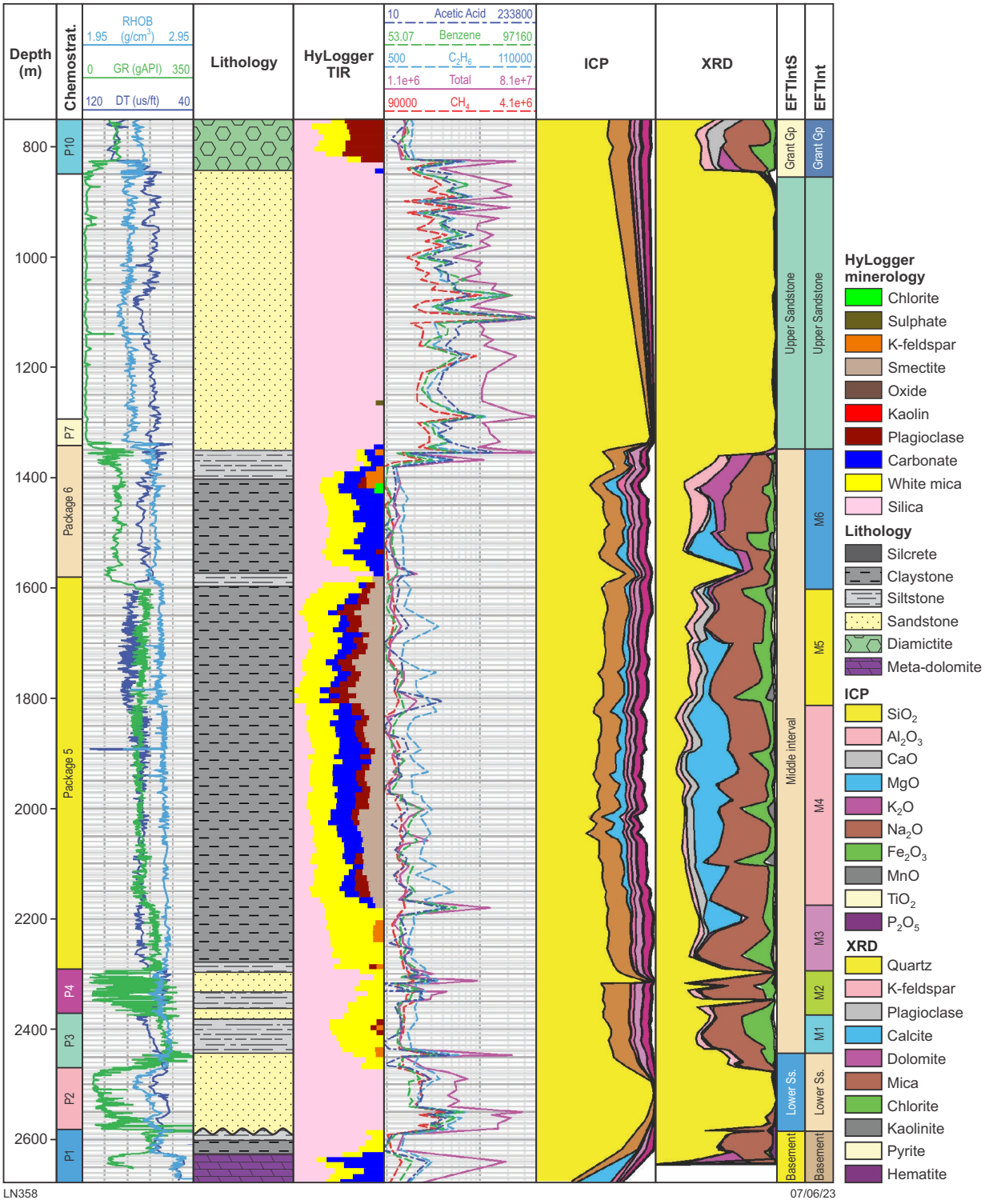

Figure 26. Definition of internal zones based on lithological sequences, well logs, chemostratigraphy and mineral assemblages in Barnicarndy 1 (Wang et al., 2020). Column 1: measured depth (MD); Column 2: chemostratigraphic packages; Column 3: gamma ray (GR), compressional slowness (DT) and bulk density (RHOB); Column 4: lithological descriptions of cores (LithID); Column 5: HyLogger thermal infrared results (TIR); Column 6: responses of methane (CH_4), ethane (C_2H_6), benzene, acetic acid and total from fluid inclusion results; Column 7: Inductively coupled plasma (ICP) testing results; Column 8: X-ray diffraction (XRD) results; Columns 9, 10: two orders of lithological zones

Table 4. Reservoir quality and distribution in Barnicarndy 1

Reservoir no.	Stratigraphic unit	Depth (m)	Thickness (m)	Net porous reservoir (m)	Average porosity (%)	Net/Gross (%)	Water Salinity (ppm)
1	Grant Group	370–473	103	89.1	18.6	86	45,000
2	Grant Group	557–653	96	54	19.9	56	45,000
3	Basal Grant Group/ Barnicarndy Formation	825–1337	512	500.8	16.5	98	82,000/25,000 *Saline over fresh boundary at 1050 m
4	Yapukarninjarra Formation	2471–2585	114	33	12.1	30	116,000

Paleontology and biostratigraphy

As the only record of pre-Permian paleontology within the Barnicarndy Graben, Barnicarndy 1 has provided ample opportunities for biostratigraphic, paleoenvironmental and paleoecological studies, and will continue to do so well into the future. To date, numerous groups have been targeted for study in various parts of the well stratigraphy, including palynology, conodonts and microvertebrates, ichnology and invertebrate macropaleontology, the results of which are summarized in the sections below. Much of this work is in early stages or is preliminary as of the publication of this well completion report, and additional results will emerge in the coming years.

Detailed reports for some of these studies — the GSWA-led palynology results, preliminary conodont and preliminary macrofossil work — are referenced in-text and can be downloaded from the eBookshop website <www.dmp.wa.gov.au/ebookshop-1508.aspx>. Palynology work conducted by Geoscience Australia is referenced similarly, and the final report can be accessed via the GA website <www.ga.gov.au>.

Palynology

Spore-pollen palynology

Results from palynological sampling in the Cenozoic and Grant Group are summarized in Table 5 and discussed in more detail in Martin et al. (2021b) and Foster et al. (2021).

Two phases of palynological sampling were undertaken within the shallow section of Barnicarndy 1 by GSWA (Fig. 16). Set one consisted of three cuttings samples analysed, by MGPalaeo Pty Ltd (Hannaford, 2020), which was later followed by two shallower ditch cuttings and four deeper core samples analysed by Backhouse Biostrat Pty Ltd (Backhouse, 2020). Although spores were obtained from all samples, the yields were generally low, making age determinations difficult for some depths.

In addition, Geoscience Australia collected five additional samples between 610.0 and 841.62 m, of which one sample was not processed (Foster et al. 2021). Although the GA report lists all of these samples as being from the lower Grant Group, the two shallowest samples (at

Table 5. Summary of Grant Group palynological results from Barnicarndy 1. See cited reports for more details

GSWA no.	Depth (m)	Sample type	Stratigraphic unit	Zone	Age	Reference
231420	75–78	DC	Cenozoic	indeterminate	-	Backhouse, 2020
231405	96–99	DC	upper Grant Group	Pseudoreticulatispora confluens	Asselian	Backhouse, 2020
237936	180–183	DC	upper Grant Group	Pseudoreticulatispora confluens	Asselian	Hannaford, 2020
237937	333–336	DC	upper Grant Group	Pseudoreticulatispora confluens	Asselian	Hannaford, 2020
237938	576–580	DC	upper Grant Group	Pseudoreticulatispora confluens	Asselian	Hannaford, 2020
n/a	610.00	CC	upper Grant Group	Microbaculispora tentula	Gzhelian	Foster et al., 2021
231406	650.03	CC	upper Grant Group	Microbaculispora tentula	Gzhelian	Backhouse, 2020
n/a	669.10	CC	upper Grant Group	Microbaculispora tentula	Gzhelian	Foster et al., 2021
231407	759.25	CC	lower Grant Group	Microbaculispora tentula	Gzhelian	Backhouse, 2020
n/a	774.43	CC	lower Grant Group	Microbaculispora tentula	Gzhelian	Foster et al., 2021
n/a	787.21	CC	lower Grant Group	not processed	-	Foster et al., 2021
231408	787.30	CC	lower Grant Group	Microbaculispora tentula	Gzhelian	Backhouse, 2020
231422	823.17	CC	lower Grant Group	Vallatisporites arcuatus	Gzhelian–Kazimovian	Backhouse, 2020
231422	823.21 (resample)	CC	lower Grant Group	Vallatisporites arcuatus	Gzhelian–Kazimovian	Backhouse, 2020
n/a	841.62	CC	lower Grant Group	indeterminate	latest Carboniferous	Foster et al., 2021

Sample types: DC = ditch cuttings, CC = core

610.00 and 669.10 m) fall within what is now correlated with the upper Grant Group (Fig. 16). Of the four samples processed, the shallowest three samples are consistent with the results obtained by Hannaford (2020) and Backhouse (2020). The deepest sample from the set suggests a latest Carboniferous age, but could not be assigned to a zone due to the poor assemblage recovered.

Acritarchs and associated organic-walled microfossils

An additional 53 samples were collected by Geoscience Australia from the pre-Permian section of Barnicarndy 1 for palynological studies (Foster et al., 2021). Although five were not considered suitable for this work (two from the Barnicarndy Formation, one from the Nambeet Formation and two from the Yeneena Basin unit), the remaining samples were processed for acid resistant, organic-walled microfossils, collectively referred to as palynomorphs. All of the processed samples from the Yapukarninjarra Formation and Yeneena Basin unit proved to be barren, as were three samples from the Nambeet Formation. The remaining 42 samples from the Nambeet Formation, spanning 1354.80 – 2434.99 m, yielded palynomorphs (Foster et al., 2021). The total organic matter in this section is typically low (≤0.2 wt%; Grosjean et al., 2020b) as sediments were deposited in an oxic marine environment. The stratigraphic distribution of selected taxa is shown in Foster et al. (2021), and typical forms illustrated in Figures 27 to 31.

Acritarchs belonging to the *Rhopaliophora pilata* – *R. palmata* complex (Fig. 27d,e; Fig. 27d taken from Foster et al., 2021, fig. 3.13d) occur in assemblages throughout the formation, and may be the most common forms within those assemblages. Although recovered from fewer samples, *Aryballomorpha grootaertii* (Fig. 31a–c; Fig. 31b taken from Foster et al., 2021, fig. 3.23k), *Athabascaella*? sp. cf. *Ammonidium aduncum, Athabascaella playfordii* (Fig. 27c), *Baltisphaeridium* spp., *Gorgonisphaeridium martiniae* (cf. Fig. 28h, taken from Foster et al., 2021, fig. 3.28a), *Loeblichia heterorhabda* (cf. Fig. 28g, taken from Foster et al., 2021, fig. 3.30d), *Lophosphaeridium aequicuspidatum*, *Micrhystridium* spp. (Fig. 27b), *Polygonium canningianum* (Fig. 27a), and *Tenuirica*? spp. (Fig. 27h, taken from Foster et al., 2021, fig. 3.4c) occur within assemblages from both Nambeet Formation members.

In addition to acritarchs, fragments of graptolites are commonly preserved, and may be the dominant component in some assemblages (e.g. 1824.25 and 1835.00 m; Fig. 29e,f, taken from Foster et al., 2021, fig. 3.14a,b) in Barnicarndy 1. Organic-walled tubes of various shapes and wall thicknesses (Fig. 30e–h, Fig. 30e taken from Foster et al., 2021, fig. 3.6a) are present and at least some are likely to be of either fungal or cyanobacterial origin. Several species of *Leiosphaeridia*, representing unicellular green algae belonging to the Class Prasinophyceae, are also identified in assemblages from the core samples (Foster et al., 2021). However, there are compositional differences between the microfossil assemblages recovered from the Fly Flat and Samphire Marsh members, although this observation is tempered by low organic yields and difficulties in processing samples.

Like the conodont faunas, the organic-walled microfossils (acritarchs, chitinozoa and graptolites) recovered from the Samphire Marsh Member of the Nambeet Formation in Barnicarndy 1 provide evidence for deposition in marine to nearshore environments, with inputs of cryptospores from early land plants during the late Tremadocian to early Floian (Foster et al., 2021; Zhen et al., 2021). The early land-plant spores of probable bryophyte and aeroterrestrial charophyte algae are important as they herald the emergence of plants onto wetlands during the Early Ordovician, and demonstrate a supply of terrestrial material into the marine environment during deposition of the Samphire Marsh Member (Foster et al., 2021). Strother and Foster (2021) discuss in detail the evolutionary significance of cryptospores recovered from the Nambeet Formation in Samphire Marsh 1. Beyond the land-plant spores, a small number of acritarch taxa in the Samphire Marsh Member warrant further study, including one form that also occurs in assemblages from the Nambeet Formation type section in Samphire Marsh 1 (Foster et al., 2021). The acritarch genera that are reported only in the Samphire Marsh Member in Barnicarndy 1 include: ?*Baltisphaeridium omnivagum*, *Lophosphaeridium* sp. cf. *L. aequalium* (Fig. 27f), *Melikeriopalla*? sp., *Rhopaliophora palmata* (Fig. 27d, taken from Foster et al., 2021, fig. 3.13d), *Loeblichia nambeetense* (Fig. 27g), *Polygonium* sp., and ?*Polyancistrodorus radiosus*.

In addition to the ubiquitous graptolite remains (Fig. 29e,f), chitinozoans (Fig. 29g,h, Fig. 29h taken from Foster et al., 2021, fig. 3.16h) and scolecodonts (polychaete worm jaws) are also recorded in the Samphire Marsh Member. The chitinozoa provide a possible link to Nambeet Formation assemblages from Olympic 1 and should also be studied further. *Gloeocapsomorpha prisca* (Fig. 29a,b) and ?*Eomerismopedia maureeniae* (Fig. 29c,d, taken from Foster et al., 2021, figs 3.12b and 3.19f) of possible cyanobacterial origin were identified within the Samphire Marsh Member. Early land-plant spores, sometimes associated with irregularly-shaped spore clusters likely from aeroterrestrial charophyte algae, are present in 23 samples from the Samphire Marsh Member and are grouped under the heading 'Cryptospores' (Fig. 30a–d, Fig. 30a,b,d taken from Foster et al., 2021, fig. 3.8d, 3.8f and 3.15b). *Grododowon orthagonalis*, superficially similar to *E. maureeniae*, and recorded from some samples (Foster et al., 2021), is considered to be of charophyte algal origin (Strother et al., 2017), and is also recorded in this member (Foster et al., 2021).

Almost exclusively marine microfossils were identified in the Fly Flat Member in Barnicarndy 1 (Foster et al., 2021). Acritarchs apparently confined to this member include: *Aremoricanium*? (Fig. 28b); cf. *Athabascaella rossii* (Fig. 28a, taken from Foster et al., 2021, fig. 3.28b); *Comasphaeridium*? sp. (Fig. 28e); *Dactylofusa* sp., which is common in one assemblage only (Fig. 28c,d, Fig. 28c taken from Foster et al., 2021, fig. 3.29a); and *Navifusa* sp. (Fig. 28f, taken from Foster et al., 2021, fig. 3.29e). The exception to the marine acritarchs are organic-walled tubes in the sample from 2375.82 m (Fig. 30g,h, taken from Foster et al., 2021, fig. 3.31f,b); their morphology suggests a possible fungal origin.

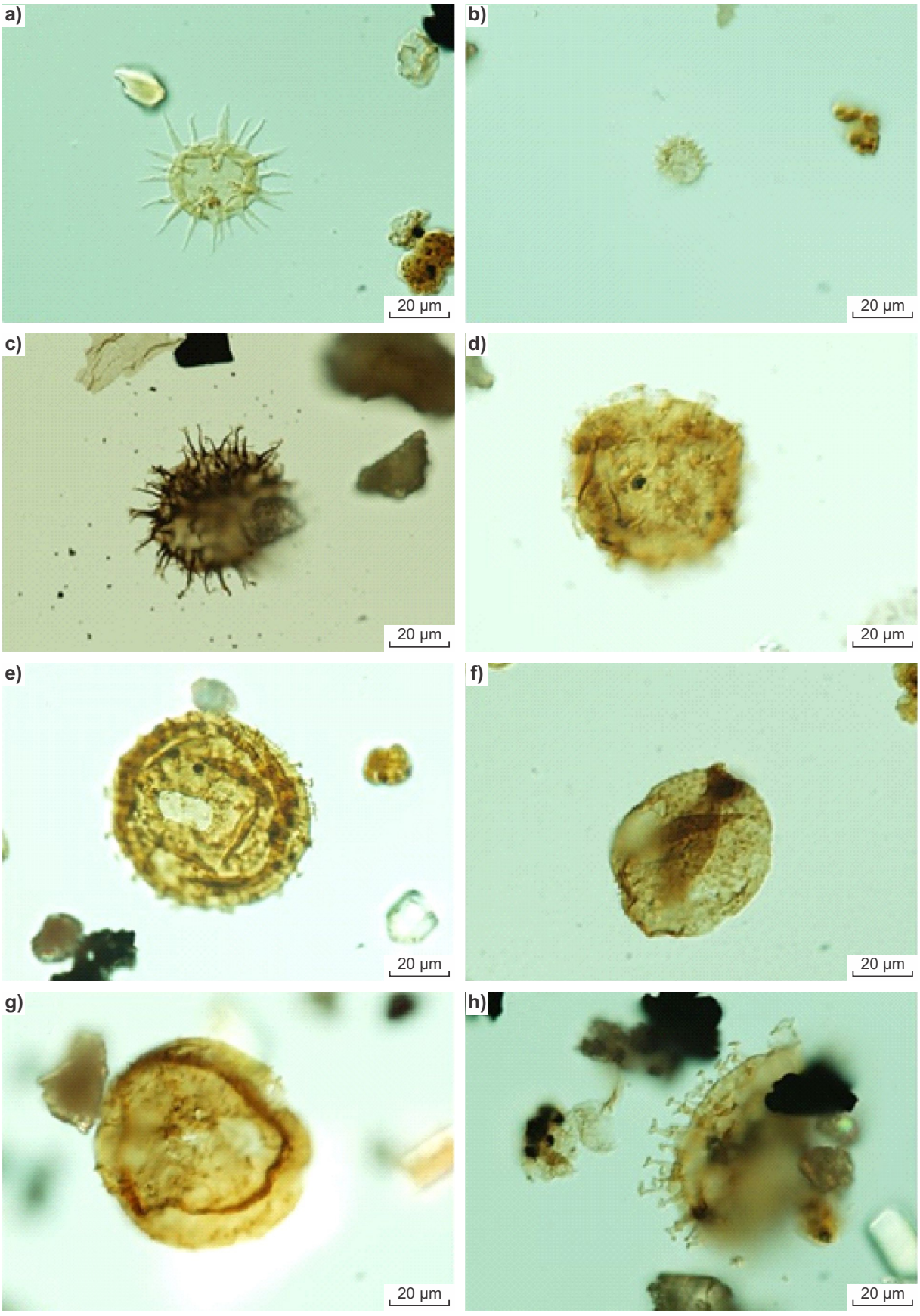

Figure 27. Acritarchs from the Samphire Marsh Member, Nambeet Formation, Barnicarndy 1, documented in Foster et al. (2021); image numbers from appendix 2 of that publication: a) *Polygonium canningianum,* 1769.03 m, image 889; b) *Micrhystridium* sp. cf. *M. infrequens,* 1769.03 m, image 908; c) *Athabascaella playfordii*, 2244.08 m, image 1553; d) *Rhopaliophora palmata,* 1684.86 m, image 784 (image 784 taken from Foster et al., 2021, figure 3.13d); e) *Rhopaliophora pilata*, 1769.03 m, image 904; f) *Lophosphaeridium* sp. cf. *L. aequalium*, 1684.86 m, image 745; g) ?*Loeblichia nambeetense*, 1519.15 m, image 1688; h) ?*Tenuirica sp.*, 1519.15 m, image 1685 (image 1685 taken from Foster et al., 2021, figure 3.4c)

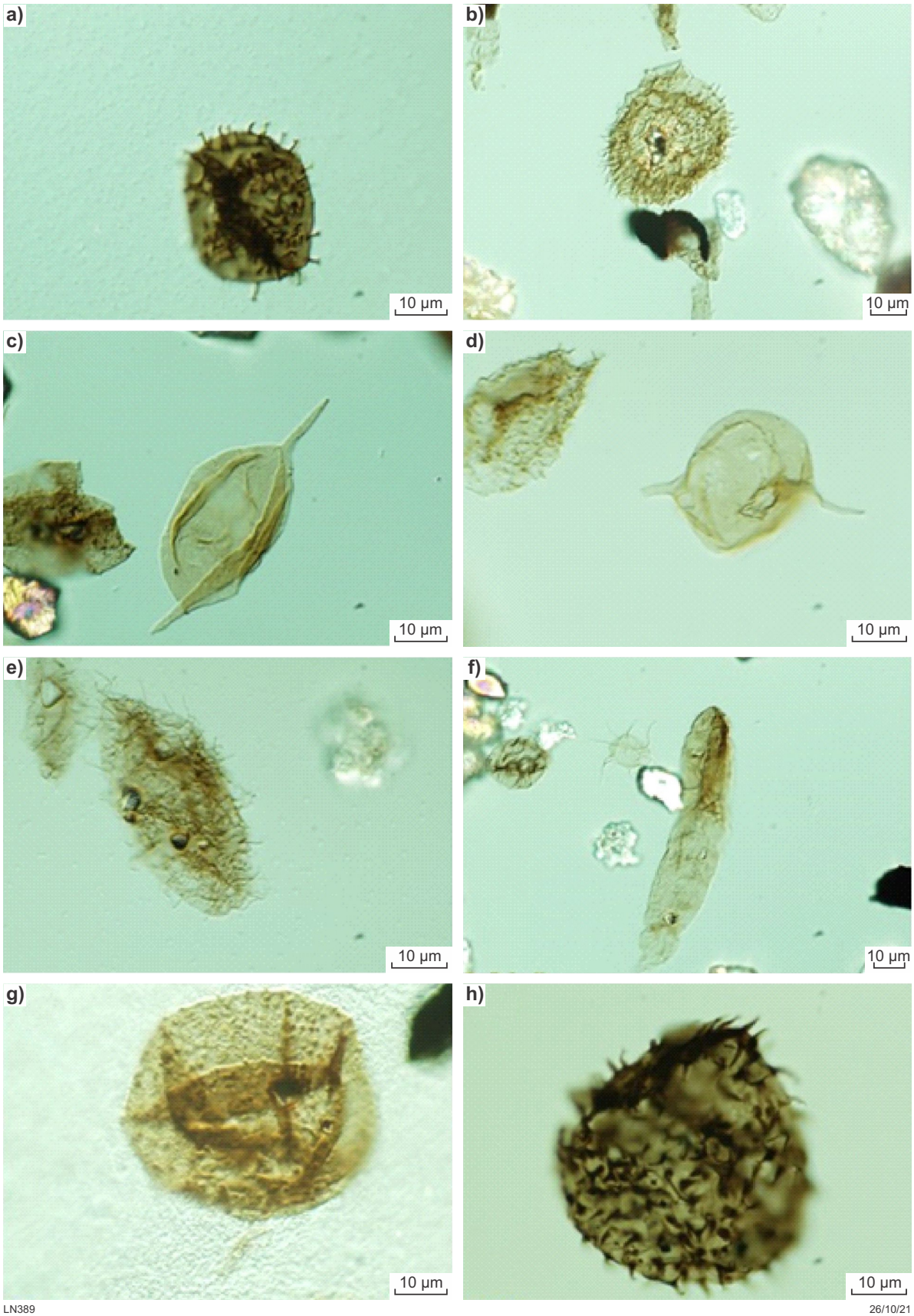

Figure 28. Acritarchs from the Fly Flat Member, Nambeet Formation, Barnicarndy 1, documented in Foster et al. (2021); image numbers from appendix 2 of that publication: a) cf. *Athabascaella rossii*, 2209.06 m, image 1731 (image 1731 taken from Foster et al., 2021, figure 3.28b); b) *Aremoricanium*? sp., 2375.82 m, image 1615; c) and d) *Dactylofusa* sp., 2325.03 m, images 1484 and 1586, (image 1586 taken from Foster et al., 2021, figure 3.29a); e) *Comasphaeridium*? sp., 2325.03 m, image 1584; f) *Navifusa* sp., 2325.03 m, image 1470 (image 1470 taken from Foster et al., 2021, figure 3.29e); g) ?*Loeblichia heterorhabda*, 2375.82 m, image 589 (image 1589 taken from Foster et al., 2021, figure 3.30d); h) *Gorgonisphaeridium* sp. cf. *G. martiniae*, 2290.06 m, image 1744 (image 1744 taken from Foster et al., 2021, figure 3.28a)

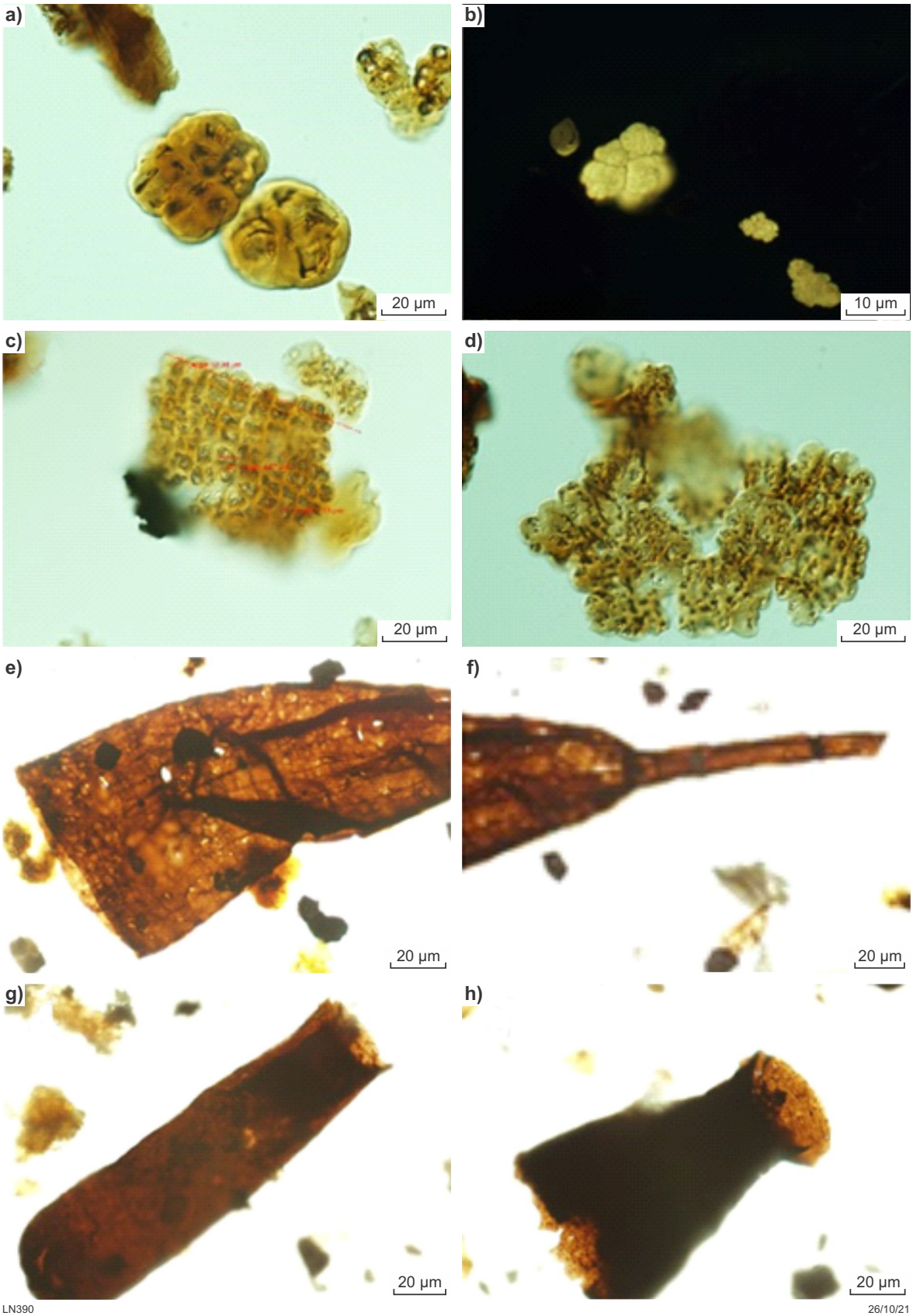

Figure 29. Photomicrographs of species of marine microfossils recovered from the Early Ordovician Samphire Marsh Member, Nambeet Formation, Barnicarndy 1, documented in Foster et al. (2021); image numbers from appendix 2 of that publication: a) *Gloeocapsomorpha prisca,* 1670.02 m, image 715 (image 715 taken from Foster et al., 2021, figure 3.12a); b) *G. prisca* under UV light, 1835.05 m, image 598 (image 598 taken from Foster et al., 2021, figure 3.18a); c) ?*Eomerismopedia maureeniae,* 1670.02 m, image 718, (image 718 taken from Foster et al., 2021, figure 3.12b); d) ?*E. maureeniae,* 1893.00 m, image 1468 (image 1468 taken from Foster et al., 2021, figure 3.19f); e) and f) graptolite fragment, 1748.06 m, images 1757 and 1759 (images 1757 and 1759 taken from Foster et al., 2021, figure 3.14a,b); g) unidentified chitinozoan, 1354.8 m, image 1445; h) chitinozoan ?*Lagenochitina cylindrica Eisenack,* 1769.03 m, image 1769 (image 1769 taken from Foster et al., 2021, figure 3.16h)

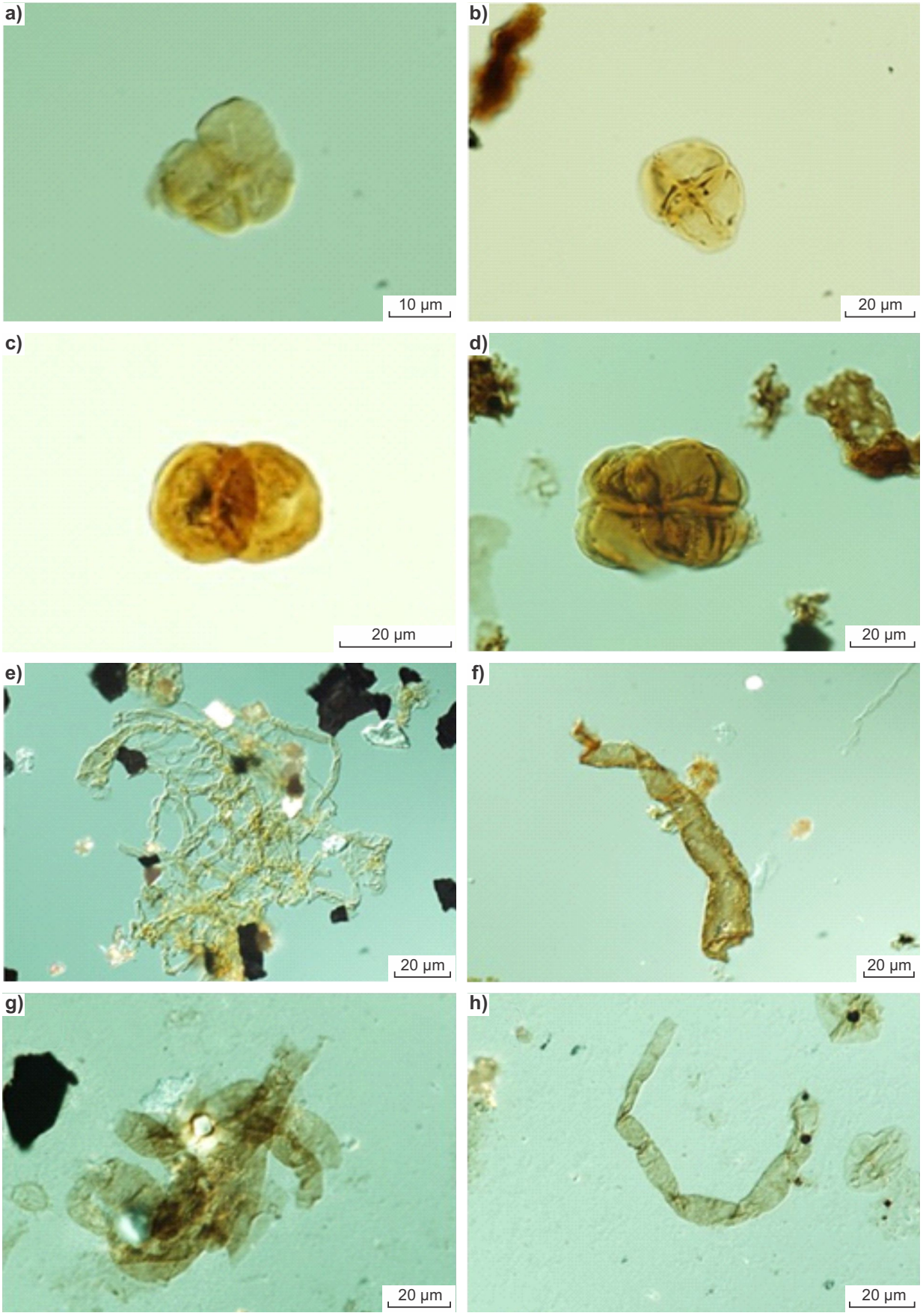

Figure 30. Photomicrographs of early land-plant spores and organic-walled tubes of possible fungal origin, recovered from the Early Ordovician Nambeet Formation, Barnicarndy 1, documented in Foster et al. (2021); image numbers from appendix 2 of that publication: a)–d) cryptospores, 1600.02 m, 1600.02 m, 1670.02 m and 1753.03 m, images 1715, 1728, 690 and 1767 (image 1715, 1728 and 1767 taken from Foster et al., 2021, figures 3.8d,f and 3.15b); e)–h) organic-walled tubes, 1579.82 m, 1354.80 m, 2375.82 m and 2375.82 m, images 817, 624, 1602 and 1610 (image 817, 1602 and 1610 taken from Foster et al., 2021, figures 3.6a, 3.31f,b)

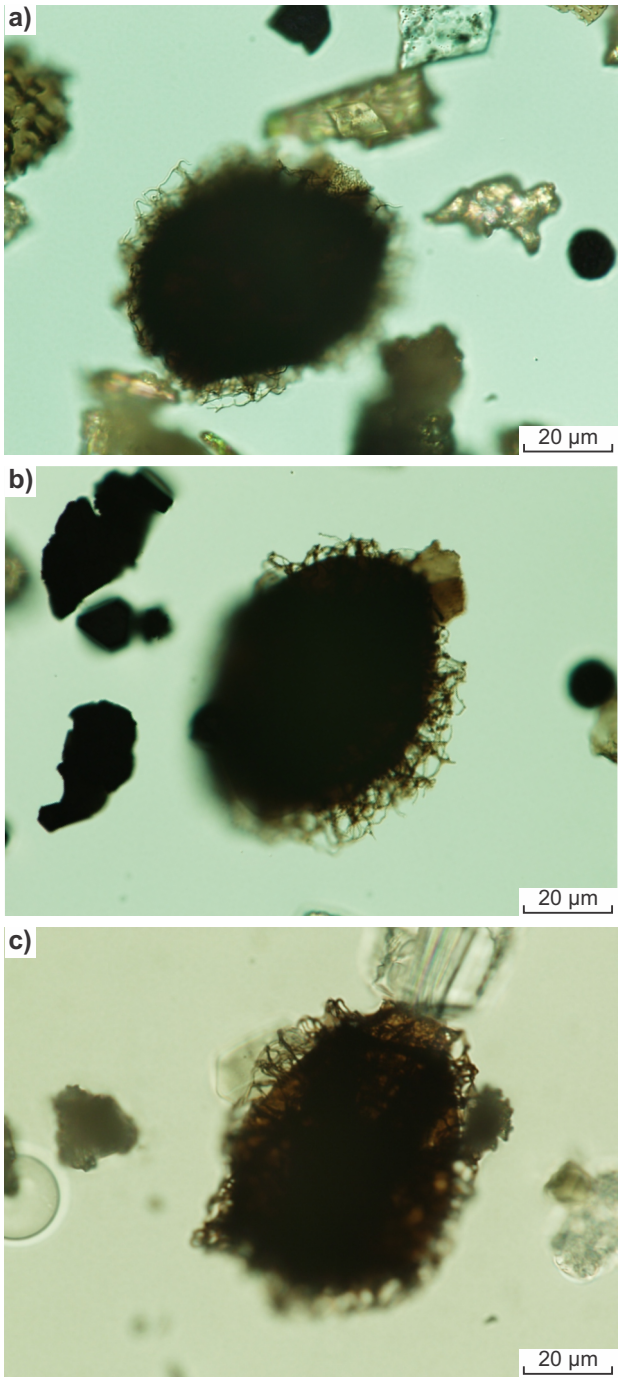

Figure 31. The acritarch *Aryballomorpha grootaertii* from the Nambeet Formation, Barnicarndy 1, documented in Foster et al. (2021); image numbers from appendix 2 of that publication: a) 2244.08 m, Samphire Marsh Member, image 2405; b) 2194.10 m, image 2473, Samphire Marsh Member; (image 2473 taken from Foster et al., 2021, figure 3.23k); c) 2255.05 m, image 2381, Samphire Marsh Member

Conodonts and fish microfossils

Three sets of samples collected from the Ordovician section of Barnicarndy 1 were processed for conodont and fish microfossils (Zhen et al., 2021). The first set of 10 samples were collected from carbonate-rich layers between 1354 and 2248 m, followed by a second set of seven samples from the lower section of the core between 2292 and 2585 m, and a final set of seven samples collected from the upper part of the well between 871 and 1328 m (Fig. 16). Of these three sets, the first two were primarily sampled for conodonts, whereas the third set was primarily collected for fish microfossils, but was also examined for conodonts. The depths across all three sets were selected to be widely spaced to provide good coverage across the core (Table 6). Although the first set of samples were relatively rich in conodont elements, none of the samples from sets 2 or 3 yielded any diagnostic elements.

A preliminary report on the sampling, processing and analysis of phosphatic microfossils, including age-diagnostic conodonts, can be found in Zhen et al. (2021), with Zhen et al. (2022) presenting the more detailed taxonomic descriptions of this same material. Three conodont biozones were identified with age-diagnostic taxa in Zhen et al. (2022) *Jumudontus ganada* Biozone (Fig. 32a), *Oepikodus communis* Biozone (Fig. 32b,c) and *Paroistodus proteus* Biozone (Fig. 3g–i). A total of 22 species have been identified to date, including one new species, *Juanognathus*? *denticulatus* (Zhen et al. 2022; Fig. 32d–f).

Macrofossils

A preliminary paleontological summary for Barnicarndy 1 is provided in Martin et al. (2021b) with core intervals separated based on coarse informal lithostratigraphic divisions. The diamictite and silty sandstone interval of Martin et al. (2021b) equates to the Grant Group, the upper sandstone interval to the Barnicarndy Formation, the shale and limestone interval to the Nambeet Formation, and the lower sandstone and shale to the Yapukarninjarra Formation.

The Grant Group does not contain any in situ macrofossils, only unidentified gastropods and shells in a large carbonate clasts at 847.4 m. Shelly macrofossils (bivalves and brachiopods) were noted sparsely in the Barnicarndy Formation, but these are poorly preserved and provide no useful age constraints. The Yapukarninjarra Formation and Yeneena Basin unit were both noted to be barren of visible macrofossils.

The Nambeet Formation section, in comparison, is richly and diversely fossiliferous, with preliminary examinations identifying numerous invertebrate macrofossil groups (Fig. 33). Trilobites dominate the macrofossil record in this part of the well, showing a wide variety of forms and sizes, with the abundance increasing below 1591 m in the upper Samphire Marsh Member (Fig. 33a). The lower Samphire Marsh Member in particular contains an interesting assemblage of asaphid pygidia (Fig. 33b) with distinctive axial spines ranging from long, straight to smooth and barbed spines. A description of 23 trilobite taxa from the Nambeet Formation, including one new genus and six new species (Smith and Allen, 2023), was published during production of this Report.

A range of phyllograptid, dichograptid, tetragraptid and didymograptid graptolite taxa are found throughout the Samphire Marsh Member, some of which are strongly reminiscent of better-studied Tremadocian and Floian assemblages in eastern Australia (Fig. 33c). Brachiopods are most abundant in the upper Samphire Marsh Member but are common throughout the core and are represented by both articulate (Fig. 33d) and inarticulate (Fig. 33e) brachiopods. Bivalves (Fig. 33f) and rostroconchs are more common in the middle to lower intervals of the Samphire Marsh Member. A variety of other macrofossil are found more sporadically throughout the Nambeet Formation section including cephalopods (Fig. 33g), gastropods (Fig. 33h), crinoids, bryozoans, hyoliths, conulariids and ostracods (Fig. 33i). More groups are likely to be identified as taxonomic work progresses. Fossils in this section are considered broadly similar to Tremadocian to Floian taxa seen elsewhere in the Canning Basin, and in adjoining basins in central Australia (Martin et al., 2021b).

Table 6. List of samples collected for phosphatic microfossil (conodont and fish) processing from Barnicarndy 1

Set no.	*GSWA no.*	*Depth (m)*	*Analysis type*	*Stratigraphic unit*	*Zone*	*Age*
1	231409	1354.85 – 1355.70	conodonts	Samphire Marsh Member	*Jumudontus gananda*	upper Floian to lower Dapingian
1	231410	1394.20 – 1395.33	conodonts	Samphire Marsh Member	*Oepikodus communis*	middle Floian
1	231411	1528.63 – 1529.75	conodonts	Samphire Marsh Member	*Oepikodus communis*	middle Floian
1	231412	1628.05 – 1629.42	conodonts	Samphire Marsh Member	*Oepikodus communis*	middle Floian
1	231413	1712.76 – 1713.98	conodonts	Samphire Marsh Member	*Oepikodus communis*	middle Floian
1	231414	1846.52 – 1847.60	conodonts	Samphire Marsh Member	*Oepikodus communis*	middle Floian
1	231415	1916.08 – 1917.19	conodonts	Samphire Marsh Member	indeterminate	-
1	231416	2047.02 – 2048.13	conodonts	Samphire Marsh Member	*Paroistodus proteus*	upper Tremadocian to lower Floian
1	231417	2146.53 – 2147.55	conodonts	Samphire Marsh Member	indeterminate	-
1	231418	2246.06 – 2247.17	conodonts	Samphire Marsh Member	*Paroistodus proteus*	upper Tremadocian to lower Floian
2	231423	2292.84 – 2293.71	conodonts	Fly Flat Member	indeterminate	-
2	231424	2340.89 – 2341.99	conodonts	Fly Flat Member	indeterminate	-
2	231425	2378.31 – 2379.19	conodonts	Fly Flat Member	indeterminate	-
2	231426	2424.05 – 2424.97	conodonts	Fly Flat Member	indeterminate	-
2	231427	2468.46 – 2469.67	conodonts	Yapukarninjarra Formation	indeterminate	-
2	231428	2551.76 – 2553.15	conodonts	Yapukarninjarra Formation	indeterminate	-
2	231429	2583.38 – 2584.39	conodonts	Yapukarninjarra Formation	indeterminate	-
3	231430	1327.43 – 1327.92	conodonts, fish	Barnicarndy Formation	indeterminate	-
3	231431	1247.59 – 1248.09	conodonts, fish	Barnicarndy Formation	indeterminate	-
3	231432	1166.83 – 1167.29	conodonts, fish	Barnicarndy Formation	indeterminate	-
3	231433	1080.53 – 1081.05	conodonts, fish	Barnicarndy Formation	indeterminate	-
3	231434	1018.57 – 1019.09	conodonts, fish	Barnicarndy Formation	indeterminate	-
3	231435	960.33 – 961.04	conodonts, fish	Barnicarndy Formation	indeterminate	-
3	231436	871.70 – 872.19	conodonts, fish	Barnicarndy Formation	indeterminate	-

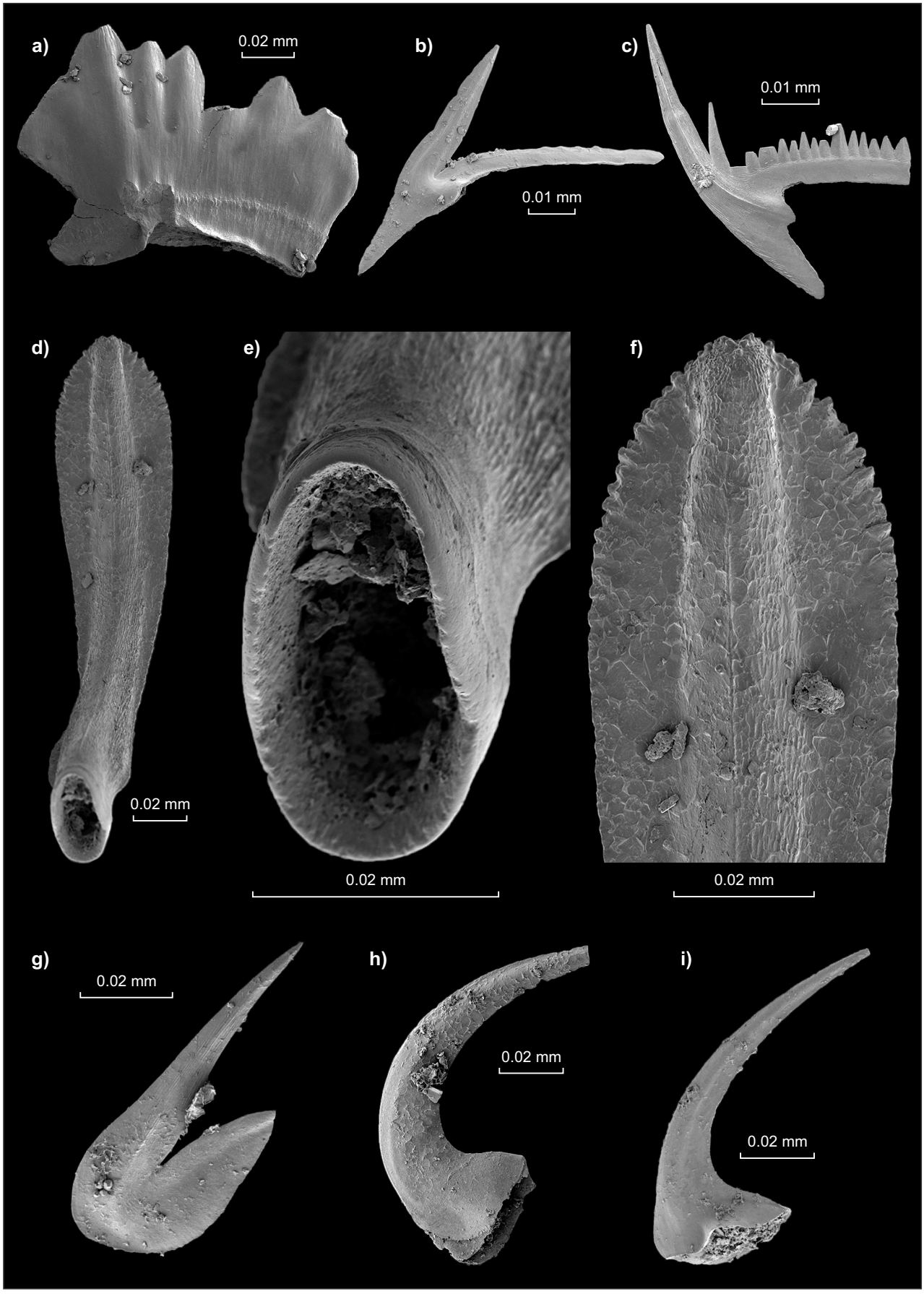

LN413 05/08/22

Figure 32. (page 44) Photomicrographs of representative age-diagnostic conodonts and the recently identified species *Juanognathus? denticulatus* from the Lower Ordovician Samphire Marsh Member, Nambeet Formation, Barnicarndy 1; all images from Zhen et al. (2022): a) *Jumudontus gananda*; Pa element, GSWA F55231, from GSWA 231409, outer-lateral view (IY427-001); b),c) *Oepikodus communis*; b) M element, GSWA F55232, from GSWA 231412, posterior view (IY429-029); c) Sd element, GSWA F55241, from GSWA 231410, outer-lateral view (IY427-028); d)–f), *Juanognathus? denticulatus* Sa element, GSWA F55229, holotype, from GSWA 231411: d) posterior view (IY429-006); e) close-up of the basal cavity, basal view (IY429-007); f) close-up of the distal cusp showing minute denticles, posterior view (IY429-008); g)–i), *Paroistodus proteus*; g) M element, GSWA F55251, from GSWA 231414, anterior view (IY430-006); h) Sb element, GSWAF55253, from GSWA 231414, outer-lateral view (IY430-007); i) Pa element, GSWA F55256, from GSWA 231416, outer-lateral view (IY430-014)

Ichnology

Following observations of trace fossils in Barnicarndy 1 during onsite core logging, in 2020 GSWA geologists conducted a preliminary ichnology analysis. This analysis, presented in Martin et al. (2021b), identified some sections with trace fossils worthy of more detailed study. On that basis, Amely Allgöwer of MGPalaeo Pty Ltd was contracted to conduct a detailed analysis of Barnicarndy and Yapukarninjarra Formation ichnology in early 2021. The results of this work are briefly summarized here with the full report available in Appendix 4, in which the Barnicarndy Formation is referred to as the 'upper sandstone' and the Yapukarninjarra Formation as the 'lower sandstone'.

Combining sedimentary structures with trace fossil abundance, diversity and ichnotaxa size has helped to broadly define a lower and upper unit within the Barnicarndy Formation, and has also allowed a more detailed subdivision into seven distinct intervals (Fig. 17). At the base of the Barnicarndy Formation, the ichnology indicates an up-section transition from fully marine conditions in the upper Nambeet Formation into more stressed brackish environments with fresh water input at the transition into the Barnicarndy Formation at ichnology interval (II) 1 (II 1; Fig. 17). An example of the trace fossil diversity in II 1 is shown at a depth of 1342.5 m with the following trace fossils; *Arenicolites, Cylindrichnus, Palaeophycus* (Pa) and *Teichichnus* (Te) (Fig. 34a).

The remaining six II's help define variations in depositional environment throughout the Barnicarndy Formation and, alongside the sedimentary structure and ATV data, validate a subdivision into distinct upper and lower units. Trace fossils in II 2 (1335–1172 m) become more sporadic and sparse, and the assemblage is dominated by vertical traces such as *Diplocraterion* (Fig. 34b) indicating a high-energy environment, such as upper shoreface or distributary channels. This is followed by a brief interval (II 3), from 1172 m to a distinctive lag deposit at 1166 m, characterized by a fully marine tolerant, diverse trace fossil assemblage (Fig. 34c). The start of II 4 records a return to the sparse and sporadic vertical trace fossils seen in II 2, suggesting a return to high-energy settings (Fig. 34d). The core over interval II 5 (1118.5 – 1074.0 m) is disintegrating in the core trays and thus the ichnology and sedimentary structures are difficult to interpret (Fig. 34e). II 6 (1074.0 – 998.0 m) exhibits an increase in bioturbation intensity and frequency with vertical traces again dominating (Fig. 34f). The occurrence of possible herringbone cross-bedding and paired mudstone drapes indicates a distinctive tidal influence over this interval. The final ichnology interval, (II 7) (998–855 m), corresponds to the upper Barnicarndy Formation (Fig. 17). This interval displays more frequent and intense bioturbation with a diverse trace fossil assemblage (Fig. 34g) indicating a fully marine depositional environment. Frequent hiatal surfaces and numerous metre-thick intervals devoid of bioturbation indicate a high-energy, possibly upper shoreface, setting. However, it is important to note that liesegang banding is common throughout the Barnicarndy Formation and can cause difficulties in distinguishing trace fossils from sedimentary structures (see also the ichnology section of Martin et al., 2021; Fig. 34h).

The trace fossil assemblage from the Yapukarninjarra Formation, or 'lower sandstone' of Appendix 4, is very sparse and sporadic near the base (Fig. 34i), and gradually increases in bioturbation intensity and diversity near the top of the formation (Fig. 34j). Diagenetic overprint is pervasive in places, obliterating bioturbation and sedimentary structures (Fig. 34k). Questionable synaeresis/desiccation cracks are noted from 2586.2 to 2577.0 m, (Fig. 34l,m) possibly indicating salinity changes or sub-aerial exposure, respectively. Slabbing of core may help define the 3D expression of the cracks and therefore the differentiation between the two types of structures.

Geochronology

A total of 59 core samples were submitted for geochronology (Appendix 10). Of these, 50 samples of bentonites were submitted to Boise State University Isotope Geology Laboratory, Boise, Idaho, for U–Pb zircon analysis by chemical abrasion isotope dilution thermal ionization mass spectrometry (CA-IDTIMS). An additional nine sandstone samples were dated by GSWA, with sample preparation completed at the GSWA Laboratory. Detrital zircons from these samples underwent U–Pb analyses using the sensitive high resolution ion microprobes (SHRIMP) at the John de Laeter Centre, Curtin University, Perth, Western Australia. All ages reported in this section are quoted with 95% or 2 sigma uncertainties. Table 7 provides a list of samples that were dated successfully (Fig. 16), together with associated references.

U–Pb detrital zircon geochronology

SHRIMP U–Pb geochronology was conducted on detrital zircons separated from nine samples of clastic units (Table 7), typically sandstone, with the aim of providing constraints on sediment provenance and maximum depositional ages. Detailed reports for each of the nine samples, including methodology, are linked in the reference section and can also be downloaded from the GSWA eBookshop <www.dmirs.wa.gov.au/ebookshop>. A compilation of the detrital zircon age spectra for all nine samples is presented as stacked probability density plots in Figure 35. This collection of data shows a number of common age components, also seen in previously published detrital zircon data from the Canning and Yeneena basins (Bagas and Nelson, 2007; Haines et al., 2013).

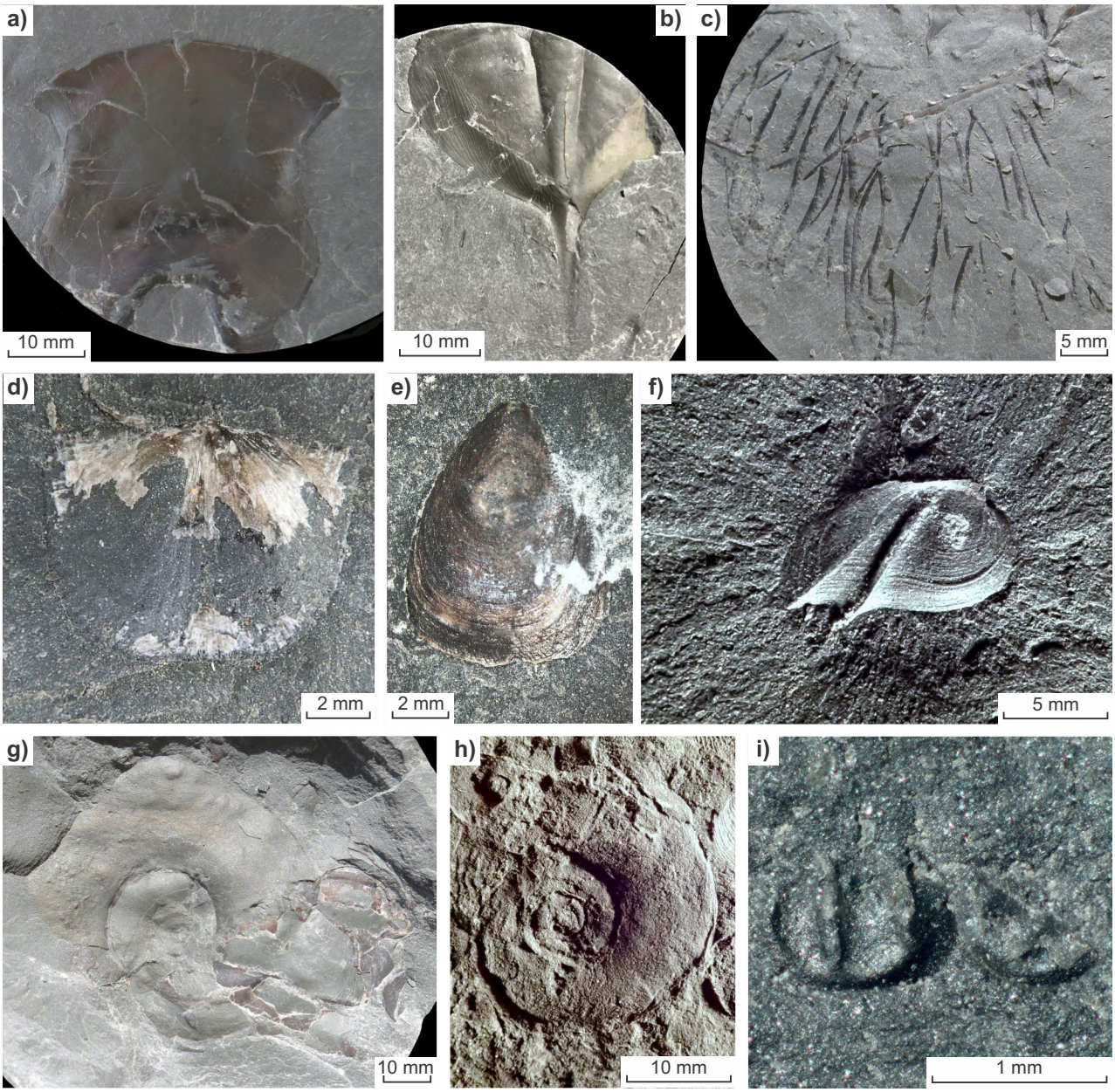

Figure 33. Selection of macrofossils recorded in Barnicarndy 1 having biostratigraphic or paleonvironmental significance: a) *Lycophron* sp. (from Martin et al., 2021b, fig. 3a), 1642.95 m, a trilobite genus considered indicative of the younger part of the Bendigonian (Floian); b) ?*Penchiopsis* sp. (from Martin et al., 2021b, fig. 4j), 2030.76 m, a spined trilobite pygidium previously recorded only from the oldest trilobite zone of the Emanuel Formation; c) graptolite cf. *Clonograptus erdtmanni* (Rickards and Chapman, 1991; from Martin et al., 2021b, fig. 9c), 2110.97 m, a stellate form similar to Bendigonian (Floian) taxa from key Ordovician assemblages in Victoria; d) *Tritoechia* sp. (from Martin et al., 2021b; fig. 5d), 2026.71 m, a cosmopolitan Lower Ordovician articulate brachiopod genus common in northern Australia; e) *Libecoviella* sp. (from Martin et al., 2021b, fig. 6b), 2184.46 m, an inarticulate brachiopod genus also recorded from the Emanuel Formation whose strongly textured shell microstructure suggests an infaunal lifestyle; f) *Colpantyx woolleyi* (Pojeta and Gilbert-Tomlinson, 1977; from Martin et al., 2021b, fig. 7a), 2182.98 m, a bivalve species also known from equivalent-aged units in the Amadeus Basin; g) *Aethoceras*? sp. (from Martin et al., 2021b, fig. 10b), 2154.64 m, a tortonic cephalopod superficially similar in form to taxa recorded in the Emanuel Formation; h) cf. *Peelerophon oehlerti* (Bergeron, 1889; from Martin et al., 2021b, fig. 10l), 2180.36 m, which closely resembles a species previously recorded from the Emanuel Formation; i) unidentified ostracods (from Martin et al., 2021b, fig. 10s), 2160.00 m similar to Tremadocian taxon *Eopilla* Schallreuter, 1993. All specimens are from the Samphire Marsh Member of the Nambeet Formation

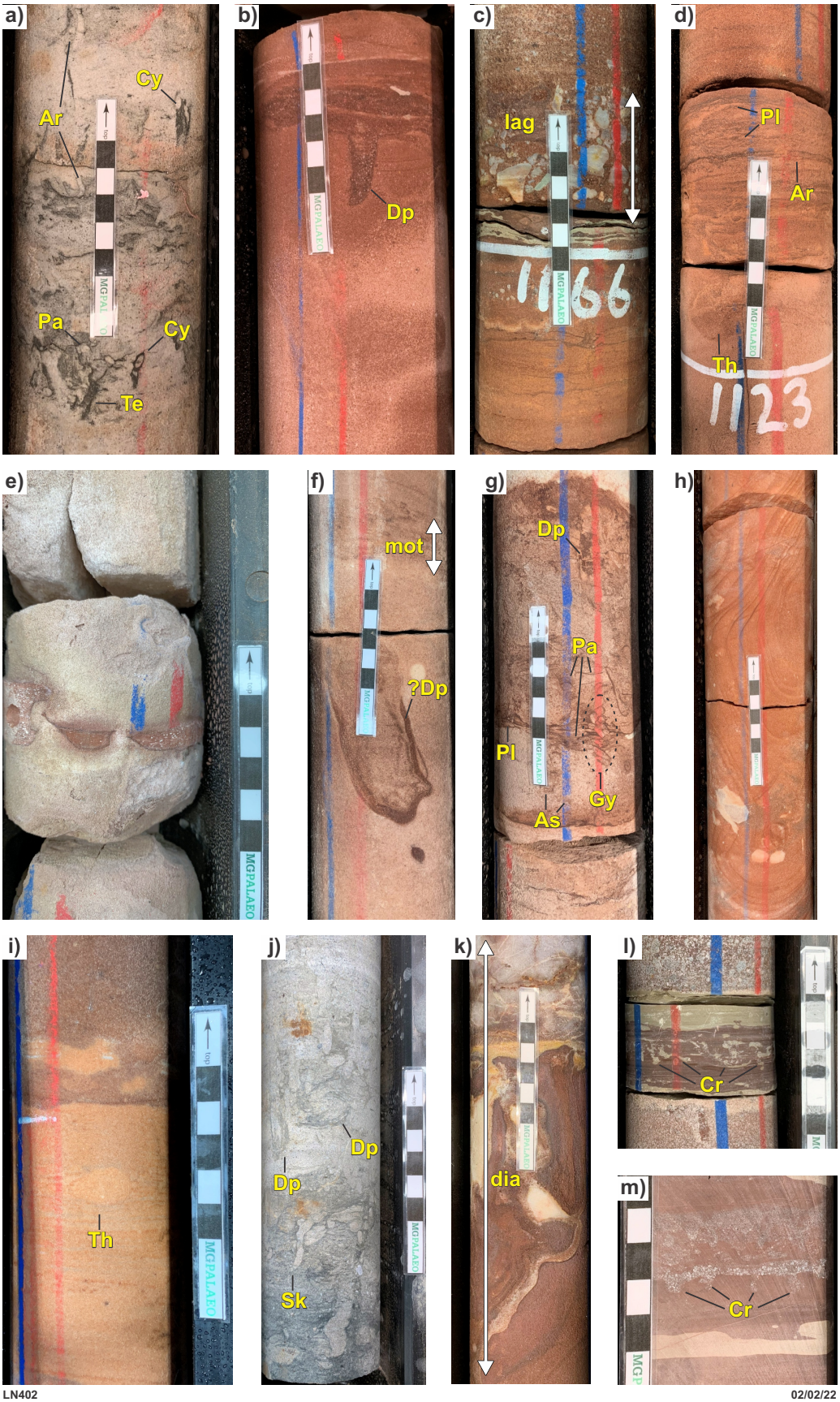

Figure 34. Ichnology from the Barnicarndy Formation: a) II 1, diverse trace fossil assemblage at 1342.50 m, *Arenicolites* (Ar), *Cylindrichnus* (Cy), *Palaeophycus* (Pa), and *Teichichnus* (Te); b) II 2, 1226.70 m, *Diplocraterion* (Dp); c) II3, lag deposit at 1166.00 m; d) II4, 1122.95 m, *Planoloites* (Pl), *Arenicolites* (Ar) and *Thalassinoides* (Th); e) disintegration of core, 1112.85 m; f) II5, 1040.15 m, *Diplocraterion* (Dp); g) II6, 878.80 m, *Diplocraterion* (Dp), *Palaeophycus* (Pa), *Planoloites* (Pl), *Gyrolithes* (Gy) and *Asterosoma* (As); h) liesegang rings at 990.25 m. Ichnology from the Yapukarninjarra Formation; i) *Thalassinoides* (Th), 2514.50 m; j) *Diplocraterion* (Dp) and *Skilithos* (Sk), 2451.85 m; k) diagenetic overprint at 2492.30m; l) and m) synaeresis or desiccation cracks, 2581.40 m and 2584.15 m (Images from Appendix 4)

Black horizontal bars in Figures 35–40 represent expected age ranges of magmatic and metamorphic zircons from surrounding basement terranes. Nevertheless, the high likelihood of multiple zircon recycling and long-distance transport make simple interpretations difficult or untenable. Furthermore, the overlap in age between events in multiple terrains makes interpretations based on age alone ambiguous. Therefore, additional constraints, such as zircon isotope data, or analyses of detrital minerals less susceptible to reworking, such as feldspars, may be required for more robust provenance interpretations.

Grant Group

Detrital zircon sample GSWA 246758 (Wingate et al., 2021i) is a heterogeneous, very fine to fine-grained feldspathic sandstone from the upper Grant Group between the *P. confluens* and the *M. tentula* Spore-Pollen Zones. Spore-pollen biostratigraphy constrains the depositional age of this sample to Asselian (298.9 – 293.5 Ma) of the lower Permian whereas SHRIMP data indicate a youngest zircon at 304 ± 4 Ma and a conservative maximum depositional age of 566 ± 14 Ma for the youngest coherent group of five analyses.

The age spectrum for GSWA 246758 is compared in Figure 36 with data from the Grant Group in petroleum exploration well Samphire Marsh 1 (Chemostrat Australia, 2019) and more distant wells on the Barbwire Terrace and Fitzroy Trough (Martin et al., 2019). The detrital zircon age signatures are broadly comparable between these datasets. The ages of the youngest zircon are typically very close to the age of deposition inferred from biostratigraphic data. Some dates younger than the inferred depositional age in the Samphire Marsh 1 samples likely reflect minor downhole contamination given that most of these samples were of cuttings.

Sample GSWA 246758 contained several Archean zircons, which are also seen in the Samphire Marsh 1 samples but are mostly absent in samples from other wells (Fig. 36). The main zircon age components are late Paleoproterozoic to early Neoproterozoic and late Neoproterozoic to Cambrian. The ultimate sources of the zircons, which may have seen multiple reworking, could include a number of adjacent terranes, and possibly include a more distal 'pan-Gondwana' component as discussed in Haines et al. (2013). The youngest detrital zircons, present in all of the Canning Basin samples, yield dates very close to the biostratigraphically determined depositional age, and may represent a component from nearby late Carboniferous volcanism (Reeckmann and Mebbersson, 1984). Ages consistent with nearby Paterson Orogen intrusive rocks (645–629 Ma; Maidment et al., 2010) are not a significant component in GSWA 246758 or in other Grant Group samples (Martin et al., 2019).

Barnicarndy Formation

Two detrital zircon samples were collected from the Barnicarndy Formation. The upper sample consists of sandstone (GSWA 246757; Wingate et al., 2021a), whereas the lower is a sericitic laminated siltstone bed with lenticular fine-grained sandstone interbeds (GSWA 246756; Wingate et al., 2021b). The youngest zircon ages (1σ) are 512 ± 5 and 456 ± 8 Ma. The younger date, although based on a single zircon, may provide a useful maximum constraint for the age of the upper Barnicarndy Formation in the absence of biostratigraphic data.

Although the Barnicarndy Formation samples contain minor Archean zircons, the majority of dates are upper Paleoproterozoic to Mesoproterozoic and upper Neoproterozoic to Cambrian. The significant age peaks at 1200–1050 Ma are similar to the age of several magmatic events in Australia, including the Warakurna LIP and events in the Musgrave, Madura and Coompana Provinces (Wingate et al., 2004; Wade et al., 2008; Wingate et al., 2015), and also commonly seen in the 'pan-Gondwana source'. The new zircon data were compared with a wide selection of comparable Ordovician units from across the Canning Basin (Fig. 37). Variability among these samples, particularly those from the Willara and Gap Creek Formation, suggests local differences in sediment supply, but overall the Barnicarndy Formation samples are most similar to those from the Nambeet Formation in Olympic 1, as well as from Wilson Cliffs Sandstone, and Goldwyer and Carranya formations.

Nambeet Formation

Two detrital zircon samples were selected from the Nambeet Formation in Barnicarndy 1, the upper from near the top of the Samphire Marsh Member and the lower from the Fly Flat Member. Samphire Marsh Member sample (GSWA 246755; Wingate et al., 2021h) is a calcareous quartz sandstone whereas the Fly Flat Member sample (GSWA 237998; Wingate et al., 2021g) consists of fine-grained quartz sandstone. The youngest zircons are 528 ± 6 and 590 ± 8 Ma, respectively, and are significantly older than the depositional ages provided by other constraints. As described below, a CA-IDTIMS age of 477.24 ± 0.41 Ma was obtained from a bentonite bed at 1891.87 to 1891.89 m (GSWA 237948; Table 7) and the *J. gananda*, *O. communis* and *P. proteus* conodont biozones were identified between these two detrital geochronology samples.

The age spectrum for Samphire Marsh Member sample GSWA 246755 (Fig. 38) includes multiple age components between c. 2757 and 528 Ma. A similar plot for Fly Flat Member sample GSWA 237998 (Fig. 38) yielded detrital zircon ages from c. 3274 to c. 590 Ma. The samples share broadly similar age signatures, which are also similar to some previously analysed Canning Basin Ordovician samples, particularly those from the Fly Flat Member in Sally May 2 and the equivalent Wilson Cliffs Sandstone in Wilson Cliffs 1, as well as the Carranya and Goldwyer formations, and samples of the Acacia Sandstone Member in Acacia 2.

Yapukarninjarra Formation

Three detrital zircon geochronology samples (Table 7) from the Yapukarninjarra Formation include two from thin sericitic siltstone beds (GSWA 237995, Wingate et al., 2021d; GSWA 237997, Wingate et al., 2021f) and a fine-grained quartz sandstone (GSWA 237996; Wingate et al., 2021e). The youngest zircons in these samples are dated at 630 ± 5, 608 ± 6, and 510 ± 5 Ma, respectively. There are no CA-IDTIMS dates on volcanic zircons or biostratigraphic information available for this unit, therefore the youngest date for a single zircon provides a tentative maximum depositional age constraint for the lower part of the formation. A firm maximum depositional age of 593 ± 7 Ma can be based on the youngest coherent group of three analyses in GSWA 237995.

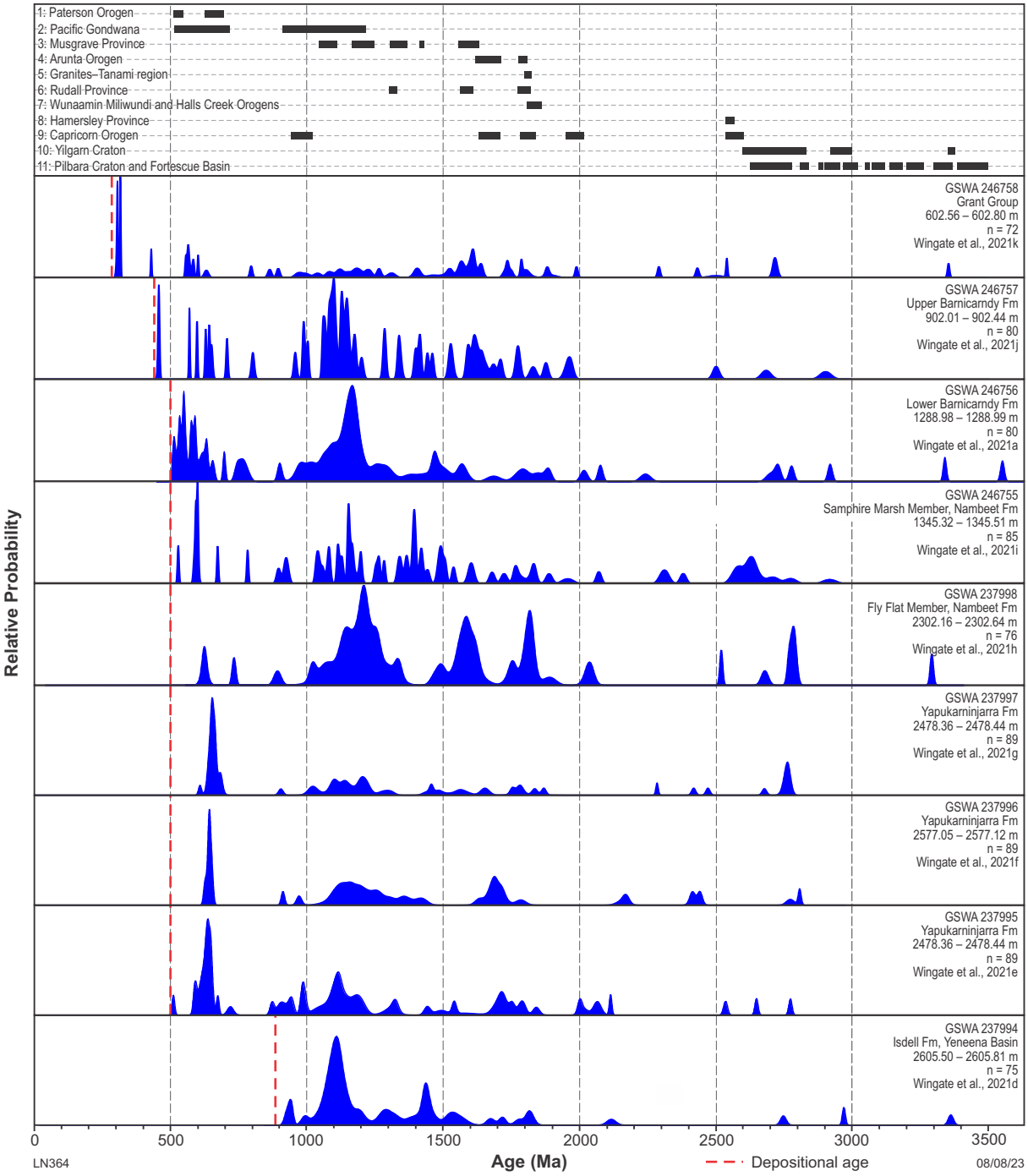

Figure 35. SHRIMP U–Pb detrital zircon age spectra for Barnicarndy 1 samples; n, number of analyses

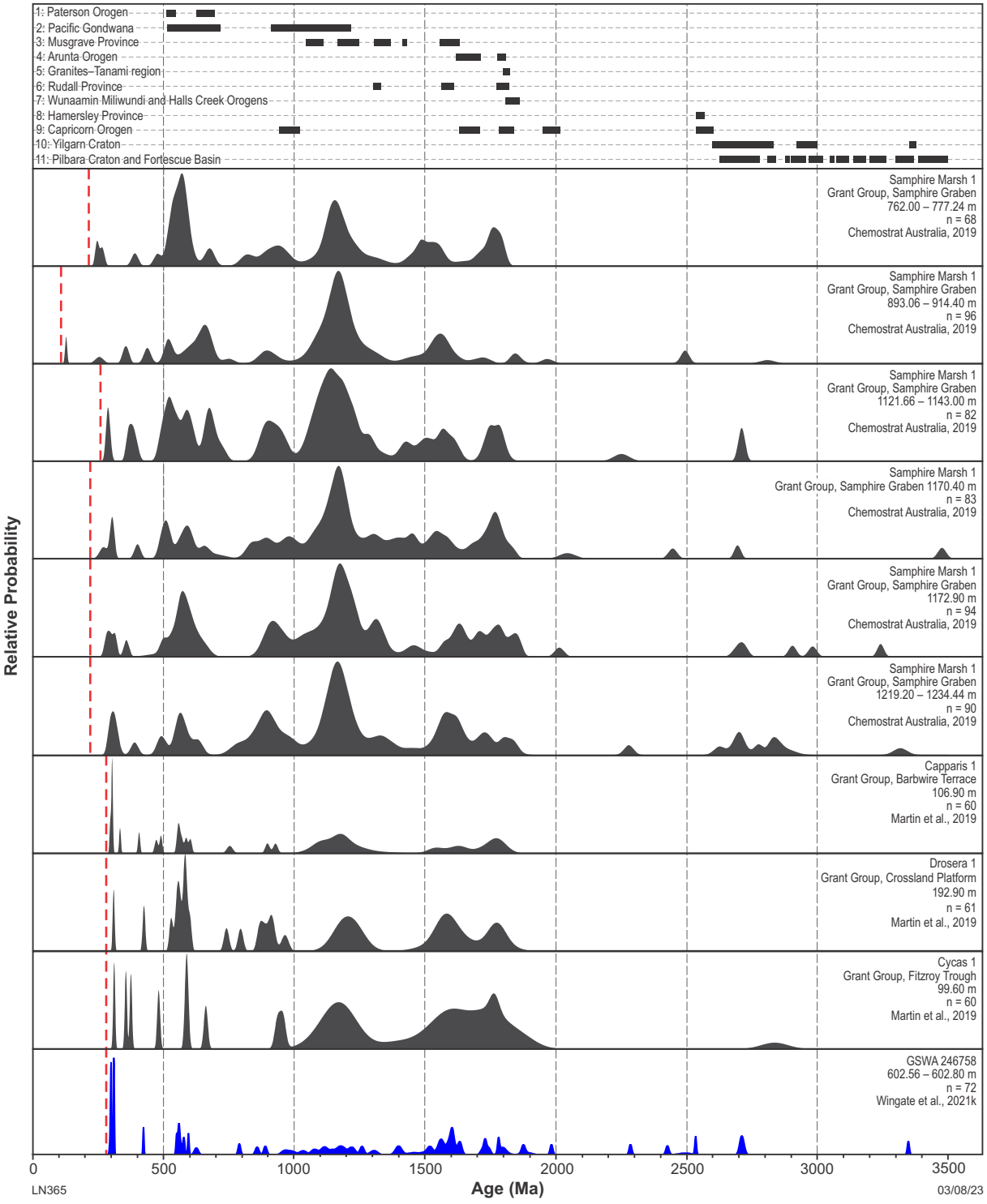

Figure 36. SHRIMP U–Pb detrital zircon age spectra for a sample of Grant Group in Barnicarndy 1 (blue) compared with previously published samples of the Grant Group across the Canning Basin; n, number of analyses

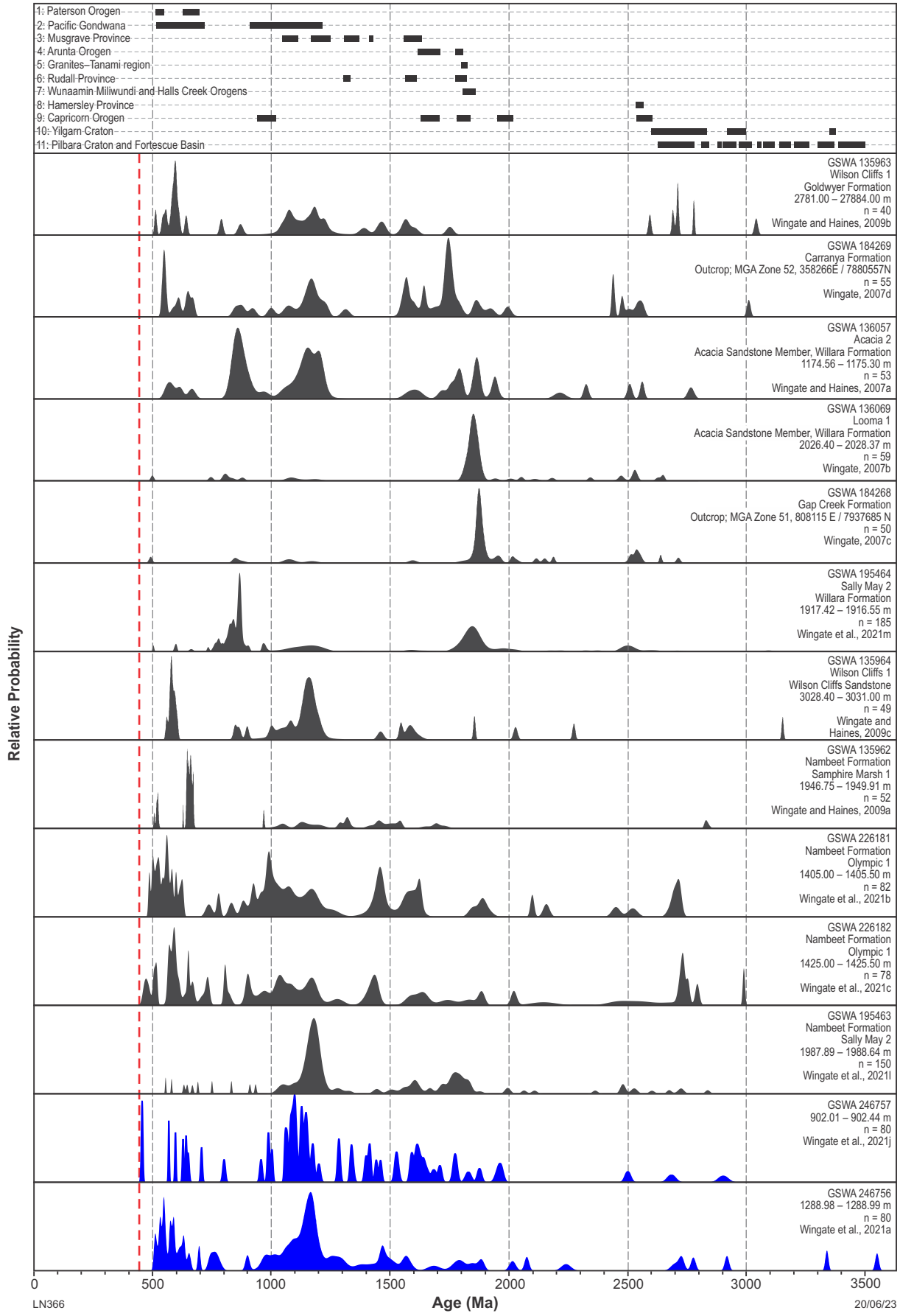

Figure 37. SHRIMP U–Pb detrital zircon age spectra for samples of the Barnicarndy Formation in Barnicarndy 1 (blue) compared with previously published Ordovician samples from across the Canning Basin; n, number of analyses

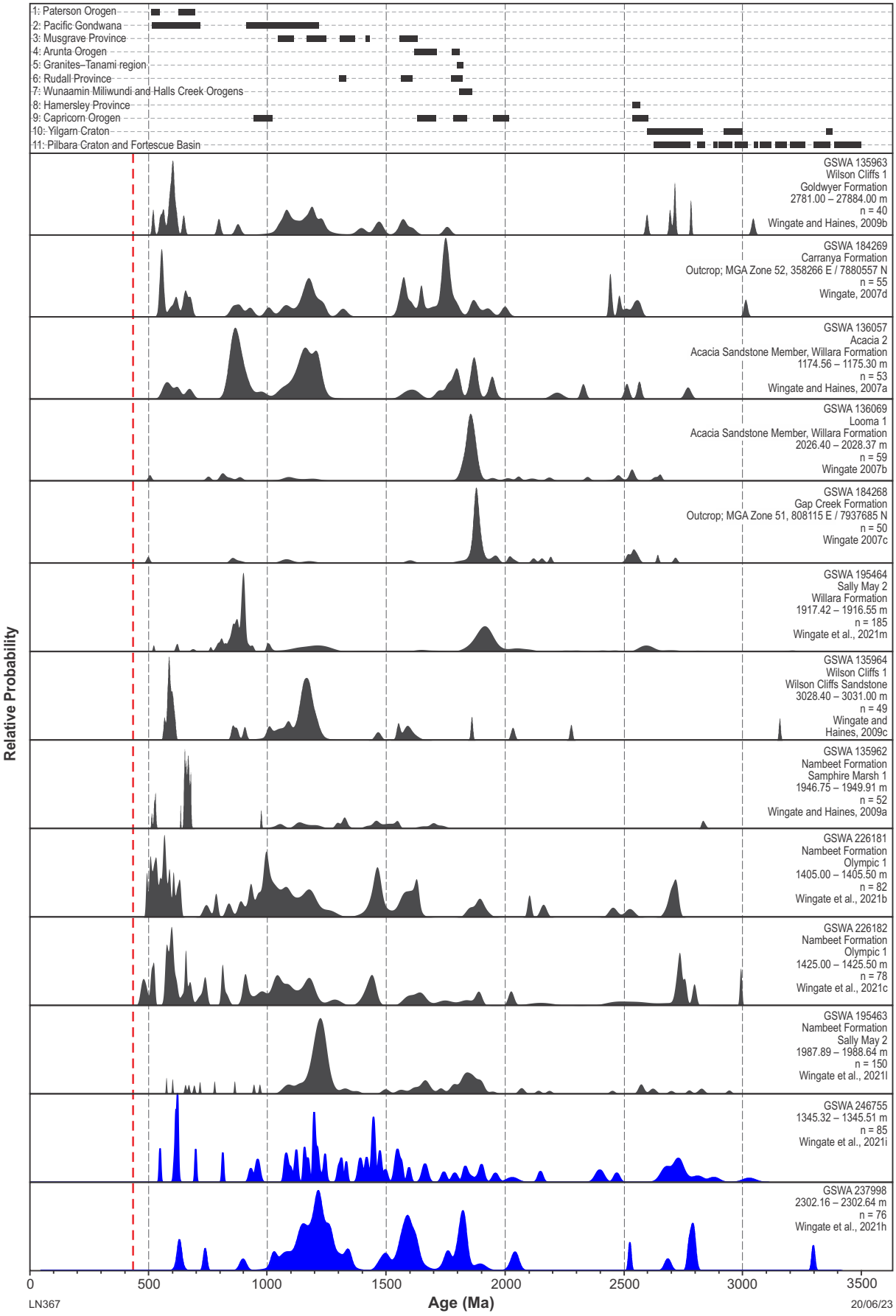

Figure 38. SHRIMP U–Pb detrital zircon age spectra for samples of the Nambeet Formation in Barnicarndy 1 (blue) compared with previously published Ordovician samples from across the Canning Basin; n, number of analyses

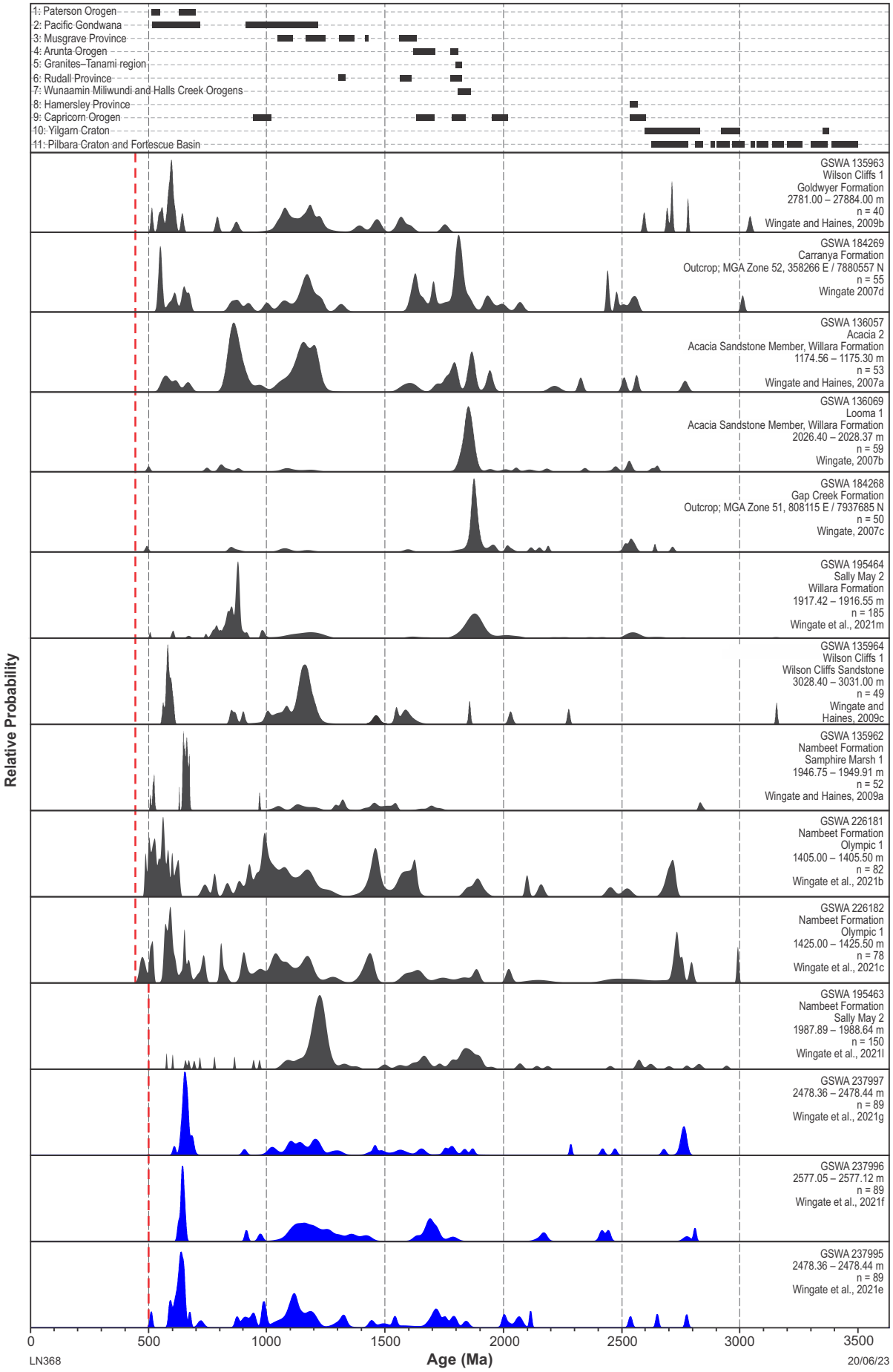

Figure 39. SHRIMP U–Pb detrital zircon age spectra for samples of the Yapukarninjarra Formation in Barnicarndy 1 (blue) compared with previously published Ordovician samples from across the Canning Basin; n, number of analyses

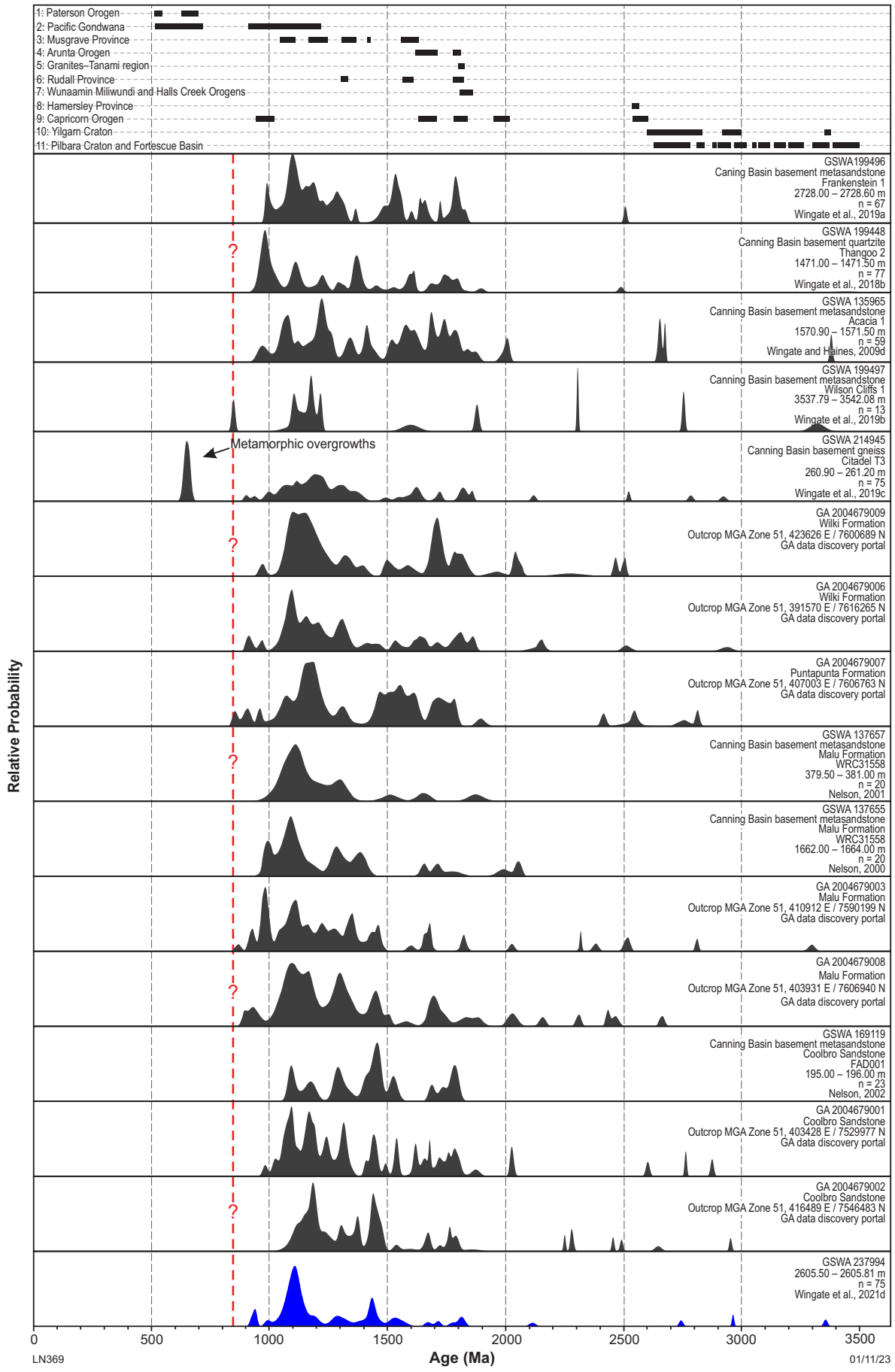

Figure 40. SHRIMP U–Pb detrital zircon age spectra for a sample of the Yeneena Basin in Barnicarndy 1 (blue) compared with previously obtained samples of the Yeneena Basin; n, number of analyses; unpublished Geoscience Australia (GA) sample data can be obtained through the Geochron Delivery section of the GA data discovery portal (www.ga.gov.au/geochron-sapub-web/geochronology/shrimp/search.htm)

Table 7. U–Pb geochronology and results

GSWA no.	Depth from (m)	Depth to (m)	Analysis method	Stratigraphic unit	Youngest single zircon (Ma)	MDA* (Ma)	Age range (Ma)	Reference/ Appendix
246758	602.56	602.80	SHRIMP	Grant Group	304 ± 4	566 ± 14	304–3355	Wingate et al, 2021i
246757	902.01	902.44	SHRIMP	Barnicarndy Formation	456 ± 8	637 ± 25	456–3042	Wingate et al, 2021h
246756	1288.98	1288.99	SHRIMP	Barnicarndy Formation	512 ± 5	531 ± 18	512–3551	Wingate et al, 2021a
246755	1345.32	1345.51	SHRIMP	Barnicarndy Formation	528 ± 6	595 ± 5	528–2757	Wingate et al, 2021g
237948	1891.87	1891.89	CA–IDTIMS	Samphire Marsh Member	477.24 ± 0.58	477.24 ± 0.58	477–1165	Appendix 11a
237949	1891.93	1891.95	CA–IDTIMS	Samphire Marsh Member	477.24 ± 0.41	477.24 ± 0.41	477–2766	Appendix 11a
237953	2009.05	2009.06	CA–IDTIMS	Samphire Marsh Member	652.61 ± 0.84	652.61 ± 0.84	653	Appendix 11a
237998	2302.16	2302.64	SHRIMP	Fly Flat Member	1007 ± 18	1007 ± 18	3274–590	Wingate et al, 2021f
237960	2380.05	2380.05	CA–IDTIMS	Fly Flat Member	1544.6 ± 1.2	1544.6 ± 1.2	1545	Appendix 11a
237997	2478.36	2478.44	SHRIMP	Yapukarninjarra Formation	608 ± 6	654 ± 4	608–2763	Wingate et al, 2021e
237996	2531.51	2531.91	SHRIMP	Yapukarninjarra Formation	630 ± 5	643 ± 6	630–2828	Wingate et al, 2021d
237995	2577.05	2577.12	SHRIMP	Yapukarninjarra Formation	510 ± 5	593 ± 7	510–2772	Wingate et al, 2021c
237994	2605.30	2605.81	SHRIMP	Yeneena Basin	918 ± 11	923 ± 9	918–3393	Wingate et al, 2021b

*MDA, conservative maximum depositional age; for SHRIMP data, this is the average date for the youngest coherent group of three or more analyses, reported with 95% uncertainty

The age spectra for the three Yapukarninjarra Formation samples are very consistent (Fig. 39). The oldest zircons are 2800–2650 Ma, similar to the ages of magmatic events in the Yilgarn Craton. All three samples yield late to mid-Paleoproterozoic peaks. Other significant age components include 1300–900 Ma and 650–630 Ma. These younger Proterozoic age components resemble typical detrital zircon ages from Yeneena Basin samples (Maidment et al., 2008), and the ages of felsic intrusions into the Paterson Orogen near the Barnicarndy Graben (Czarnota et al., 2007). The youngest maximum depositional ages, from 654–593 Ma (Table 7), are similar to the 654–603 Ma age range of the O'Callaghans Supersuite in Canning Basin basement east of the Barnicarndy Graben (Kelsey et al., 2022). It is thus possible that the Yapukarninjarra Formation contains a significant component of material derived locally from the erosion of the Paterson Orogen, which may also include older multi-cycle zircons. A detrital zircon sample from the base of Samphire Marsh 1 (GSWA 135962; Wingate and Haines, 2009) tentatively in the Yapukarninjarra Formation, also includes a major c. 650 Ma and minor mid-Cambrian age component, combined with a range of late Paleoproterozoic to early Neoproterozoic zircon ages.

Yeneena Basin

The Yeneena Basin detrital zircon sample (Table 7) is a red, iron-stained, diffusely laminated siltstone (Wingate et al., 2021c). SHRIMP zircon dates range between 3363 and 918 Ma (Fig. 40) and the maximum depositional age based on the weighted mean of three analyses, is 923 ± 9 Ma. Archean and early Paleoproterozoic dates are rare, and the main age components are between 1850 and 900 Ma. The age spectrum is broadly similar to available detrital zircon data from a number of Yeneena Basin units and basement samples from beneath the Canning Basin, with best matches to the Coolbro Sandstone and Malu Formation (Fig. 40).

U–Pb bentonite zircon geochronology

Beds visually identified as consisting of bentonite (clay-rich material derived from diagenetic alteration of volcanic ash) were observed in the Yapukarninjarra, Nambeet and Barnicarndy formations. These beds closely resemble previously sampled Canning Basin bentonites that have successfully yielded euhedral zircons that provided precise CA-IDTIMS ages (Normore et al., 2018). Most of the 50 samples from Barnicarndy 1 were collected at the drill site (details in Appendix 10) and most were typically very small because the bentonite beds are very thin (millimetres to centimetres). Despite the previous success rate with CA-IDTIMS dating of Canning Basin bentonites, 37 of 50 (74%) of bentonite beds sampled in Barnicarndy 1 yielded only rounded detrital zircons and eight of 50 (16%) yielded no zircon crystals. Only five of 50 (10%) yielded euhedral zircons, with one of those samples (GSWA 237950) providing zircons that were too small to mount for analysis.

CA-IDTIMS samples and analytical methods are described in Appendix 11a and the data are provided in Appendices 11b,c. Two samples from a thick bentonite bed, GSWA 237948 and 237949 (Fig. 41a; Table 7), yielded CA-IDTIMS dates that can be interpreted as maximum depositional ages. Seven zircons from GSWA 237949 dated by laser ablation – inductively coupled plasma – mass spectrometry (LA-ICP-MS) yielded dates of 2766–465 Ma (circles in Fig. 41b,c), and four zircons dated by CA-IDTIMS (labelled z1–z4 in Fig. 41b,c) provided $^{238}U/^{206}Pb$ dates of 479.73 ± 0.32, 478.78 ± 0.37, 478.14 ± 0.43, and 477.24 ± 0.41 Ma (all uncertainties are ±2 sigma).

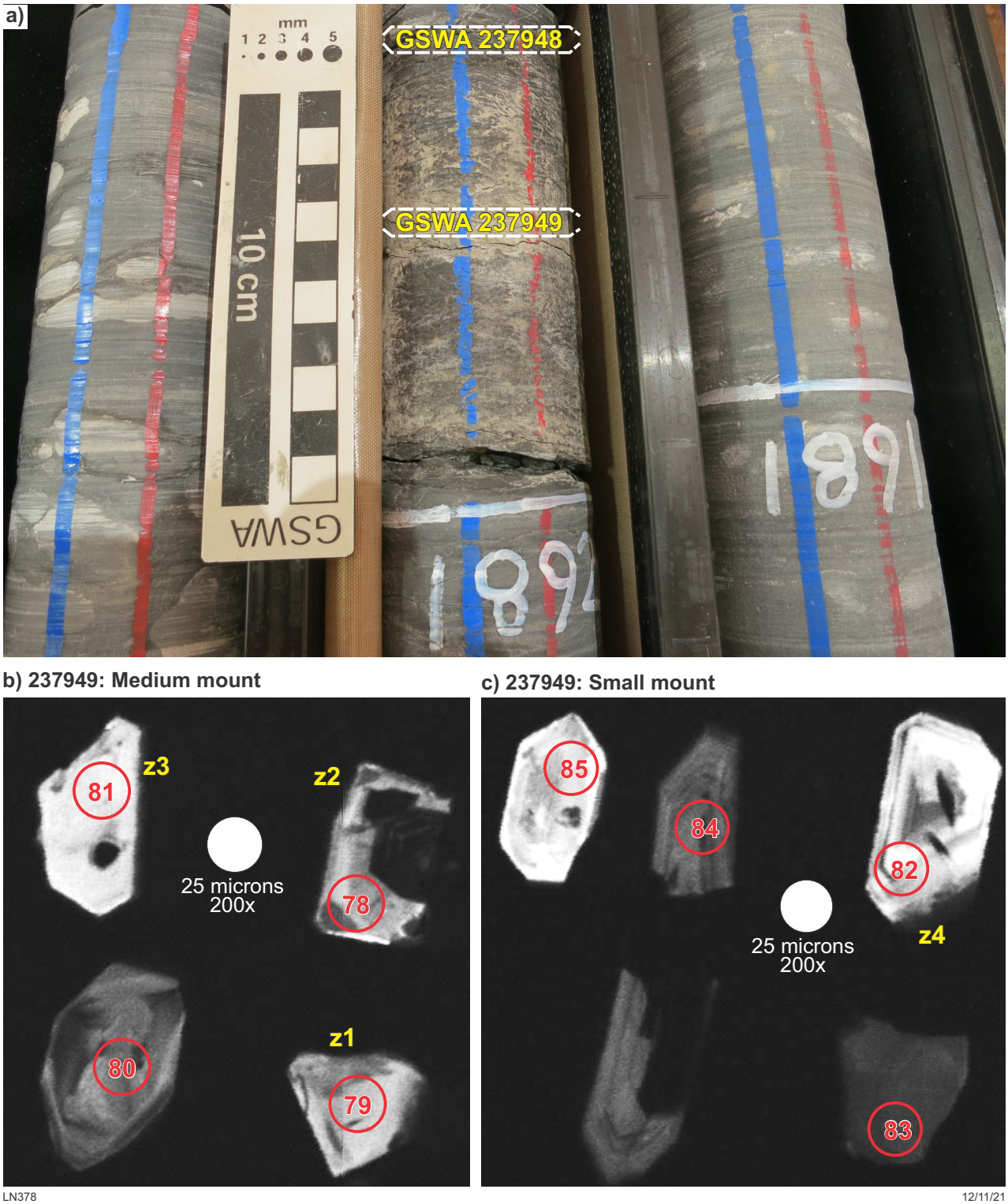

Figure 41. Nambeet Formation bentonite bed dated by CA-IDTIMS: a) location of samples within 10 cm thick bentonite bed; b)–c) representitive zircon grains within two mounts from sample GSWA 237949 showing the location of spots for preliminary LA-ICP-MS dating (red circles) and grains subsequently selected for CA-IDTIMS dating (z1–z4)

Sample GSWA 237948, from the upper part of the same bentonite horizon as GSWA 237949 contained two sharply faceted grains, one of which indicated a $^{207}Pb/^{206}Pb$ date of 1165.13 ± 4.81 Ma and the other a $^{238}U/^{206}Pb$ date of 477.24 ± 0.58 Ma. Two additional samples, GSWA 237960 and 237953, yielded euhedral zircon crystals dated 1544.60 ± 1.29 and 652.61 ± 0.84 Ma, respectively (Table 7). The two youngest dates for GSWA 237948 and 237949 are identical and yield a weighted mean $^{238}U/^{206}Pb$ date of 477.24 ± 0.33 Ma. This date is interpreted as a maximum depositional age (Table 7), and the older zircons in all four samples are interpreted as inherited or detrital.

This maximum depositional age is very similar to the CA-IDTIMS $^{238}U/^{206}Pb$ dates from the Samphire Marsh Member in Olympic 1 (Normore et al., 2018; Dent et al., 2021); 477.03 ± 0.16 Ma (GSWA 221478) and 479.37 ± 0.16 Ma (GSWA 221480). These samples fall within an indeterminate conodont assemblage lying between occurrences of the *O. communis* and *P. proteus* Conodont Biozones (Fig. 16). This correlates well between the lower Samphire Marsh Member of Barnicarndy 1 and Olympic 1 and may suggest the extension of the *P. proteus* Biozone up to 1891 m in Barnicarndy 1 (see Plate 1, Correlation panel).

Thermochronology

The thermal evolution of Barnicarndy 1 was investigated using Uranium–Thorium/Helium [(U–Th)/He] thermochronology of zircon and apatite (Appendix 12; Danišík, 2021). Heavy mineral concentrates from existing SHRIMP geochronology samples were used for this study (Table 8), resulting in six suitable samples for zircon (U– Th)/He (ZHe) analysis and two samples suitable for apatite (U–Th)/He (AHe) analysis (Fig. 16). Additional samples were selected for future fission track analysis.

The thermochronometry sensitivity range or partial retention zone of apatite is between 40 and 90 °C (Flowers et al., 2009) whereas the zircon thermochronometry sensitivity range is between 140 and 220 °C (Guenthner et al., 2013). The downhole temperatures quickly reach the apatite sensitivity range, so only the shallowest two samples are practical for the AHe technique. Grant Group sample GSWA 246758 (602.56 – 602.80 m) demonstrates the utility of both the AHe and ZHe techniques and the resulting thermal history modelling (Fig. 42). All 14 zircons analysed for ZHe from this sample (Fig. 42a) yield dates older than the c. 295 Ma depositional age interpreted from spore-pollen zonation (Backhouse, 2020), indicating these crystals were not thermally reset and that post-depositional temperatures did not reach 140 °C. With one outlier excluded from the AHe results, 13 apatite crystals yield dates equal to or younger than the depositional age (Fig. 42b), indicating that most apatites were thermally reset and post-depositional temperatures exceeded 40–90 °C. Thermal history modelling uses the He FTy program (Ketcham, 2005) based on the youngest ZHe and AHe age components of GSWA 246758 to display time–temperature (tT) trajectories or inflection points of tT trajectories (Fig. 42c). The modelled maximum burial temperature is estimated to be 100 to 110 °C based on ZHe + AHe + vitrinite reflectance inputs. With a current downhole temperature of 48 °C, this specifies a temperature difference range of 52–62 °C, suggesting 2.1 – 2.5 km of missing section based on a geothermal gradient of 25 °C/km.

Table 8 lists the thermochronology data from Appendix 12 (Danišík, 2021) including temperature change and the interpreted amount of erosion or missing section from each sample. When comparing the depth vs age profile (Fig. 43) and the calculated missing section for the various stratigraphic units (Table 9), it can be demonstrated that the majority of the missing 2–3 km was removed by uplift and erosion of the Barnicarndy Graben since the Permian. This supports interpretations of maturity based on vitrinite and vitrinite equivalence studies (see under Organic geochemistry below), as well as seismic velocity anomalies (Zhan, 2021).

Geochemistry

Inorganic geochemistry

This section details the inorganic geochemical and isotopic analyses undertaken for chemostratigraphic studies over the entire Barnicarndy 1 stratigraphic section, with multi-element geochemistry analysis focused on the pre-Canning Basin basement interval. Sampling for standard XRD analysis mirrored the regular thin section sampling, while the in-house pXRD analysis focused on eight samples for confirmation of mineralogy identified from infrared hyperspectral analysis (GSWA HyLogger 3-2, Hancock et al., 2013).

Chemostratigraphy

The chemostratigraphic analysis of Forbes et al. (2020; Appendix 8) is first discussed and reviewed, prior to the assessment of additional data from the Yeneena Basin. The Forbes et al. (2020) chemostratigraphic study involved initial elemental analysis of 100 samples over the 610.03 – 2679.07 m interval by Inductively Coupled Plasma Optical Emission Spectrometry (ICP-OES) and Inductively Coupled Plasma Mass Spectrometry (ICP-MS). The Ca abundance data from the initial analyses allowed the selection of a subset of 75 samples for stable carbon and oxygen isotope analysis ($\delta^{13}C$ and $\delta^{18}O$ carbonate) from 1350.42 – 2679.07 m, with only seven of the 75 samples unsuccessful.

The main conclusions from the Forbes et al. (2020) study include:

- division of the sampled interval into nine chemostratigraphically distinct packages
- identification of six major chemostratigraphic boundaries possibly representing unconformities, hiatal surfaces or sediment provenance changes
- identification of a unique Ordovician chemostratigraphic signature for the Barnicarndy 1 well that is distinct from that of other Canning Basin wells suggesting a different sediment provenance
- tentative correlation of the Barnicarndy 1 carbon-isotope curve to the Argentine Precordillera and the Yangtze Platform suggesting an age range of latest Cambrian to Middle Ordovician.

Table 8. Thermochronology samples: methylene iodide (MI) light – 2.9 – 3.3 g/cm³; MI heavy – >3.3 g/cm³; FT – fission track analysis; He - (U–Th/He analysis)

GSWA no.	*Depth from (m)*	*Depth to (m)*	*Stratigraphic unit*	*Mineral fraction*	*Mineral analysed*	*Temperature reached (°C)*	*Delta T (°C)*	*Missing section (km)*
246758	602.56	602.80	Grant Group	MI heavy MI light	zircon apatite	between 90 and 140	42–62	2.1 – 2.5
246757	902.01	902.44	Barnicarndy Formation	MI heavy MI light	zircon	3 of 14 zircons reached 220	60–80	2.0 – 2.8
246755	1345.32	1345.51	Samphire Marsh Member	MI heavy MI light	zircon apatite	7 of 13 zircons reached 220	64–79	2.2 – 2.8
237998	2302.16	2302.64	Fly Flat Member	MI heavy MI light	zircon	8 of 13 zircons reached 220	70–85	2.4 – 3.0
237997	2478.36	2478.44	Yapukarninjarra Formation	MI heavy MI light	zircon	11 of 14 zircons reached 220	66–91	2.2 – 2.8

Notes: MI, methylene iodide light <3.3 g/cm^3; MI heavy >3.3 g/cm^3

Table 9. TOC and Rock-Eval 6 pyrolysis data statistics for Barnicarndy 1. Statistics for HI values are only provided for the Grant Group and Samphire Marsh Member

Property	*Stratigraphic unit*	*N*	*Min*	*Max*	*Mean*	*Std Dev*	*10th ile*	*50th%ile*	*90th %ile*
TOC (wt.%)	All	203	0.00	4.88	0.16	0.35	0.01	0.11	0.28
	Grant Group	42	0.04	4.88	0.32	0.73	0.09	0.22	0.31
	Barnicarndy Formation	41	0.01	0.09	0.03	0.02	0.01	0.02	0.05
	Nambeet Formation	97	0.00	0.67	0.17	0.11	0.03	0.16	0.31
	Yapukarninjarra Formation	17	0.01	0.13	0.02	0.03	0.01	0.01	0.04
	Undivided Yeneena Basin	4	0.01	0.29	0.11	0.13	0.01	0.06	0.29
S2	All	202	0.00	10.86	0.14	0.76	0.01	0.08	0.17
(mg HC/g rock)	Grant Group	42	0.00	10.86	0.34	1.66	0.01	0.08	0.17
	Barnicarndy Formation	41	0.01	0.30	0.13	0.06	0.03	0.12	0.19
	Nambeet Formation	97	0.00	0.46	0.07	0.08	0.01	0.05	0.15
	Samphire Marsh Member	75	0.00	0.46	0.07	0.07	0.01	0.04	0.14
	Fly Flat Member	22	0.00	0.34	0.08	0.08	0.01	0.07	0.17
	Undivided Yeneena Basin	4	0.03	0.09	0.06	0.03	0.03	0.06	0.09
HI (mg HC/gTOC)	Grant Group	41	4	223	43	35.75	14.00	37.00	68.00
	Samphire Marsh Member	72	1	143	34	23.87	11.00	30.00	59.70

N = # of samples, Min = minimum value for set, Max = maximum value for set, Std Dev = standard deviation, 10th %ile = 10th percentile, 50th%ile = 50th percentile and 90th %ile = 90th percentile

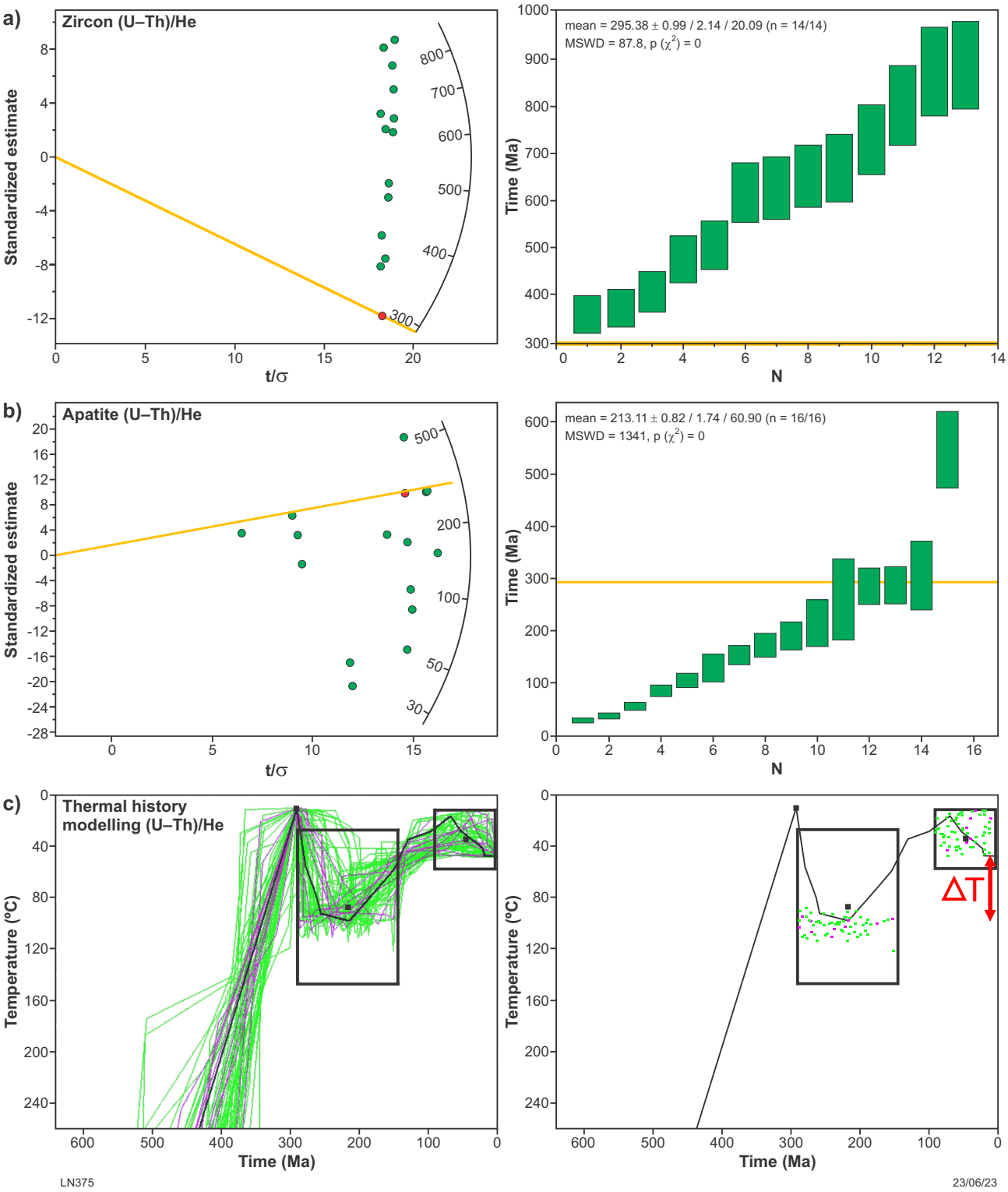

Figure 42. Thermochronology data for sample GSWA 246758 (602.56 – 602.80 m) from the Grant Group (modified from Appendix 12; Danišík, 2021): a) alpha-ejection corrected zircon (U–Th)/He (ZHe) dates displayed in radial plot (Galbraith, 1988) in left panel and ranked order plot in right panel, with depositional age indicated by yellow lines; b) alpha-ejection corrected apatite (U–Th)/He (AHe) dates displayed in radial plot in left panel and ranked order plot in right panel, with depositional age indicated by yellow lines; c) thermal history modelling results based on the youngest ZHe and AHe age components, displayed in time-temperature plots as time-temperature (tT) trajectories (left diagram) or as inflection points of tT trajectories (right diagram); green paths/dots are statistically 'acceptable' fits (goodness of fit [GOF] value between 0.05 – 0.49); magenta paths/dots are statistically 'good' results (GOF ≥0.50 – 1.00); black path is the statistically 'best' solution; rectangles are time-temperature constraints based on prior information; ΔT is the difference between modelled maximum temperature and current downhole temperature

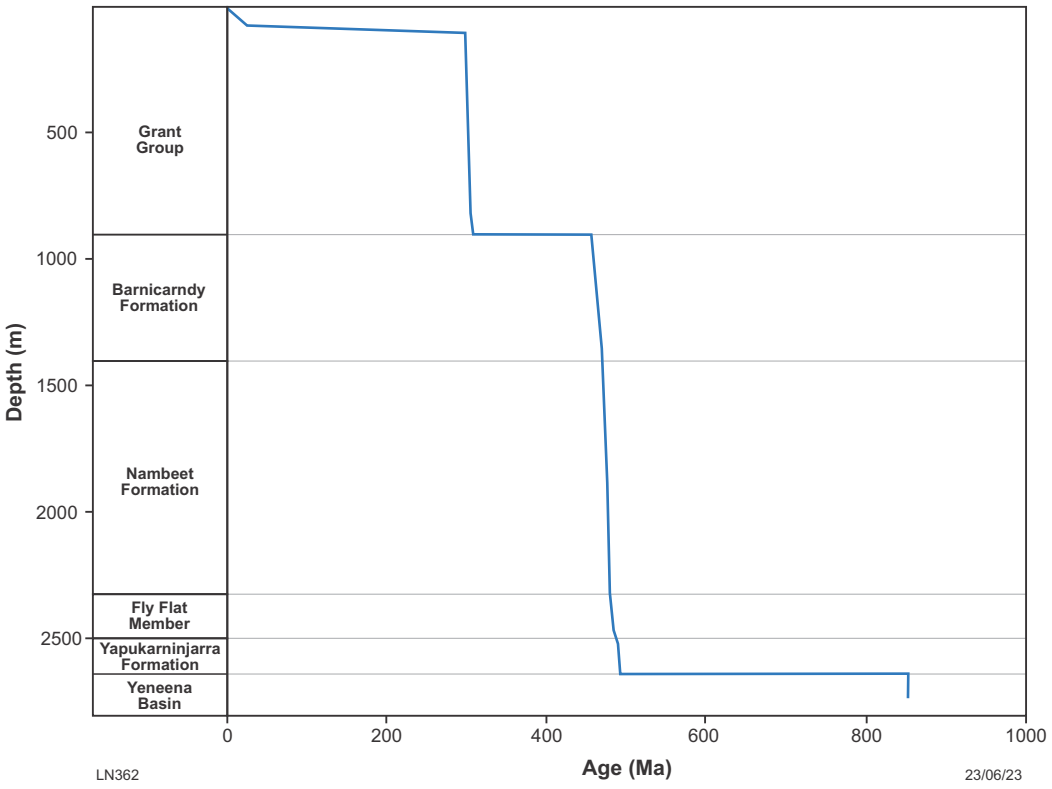

Figure 43. Age vs depth profile for Barnicarndy 1

The chemostratigraphic boundaries and packages identified in Forbes et al. (2020) match very closely to the final formal well stratigraphy of Barnicarndy 1, but potentially provide the basis for additional division of both the Fly Flat and Samphire Marsh members of the Nambeet Formation. The raw elemental data can be found in the Western Australian Petroleum and Geothermal Information Management System (WAPIMS) website <www.wapims.dmp.wa.gov.au/wapims> (Forbes et al., 2020). The preliminary interpretation of the Barnicarndy 1 carbon isotope results can be refined by the integration of conodont biozones, available throughout the Samphire Marsh Member and a single accompanying CA-IDTIMS zircon date, as discussed below.

Isotope-ratio mass spectrometry

Two separate sample sets were analysed by isotope-ratio mass spectrometry (IRMS) to provide $\delta^{13}C$ and $\delta^{18}O$ data (Fig. 44). The first dataset (obtained from 68 of 75 samples) primarily covers the Samphire Marsh Member of the Nambeet Formation with one sample collected from the Yeneena Basin section, whereas the second dataset (for 18 of 19 samples) was collected entirely within the Yeneena Basin. Both datasets are presented in Appendix 13.

Canning Basin

Forbes et al. (2020) tentatively correlated the Barnicarndy 1 carbon isotope ($\delta^{13}Ccarb$) data from the Samphire Marsh Member to the biostratigraphically constrained Argentine Precordillera and Yangtze Platform sections, suggesting an age range from the latest Cambrian to Middle Ordovician (early Dapingian). The subsequent availability of conodont biostratigraphy and a single CA-IDTIMS zircon date both suggest an early Floian age for the base of the Samphire Marsh Member in Barnicarndy 1. The new data requires corrections to the interpretation, facilitated by correlating the isotope curves directly to wells drilled elsewhere within the Canning Basin (Samphire Marsh 1, Willara 1 and Olympic 1, see Plate 1, Correlation panel).

The Samphire Marsh 1 $\delta^{13}Ccarb$ isotope curve correlates to the lower portion of the Samphire Marsh Member in Barnicarndy 1 and extends below into the Fly Flat Member and Yapukarninjarra Formation, which were not sampled for isotopes in Barnicarndy 1 due to low carbonate levels. This correlation suggests significant erosion of the upper Nambeet Formation prior to deposition of the Grant Group at the Samphire Marsh 1 location and also confirms the absence of the Willara and Goldwyer formations when the curve is correlated to Willara 1. Tentative correlations of the Barnicarndy 1 isotope curve over the Canning Basin interval with those of Argentina and China will need to be revisited once further fill-in analysis of the Barnicarndy 1 well is completed.

Yeneena Basin

Samples taken every three metres over the fresh dolomitic section of the Yeneena Basin in Barnicarndy 1 from 2624–2680 m were analysed for carbon and oxygen isotopes at the West Australian Biogeochemistry Centre, School of Biological Sciences, The University of Western Australia. The $\delta^{13}C$ results range from 3.3 to 5.1‰ Vienna Peedee Belemnite (VPDB) with $\delta^{18}O$ ranging from -10.9 to -14.2‰ VPDB (Fig. 44). Although direct correlation to the Neoproterozoic carbon isotope curve is not possible with such a stratigraphically restricted sample set, a minimum

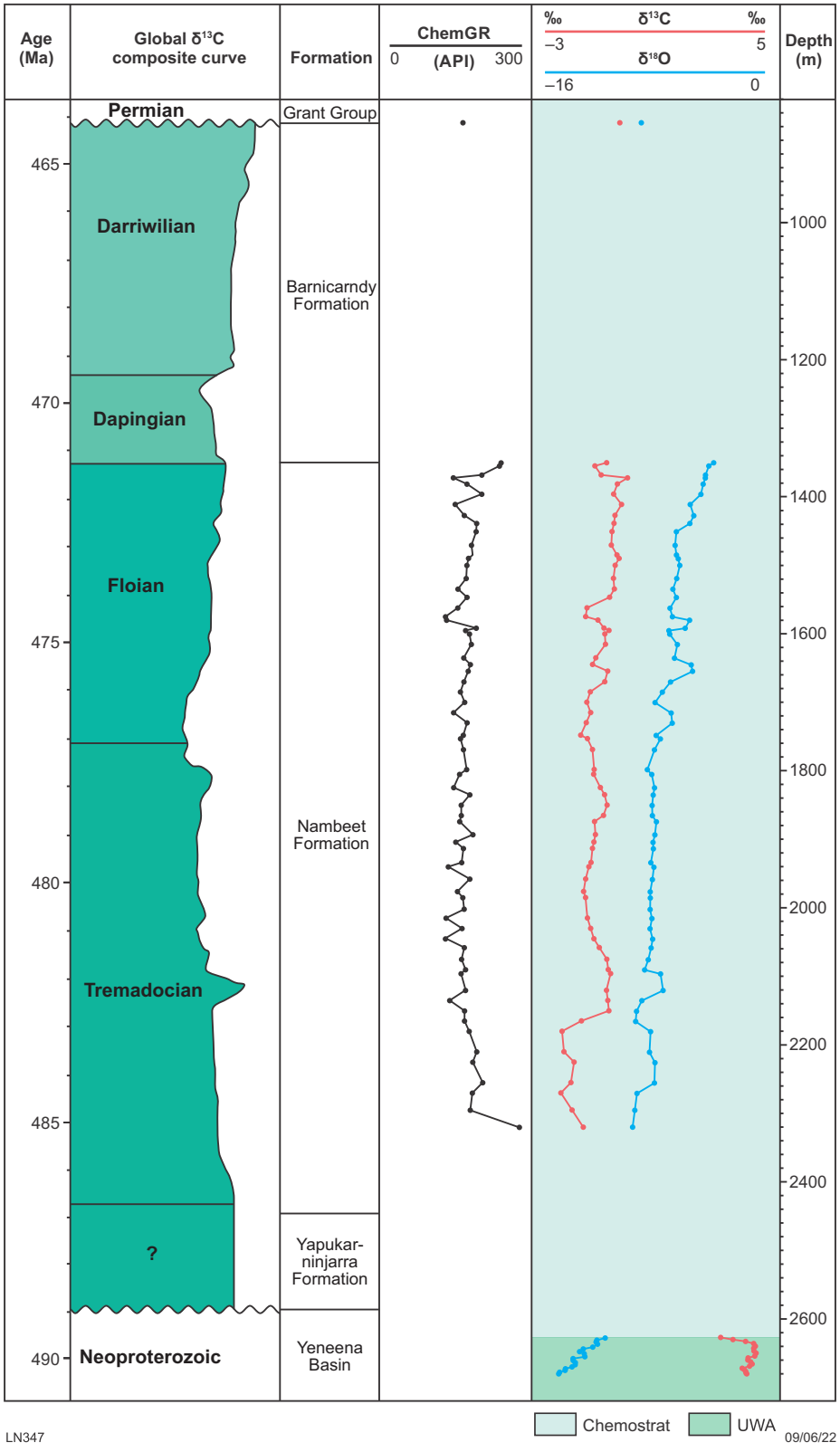

Figure 44. Barnicarndy 1 carbon and oxygen isotope data compared to global Ordovician carbon isotope curve

Cryogenian age can be inferred by comparison to the global Neoproterozoic carbon isotope curve of Cox et al. (2016; Fig. 45). However, the Yeneena Basin succession was intruded by granites during the Cryogenian (Haines et al., 2018b), making isotopic comparisons to the Tonian curve more relevant.

Multi-element geochemistry

Two elemental geochemical datasets were collected from Barnicarndy 1 core (Appendix 14). The first set paralleled the nine GSWA geochronology samples and the second set of 12 samples targeted the Yeneena Basin section of the core.

The Yeneena Basin samples include eight from unweathered slightly metamorphosed dolomitic siltstone at the base of the core and four samples from the overlying weathered horizon. Calculation of the chemical index of alteration (CIA; Wang et al., 2020) clearly distinguishes the paleo-regolith from the fresh metasedimentary rocks of the Yeneena Basin (Fig. 46) with the four regolith samples plotting in a tight range above 0.7 CIA, whereas the fresh samples have a range between 0.1 and 0.4 CIA.

Two samples were also selected from the Yeneena Basin section based on visible mineralization. Only sample 226264 at 2661.13 m yielded an anomalous copper value of 1240 ppm. The sulfide mineralization in this sample was disseminated within a stratiform quartz layer 5 mm thick (Fig. 47).

X-ray diffraction

Two sample sets were analysed for mineralogy by X-ray diffraction (XRD). Eight samples were analysed in-house for semi-quantitative XRD using the GSWA benchtop XRD instrument to correlate samples with hyperspectral data from GSWA HyLogger 3-2 system (Appendix 15). A second subset of 47 samples was completed in conjunction with petrography undertaken at Core Laboratories, Perth, with results presented in Appendix 16.

Rapid validation and quantification of mineralogy identified from infrared hyperspectral analysis (GSWA HyLogger 3-2, Hancock et al., 2013) and visual logging of the Barnicarndy 1 drillcore was performed via portable X-ray diffractometry (pXRD). Eight samples of selected core intervals were crushed and sieved to <150 µm powder, from which 20 mg aliquots were analysed using the GSWA pXRD instrument (Olympus BTX-II with Co-anode and kapton windows, Wawryk and Hancock, 2019). Clay separation is not performed as part of routine analysis with this instrument, as it is used to provide rapid results without significant sample preparation.

Mineral fingerprinting and relative intensity ratio quantification of pXRD data was performed using the XPowder software package. Samples GSWA 246812, 246813, 246818, 246819 were collected to confirm general mineralogy, samples GSWA 246815, 246816, 246817 were collected to determine the identity of visually prominent but ambiguous crystalline phases, and sample GSWA 246814 was collected to analyse the mineralogy of a suspected ash bed. The full semi-quantitative results are shown in table 1 of the Barnicarndy 1 GSWA pXRD report (Appendix 15; Wawryk, 2020).

Fundamental limitations of the technique and analytical resolution of the GSWA pXRD instrument preclude distinguishing between illite and mica, which possess near-identical crystal structures and hence diffraction patterns. Similarly, precise classification of dolomite/ankerite, which form a complex solid solution series with very similar diffraction patterns, is not possible. Analysis of the pXRD pattern for sample GSWA 246814, which probably represents a diagenetically altered ash bed (bentonite), provides a composition of predominantly illite/mica with major quartz, but no other significant phases. The absence of distinguishable diffraction peaks at about 14Å and about 7Å indicates the lack of other significant separate or interlayered clays (e.g. smectites, kaolins, chlorites), although these may be present but beyond the resolution of the instrument or require clay separation techniques to be measurable.

Analyses of the pXRD pattern for samples GSWA 246815 and GSWA 246817 demonstrate that the visually distinctive white crystalline phases observed are dolomite/ankerite, in contrast to calcite, which features more prominently in the rest of the well. Similarly, analysis of sample GSWA 246816 demonstrates that the visually distinctive white crystalline phase is predominantly anhydrite with significant dolomite/ankerite also present. The observation of red fluorescence of this mixed phase under ultraviolet light is consistent with, but not exclusively diagnostic of, the presence of anhydrite and dolomite/ankerite.

Organic geochemistry

The baseline for the organic geochemistry analysis on Barnicarndy 1 was provided by Rock-Eval pyrolysis and fluid inclusion stratigraphy throughout the entire stratigraphic interval including samples from ditch cuttings and core. These initial results indicate limited source rock potential for units intersected in Barnicarndy 1, but still allowed enough organic material for detailed investigations by organic petrology analysis, including the visual estimation of dispersed organic matter and determination of thermal maturity (Ranasinghe and Crosdale, 2020; Appendix 19). The samples with the highest organic matter content were also analysed in detail for carbon and hydrogen isotopes, allowing molecular characterization of organic matter within the Nambeet Formation. Additional source rock biomarker analysis included molecular source rock characterization by gas chromatography (GC), gas chromatography mass spectrometry (GC-MS) and compound specific isotope analysis (CSIA). Distinctive organic matter sources are suggested for the Samphire Marsh and Fly Flat Members of the Nambeet Formation, which are different from previously measured Ordovician-sourced Canning Basin oils.

Organic petrological data, programmed pyrolysis Tmax and molecular maturity parameters were used in combination for estimation of thermal maturity within the Barnicarndy 1 sedimentary section. Results suggest the oil window is as shallow as 500 m within the Grant Group section. Some variability on interpretations of the depth of the top of the gas window is shown with a 2000 m depth in the Samphire Marsh Member based on vitrinite reflectance equivalence, while maturity parameters extend the oil window deeper in to the Fly Flat Member.

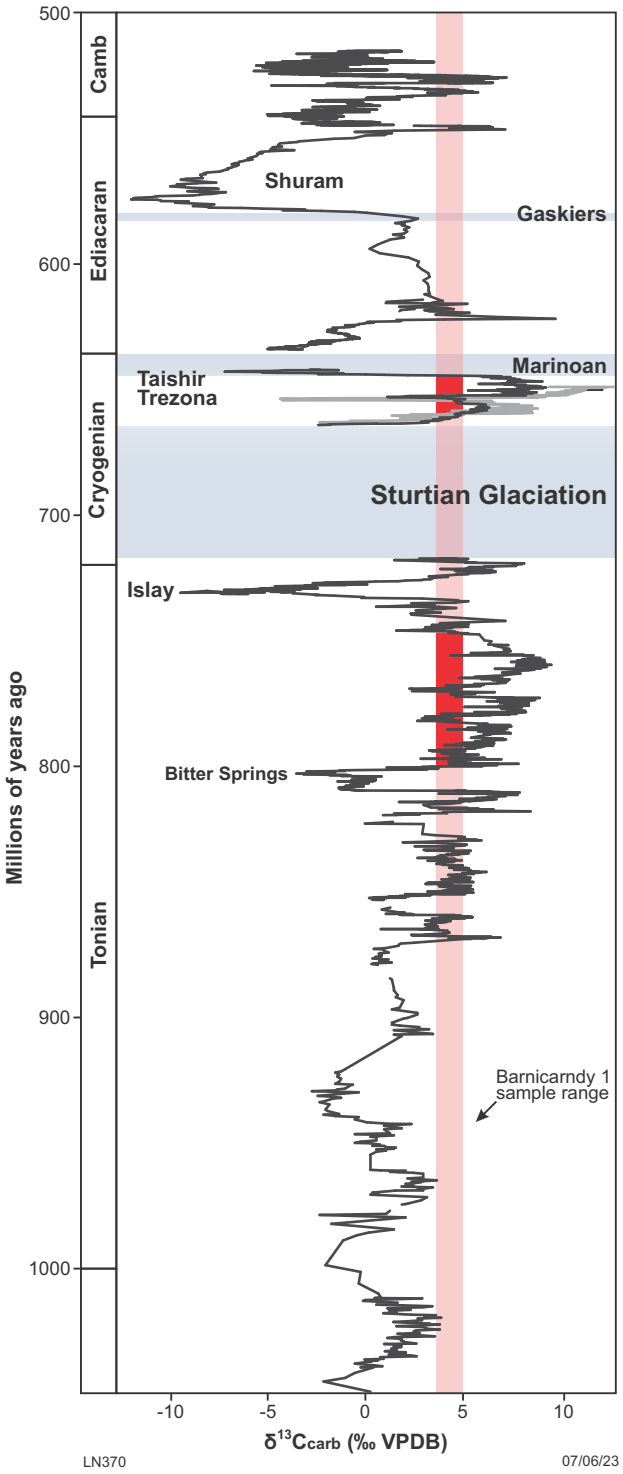

Figure 45. Comparison of Barnicarndy 1 Yeneena Basin carbon isotope data range to the global Neoproterozoic carbon isotope curve from Cox et al. (2016)

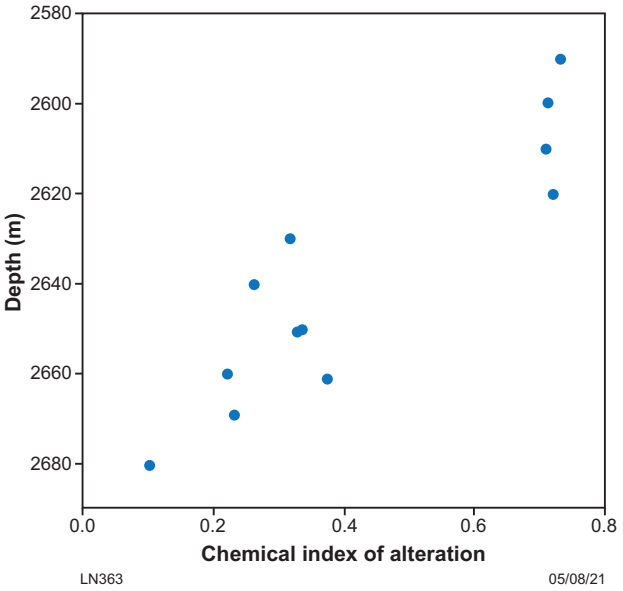

Figure 46. Chemical index of alteration vs depth for Barnicarndy 1 Yeneena Basin samples

Figure 47. Visible copper mineralization in GSWA sample 226264 at 2661.13 m; multi-element analysis yeilded 1240 ppm Cu

Fluid inclusion stratigraphy identified two distinctive hydrogen-enriched zones with two distinctive hydrogen sources. An upper hydrogen zone corresponds mainly to the Barnicarndy Formation while the second zone shows highest enrichment in the Yapukarninjarra Formation. A single helium-enriched zone corresponds to the lower hydrogen zone. This suggests a common source related to a combination of radioactive decay within U- and Th-bearing minerals to produce He and radiolysis of water to produce H_2. Upper to moderate gravity petroleum inclusions were imaged in the Barnicarndy Formation.

Rock-Eval pyrolysis

The hydrocarbon-generating potential of the sedimentary succession in Barnicarndy 1 was assessed by programmed pyrolysis of powdered ditch cuttings and whole core samples collected at regular intervals down the well (Appendix 17; Grosjean et al., 2020b). Present-day statistics for pyrolysis data from the well are provided in Table 9 and a histogram of Total Organic Carbon (TOC) content is shown in Figure 48. Of the 201 rock samples analysed for TOC content, all but two samples have a TOC content less than 0.5%, the threshold below which a rock is not considered a source rock for hydrocarbon generation (Peters and Cassa, 1994).

The sample with the highest TOC content (4.88 wt%) is from 438 m in the upper Grant Group, with an associated S2 of 10.86 mg hydrocarbons (HC)/g rock and Hydrogen Index (HI) of 223 mg HC/g TOC (Fig. 49). S2 indicates the volume of hydrocarbons released during thermal pyrolysis of the sample. The second most organic-rich sample (0.67 wt%) is from 1835 m in the Samphire Marsh Member of the Nambeet Formation. This sample has a much lower S2 value of 0.46 mg HC/g rock and HI of 69 mg HC/g TOC (Fig. 49).

Overall, the pyrolysis data indicate that samples in Barnicarndy 1 are typically organically lean, with the Grant Group having the highest average organic carbon content of 0.32 wt%, albeit skewed by the one organic-rich sample (50th percentile for TOC being 0.22 wt%). The average S2 and HI values for the group is 0.34 mg HC/g rock and 43 mg HC/g TOC respectively, indicating no source potential to generate hydrocarbons. Within the Paleozoic sedimentary succession, the Samphire Marsh Member has the highest average TOC content of 0.18 wt%, as obtained from 75 samples which were measured throughout the thick (925 m) succession of marine calcareous claystones. The average S2 and HI values for the member is 0.07 mg HC/g rock and 34 mg HC/g TOC respectively. The Barnicarndy Formation, the Fly Flat Member of the Nambeet Formation and the Yapukarninjarra Formation have mean TOC contents of 0.03 wt%, 0.11 wt% and 0.02 wt% respectively, with similarly low average TOC content (0.11 wt%) for the Yeneena Basin metasediments (Table 9). It should be noted that the resultant high hydrogen indices of some samples from these units reported in Grosjean et al. (2020b) are an artefact from reporting TOC values <0.08 wt% and hence are not summarised in Table 9. It is concluded that at Barnicarndy 1, there is no present-day source potential for the sedimentary succession penetrated in the well.

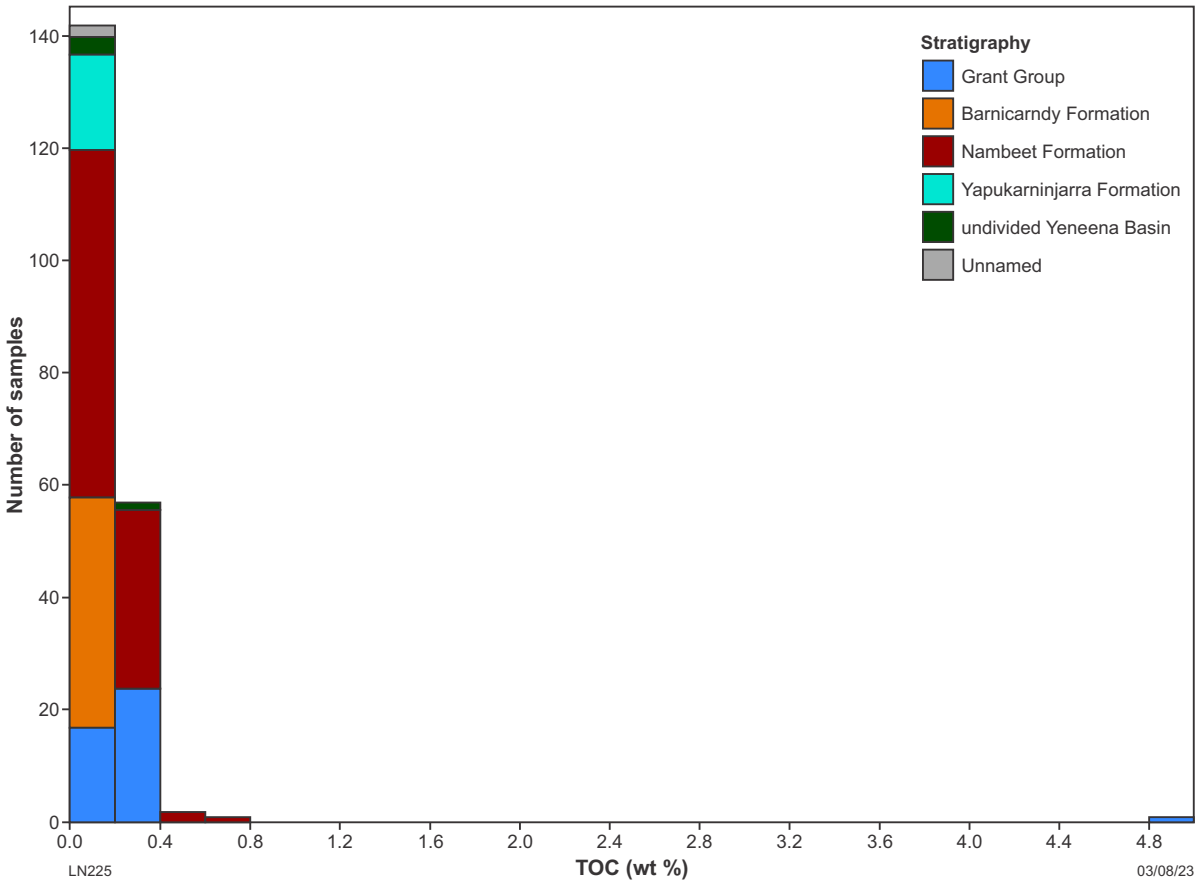

Figure 48. Histogram of TOC content in cuttings and core samples from Barnicarndy 1

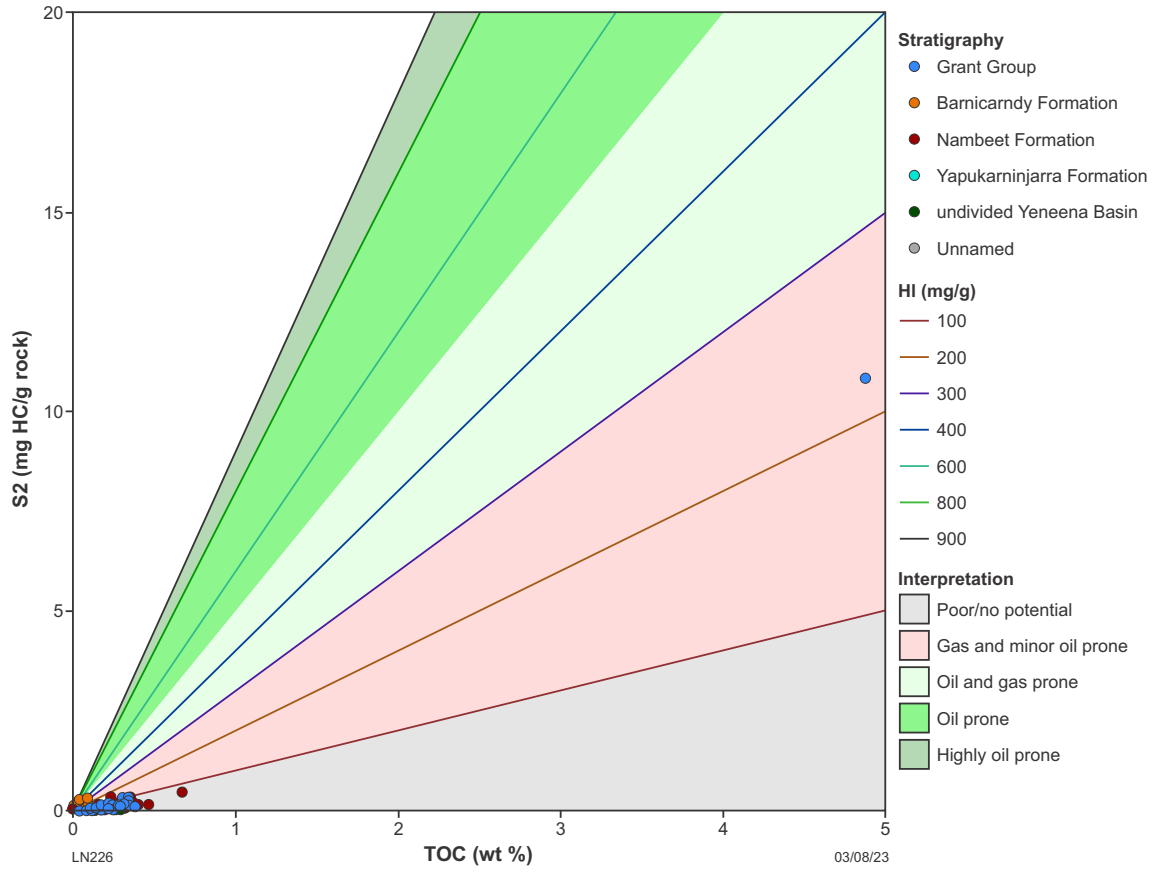

Figure 49. Cross-plot of TOC vs S2 for the samples from Barnicarndy 1

Organic petrology maceral analysis

From the Barnicarndy 1 well, 42 samples were chosen for organic petrological studies, from which a subset of 20 samples were selected for detailed organic petrographic analysis, including the visual estimation of the dispersed organic matter and determination of thermal maturity (Ranasinghe and Crosdale, 2020). Source richness was determined by a visual estimation method under the microscope using both reflected white light and blue light excitation. Organic matter was present in all samples examined, but in very low volumes. The distribution of the maceral groups described from the Grant Group (Paterson Formation-equivalent) and the Paleozoic (mostly Lower Ordovician) sedimentary section is graphically illustrated in Figure 50.

The organic matter content in the stratigraphic section is consistently low, with most samples containing less than 0.5% total organic matter by volume, which is consistent with the low TOC contents measured by Rock-Eval pyrolysis. Samples examined from the Grant Group and the Samphire Marsh Member of the Nambeet Formation contained the highest abundance of macerals in the well. The uppermost six samples of the Permian Grant Group contained land-plant sourced phytoclasts that varied from 0.20% to 0.40%, with the highest organic matter content being found in the ditch cuttings from 477–480 m depth (Ranasinghe and Crosdale, 2020). Liptinite, which consists primarily of the land-plant macerals sporinite (Fig. 51a,b) and cutinite (Fig. 51c,d), is the prevailing maceral together with inertinite. The sporinite and rare liptodetrinite fluoresce bright yellow to dull orange, whereas *Botryococcus*-related telalginite (Fig. 51e,f) fluoresces bright orange. Vitrinite is typically either very low or absent in this group at Barnicarndy 1. Pyrite and iron oxides are only rarely observed in these sedimentary rocks.

In the Lower Ordovician Nambeet Formation, organic matter is typically sparse with liptinite being the dominant maceral (Fig. 52a–f). Over the depth range 1354.80 – 2095.96 m in the Samphire Marsh Member, liptinite consists of lamalginite, liptodetrinite and telalginite (Ranasinghe and Crosdale, 2020), arising from marine acritarchs, and the (possible) cyanobacterial microfossils *Gloeocapsomorpha prisca* and ?*Eomerismopedia maureeniae* (Foster et al., 2021). These liptinites exhibit bright to dull orange fluorescence down to a depth of around 1874 m, after which the fluorescence either fades to dull orange or weak brown, or is extinguished in the deeper samples. Zooclasts, consisting predominantly of graptolites (Fig. 52a,b) with rare chitinozoans, occur as minor maceral components throughout the Samphire Marsh Member from 1354.80 to 2244.08 m. The core sample from 1591.47 to 1591.53 m depth in the Samphire Marsh Member had the highest total organic matter by volume of 1.2% in the well (Fig. 50). However, the TOC content for this particular sample measured by Rock-Eval pyrolysis was only 0.28 wt%, with a HI of 68 mg HC/g TOC. Nevertheless, palynological analyses record that a moderate yield of kerogen was recovered and that organic debris is common (Foster et al., 2021). The identification of *G. prisca*, acritarchs, whole chitinozoans and graptolite fragments corroborate the relatively high liptinite and zooclast abundances recorded in the maceral assemblage at this depth. The Samphire Marsh Member samples contain common to abundant pyrite, sparse glauconite and sparse to rare iron oxides.

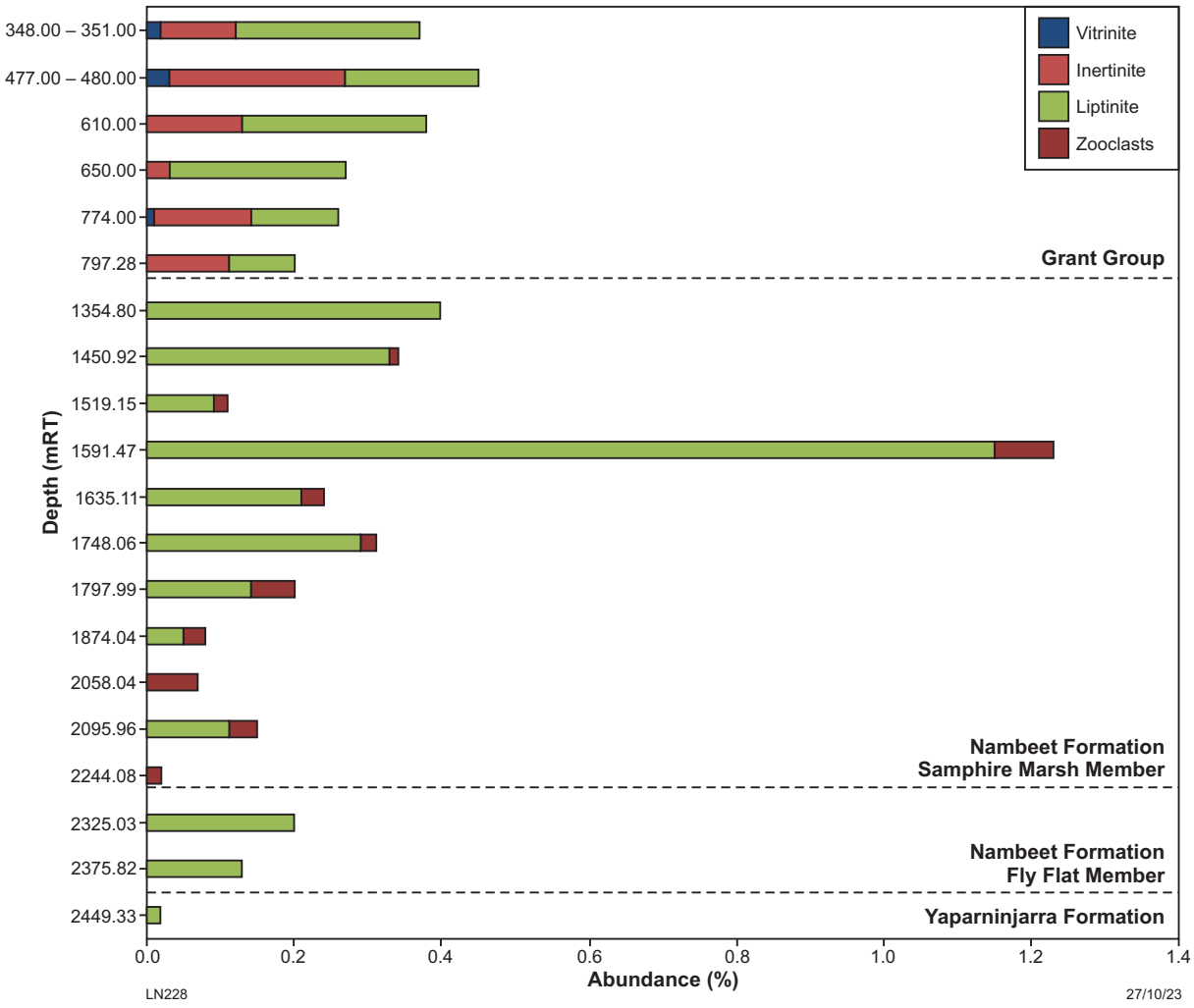

Figure 50. Distribution of maceral groups including zooclasts in samples from Barnicarndy 1

In the core samples examined from the Fly Flat Member of the Nambeet Formation, at depths 2325.03 and 2375.82 m, liptinite is still the dominant maceral but it consists primarily of alginite, which occurs as narrow elongated strands, probably a form of lamalginite (Ranasinghe and Crosdale, 2020). *G. prisca* and zooclasts are absent at these depths. Rare to sparse acritarchs fluoresce orange to dull orange and rare alginite either fluoresce weak brown or have no fluorescence. These observations are consistent with the change in the microfossil assemblages recorded between the Samphire Marsh and Fly Flat members (Foster et al., 2021). Pyrite is common to abundant whereas iron oxides are rare and glauconite is not reported.

One core sample from the Yapukarninjarra Formation from 2449.33 to 2449.39 m depth was examined. It comprised argillaceous siltstone with minor sandstone lithologies. Although dispersed organic matter is rare, possible alginite occurs as narrow, non-fluorescing strands, with background mineral fluorescence being pervasive and dull orange. The high level of maturity of this sample is indicated by the narrow, highly reflecting strands sheathed in diffuse organic matter that are presumably highly coalified lamalginite. Pyrite is abundant; glauconite sparse and iron oxides are rare.

Molecular and isotopic characterization of organic matter within the Nambeet Formation

Seven core samples were selected from the Lower Ordovician Nambeet Formation to provide insights into the type of organic matter preserved and the redox conditions of the sediments during deposition of the succession in the marine embayment of the Barnicarndy Graben (Table 10). Detailed molecular and carbon and hydrogen isotopic analyses were carried out on the most organic-rich cores, albeit with an average TOC content of 0.17 wt%, as identified from Rock-Eval pyrolysis. On average, the cores from the Samphire Marsh Member have slightly higher organic matter content (average TOC = 0.18 wt%; Table 9) than those of the Fly Flat Member (average TOC = 0.11 wt%), but analyses throughout the Nambeet Formation were undertaken in an attempt to provide molecular evidence for the level of thermal maturity. Two cores that may possibly contain oil staining at 2304.63 m and 2321.19 m were also included in the analyses (Table 10). The possibility of oil staining was identified on the basis that the core fluoresced dull yellow under UV light and results from the HAWK pyrolysis data show depressed Tmax and elevated PI values (Table 10).

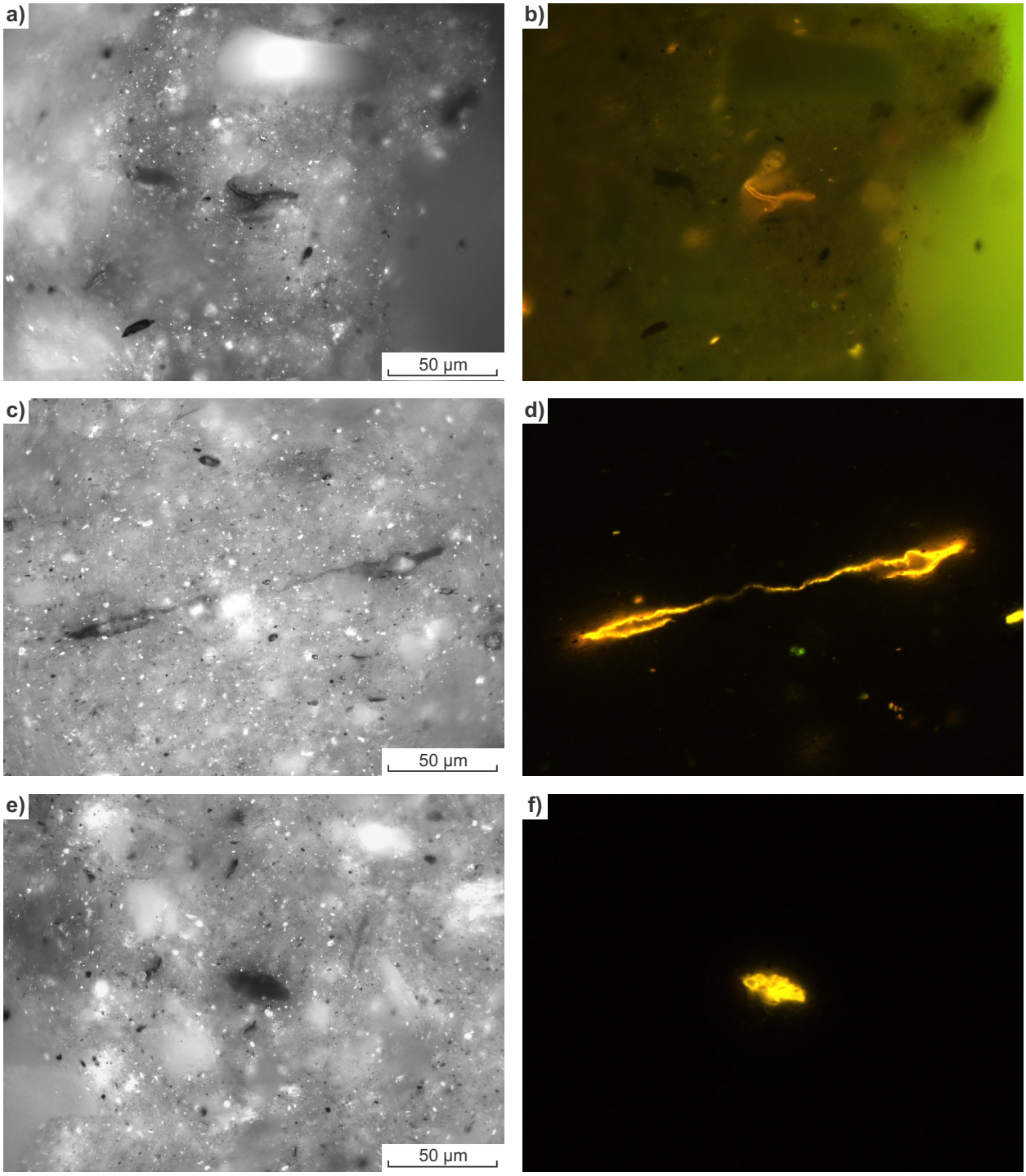

Figure 51. Maceral assemblages from the Grant Group, Barnicarndy 1: a),b) sporinite in claystone, sample GA 3307469, 348–351 m, Rv max = 0.47%, magnification x50 in reflected white light and blue light excitation; c),d) cutinite in claystone, sample GA 3307491, 610.00 – 610.03 m, Rv max = 0.66%, magnification x50 in reflected white light and blue light excitation; e),f) botryococcus-related telalginite in claystone, sample GA 3307493, 650.00 – 650.04 m, magnification x50 in reflected white light and blue light excitation

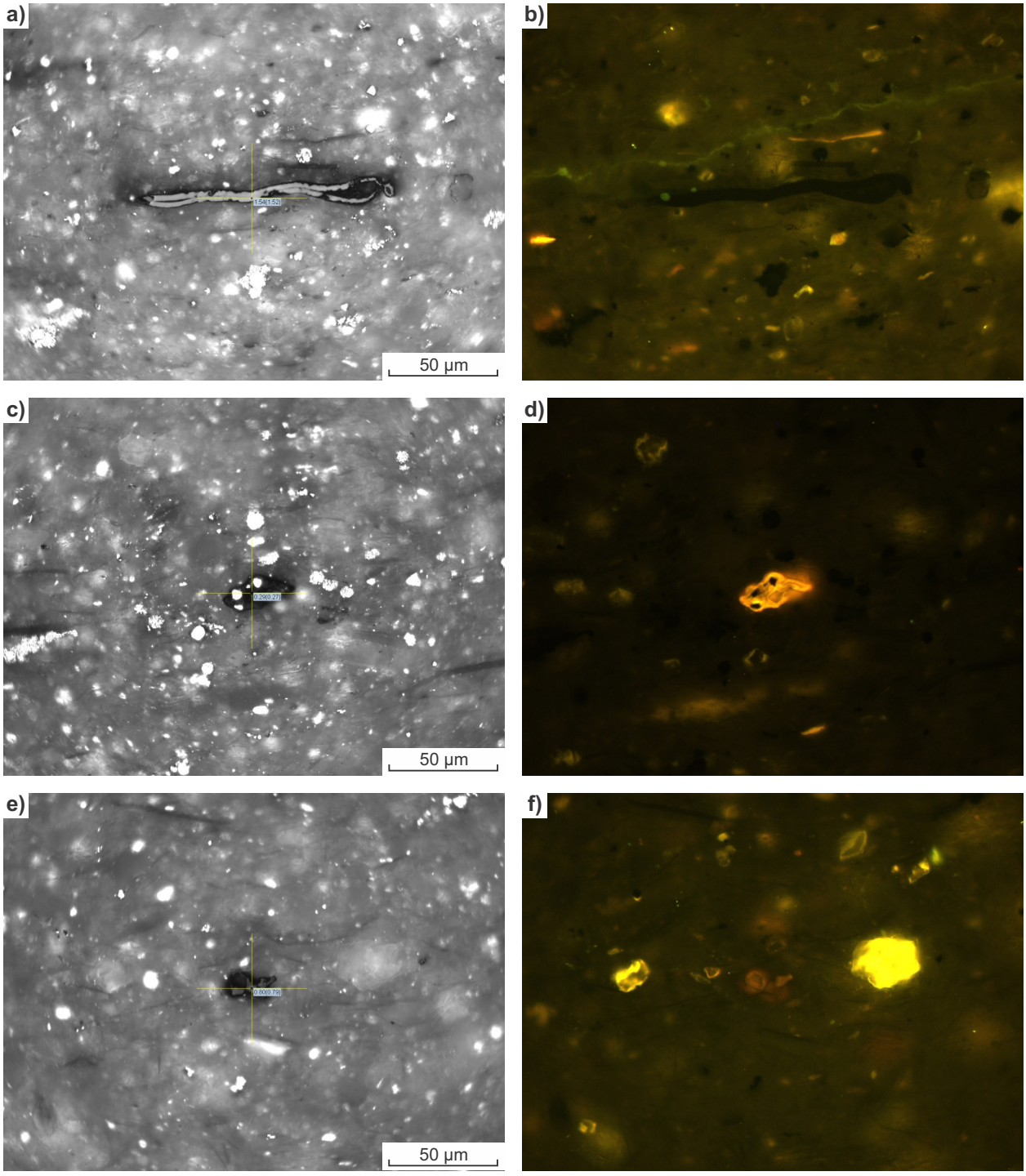

Figure 52. Maceral assemblages from the Nambeet Formation, Barnicarndy 1; a),b) graptolite in siltstone, sample GA 3311584, 1748.06 – 1748.16 m, $R_{Zooclast\ max}$ = 1.54%, $R_{Zooclast\ min}$ = 1.14%, magnification x50 in reflected white light and blue light excitation; c),d) telalginite (Gloecapsomorpha) in siltstone, sample GA 3311594, 1874.04 – 1874.17 m, $R_{Alginite}$ = 0.29%, magnification x50 in reflected white light and blue light excitation; e),f) telalginite in claystone, sample GA 3311612, 2095.96 – 2096.02 m, $R_{Alginite}$ = 0.80%, magnification x50 in reflected white light and blue light excitation

Table 10. TOC from Rock-Eval 6 and pyrolysis data from HAWK intrument for core samples selected for compositional analyses

GA no.	Depth from (m)	Depth to (m)	Stratigraphic unit	TOC (wt.%)	T_{max} (°C)	T_{max} (°C)	S1 (mg HC/g rock)	S2 (mg HC/g rock)	PI	Organic extract (ppm rock)	Study sample type
3307557	1427.34	1427.37	Samphire Marsh Mbr	0.38	425	429	0.07	0.25	0.22	54	OM
3311585	1753.03	1753.09	Samphire Marsh Mbr	0.46	424	430	0.05	0.37	0.12	121	OM
3311590	1824.25	1824.34	Samphire Marsh Mbr	0.4	426	433	0.05	0.16	0.24	94	OM
3311591	1835	1835.05	Samphire Marsh Mbr	0.67	430	434	0.08	0.88	0.08	148	OM
3311598	1933.72	1933.78	Samphire Marsh Mbr	0.13	nd	nd	nd	nd	nd	121	OM
6661398	2304.63	2304.70	Fly Flat Mbr	0.03	0.08	305	0.08	0.02	0.80	9	?oil stain
3311630	2317.05	2317.10	Fly Flat Mbr	0.32	0.09	441	0.09	0.65	0.12	231	OM
6661399	2321.25	Fly Flat	Fly Flat Mbr	0.11	0.04	439	0.04	0.07	0.36	115	?oil stain
3311633	2330.12	2330.17	Fly Flat Mbr	0.35	440	443	0.07	0.49	0.13	184	OM

All methods and results related to the gas chromatography (GC), gas chromatography mass spectrometry (GC-MS), and gas chromatography-temperature conversion mass spectrometry (GC-TC-IRMS) analyses are reported in Edwards et al. (2021). This is the first time that samples from the Lower Ordovician Nambeet Formation have been analysed for their biomarker and isotopic distributions, with only two GC-MS chromatograms being available for the Nambeet Formation in Olympic 1 (Normore and Dent, 2017a).

Molecular source characterization of organic matter within the Nambeet Formation by gas chromatography

Gas chromatograms, the identification of peaks and quantification of peak areas for Barnicarndy 1 can be found in Appendix 3 of Edwards et al. (2021). The gas chromatograms of the saturated hydrocarbon fractions from the Nambeet Formation rock extracts display linear or normal alkane distributions from C_{14} to >C_{40}, although their abundance decreases rapidly after C_{30} (Figs 53, 60). The five cores analysed over the depth range 1427.34 to 1933.72 m are within the Samphire Marsh Member that contains the remains of *G. prisca* (Table 11; Ranasinghe and Crosdale, 2020; Foster et al., 2021). The saturated hydrocarbon fractions of *G. prisca*-rich rocks are typically characterized by a strong odd-over-even carbon number predominance (OEP) in the C_{15}–C_{19} *n*-alkane range, as documented from the Goldwyer Formation in the Canning Basin (Hoffmann et al., 1987; Spaak et al., 2017). This distinct feature is not observed in any of the core samples analysed from Barnicarndy 1, which is not unexpected since the maximum *G. prisca* abundance was only 0.15% in all samples analysed by organic petrology (Ranasinghe and Crosdale, 2020), and Spaak et al. (2017) noted that the *n*-alkane OEP was only observed when the *G. prisca*-rich liptinite visual abundance was at least 5% of the sample.

However, a predominance of the C_{16} and C_{18} *n*-alkanes is observed in the cores from the Samphire Marsh Member at 1753 and 1824 m (Fig. 53). This *n*-alkane distribution is unusual and is suspected to be the result of hydrocarbon contamination.

The water used to prepare the drill mud, the Talcor Breakout Blue (used as an antiseize lubricant on casing joints during the drilling of the well) and the plastic bags used to store the core samples could have contributed to the increased levels of C_{16} and C_{18} *n*-alkanes as they came in contact with the cores (Grosjean et al., 2021). Due to the low TOC amounts and minor organic extracts yields recovered from the solvent extraction of the cores, any low level of organic contamination of an anthropogenic nature has the potential to have a significant impact on hydrocarbon distributions (Brocks et al., 2008).

Although this issue of possible contamination is of concern, it is noted that the *n*-alkane envelope maximises at either C_{18} or C_{20} in the other rock extracts from both the Samphire Marsh and Fly Flat members in Barnicarndy 1 and at C_{16} in the rock extract of the Fly Flat Member from Olympic 1 (Fig. 54d), and hence this *n*-alkane signature may be indigenous. Typically, short-chain *n*-alkanes (more often maximizing at C_{19}) are attributed to an algal source (Peters et al., 2005).

Interestingly, the *n*-alkane distribution (from GC-MS m/z 57 ion) in a Late Ordovician (Hirnantian) core extract from southern Tunisia also exhibits an even predominance of the C_{18} and C_{20} alkanes, with a maximum at C_{18} (Romero-Sarmiento et al., 2011). Also of note is that in the core from 1427.34 m, there is an abundance of the odd carbon-numbered mid-chain *n*-alkanes from C_{21} to C_{27} (Fig. 53a). Spaak et al. (2017) attributed a similar (C_{21}–C_{25}) *n*-alkane distribution to an input from macrophytes (aquatic plants growing in or near water, such as bryophytes) into the marine upper Goldwyer Formation, and perhaps this may be relevant to the types of organic matter preserved within the Nambeet Formation.

The isoprenoid alkanes, pristane (Pr) and phytane (Ph), vary in abundance throughout the samples. The Pr/Ph ratio ranges from 1.07 to 3.51, indicative of an oxidizing depositional environment (Table 11). From the limited data available, the Pr/*n*C_{17} and Pr/*n*C_{18} ratios are variable throughout the Nambeet Formation, although they are consistently lower in the two samples from the Fly Flat Member in Barnicarndy 1 compared with those from the

Samphire Marsh Member, which is in contrast to the rock extract from the Fly Flat Member in Olympic 1. Hence, more work is required on the Nambeet Formation to understand the geochemical variation across the Canning Basin.

The possible oil stain from 2304.63 to 2304.70 m has a low concentration of extractable organic compounds (9 ppm; Table 10), with a gas chromatogram dominated by an unresolved complex mixture and low n-alkane abundance (not provided). In contrast, the saturated hydrocarbon abundance from the whole rock extract as analysed by GC-MS/MS is unrealistically high compared to the aromatic hydrocarbon fraction and exhibits some unexplained biomarker ratios. Hence, this sample is not considered further.

The possible oil stain from 2321.19 to 2321.25 m exhibits an *n*-alkane distribution (Fig. 54b) similar to the core extracts from the Fly Flat Member from 2317.05 to 2317.10 m (Fig. 54a), that maximizes at nC_{20}, although the Pr/Ph ratio of 2.81 and Pr/nC_{17} of 0.33 are slightly higher, but are still within the range of the Nambeet Formation extracts (Table 11).

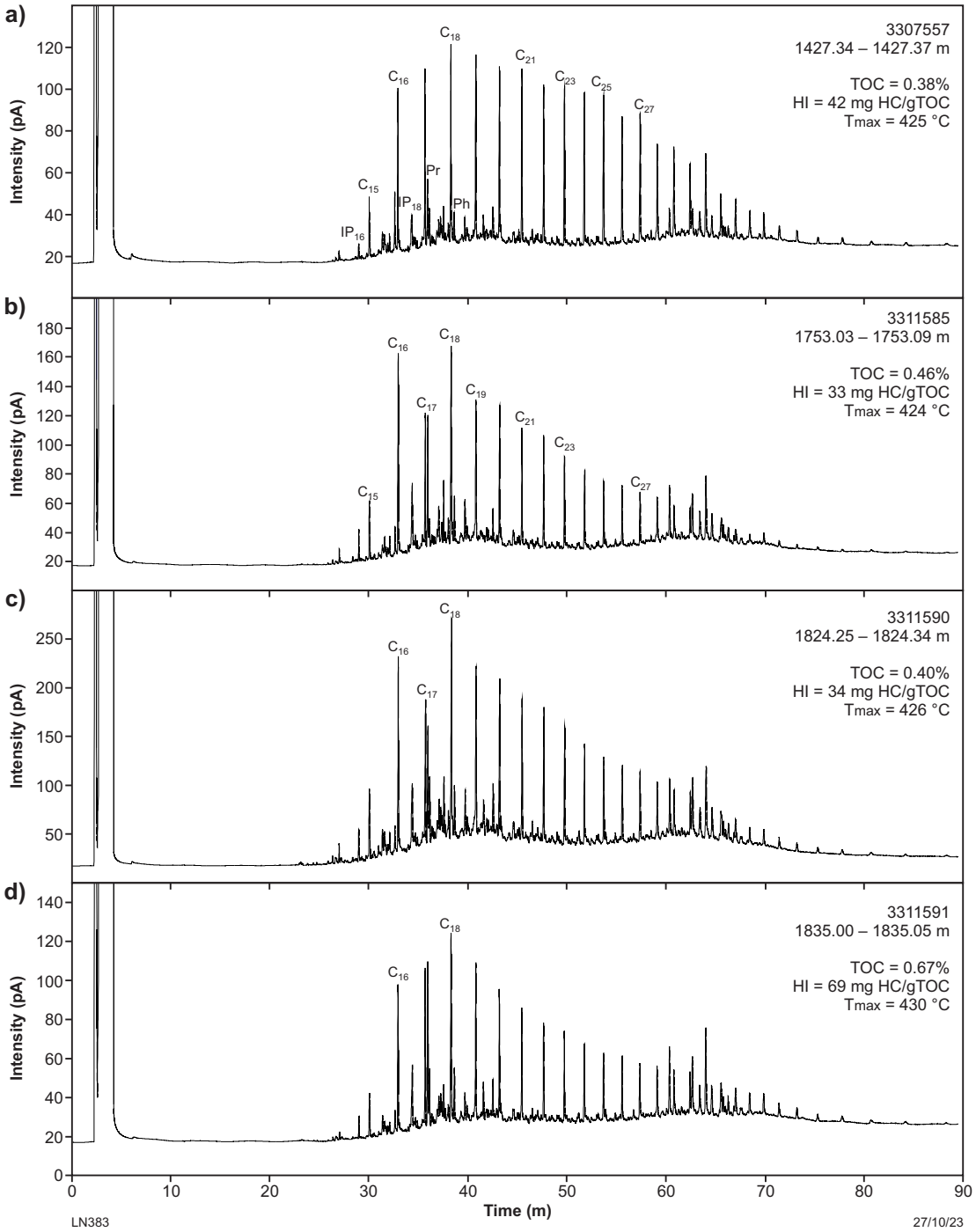

Figure 53. Gas chromatograms of saturated hydrocarbon fractions of core extracts from Samphire Marsh Member samples: a) GA 3307557; b) GA 3311585; c) GA 3311590; d) GA 3311591. Normal (*n*-) alkanes are indicated by their carbon number. Abbreviations: IP, isoprenoid; Pr, pristane; Ph, phytane

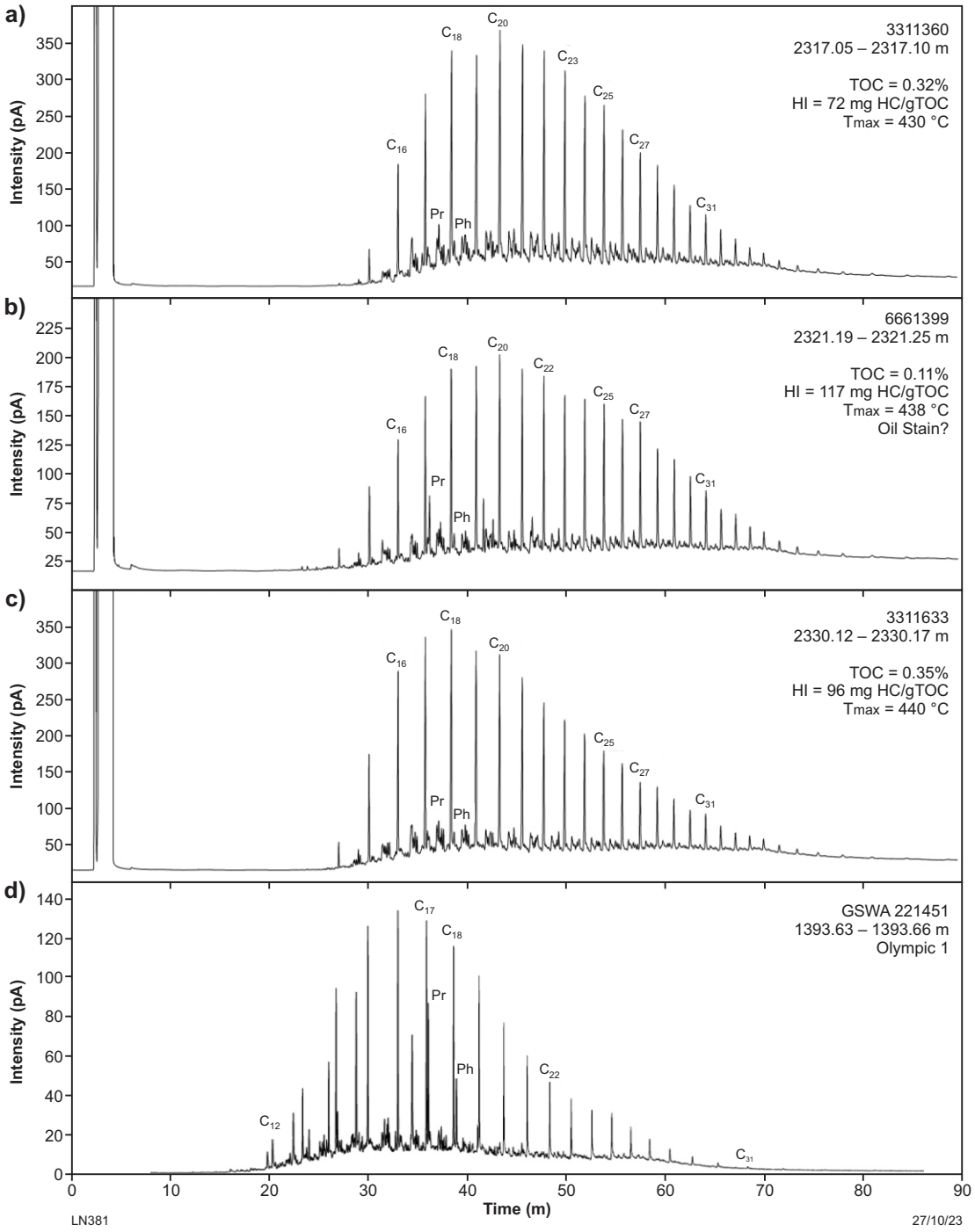

Figure 54. Gas chromatograms of saturated hydrocarbon fractions of core extracts from the Fly Flat Member, Barnicarndy 1 compared to a whole rock extract analysed by gas chromatography mass spectrometry (GC-MS) from the Fly Flat Member in Olympic 1 (Normore and Dent, 2017a,b). Barnicarndy 1 samples: a) GA 3311360 b) GA 6661399 c) GA 3311633; and Olympic 1 sample: d) GSWA 221451. Normal (*n*-) alkanes are indicated by their carbon number. Abbreviations: Pr, pristane; Ph, phytane

Table 11. GC ratios for the saturated hydrocarbon fraction of selected cores from the Nambeet Formation, Barnicarndy 1 and comparison to GC-MS analysis of whole core extracts from Olympic 1 (Normore and Dent, 2017a,b). Definition of column heading is given in Appendix 18, table A1.1

GA No.	Depth from (m)	Depth to (m)	Stratigraphic unit	Study sample type	G. prisca Foster et al. (2021)	Pr/Ph	Pr/ nC17	Ph/ nC18	nC17/ nC27	Wax ratio	CPI 14_24
Barnicarndy 1											
3307557	1427.34	1427.37	Samphire Marsh Mbr	OM	nd	2.26	0.43	0.15	1.18	1.38	0.97
3311585	1753.03	1753.09	Samphire Marsh Mbr	OM	Y	2.90	1.06	0.25	2.27	2.65	0.83
3311590	1824.25	1824.34	Samphire Marsh Mbr	OM	Y	2.80	0.88	0.22	2.07	2.42	0.88
3311591	1835.00	1835.05	Samphire Marsh Mbr	OM	Y	3.51	1.20	0.28	2.39	1.99	0.99
3311598	1933.72	1933.78	Samphire Marsh Mbr	OM	nd	1.46	0.33	0.11	2.76	2.79	0.81
6661398	2304.63	2304.70	Fly Flat Mbr	?oil stain	nd	0.65	0.55	0.19	0.04	0.72	1.00
3311630	2317.05	2317.10	Fly Flat Mbr	OM	nd	1.07	0.12	0.09	1.34	2.25	1.03
6661399	2321.19	2321.25	Fly Flat Mbr	?oil stain	nd	2.81	0.33	0.10	1.11	1.64	1.06
3311633	2330.12	2330.17	Fly Flat Mbr	OM	nd	1.35	0.10	0.07	2.59	3.02	1.01
Olympic 1											
–	1128.26	1128.30	Samphire Marsh Mbr	OM	nd	2.00	0.19	0.19	65.93	7.45	1.25
–	1393.63	1393.66	Fly Flat Mbr	OM	nd	1.89	0.74	0.45	8.97	6.03	1.04

Molecular source characterization of organic matter within the Nambeet Formation by gas chromatography mass spectrometry

The mass fragmentograms from the GC-MS-selected ion monitoring (SIM) and GC-MS/MS (or QQQ) analyses, and the identification of peaks and quantification of peak heights and areas for Barnicarndy 1 can be found in Appendix 5 and 6 respectively of Edwards et al. (2021), with a summary of key biomarker ratios provided in Table 12 and Table 13. The C_{19}–C_{26} tricyclic triterpanes, C_{27}–C_{35} hopanes (Fig. 55) and C_{27}–C_{29} steranes (Fig. 56) were identified using SIM mode and GC-MS/MS.

The pentacyclic terpanes (mainly hopanes) dominate all of the core extracts from the Nambeet Formation, with significantly lower proportions of tricyclic terpanes. Steranes are present in the lowest relative abundance (Table 13; Figs 55 and 56).

The C_{19}–C_{26} tricyclic terpanes are present in all samples, with the marine algal-derived C_{23} homologue typically being the dominant peak. The possibly oil stained core sample from 2321.19 to 2321.25 m is the exception, where the C_{20} homologue has the greatest concentration (Fig. 55). The C_{24} tetracyclic terpane is present in all samples.

The most abundant hopanes are the C_{30} 17α,21β-hopane in the Samphire Marsh Member and the C_{29} 17α,21 β-hopane in the Fly Flat Member core extracts, as well as the possible oil stained sample from 2321.19 – 2321.25 m (Fig. 55). The hopane distributions typically include the C_{31} to C_{35} homohopanes. The C_{35} hopane 22S is co-eluting with an unknown compound in most samples. However, a specific contaminant could not be identified to be affecting the biomarker distributions (Grosjean et al., 2021). The Breakout Blue antiseize lubricant used on casing joints had the potential to be a contaminant since it contains biomarker compounds. However, the significant amounts of extended C_{31}–C_{35} hopanes and the high abundance of the C_{29} 5α,14β,17β-steranes (an indicator of relatively high thermal maturity) are not observed in the core extracts from Barnicarndy 1. Both the solvent extracts of the plastic bag and the plastic core tray resulted in several large peaks being present in the m/z 191 trace within the elution time of the C_{34} and C_{35} hopanes; however, only a single peak is recorded in the core extracts from Barnicarndy 1 (Fig. 55) which negates these contaminants as the source of the unknown compound. Gammacerane is present in all samples (Fig. 55), with an origin from bacterivorous ciliates (eukaryotes), which lived at the oxic-anoxic interface being proposed by Sinninghe Damste et al. (1995). Alternatively, gammacerane may be indicative of a stratified water column (Tulipani et al., 2015).

The ratio of hopanes versus steranes reflects the respective inputs of bacteria versus algae to the organic matter (Peters et al., 2005). This ratio is high (6.0 – 14.0) in all five samples (Table 13) indicating a strong contribution from bacteria, a feature observed in Ordovician-sourced oils of the Canning Basin (Edwards et al., 1997; Edwards and Zumberge, 2005; Spaak et al., 2017) and significantly above the global average (0.5 – 2.0) for Paleozoic marine oils (Peters et al., 2005). These results are consistent with the findings from the examination of the cores under reflected light (Ranasinghe and Crosdale, 2020) where *G. prisca* (a probable cyanobacteria) is identified. Palynological analysis of the kerogen under transmitted light confirms the presence of *G. prisca* as well as ?*Eomerismopedia maureeniae*, probably an ancestor of the extant cyanobacteria *Merismopedia* (Foster et al., 2021), which are present throughout the samples examined from the Samphire Marsh Member and most likely a source for hopanoids.

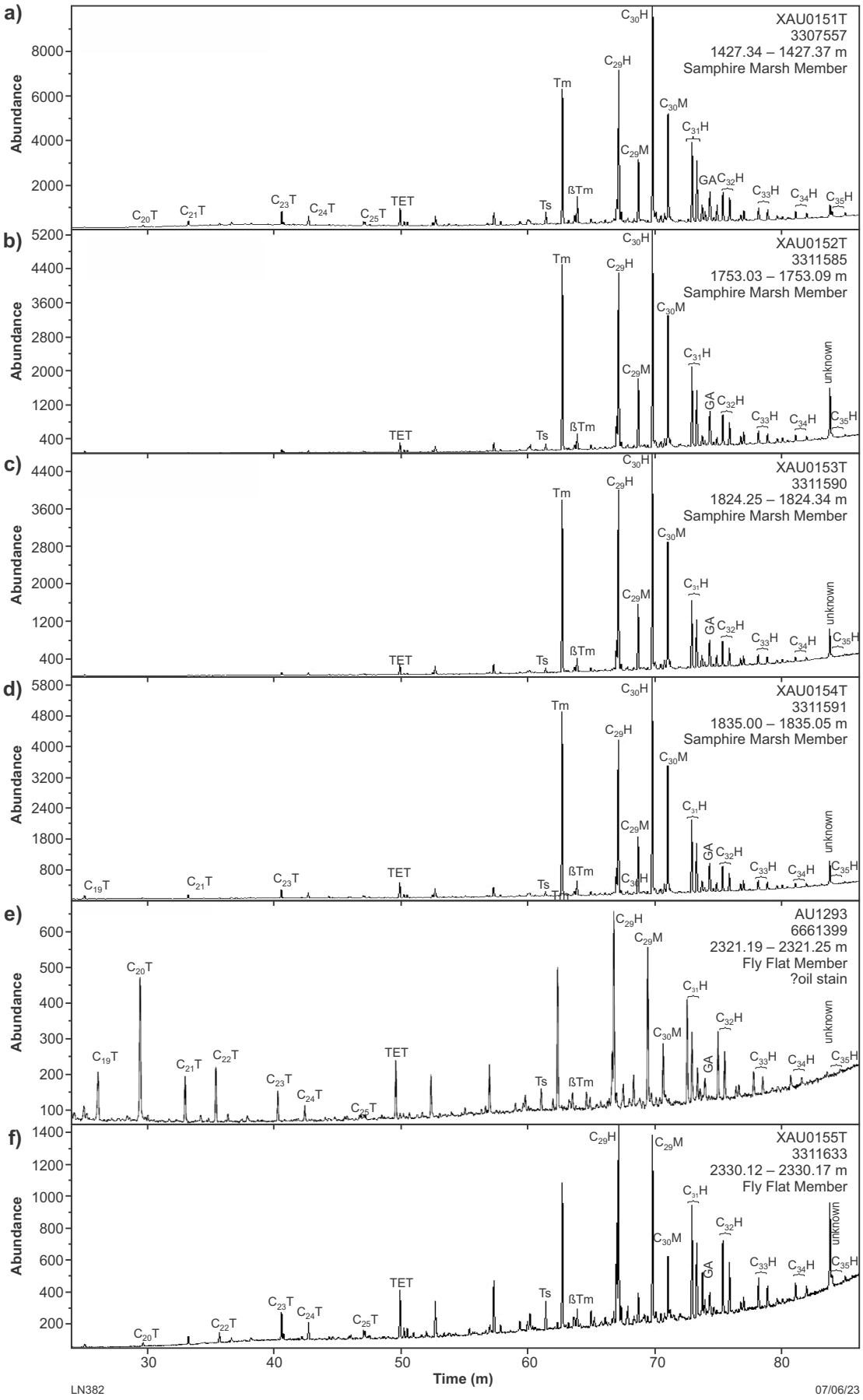

Figure 55. Selected m/z 191 chromatograms showing the triterpane and hopane biomarkers of core extracts analysed by GC-MS-SIM from Nambeet Formation samples: a) GA 3307557 b) GA 3311585 c) GA 3311590 d) GA 3311591 e) GA 6661399 and f) GA 3311633. Definition of peak names is given in Appendix 18, table A1.2

Table 12. Selected isoprenoid, triterpane and hopane biomarker ratios of core extracts analysed by GC-MS-SIM from Barnicarndy 1. Definition of column heading is given in Appendix 18, table A1.1 and A1.4

GA no.	*Stratigraphic unit*	*Pr/Ph*	*C19T /C23T*	*C24T /C23T*	*Tet /C23T*	*C29H /C30H*	*GA /C31HR*	*C35 HHI*
3307557	Samphire Marsh Mbr	2.3	0.03	0.66	1.31	0.69	0.28	3.70
3311585	Samphire Marsh Mbr	2.9	0.03	0.78	2.90	0.80	0.18	2.68
3311590	Samphire Marsh Mbr	2.8	0.05	0.68	3.71	0.83	0.25	2.04
3311591	Samphire Marsh Mbr	3.5	0.03	0.63	1.72	0.71	0.24	1.45
3311598	Samphire Marsh Mbr	1.5	0.80	0.54	1.98	1.21	0.07	3.85
3311630	Fly Flat Member	1.1	1.50	0.48	1.64	0.81	0.15	2.91
6661399	?oil stain	2.8	1.59	0.54	1.95	1.22	0.21	3.70
3311633	Fly Flat Member	1.4	0.01	0.63	1.74	1.07	0.57	4.55

Table 13. Selected triterpane, terpane and sterane biomarker ratios of core extracts analysed by GC-MS-SIM from Barnicarndy 1. Definition of column heading is given in Appendix 18, table A1.4

GA no.	*Depth (m)*	*Pentacyclic terpanes (%)*	*Tricyclics Terpanes (%)*	*Steranes (%)*	*Hopanes/ steranes*	*Steranes (%)*			*Diasteranes 20S/ Steranes 20R*
						C_{27}	C_{28}	C_{29}	
3307557	1427.34	77.94	11.35	10.71	6.19	34	28	37	0.55
3311585	1753.03	88.37	5.81	5.82	12.84	42	25	33	0.30
3311590	1824.25	89.40	5.71	4.89	15.35	41	25	34	0.31
3311591	1835.00	85.53	7.93	6.54	10.97	37	34	28	0.23
3311598	1933.72	81.57	15.51	2.93	23.64	50	10	40	0.29
3311630	2317.05	69.38	26.92	3.70	16.07	57	26	17	1.20
6661399*	2321.19	67.38	28.28	4.34	13.54	39	30	30	0.73
3311633	2330.12	73.52	17.55	8.93	7.20	36	28	36	1.24

*Possible oil stain

Even though steranes are in much lower concentrations compared to the hopanes, they are nevertheless present and the respective contributions of C_{27}-C_{28}-C_{29} steranes can provide insights into depositional environments (Huang and Meinschein, 1979). The sterane distribution of the Barnicarndy 1 core extract data plots in the open marine environment field in the ternary diagram (Fig. 57). Numerous genera and species of acritarch, predominantly derived from eukaryotic phytoplankton, make up the majority of the organic-walled microfossil assemblages in the Nambeet Formation in Barnicarndy 1 (Foster et al., 2021), Samphire Marsh 1 and Acacia 2 (Foster and Wicander, 2015), and would be a source for sterols. The regular steranes are present from C_{27} to C_{29} in the 5α,14α,17α and the 5α,14β,17β configurations, as are the rearranged steranes in the 13β,17α configuration (Fig. 55). The C_{27} steranes are prevalent in most samples with the exception of the shallower sample at 1427 m where C_{29} steranes dominate slightly over the C_{27} steranes (Table 13; Figs 56, 57). The C_{27} steranes in marine sediments are typically derived from red algae (Volkman, 1986), which are predominantly macrophytes. Although C_{29} steranes are usually considered as being biomarkers for a land-plant contribution to the organic matter preserved in sedimentary rocks, marine algae are also an important source of C_{29} sterols (Volkman, 1986).

Algal classes synthesizing C_{29} sterols include *Chlorophyta* (green algae), whereas Prasinophyceae (unicellular flagellate green algae) synthesize C_{28} sterols (Volkman, 1986). Notably, the presence of *Leiosphaeridia*, a genus of Prasinophyceae, is documented throughout the Samphire Marsh Member, along with many species of acritarchs in Barnicarndy 1 (Foster et al., 2021). These most likely represent the fossilised remains of various life stages of algae. Hence, the variation in the C_{27}, C_{28} and C_{29} sterane distributions reflects changes in the algal microflora within the open marine environment during deposition of these rocks (Fig. 57). The presence of diasteranes together with a low 30-norhopane/ C_{30} hopane ratio ($C_{29}H/C_{30}H$; Table 12) are in agreement with a clastic rather than carbonate lithology.

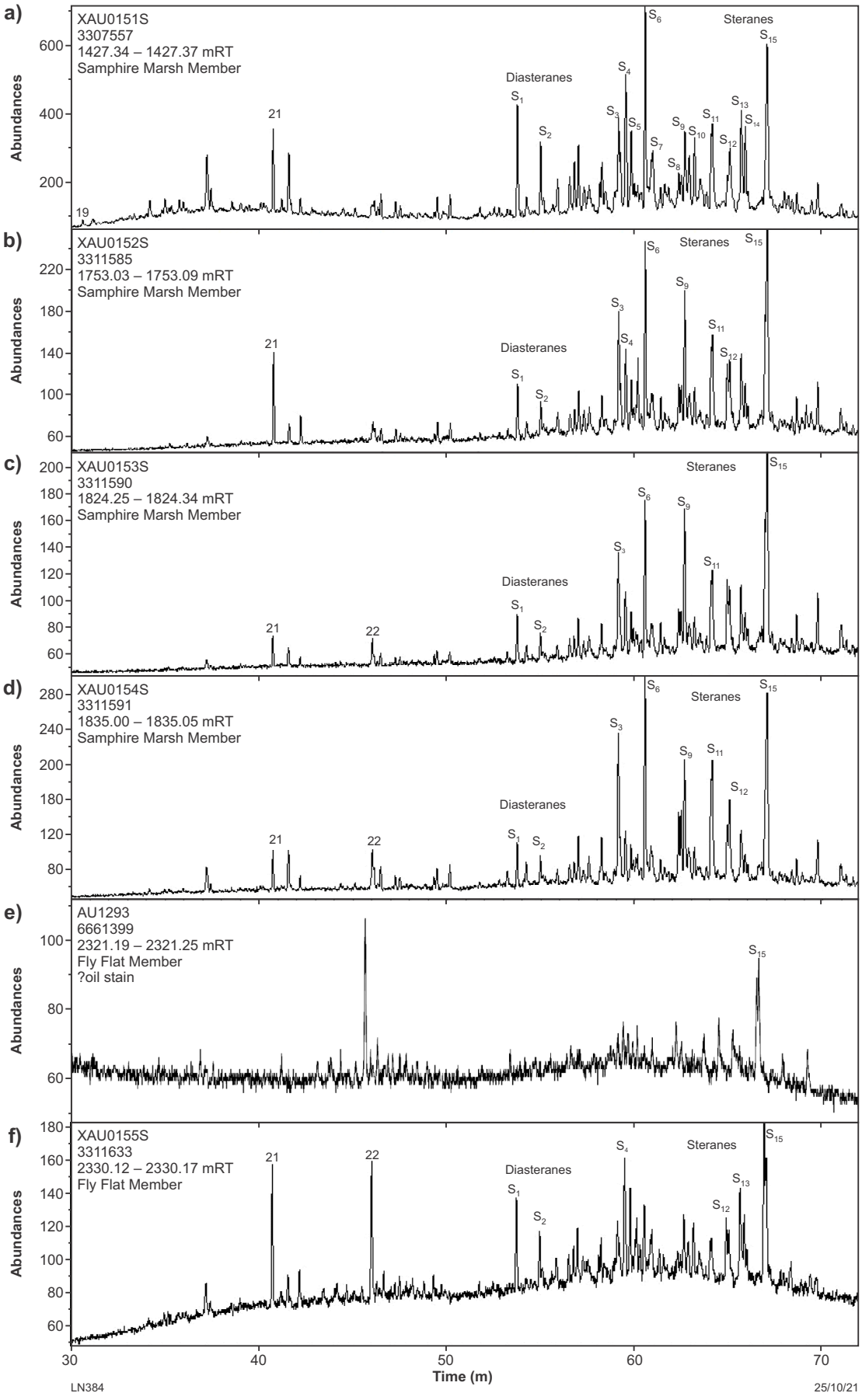

Figure 56. Selected m/z 217 chromatograms showing the sterane biomarkers of core extracts analysed by GC-MS-SIM from Nambeet Formation samples: a) GA 3307557 b) GA 3311585 c) GA 3311590 d) GA 3311591 e) GA 6661399 and f) GA 3311633. Definition of peak names is given in Appendix 18, table A1.3

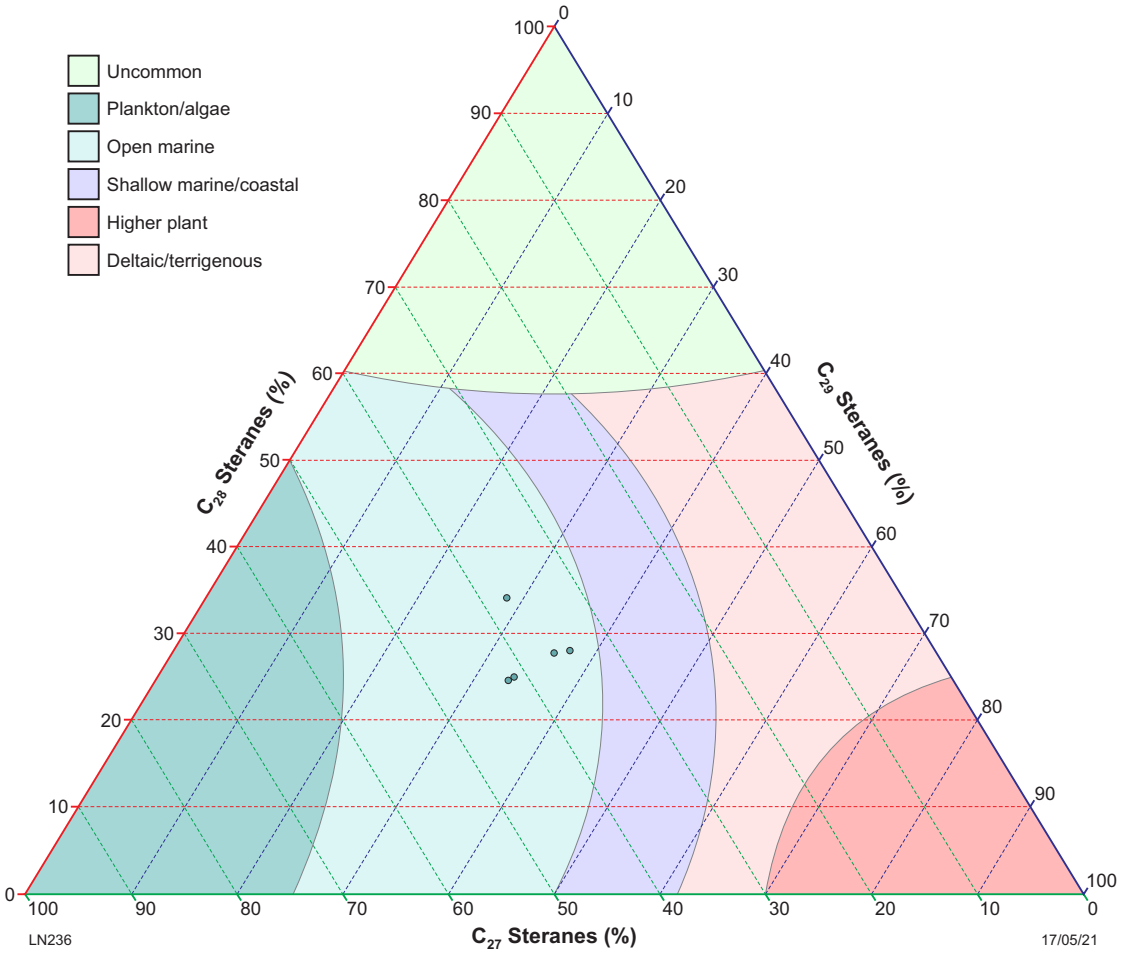

Figure 57. Ternary plot of C_{27}-C_{28}-C_{29} steranes inputs in % for samples GA 3307557, 3311585, 3311590, 3311591 and 3311633

Another source of sterols could be from the earliest plants (embryophytes) that colonized the land during the earliest Ordovician, with the oldest known organisms being charophyte algae (Strother and Foster, 2021) and then bryophytes (Rubenstein et al., 2010), given that cryptospores (spore-like structures) are found within the Samphire Marsh Member (Foster et al., 2021). However, molecular and isotopic data are scarce on the aliphatic and aromatic biomarker signatures of Early Ordovician plants, with only limited information being available for Late Ordovician and Devonian plants (Romero-Sarmiento et al., 2011).

Collectively, the pristane to phytane (Pr/Ph) ratios in excess of 1.4 together with low C_{35} homohopane indices (C_{35} HHI; Table 12) suggest deposition of the organic matter under relatively oxygenated conditions (Peters et al., 2005) in the Nambeet Formation in Barnicarndy 1. Yet, the four shallower samples have low but discernible amounts of the C_{40} carotenoid-derived aromatic compound, isorenieratane (Fig. 58; and lesser amounts of β-isorenieratane, not shown), a marker for brown-pigmented green sulphur bacteria (Chlorobiaceae), which are strictly anaerobic organisms living in the photic zone. It is interesting to note the limited carotenoid compounds present in the Samphire Marsh Member core extracts, whereas isorenieratane and other carotenoid-derivatives were not detected in the Fly Flat Member extracts. This is in contrast to the numerous carotenoids present in the Ordovician-source oil from Dodonea 1, where paleorenieratane is the dominant peak, with subordinate amounts of isorenieratane and renieratane (Fig. 58; Edwards et al., 2018). Furthermore, there is an absence of the saturated biomarker β-carotane, derived from algae and cyanobacteria that occupy the sunlit and oxygenated part of the water column, in the Nambeet Formation core extracts in Barnicarndy 1. The presence of isorenieratane (and related compounds) has been used as an indication of water stratification and the development of photic zone euxinia (PZE; French et al., 2015). The low abundance of isorenieratane in some Canning Basin samples has been interpreted as the development of PZE over short periods of time, being interrupted by frequent mixing and oxygenation of the water column (Spaak et al., 2017). However, an alternative mechanism could be that β-isorenieratane is not derived from the β-isorenieratene biosynthesized by Chlorobiaceae, but instead is a product from the aromatization of β-carotene (Koopmans et al., 1996), presumably occurring during diagenesis and thermal maturation, which may offer an alternative explanation for the lack of diversity of the carotenoid biomarkers seen in the Barnicarndy 1 core extracts.

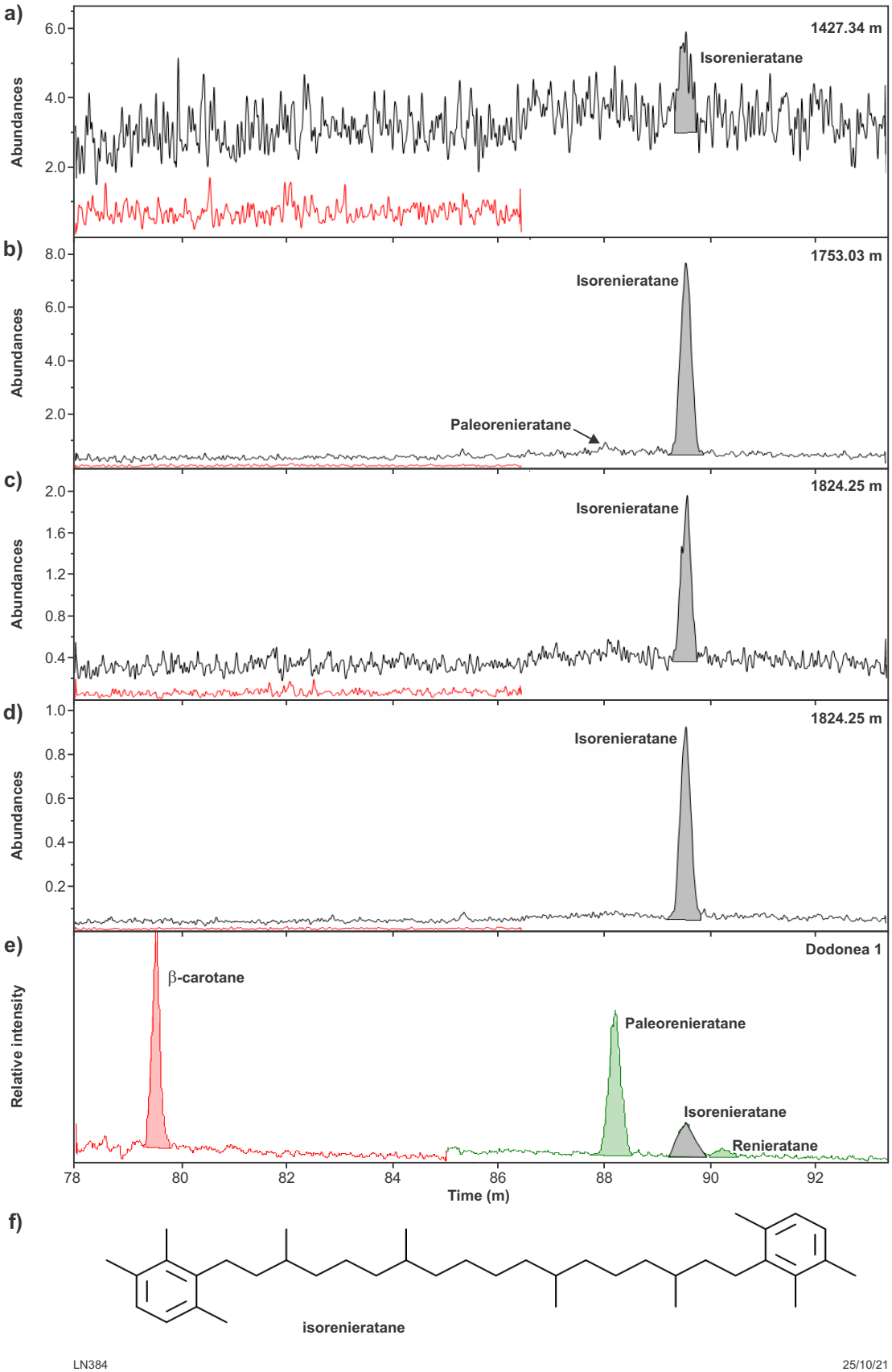

Figure 58. Selected parent m/z 554.5, 552.5 and 546.5 to daughter m/z 134.1 ion transitions from GC-MS/MS analyses (Appendix 18, table A1.5) showing the carotenoid biomarkers of core extracts from: a)–d) the Samphire Marsh Member in Barnicarndy 1 and e) comparable stratigraphy in Dodonea 1; f) chemical structure of isorenieratane biomarker

The aromatic hydrocarbon fractions of the core extracts from the Nambeet Formation in Barnicarndy 1 are dominated by either: the monoaromatic compounds (long-chain alkyl benzenes and their di-, tri- and tetra-methylated derivatives in decreasing concentration and monoaromatic steroids); or the heterocyclic aromatics (dibenzothiophenes, methyldibenzofurans and methylcarbazoles). The di-aromatic (naphthalenes and isorenieratane), tri-aromatic (phenanthrenes and steroids) and tetra-aromatic (e.g. methylchrysene) compounds and their di-, tri- and tetra-methylated derivatives are present in decreasing concentrations with increasing aromatization and methylation. Key aromatic ratios were used to estimate maturity (Table 14).

Trace quantities of retene were identified in core extracts from the Nambeet Formation (appendix 6 of Edwards et al., 2021), which is unexpected given that it is a diagenetic product of the conifer constituent abietic acid (Alexander et al., 1987; van Aarssen et al., 2000). However, it has been proposed that retene may also originate in phytoplankton (Zhang et al., 1999) and early land plants, such as bryophytes (Romero-Sarmiento et al., 2010; Spaak et al., 2017), which is consistent with the microfossils identified in the Barnicarndy 1 cores.

Isotopic profiles of the organic matter within the Nambeet Formation

Compound specific isotope analysis (CSIA) for carbon and hydrogen was undertaken on the individual *n*-alkanes extracted from the six cores with the highest TOC contents in Barnicarndy 1. The results were presented in delta-notation ($\delta^{13}C$, $\delta^{2}H$) relative to the Vienna Peedee Belemnite (VPDB) standard and Vienna Standard Mean Ocean Water (VSMOW) respectively in appendix 4 of Edwards et al. (2021). The *n*-alkanes are the major component in the saturated gas chromatograms (Figs 53, 54), as opposed to the biomarker compounds, which are present in low concentrations. Hence the *n*-alkanes have the potential to discriminate between different sources of organic matter in the rock extracts, relative thermal maturity and are also useful in oil–source rock comparisons. The isotopic signatures of the ocean–atmosphere carbon and hydrogen reservoirs are recorded in sedimentary organic matter and their generated hydrocarbons (Schimmelmann et al., 2004; Sessions et al., 2004).

The C_{7+} *n*-alkane-specific carbon isotopic signatures of the core extracts from the Nambeet Formation are shown in Figure 59 and the hydrogen isotopes in Figure 54. The carbon isotopic signature in the preserved organic matter is inherited from the photosynthetic organism, whose metabolic products are depleted in ^{13}C compared to the CO_2 that it used from either the atmosphere or ocean. The carbon isotopic composition for the three core extracts from 1427.34, 1753.03 and 1824.25 m in the Samphire Marsh Member are similar, exhibiting an overall negative slope with all samples being within 0.5‰ of each other (Fig. 59a). The deeper sample from 1835.00 m shows an overall n-alkane distribution depleted in ^{13}C by about -2‰ relative to the other Samphire Marsh Member extracts. This offset suggests source differences between these extracts, since any increase in maturity would produce a more enriched isotopic profile. The C_{15}, C_{17}, C_{21} and C_{23} *n*-alkanes have values more depleted in ^{13}C than their neighbouring even carbon-numbered homologues, yet an odd carbon-numbered preference is not seen in the gas chromatogram of the *n*-alkane distribution. The carbon isotopic profile of the core at 2330.12 m from the Fly Flat Member is in contrast to those of the Samphire Marsh Member, being considerably enriched in ^{13}C (Fig. 59a), which is attributed to both source and maturity differences. For correlation purposes, the three Ordovician-sourced oil families from the Larapintine 2 (L2) Petroleum System, represented by Cudalgarra 1, Dodonea 1, Pictor 1 and Pictor 2 (Edwards et al., 2013), are compared with those of the rock extracts from the Nambeet Formation in Barnicarndy 1 (Fig. 59b). The crude oils have relatively flat carbon isotopic profiles, reflecting the homogeneity of their parent kerogens, and fall within the range exhibited by the core extracts from the Samphire Marsh Member.

Interpreting the hydrogen isotopic signals is difficult since hydrogen has the largest relative mass difference between its two stable isotopes (^{1}H and ^{2}H). Hence, its $\delta^{2}H$ values show the greatest variation of any element. Water is the main source of hydrogen, with the $\delta^{2}H$ value of the kerogen inherited from the water body inhabited and used by the photosynthetic organism (Sessions et al., 1999), with maturation and exchange potentially altering the indigenous $\delta^{2}H$ signature of the preserved organic matter and its derived hydrocarbons (Schimmelmann et al., 2004; Sessions et al., 2004; Sessions, 2016).

The hydrogen isotopic profiles of the four core extracts from 1427.34 to 1835.00 m in the Samphire Marsh Member are more depleted in ^{2}H than that of the core extract from 2330.12 m in the Fly Flat Member (Fig. 60a). The least mature sample from 1427.34 m exhibits a negatively sloping, sawtooth shape where the even carbon-numbered *n*-alkanes between C_{18} and C_{24} are more depleted in ^{2}H, compared with the C_{19}–C_{25} odd carbon-numbered *n*-alkanes. This sawtooth shape is also seen in the abundance profile of these mid-chain length alkanes in the gas chromatogram traces (Fig. 53a). The deeper samples from the Samphire Marsh Member progressively show smoother and increasingly enriched $\delta^{2}H$ profiles as maturity increases. The most mature core extract from 2330.12 m in the Fly Flat Member exhibits a smooth, positive sloping $\delta^{2}H$ isotopic profile that is exceedingly enriched in ^{2}H and is similar to the profile of the Pictor 1 and 2 oils reported by Edwards et al. (2013; Fig. 60b). Further isotopic profiles of the Nambeet Formation are required to build up a more comprehensive understanding of the effects of source and maturity on these marine sedimentary rocks, although it appears that the organic matter within the Samphire Marsh Member exhibits collectively different carbon and hydrogen isotopic profiles to those of the Fly Flat Member and the Ordovician-sourced oils of the Canning Basin.

Thermal maturity

Thermal maturity for the sedimentary section in Barnicarndy 1 was determined using a combination of organic petrological data, programmed pyrolysis Tmax and molecular maturity parameters. Organic petrological data are available on 16 samples, including five samples from the upper Carboniferous–Permian section and 11 samples from the lower Paleozoic (predominantly Ordovician) section (Appendix 19; Ranasinghe and Crosdale, 2020).

Table 14. Maturity-related parameters for core samples from Barnicarndy 1 where a vitrinite-reflectance equivalent is calculated from graptolite reflectance, Tmax and aromatic compounds

GA no.	Depth from (m)	Depth to (m)	Mean max Rv (%)	Mean max Rgrapt (%)	Rv and Eq Rv grapt (%)	Tmax Rock-Eval 6 (°C)	Eq Rv Tmax Rock-Eval 6 (%)	Tmax HAWK (°C)	Calc Rv Tmax HAWK (%)	MPI	Eq Rv MPI Rv<1.35	Eq Rv MPI Rv>1.35	VREQ-5
3307465	195.00	198.00				429	0.56						
3307472	348.00	351.00	0.45		0.45								
3307480	438.00	441.00				422	0.45						
3307482	477.00	480.00	0.47		0.47								
3307491	610.00	610.03	0.66		0.66								
3307499	774.43	774.46	0.82		0.82								
3307501	797.28	797.32	0.82		0.89								
3307550	1354.80	1354.86		0.83	0.93	425	0.50						
3307557	1427.34	1427.37				425	0.50	429	0.56	0.47	0.68		0.51
3307557	1427.34	1427.37											
3307559	1450.92	1450.97		1.00	1.02								
3311566	1519.15	1519.25		1.14	1.09								
3311572	1591.47	1591.53		1.15	1.1								
3311576	1635.11	1635.21		1.23	1.14								
3311579	1670.02	1670.08				426	0.51						
3311584	1748.06	1748.16		1.27	1.16								
3311585	1753.03	1753.09						430	0.58	0.37	0.62		
3311588	1797.99	1798.05		1.22	1.13								
3311590	1824.25	1824.34				426	0.51	433	0.63	0.42	0.65		0.59
3311591	1835.00	1835.05				430	0.58	434	0.65	0.35	0.61		0.60
3311594	1874.04	1874.17		1.19	1.12								
3311608	2058.04	2058.10		1.43	1.24								
3311612	2095.96	2096.02		1.80	1.43								
3311622	2244.08	2244.12		2.00	1.54								
3311630	2317.05	2317.10				430	0.58	441	0.76				0.90
6661399*	2321.19	2321.25				438	0.71	440	0.75				0.93[#]
3311633	2330.12	2330.17				440	0.75	443	0.80	0.76	0.85	1.85	0.91

Calculations used to derive vitrinite reflectance equivalent data: Eq Rv grapt = (0.515×GRomax)+0.50 (Luo et al., 2020); Eq Rv Tmax Rock-Eval 6 = (0.0165*Tmax)-6.5143 (Jarvie, 2021); Eq Rv Tmax HAWK = (0.0165*Tmax)-6.5143 (Jarvie, 2021); MPI = Methylphenanthrene Index = (1.5*[3MP+2MP]/[P+9MP+1MP]) where MP is methylphenanthrene (Radke and Welte, 1983); Eq Rv MPI Rv <1.35 = (0.6*MPI)+0.4 (Radke and Welte, 1983); Eq Rv MPI Rv >1.35 = (-0.6*MPI)+2.3 (Radke and Welte, 1983); VREQ-5 = value derived from a proprietary combination of aromatic hydrocarbons analysed by GC-MS/MS by GeoMark Research. *Sample containing a possible oil stain, with [#]highest VREQ5 value recorded

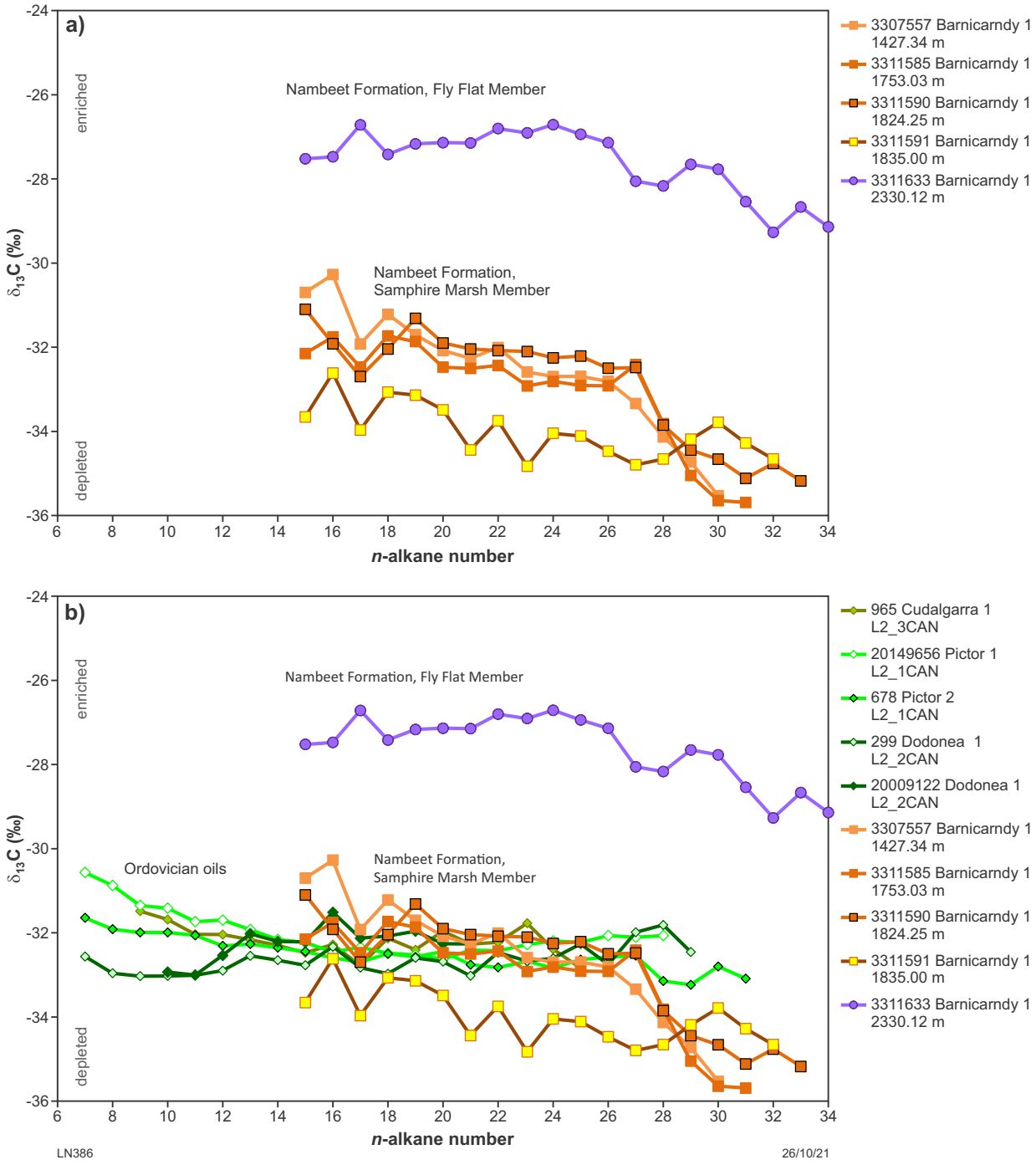

Figure 59. Carbon isotopic composition for C_{7+} *n*-alkanes: a) the Nambeet Formation in Barnicarndy 1; b) comparison of the core extracts to Ordovician-sourced oils from the Canning Basin (Edwards et al., 2013). The three Ordovician Larapintine 2 oil families are named L2_1CAN, L2_2CAN and L2_3CAN

Vitrinite reflectance (Rv) could only be acquired for the upper Carboniferous–Permian Grant Group to assess the level of thermal maturity (Table 14), with independent verification being provided by the colour and fluorescence intensity of the liptinite macerals when viewed under blue light excitation. Maximum reflectance was measured on all phytoclasts, since maximum reflectance is known to correlate better with other maturation parameters obtained from various geochemical methods compared to Rv.

In the Ordovician section, where land-plant-derived phytoclasts are not present, the mean maximum reflectance of graptolites was determined and vitrinite reflectance-equivalent (Rve) values were calculated using the relationship described by Luo et al. (2020). Graptolite bireflectance varied from low to moderate and therefore the mean maximum reflectance provided datasets with minimum scatter for the Samphire Marsh Member of the Nambeet Formation. Random reflectance was determined on telalginite (*Gloecapsomorpha*) where possible. However, unlike the mean maximum reflectance of graptolites, the reflectance of alginite could not be used to determine the maturation levels of associated sediments in terms of Rve because there is no current documentation on the reflectance behaviour of lower Paleozoic and Neoproterozoic alginite in relation to associated bioclasts.

Measured mean maximum Rv and Rve calculated from graptolites data are plotted against depth in Figures 61, 62. Interpretation of these data indicates that the sedimentary section in Barnicarndy 1 has reached the oil window at a depth of about 500 m (i.e. Rv >0.55%, Hantschel and Kauerauf, 2009) in the Grant Group, and the gas window is reached at a depth of about 2000 m (i.e. Rv >1.3%, Hantschel and Kauerauf, 2009) in the Samphire Marsh Member of the Nambeet Formation. The peak oil window lies between the depths of about 800 and 1400 m (green zone in Fig. 61, corresponding to a Rv 0.7 to 1.0%). Graptolites were not reported in the Fly Flat Member. Fluorescence was not observed in the highly reflective strands of possible alginite in the sample at 2449.33 to 2449.39 m depth from the Yapukarninjarra Formation signifying relatively high maturity.

Samples with TOC <0.05 wt% and/or S2 <0.2 mg HC/g rock yield low and poorly defined S2 peaks resulting in unreliable Tmax values that cannot be used as thermal maturity indicators. In Barnicarndy 1, the majority of Tmax values may not be valid since 96% of samples (192 out of 201) meet either one or the other criterion. For the few samples meeting the criteria, the Tmax values acquired from the Rock-Eval 6 and HAWK pyrolysis instruments are given in Table 14, converted to Rve using the equations by Jarvie (2021). Rve measurements calculated from Tmax values correlate well with the measured Rv in the Grant Group to a depth of 480 m, after which the Tmax values estimate a lower thermal maturity than Rv and Rve calculated from graptolite reflectance.

The molecular compositions determined on the seven core samples and one possibly oil stained core sample can also be used to estimate maturity using the parameters shown in Table 15 for the saturated hydrocarbons (Peters et al., 2005) and for the aromatic hydrocarbon parameters in Table 14.

Maturity parameters based on hopanes, steranes and aromatic hydrocarbon ratios indicate that the samples over the depth 1427.34 to 1835.05 m in the Samphire Marsh Member are in the early oil window. The deepest sample at 2330 m in the Fly Flat Member is thermally more mature and is assessed to be in the peak oil window based on these biomarker parameters. The thermal maturity predicted from Tmax, saturated hydrocarbons and the aromatic molecular parameters is consistent and predicts a lower level of maturity than that calculated from graptolite reflectance, which in this instance appears to overestimate the maturity of the Ordovician sedimentary rocks. These results need to be placed into a burial history model, with geothermal gradient and heat flow measurements on which sensitivity tests are run, to explore the effect of using these different techniques of estimating maturity. Further work is required to calibrate and convert the different maturity measurements to Rve values suitable to the Canning, and other Australian basins.

In summary, organic matter is present in all samples analysed petrographically, palynologically and geochemically from Barnicarndy 1, but in low quantities (average TOC content <0.2 wt%). These analyses provide evidence that the organic matter comprises the remains of graptolites, chitinozoans, algae (*Leiosphaeridia* and acritarchs), cyanobacteria and rare cryptospores originating from the earliest land plants (embryophytes). The sedimentary section penetrated has reached the oil window at a depth of about 500 m (Rv >0.55%) in the Grant Group and remains within the oil window in the Samphire Marsh Member of the Nambeet Formation to a depth of about 2000 m using pyrolysis and molecular maturity estimates, with relatively higher maturity levels predicted from graptolite reflectance. From a depth of greater than 2000 m, from near the base of the Samphire Marsh Member and into the Fly Flat Member, Rve calculated from graptolite reflectance place these sedimentary rocks within the gas window (Rv >1.3%), whereas the molecular maturity parameters suggest a maximum Rve of just over 0.9%, which is within the peak oil window. There is evidence of trace quantities of hydrocarbons migrating through the upper Carboniferous–Permian and Ordovician sections from the presence of gaseous fluid inclusions, and the possibility of a minor oil stain in one sample from the Fly Flat Member. However, differences in its molecular and isotopic composition precluded a match to the other core extracts in Barnicarndy 1. It is unlikely that any economically significant quantities of hydrocarbons have been generated in the stratigraphic section intersected at Barnicarndy 1.

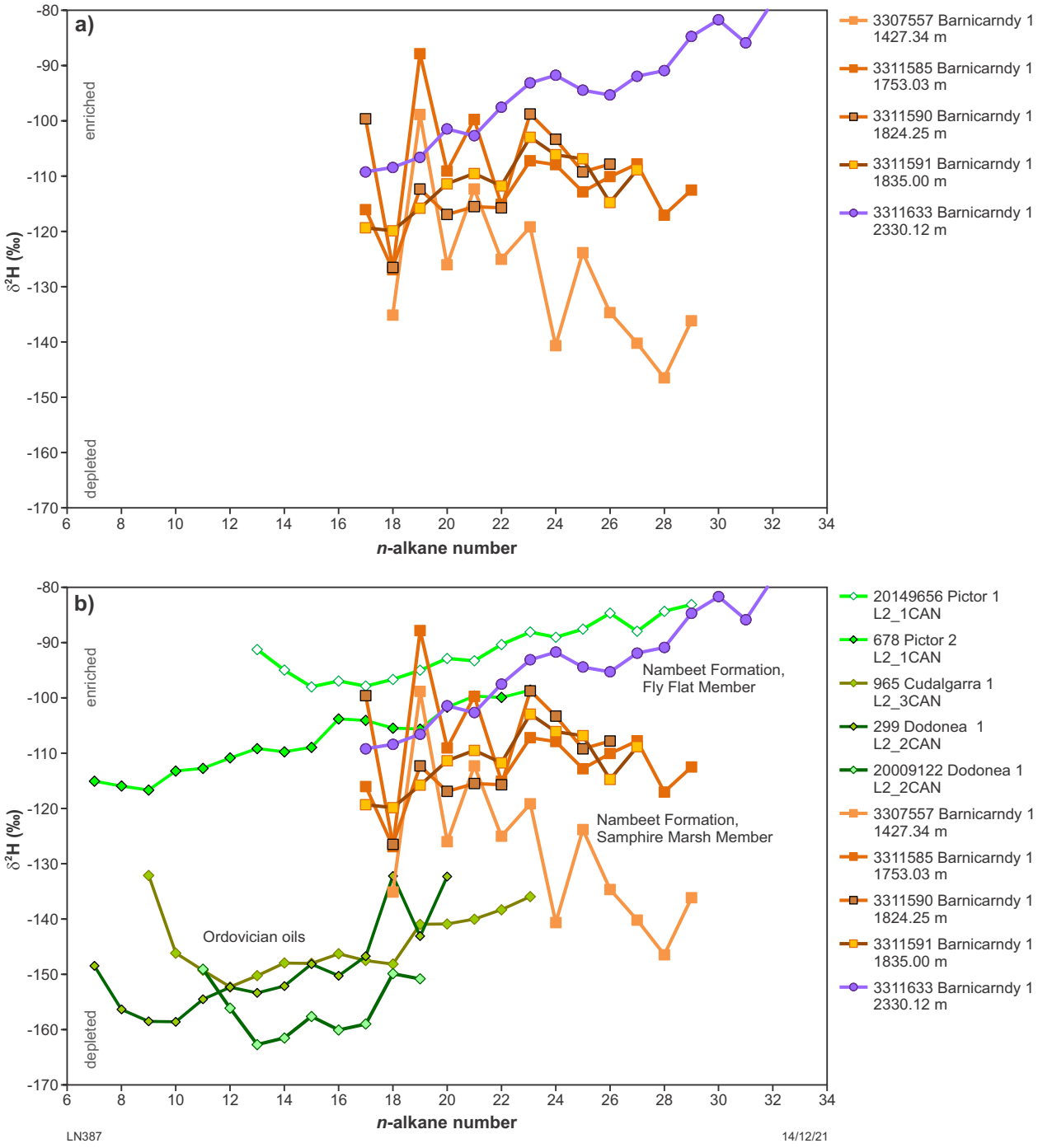

Figure 60. Hydrogen isotopic composition for C_{7+} *n*-alkanes: a) the Nambeet Formation in Barnicarndy 1; b) comparison of the core extracts to Ordovician-sourced oils from the Canning Basin (Edwards et al., 2013). The three Ordovician Larapintine 2 oil families are named L2_1CAN, L2_2CAN and L2_3CAN

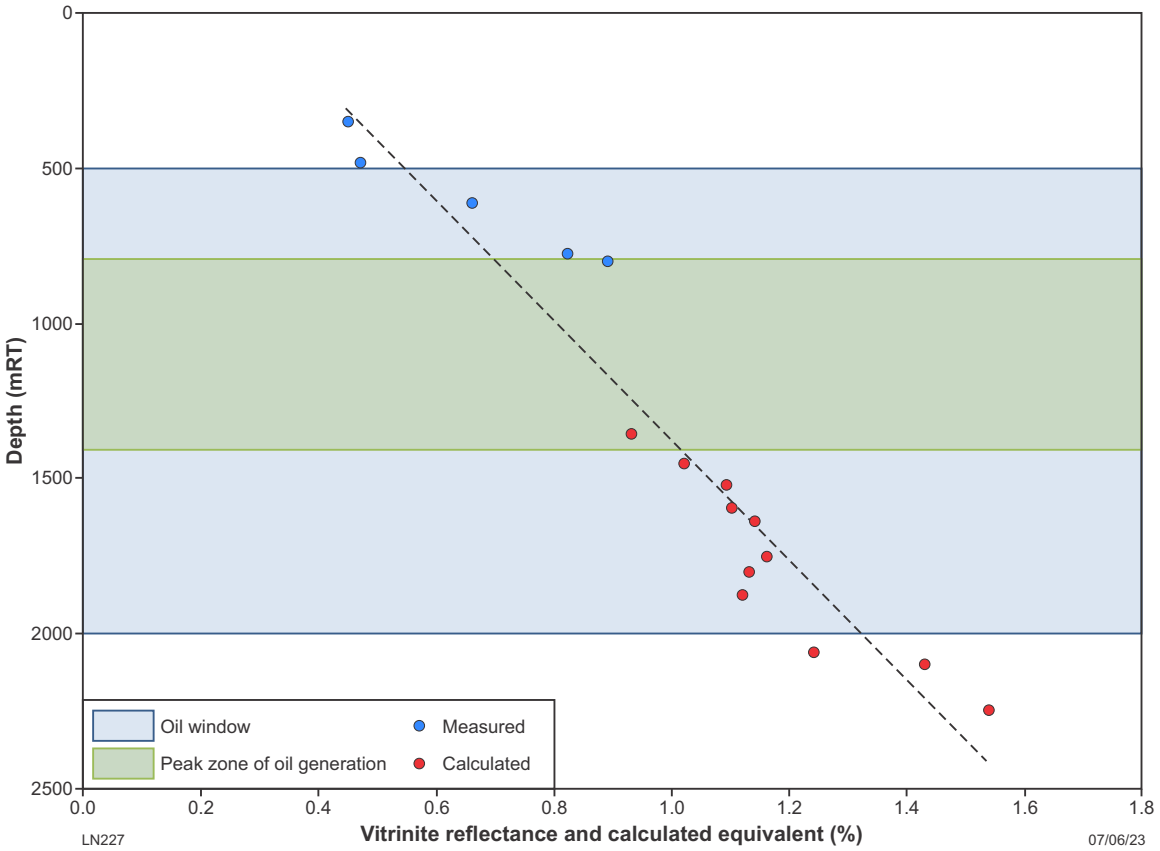

Figure 61. Profile of measured vitrinite reflectance and calculated equivalent vitrinite reflectance from graptolite reflectance. Estimates of thermal maturity use the definition from Hantschel and Kauerauf (2009)

Fluid inclusion stratigraphy

A total of 180 samples, comprising 24 cuttings (195.0 – 579.0 m) and 156 core samples (240.0 – 2679.1 m) were submitted to Fluid Inclusion Technologies (a subsidiary of Schlumberger) for fluid inclusion stratigraphy (FIS) analysis (Appendix 20; Fluid Inclusion Technologies, 2021). The raw data and report can be found in WAPIMS. Selective mass spectral responses and response ratios are shown in Figure 63. The data define three zones discussed below.

Zone 1: Grant Group

The upper zone between 240.0 and 823.2 m (Grant Group) displays mostly sub-anomalous mass spectral intensity responses when considered on a global concentration scale, with weak dry gas responses at 333.0 m and 522.0 – 543.0 m. No water-soluble hydrocarbon anomalies (proximity -to pay indicators) are recorded in this zone. No thin sections were prepared from this interval.

Zone 2: mainly Barnicarndy Formation

The underlying zone at 827.0 – 1381.0 m (base of Grant Group to Barnicarndy Formation and upper Nambeet Formation) shows mostly dry gas responses with a single wet gas spectrum at 1111.1 m. This sample in the Barnicarndy Formation also gives the highest CH_4 response (Fig. 64). The source of the CH_4 remains unknown, since the CH_4 yield was too low to determine accurate carbon and hydrogen isotopes for that gas, compared with those obtained for other Canning Basin fluid inclusion gases (Boreham et al., 2020). Trace liquid-range alkanes co-vary with CH_4 for the most part, suggesting natural hydrocarbons in the system. Anomalous concentrations of acetic acid, with or without benzene, are recorded intermittently in this sandstone-dominated section. In general, samples containing acetic acid anomalies suggest the nearby presence of liquid petroleum (oil or condensate). Sulphur species are sporadically present. For instance, sulphur dioxide (SO_2) ± sulphur (S_2) is identified at 890.9, 1179.6 and 1289.9 m. These specific sulphur species are generally associated with water-bearing, porous reservoir rock. Higher H_2S signals are noted at 1289.9 and 1354.9 m. Overall, the data suggest the potential for slightly altered petroleum in this section.

Six thin sections were prepared, five in the Barnicarndy Formation (910.9, 1069.8, 1111.1, 1179.6 and 1289.9 m) and one in the Samphire Marsh Member of the Nambeet Formation (1354.9 m). All six samples consist of sandstone. Rare, white-fluorescent upper-moderate gravity petroleum inclusions were imaged at 1069.8 m (Fig. 65). Rare mixed (oil and brine) petroleum inclusions are noted at 910.9, 1111.1 and 1179.6 m. In addition, rare, yellow-fluorescent, moderate gravity petroleum inclusions were recorded at 1111.1 m. Low inclusion abundance suggests petroleum migration through these zones at some time. No petroleum inclusions were identified at 1289.9 and 1354.9 m.

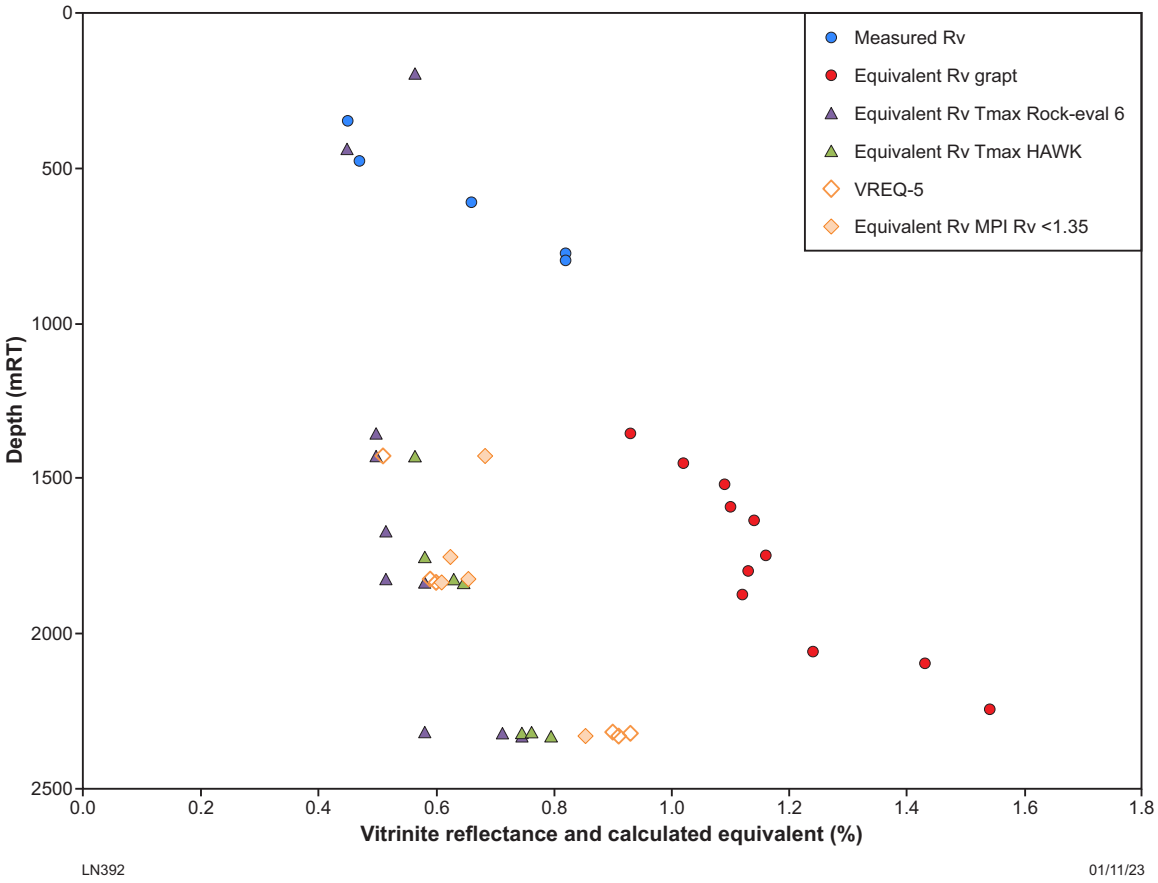

Figure 62. Comparison of equivalent vitrinite reflectance values calculated from pyrolysis and molecular maturity parameters. Definitions of calculated equivalent vitrinite reflectance provided in caption of Table 15

Table 15. Maturity-related saturated hydrocarbon parameters for core samples analysed by GC-MS-SIM in Barnicarndy 1. Definition of ratios is given in Appendix 18, table A1.4

GA no.	*Depth from (m)*	*Depth to (m)*	*Stratographic unit*	*Ts/ (Ts+Tm) %*	*C_{32}Hopanes 22S/ (22S+22R) %*	*C_{29} Steranes 20S/ (20S+20R) %*	*C_{29} Steranes ββ RS/ (ββ RS+αα SR) %*
3307557	1427.34	1427.37	Samphire Marsh Mbr	8.40	55.1	28.6	43.3
3311585	1753.03	1753.09	Samphire Marsh Mbr	3.32	57.6	21.9	32.2
3311590	1824.25	1824.34	Samphire Marsh Mbr	2.85	57.7	25.3	28.4
3311591	1835	1835.05	Samphire Marsh Mbr	2.44	58.2	28.6	23.0
3311598	1933.72	1933.78	Samphire Marsh Mbr	4.48	59.57	7.4	22.9
3311630	2317.05	2317.10	Fly Flat Mbr	9.59	60.21	14.8	50.0
6661399	2321.19	2321.25	?oil stain	13.73	57.88	17.1	28.6
3311633	2330.12	2330.17	Fly Flat Mbr	16.58	58.7	32.1	47.8

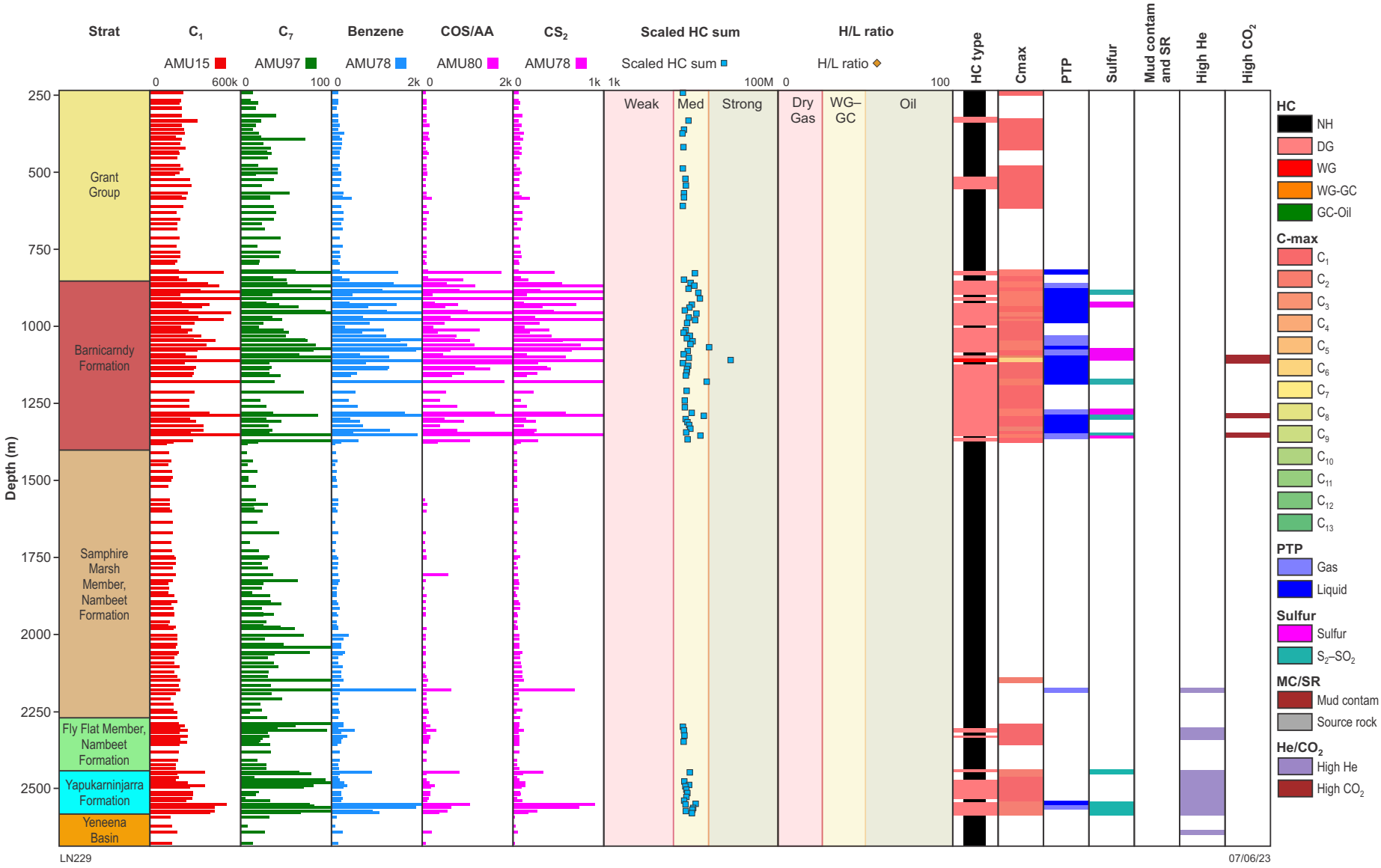

Figure 63. Downhole depth log summarizing the results of a fluid inclusion stratigraphy study (see Fluid Inclusion Technologies, 2021 in Appendix 20 for description of mass values used to identify the various components and the key to the figure). Abbreviations: C_1, methane; C_7, heptanes; COS, carbonyl sulphide; AA, acetic acid; CS_2, carbon disulphide; HC, hydrocarbons; H/L, heavy over light species based on the weighted (scaled) sum of heavy hydrocarbons over methane; Cmax, maximum hydrocarbon reported; PTP, proximity to pay; MC, mud contamination; SR, source rock; He, helium; CO_2, carbon dioxide; NH, no hydrocarbons; DG, dry gas; WG, wet gas; GC, gas condensate

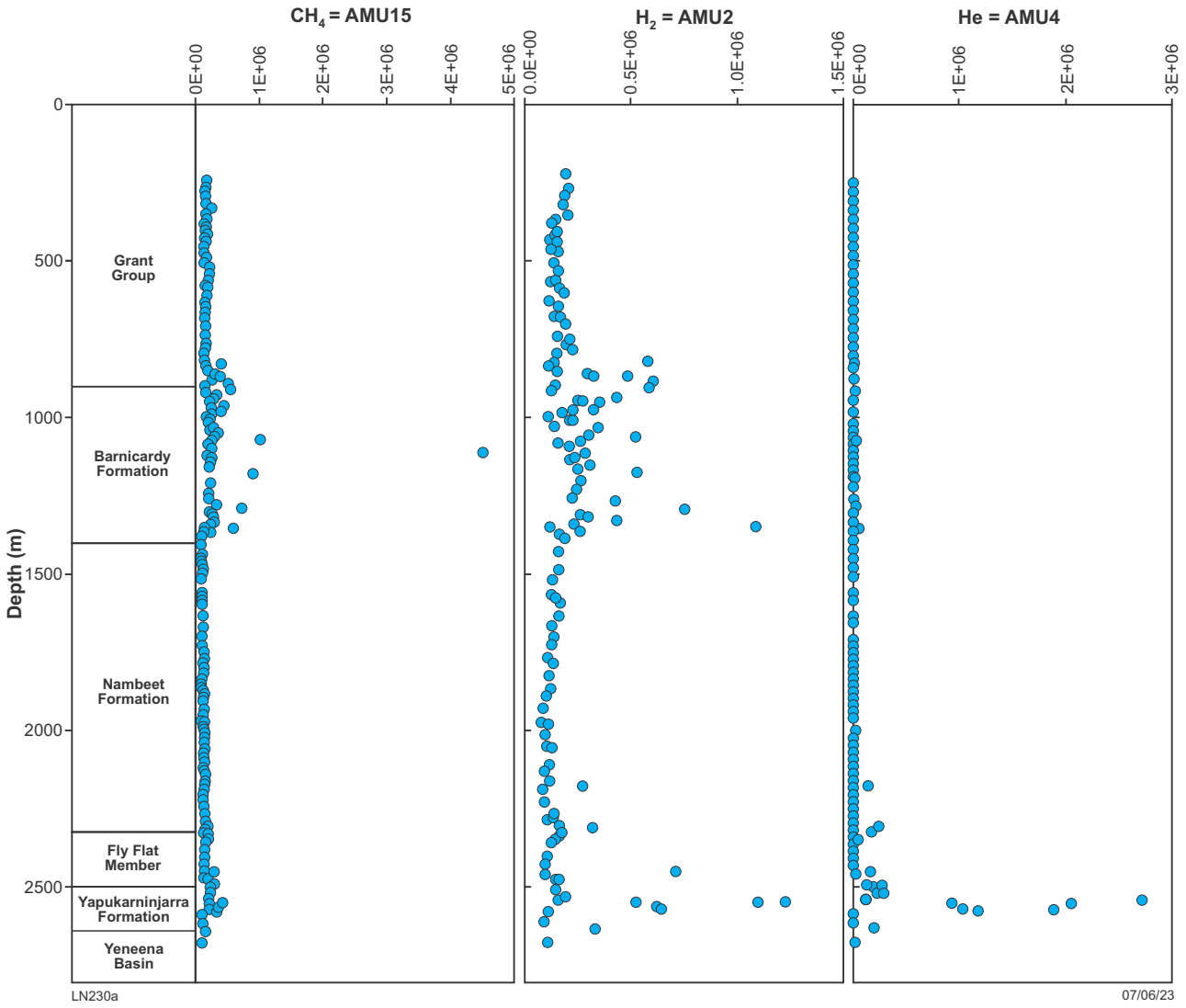

Figure 64. Depth profile of methane (CH_4), hydrogen (H_2) and helium (He) abundance response from bulk fluid inclusions based on mass spectra corresponding to 15, 2 and 4 AMU respectively. Abbreviation: AMU, atomic mass unit

Zone 3: Nambeet to Yapukarninjarra Formations and the Yeneena Basin

The lower section of the well between 1411.3 – 2679.1 m (Ordovician to Yeneena Basin basement) exhibits mostly sub-anomalous FIS responses, when considered on a global concentration scale, with dry gas spectra at 2312.1, 2331.8, 2447.4, 2478.0 – 2530.1 and 2550.3 – 2580.3 m. The highest CH_4 and liquid hydrocarbon responses were recorded at 2550.3 – 2580.3 m in the Yapukarninjarra Formation (Fig. 63). Anomalous benzene was recorded at 2180.1, 2550.3 and 2560.7 m, and anomalous acetic acid was noted at 2550.3 m. Benzene anomalies without organic acid may indicate nearby wet gas. $SO_2 \pm S_2$ was notable at 2447.4 and 2550.3 – 2580.3 m, again suggesting potential for water-bearing porous reservoir rock.

Seven thin sections were prepared from this zone at 2550.3, 2551.1, 2560.7, 2571.1, 2574.2, 2580.3 and 2640.1 m. Most consist of sandstone, with sandy shale at 1354.9 m and traces of shale at 2551.1 m. The deepest sample consists mostly of shaly carbonate. No petroleum inclusions are visually detected in any of the seven thin sections. Appreciable amount of immature oil-prone kerogen was found at 1354.9 m. Hydrocarbon species up to C_6 are observed in this interval. Proximity to gas indications are intermittent. Proximity to liquid petroleum indications are intermittent. Sulphur species are intermittently present.

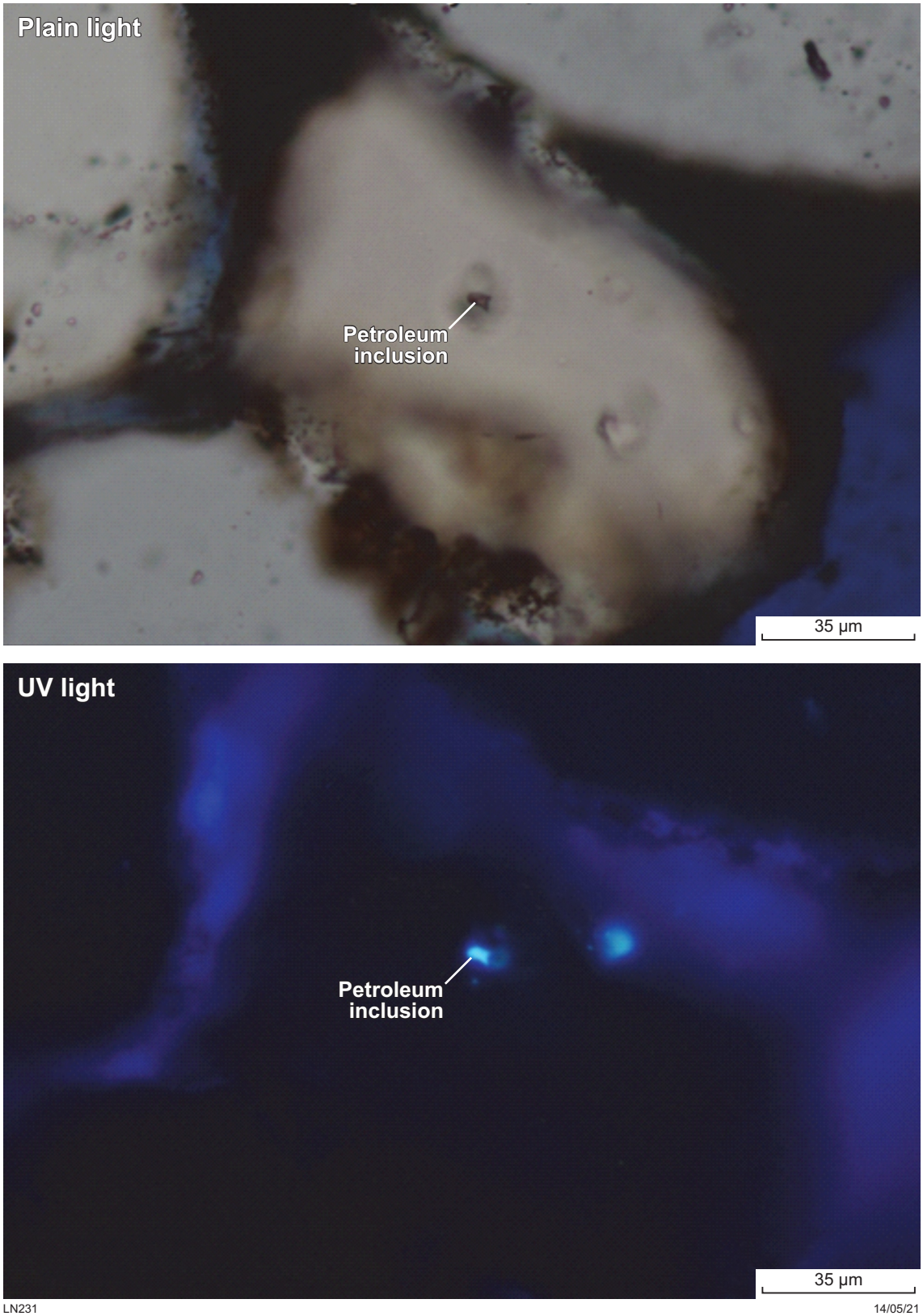

Figure 65. Petroleum inclusion identified in thin section photomicroscopy at 1069.8 m under plain (top) and UV (bottom) light (from Appendix 20; Fluid Inclusion Technologies, 2021)

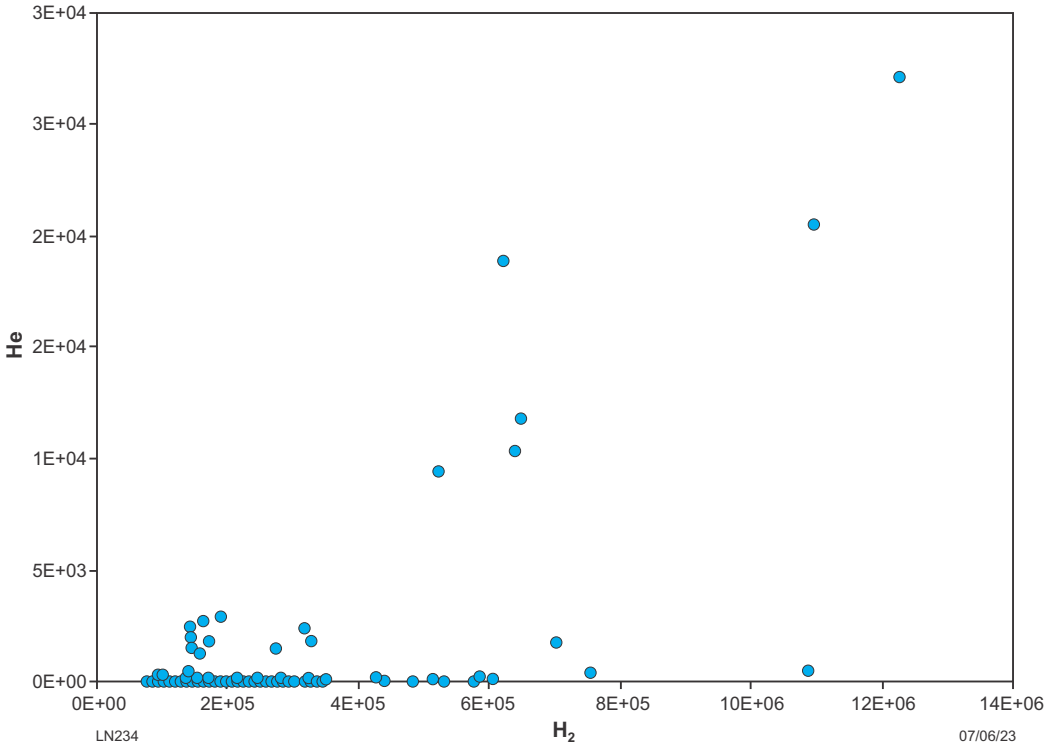

Figure 66. Cross-plot of relative abundances of hydrogen (H_2) vs helium (He) from fluid inclusion stratigraphy data

Hydrogen and helium

The relative abundances of molecular hydrogen (H_2), atomic helium (He) and CH_4 in fluid inclusions are shown in Figure 64. For H_2, there are two main intervals of enhanced abundance from 827.0 to 1354.9 m (maximum at 1354.9 m) and 2180.1 to 2640.1 m (maximum at 2550.3 m). The highest values correspond with mainly sandstone lithologies. On the other hand, He shows only a single high abundance interval corresponding in depth range and maxima to the deeper high H_2 interval. This distinction is clearly seen in the cross-plot of H_2 vs He relative abundances (Fig. 66). For the deeper interval, partly including the basement interval, the co-variance of H_2 with He suggests a common source involving 1) the radioactive decay of U- and Th-bearing minerals to release alpha particles (i.e. radiogenic ^{4}He) and 2) in combination with K-bearing minerals the radiation dosage facilitates the radiolysis of water to produce H_2 (Boreham et al., 2021b; Boreham et al., 2021a; and references therein). The absence of He in the H_2-rich upper interval points to a likely redox process involving $Fe^{2+} \rightarrow Fe^{3+}$ oxidation with the accompanying reduction of water to H_2.

Routine core analysis

Two subsets of core samples were submitted for routine core analysis (RCA) at Core Laboratories, Perth, Western Australia. Each sample consists of a horizontal core plug drilled from the submitted whole core pieces. The first set of 47 RCA samples covered the entire cored interval, with analyses including petrography, XRD, porosity, permeability and grain density. The second set focused on five samples in the Barnicarndy Formation and measured for porosity, permeability, grain density and formation resistivity factor (FRF) measurements. Both RCA datasets have been consolidated into Appendix 21.

Porosity, permeability and grain density

Porosity, permeability and grain density results are illustrated in Figure 67. The highest porosity and permeability values correspond to the Grant Group and Barnicarndy Formation, whereas the lowest values were obtained from the Nambeet Formation and Yeneena Basin samples. Grain density correlates well to lithology as demonstrated by the restricted range from 2.640 to 2.670 g/cc for quartz arenite samples (Fig. 67).

Petrography

Detailed petrographic analysis of regular thin sections for the first set of 47 RCA samples were completed by Core Laboratories, Houston, Texas (Appendix 16; Antia, 2020). The sample descriptions include Folk (1980) classification and incorporate XRD whole rock mineralogy and clay abundance. A subset of 35 of these samples was selected for scanning electron microscopy (SEM) and energy-dispersive X-ray spectroscopy (EDX). Cathodoluminescence petrography was applied to nine carbonate-bearing samples. A broad depositional environmental scheme was developed based on petrography and mineral composition (Fig. 68). Sample sets are identified next to the scheme.

Rock properties analyses

This section covers the analyses of standard petrophysical properties (bulk density, porosity, permeability, computerized tomography scans (CT scans) and simple rock mechanics properties (unconfined compressive strength, Young's modulus, Poisson's ratio) on two sets of six samples taken from the Barnicarndy 1 core.

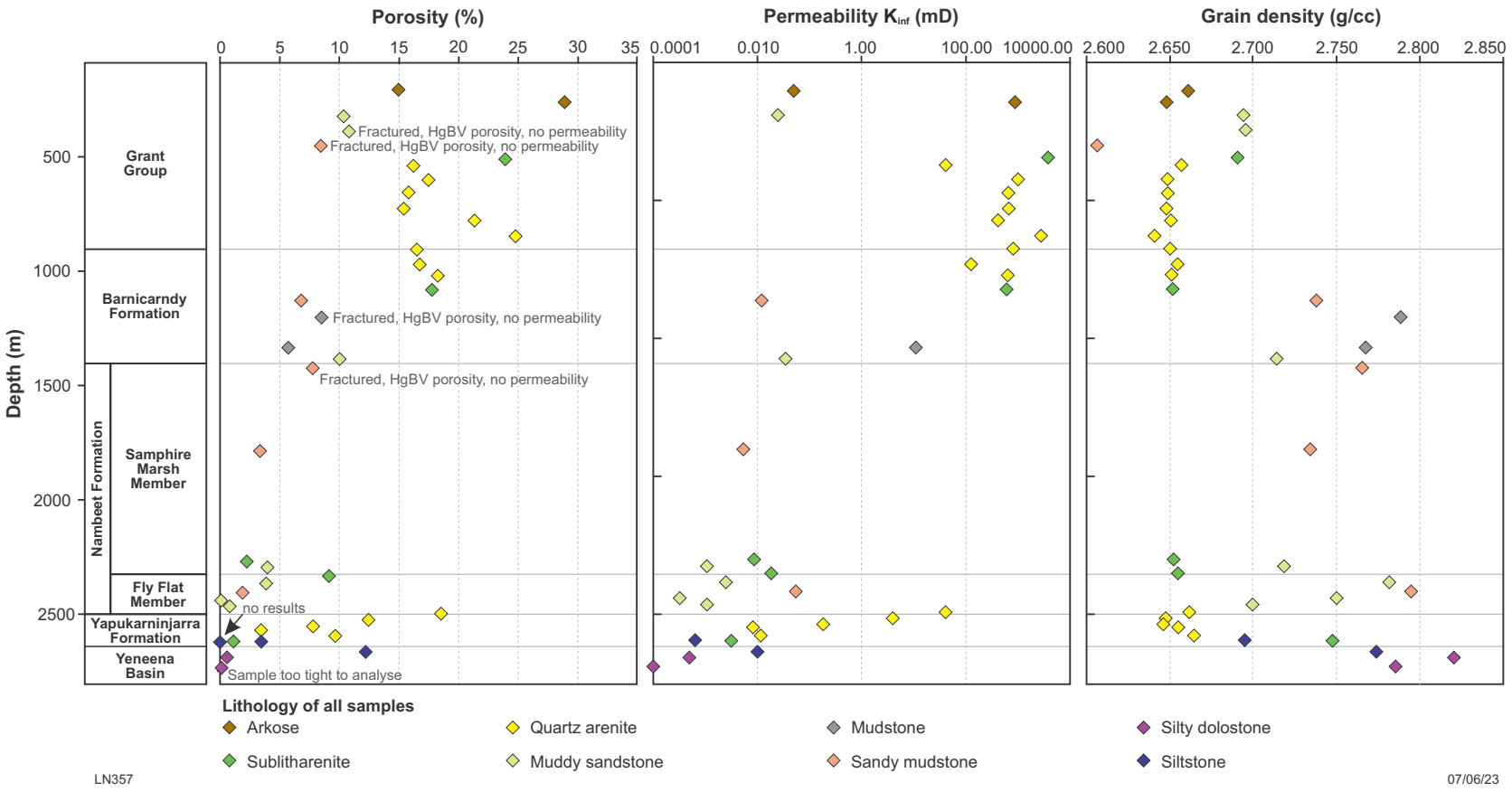

Figure 67. Routine core analysis; porosity, permeability and density plot

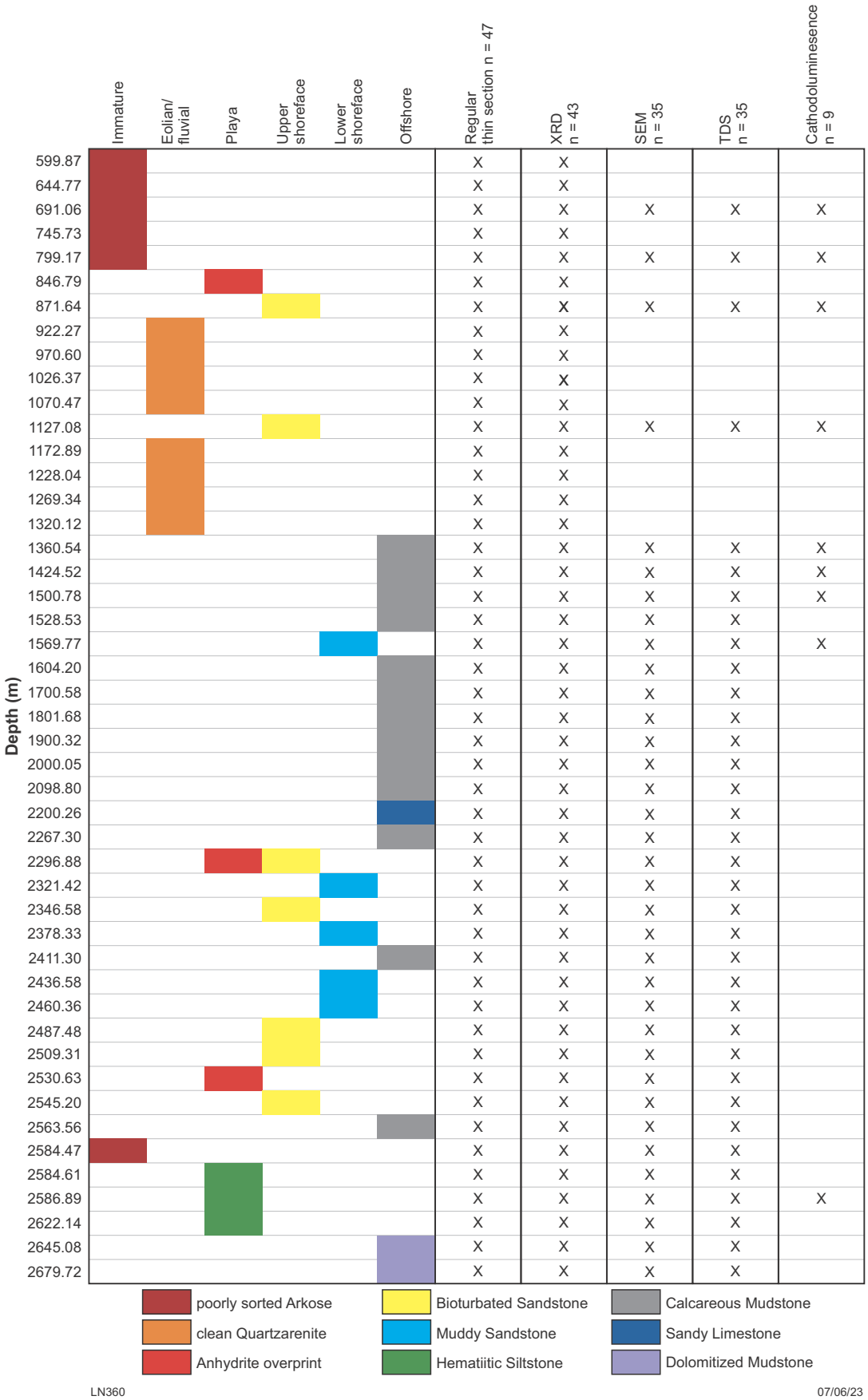

Figure 68. Summary of routine core analysis petrography samples and depositional environments

The first set included three potential reservoir-seal pairs, involving one seal of diamictite and two of mudstone overlying sandstone reservoir in each case (Table 16). These are distributed through each of the Barnicarndy 1 Canning Basin stratigraphic intervals, but not the Yeneena Basin basement. The first set of tests included CT scans with porosity and bulk density determination, gas porosity and permeability and rock mechanics tests with ultrasonic velocity measurements at 50% of peak strength (Appendix 22; Jarrett et al., 2020); (Appendix 23; Esteban et al., 2020). For these tests, the porosity and permeability measurements and unconfined compressive strength (UCS) tests were performed on the same core plugs, with the former set of tests done first.

The second set of tests focused only on seal samples with four of these samples taken from the Grant Group diamictite (about 690–850 m) and two from compact shales in the Samphire Marsh Member (about 1500 and 2100 m). The properties investigated include CT scans, rock mechanics tests and mercury injection for seal capacity (Table 17).

Methodology

Core plug preparation

Cylindrical core plugs nominally 25 mm in diameter and 50 mm in length were prepared to be as close as possible to bedding-normal. In some cases, smaller diameter samples (20 or 15 mm) were used due to closely spaced fractures in these rocks (Tables 17, 18). The plugs were extracted using a Murg endless diamond wire bandsaw and finished on a cylindrical grinder. Core plugs were photographed and CT scanned prior to poroperm and rock mechanics testing. Full details of these images are available in excel spreadsheets from WAPIMS.

X-ray computerized tomography (CT) scanning

Single energy acquisition was performed using a 140 kV and 500 mAs energy beam in helical mode in 0.4 mm steps with an extended dynamic range of attenuation up to 10 000 Hounslow Units (HU). The field of view was optimized to see the entire core section to maximize imaging of the core inside an approximate 10 cm field of view with 512 x 512 pixels that allows final voxel resolution of those cores at 215 x 215 µm and 400 µm (in standard DICOM format). A Siemens H70h algorithm was used for image reconstruction to allow edge detection of the different density materials inside the cores without over-enhancing the generated noise on the final image. Further details are contained in Jarrett et al. (2020).

Porosity and permeability testing

Gas porosity and permeability tests were undertaken on dry core plugs using a Coretest Inc. automated AP608 nitrogen Permeameter-Porosimeter. This rig can be used to measure samples with permeability >1 µD. Four samples were identified where permeability was <1 µD (at 725.00, 2269.22 2316.75 and 2395.95 m) and these ultra-tight samples were analysed using a Coretest Inc. NDL-605 apparatus designed for low permeability testing (<1 µD) as outlined below. The porosity and permeability of each of these core plugs were measured at a confining pressure of 3.45 MPa (500 psi) and repeated twice for quality checks. The best accuracy of porosity with the AP608 nitrogen Permeameter-Porosimeter apparatus is approximately 0.1%. Permeability was measured using the unsteady state pulse decay method with a measurement range from 1 to 10 D (Jones, 1972). Laboratory measurements of gas permeability were corrected for the Klinkenberg effect (Klinkenberg, 1941).

Table 16. Sample details for the first set of tests performed on samples from Barnicarndy 1, including CT scans, porosity and permeability and rock mechanics tests. Sample sizes are variable due to the fragile nature of some of the rocks

CSIRO no.	*GSWA no.*	*GA no.*	*Stratigraphic unit*	*Rock type*	*Depth (m)*	*Analysis*	*Length (mm)*	*Diameter (mm)*	*L/D ratio*	*Strain rate*	*Load rate (mm/hr)*
3413	247924	6621449	Grant Group	Compact diamictite	725.00	por/perm/ CT/ UCS/ ultrasonics	50.01	25.14	1.99	10^{-6} s^{-1}	0.18
3381	247925	6621450	Barnicarndy Fm.	Clean sandstone	1127.00	por/perm/ CT/ UCS/ ultrasonics	50.02	25.21	1.98	10^{-6} s^{-1}	0.18
3415	247926	6621451	Samphire Marsh Mbr	Compact mudstone	2269.50	por/perm/ CT/ UCS/ ultrasonics	21.04	14.11	1.49	10^{-6} s^{-1}	0.076
3412	247927	6621452	Fly Flat Mbr	Clean sandstone	2316.80	por/perm/ CT/ UCS/ ultrasonics	49.81	24.21	2.06	10^{-6} s^{-1}	0.179
3428	247927 (repeat)	6621452	Fly Flat Mbr	Clean sandstone	2316.80	por/perm/ CT/ UCS/ ultrasonics	48.04	23.93	2.01	10^{-6} s^{-1}	0.173
3417	247928	6621453	Fly Flat Mbr	Compact mudstone	2395.70	por/perm/ CT/ UCS/ ultrasonics	31.62	17.31	1.83	10^{-6} s^{-1}	0.114
3382	247929	6621454	Yapukarninjarra Fm.	Clean sandstone	2530.00	por/perm/ CT/ UCS/ ultrasonics	45.6	25	1.82	10^{-6} s^{-1}	0.164

Table 17. Sample details for the second set of tests for rock mechanics and mercury porosimetry testing. Sample sizes and loading/strain rates for UCS testing shown. MICP samples were nominally a 10 mm long by 10 mm diameter unfinished core plug

CSIRO no.	*GSWA no.*	*Stratigraphic unit*	*Rock type*	*Depth (m)*	*Analysis*	*Length (mm)*	*Diameter (mm)*	*L/D ratio*	*Strain rate*	*Load rate (mm/hr)*
3525	250544	Grant Group	Compact diamictite	691.00	UCS	41.51	19.91	2.08	10^{-6} s^{-1}	0.149
3526	250544			690.99	MICP					
3527	250545	Grant Group	Compact diamictite	745.57	UCS	42.94	20.12	2.13	10^{-6} s^{-1}	0.155
3528	250545			745.59	MICP					
3529	250546	Grant Group	Compact diamictite	799.38	UCS	41.43	19.99	2.07	10^{-6} s^{-1}	0.149
3530	250546			799.37	MICP					
3531	250547	Grant Group	Compact diamictite	852.69	UCS	40.18	20.04	2.00	10^{-6} s^{-1}	0.145
3532	250547			852.68	MICP					
3533	251801	Samphire Marsh Mbr	Compact mudstone	1498.71	UCS	40.91	20.03	2.04	10^{-6} s^{-1}	0.147
3534	251801			1498.73	MICP					
3535	251802	Samphire Marsh Mbr	Compact mudstone	2098.82	UCS	37.56	19.93	1.88	10^{-6} s^{-1}	0.135
3536	251802			2098.84	MICP					

Table 18. Measured porosity and permeability using standard techniques for reasonably permeable samples measured on the diamictite, two shales and three sandstones from Barnicarndy 1 (modified from Jarrett et al., 2020). The two shales and the diamictite are essentially below detectable limit. Measurements were taken on dried out samples. Abbreviation: Kair, air permeability

CSIRO no.	*GSWA no.*	*GA no.*	*Sample Depth (m)*	*Effective pressure (MPa)*	*Pore volume (cc)*	*Porosity %*	*Kair mD*	*Klinkenberg corrected K (mD)*	*Mean porosity (%)*	*Mean permeability (mD)*
3413	247924	6621449	725.00	2.1926	0.135	0.22	0.00393	0.00051	0.29	0.0003
				2.0203	0.214	0.36	0.00171	0.00015		
3381	247925	6621450	1127.10	2.12779	5.23	20.81	2317	2273	21.26	2269
				1.94811	5.456	21.71	2309.9	2265		
3415	247926	6621451	2269.22	2.26369	0.118	0.49	0.0037	0.0005	0.49	0.0005
3412	247927	6621452	2316.75	2.39545	1.023	4.43	0.03625	0.01051	4.2	0.0101
3428	247927 (repeat)	6621452	2316.75	1.80919	0.914	3.96	0.03493	0.00975		
3417	247928	6621453	2395.95	2.04037	0.155	1.05	0.00122	0.0001	1.05	0.0001
3428	247929	6621454	2530.25	2.09442	1.67	7.46	0.20319	0.09843	7.43	0.0965
				2.21646	1.655	7.39	0.19507	0.09457		

An NDL-605 apparatus from CoreTest Inc. was used for ultra-low permeability samples that are below the limit of detection from the abovementioned AP-608 equipment (i.e. 1 µD). The method relies on the unsteady state pulse decay principle. The addition of a small differential pressure across the sample, set at 10 psi, between the top and bottom of the sample is monitored with time until equilibration occurs. The system and tested samples were temperature stabilized at 40 °C for 48 hours to avoid thermal changes on tight permeability measurements. The confining pressure was set at 1500 psi over 2 hours before applying nitrogen gas pore pressure at 500 psi for 16 hours to allow proper equilibration. A differential pressure pulse of 10 psi was subsequently added, and pore pressure re-equilibration monitored. This measurement was repeated three times and validated only when the re-equilibration was <1% per minute. See Appendix 22 (Jarrett et al., 2020) for further details on both methods discussed here.

Rock mechanics testing

Unconfined compressive strength (UCS) tests were conducted using standard methods e.g. (Paterson, 1978) with a universal load frame having a 400 kN axial load capacity, and provisions for measurements of sample deformation and axial load. The instruments used to measure the behaviour of the test sample were:

- two diametrically-opposed Linear Variable Differential Transformers (LVDTs) mounted between the sample end platens to measure axial deformation of the sample
- four cantilever (orthogonal) radial gauges mounted at the mid-height of the sample to measure radial deformation
- a load cell located beneath the base platen to measure axial load.

High-precision computer-controlled stepping motor pumps were used to control the applied axial load. The sample was jacketed with a flexible synthetic rubber membrane and installed in between the top and bottom loading platens. The transducers for measuring the sample axial displacement and radial displacement were then installed. After a suitable stabilization period, an axial load was applied at a constant average axial strain rate of 10^{-6}/sec until the sample failed, defining the peak strength and thus the UCS.

The Young's modulus (E) and Poisson's ratio (v) are determined as the tangential slope of the curve of deviatoric stress vs average axial strain and the tangential slope of the curve of average radial strain vs average axial strain at between 40% and 60% of the maximum differential stress.

Of the 12 tests performed, six of these tests also had P-wave and S-wave ultrasonic velocity measurements taken at 50% peak strength. P- and S-wave transducers located in the end platens were used to take measurements of ultrasonic travel time during the UCS test (e.g. Inoue and Ohomi, 1981). Ultrasonic measurements were acquired automatically every 15 minutes throughout the test and the waveform closest to 50% of the UCS was evaluated as this lies in the true elastic range of the specimen. See Appendix 22 (Jarrett et al., 2020) for further details on the rock mechanics and ultrasonic testing performed here.

Mercury porosimetry

Capillary properties can be determined from the pore size distribution of shales using high-pressure mercury intrusion capillary pressure measurements (MICP). The following modification of Jurin's Law by Washburn (1921) gives the capillary pressures (Pc) required to intrude pore throats of diameter d for the air-mercury system:

$$P_c = \frac{4\gamma Cos\,\theta}{d} \quad (1)$$

where γ is interfacial tension (485 dynes/cm) and θ is the contact angle (140˚) between the fluid and solid, measured through the denser phase (Vavra et al., 1992).

Capillary pressure analysis was conducted using a Micromeritics Autopore III mercury porosimeter. This equipment is capable of injecting mercury in user-defined pressure increments up to 60 000 psi (approximately 413 MPa) into a dry sample. Cylindrical unfinished plug samples were resin coated on their sides such that mercury was forced to intrude directionally, along the plug axis.

To convert to pressures for the sub-surface brine-hydrocarbon (P_{bh}) system, the following equation is used:

$$P_{bh} = P_c \frac{(\gamma_h Cos\,\theta_h)}{(\gamma Cos\,\theta)} \quad (2)$$

where γ and θ are as defined in equation 1 for the air-mercury system and γ_h and θ_h are interfacial tension and contact angles for the rock-brine-hydrocarbon system.

MICP data and terminology used in this study are illustrated with reference to Figure 69. Initial pressure increases result in mercury entering surface voids and fractures. This process is termed conformance. Any increases in intrusion volumes recorded in this stage are subtracted from final calculations of pore volume. The entry pressure (P_e; Fig. 69) is the pressure at which mercury begins to penetrate the pores of a rock. Threshold pressure (P_{th}) is considered to be the pressure level where a continuous filament of mercury extends through the sample. Its value is determined from the lower inflection on the capillary pressure curve or the large gradient increase on the incremental capillary pressure curve.

The sample used in these tests was a rough cylindrical plug taken with a diamond wire bandsaw from the whole core. The plug was approximately 10 mm diameter x 10 mm height and was taken normal to macroscopic bedding. The sides of the rough cylinder were coated with resin to force mercury intrusion through the two rough ends of the sample. The sample was not preserved at the core store before testing and was subjected to oven drying before MICP testing to reduce vacuum down time in the porosimeter.

Porosity and permeability measurements

The gas porosity and permeability measurements on six extracted plugs from the first phase of testing (Jarrett et al., 2020) using the standard AP608 equipment (see above) are summarized in Table 18. This equipment can only accurately measure permeability at >1 µD, a level not reached in four of the six samples. Note that repeat analysis of one of the six GSWA sample numbers results in seven CSIRO sample numbers for the same dataset.

The sandstone sample from 1127.10 m has a permeability >2 D. As expected, the diamictite and the two shale samples: 725.00, 2269.22 and 2395.95 m respectively, record ultra-tight values with porosity <1% and permeability below the measurement limit of the machine. The two remaining sandstone plugs (2530.25 and 2316.75 m) have porosities of 7.4 and 4.2% respectively, though the permeabilities are low at 0.1 and 0.01 mD respectively.

The four tight samples that are close to or below the limit of reliable measurement of permeability on the AP608 equipment were selected to go through the nano-permeability rig, including the tightest sandstone sample to better define its permeability. These low permeability results are presented in Table 19 and show permeabilities between 0.1 and 0.3 µD for the shales and up to 5 µD for the tight sandstone.

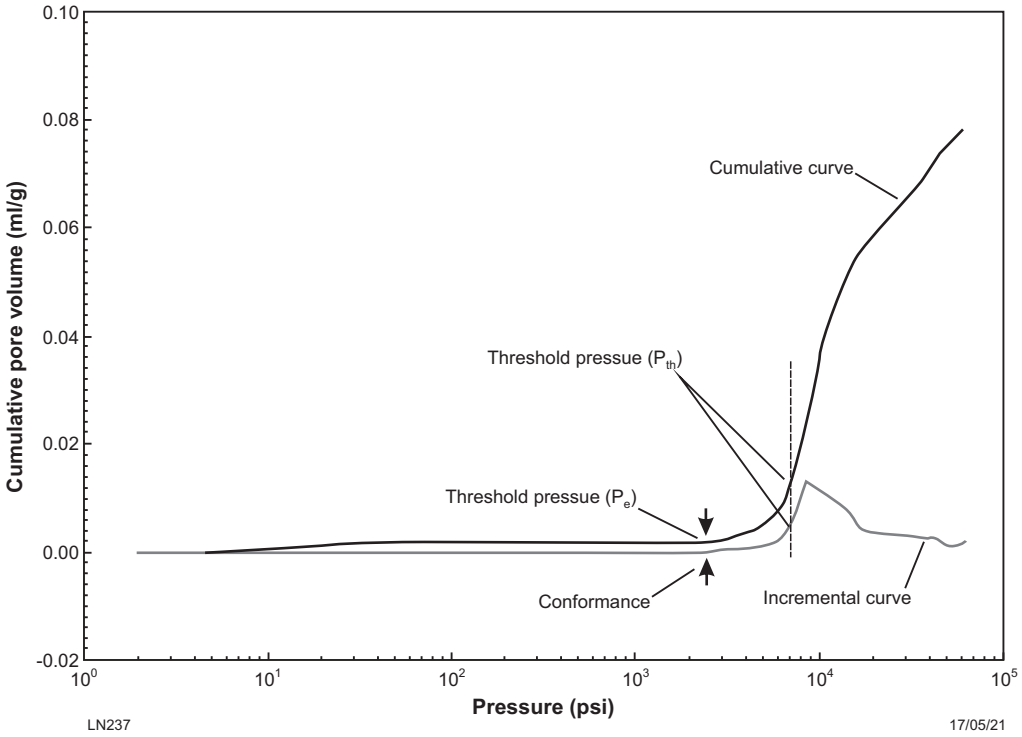

Figure 69. Terminology used for picking air-mercury threshold pressures from mercury porosimetry measurements (Dewhurst et al., 2002)

Table 19. Measured porosity and permeability using specialist low permeability techniques on the diamictite, two shales and one tight sandstone from Barnicarndy 1 (modified from Jarrett et al., 2020). Measurements were taken on dried out samples

GSWA no.	Stratigraphic unit	Depth (m)	Rock type	Duration 10 psi pulse equilibration (hours)	Confining pressure (psi)	Pore pressure mean (psi)	Permeability gas (mD)	Mean permeability (µD)
247924	Grant Group	725.00	Diamictite	6:22	1281	537.244	0.00028682	0.296
				6:44	1484	537.655	0.00032121	
				6:51	1479	537.606	0.00028055	
247926	Samphire Marsh Mbr	2269.22	Shale	8:04	1273	528.829	0.00022424	0.203
				9:15	1507	535.398	0.00019311	
				9:26	1516	532.654	0.00019303	
247927	Fly Flat Mbr	2316.75	Sandstone	3:43	1359	529.87	0.00606568	5.974
				4:47	1492	534.471	0.00594406	
				4:50	1491	532.354	0.00591119	
247928	Fly Flat Mbr	2395.95	Shale	6:45	1319	527.041	0.00014363	0.125
				7:11	1465	526.39	0.00011904	
				7:18	1460	525.957	0.00011131	

Note that two of the samples were difficult to plug initially and are slightly undersized for the low permeability rig. These samples were wrapped in Teflon to attain the requisite dimensions for the permeameter to prevent gas leakage down the sides.

Computerized tomography scans

Samples 3525, 3527, 3529 and 3531 were core plugs recovered from the whole core of Grant Group diamictite at the depths given in Table 17 (Fig. 70a–d). Given the heterogeneous texture of the diamictite, i.e. very fine-grained clay-bearing matrix with dispersed granules and pebbles, the whole rock CT scans were used to try to limit the intersection of core plugs with coarse-grained material. This is because these coarse-grained clasts can cause issues for rock properties testing, especially strength testing. Although it was not possible to avoid all coarse-grained clasts, it was possible to limit their extent in the core plugs. Samples 3533 and 3535 were core plugs from the Samphire Marsh Member at the depths given in Table 17 (Fig. 70e,f).

Rock mechanics and ultrasonic testing

Two sets of rock mechanics testing were performed. The first set investigated static elastic properties and rock strength through unconfined compressive strength (UCS) tests on three seal-reservoir pairs (one diamictite, two shale and three sandstone samples) and also included ultrasonic measurements of P-wave and S-wave velocities and subsequent evaluation of the dynamic elastic properties (Table 20; Appendix 22; Jarrett et al., 2020). The second set of tests was focused on seal only (four diamictite and two shale samples). Stress-strain curves and photographic images of the samples after the second set of tests are shown in Figure 71a–f.

The diamictite and shale results from the first set of tests are reasonably consistent with that of the second set of tests. One sandstone was highly porous and permeable (3381, depth 1127.1 m) and of reservoir quality (20%+ porosity; 2 Darcy permeability) and accordingly was the weakest of all the rocks tested. The other two sandstone samples were stronger and stiffer, consistent with recovery from much deeper in the section. A number of the samples were shorter than optimal due to difficulties in sample preparation and this contributed to axial splitting which may over-estimate rock strength. It is important to note that the shale samples were not preserved at the well site in a manner that avoids desiccation before testing. The loss of in situ pore fluids can result in clay-bearing rocks becoming much stronger and stiffer, representing significant over-estimates of rock strength and stiffness compared to the equivalent in situ, fully water saturated rock.

The first set of geomechanical tests also included ultrasonic testing at 50% of peak strength. Velocities were calculated from the arrival time of P-waves and S-waves down the axis of the core, and the resultant dynamic elastic properties (bulk, shear and Young's moduli, Poisson's ratio, Vp/Vs ratio) were calculated (Table 21). It should be noted that these samples were very short and as such, there was considerable difficulty in detecting the S-wave arrival as it was conflated with the P-wave train. Details of how S-wave picking was undertaken are contained in Jarrett et al. (2020) and the associated excel spreadsheets available from WAPIMS.

The four diamictite samples from the second set typically show brittle behaviour, with some of them failing partially by axial splitting. This tends to over-estimate rock strength and the three samples that failed in this fashion all show a UCS of about 60 MPa. The one diamictite sample that failed in shear (3531) shows a UCS of 50 MPa, and also dilated significantly before failure, which is likely closer to the true behaviour and strength for the rock. Again to emphasize, the diamictite is a clay-rich rock that was not preserved in subsurface condition before testing. Such materials, on loss of their in situ pore fluids, can become much stronger and stiffer; as such, the tests here probably represent significant over-estimates of rock strength and stiffness (Young's modulus) compared to an in situ, fully water saturated representative material.

The two Nambeet Formation shale samples tested from the second set also show brittle behaviour, with both failing in shear and would be considered good UCS tests. Again, these shales are clay-rich rocks that were not preserved before testing. Such materials on loss of their in situ pore fluids can become much stronger and stiffer; as such, the tests here probably represent significant over-estimates of rock strength and stiffness (Young's modulus) compared to an in situ, fully water saturated representative material. Full details of the calculations and correlation coefficients for the elastic properties and strength are given in supplementary excel spreadsheets available from WAPIMS.

The strength, static elastic properties and bulk density results from the tests are summarized in Table 22. The elastic properties of the diamictite samples are very variable and this is likely due to the heterogeneity of the samples as illustrated by the large inclusions that are visible in some of them (see CT scan images in Fig. 70). In addition, the bulk density of the diamictite measured on a dry cylinder in the laboratory is not consistent with the porosity measured above (<1%; Table 19), which may indicate significant porosity in pores smaller than nitrogen can access.

Seal capacity evaluation

Results for four mercury intrusion porosimetry tests on the diamictite samples from the second set are shown in Figure 72a–d. These samples in general are very tight with capillary threshold pressure estimates of about 7000 psi to about 10 000 psi, although one sample (3532) within the re-worked sandstone section of the basal Grant Group shows a lower value of about 2350 psi, which can still restrain a large hydrocarbon column. These results are consistent with the diamictite sample tested by Jarrett et al. (2020), which had an air-mercury threshold pressure of about 6900–8600 psi.

Air-mercury threshold pressures were calculated from MICP measurements and are shown in Table 23. The air-mercury threshold pressures were then recalculated to in situ brine-hydrocarbon conditions in order to calculate gas column heights (Table 24).

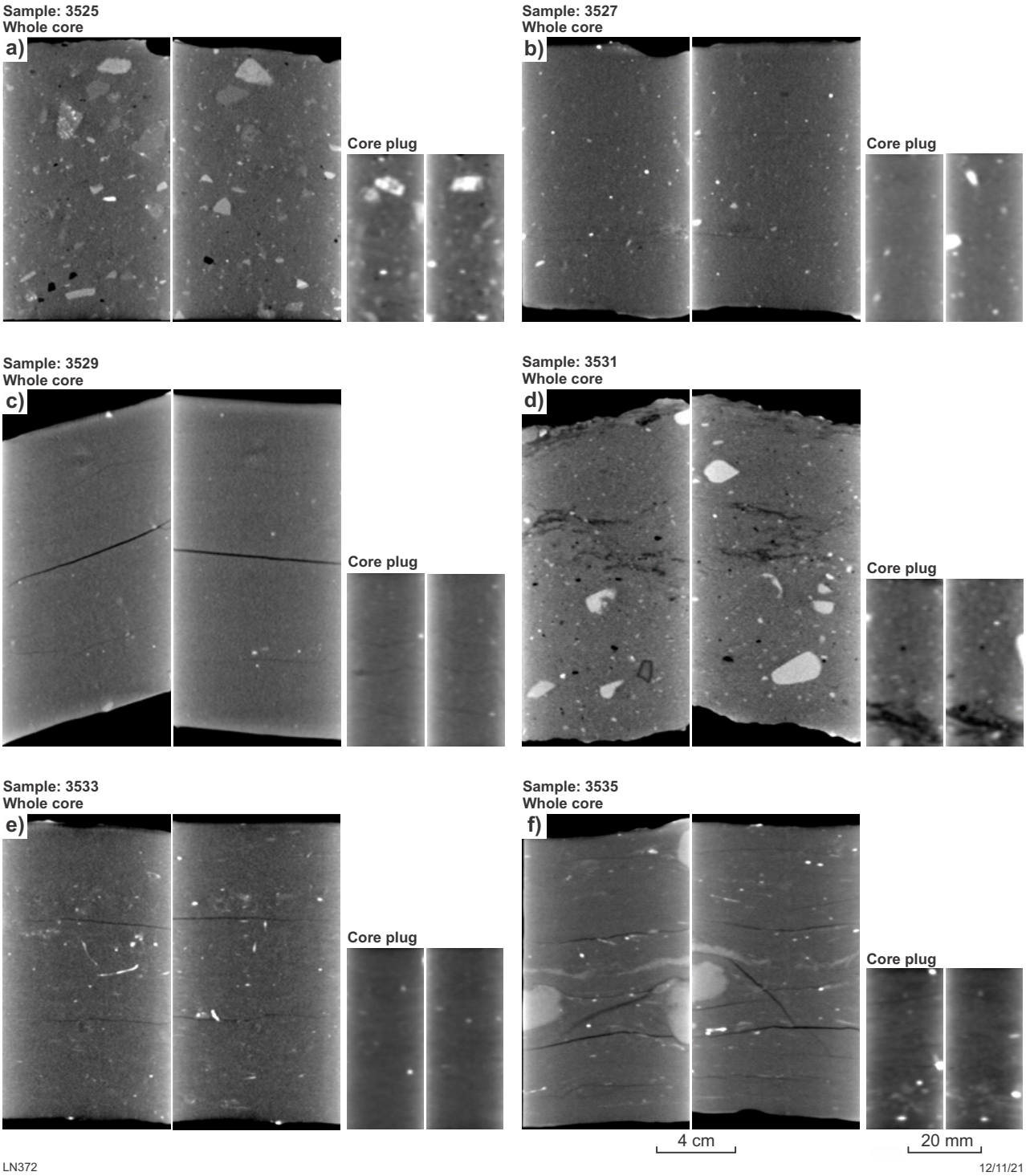

Figure 70. Whole core (larger images) and core plug (smaller images) CT scans from samples: a) 3525 (GSWA 250544); b) 3527 (GSWA 250545); c) 3529 (GSWA 250546); d) 3531 (GSWA 250547); e) 3533 (GSWA 251801); and f) 3535 (GSWA 251802) taken orthogonally, approximately through the middle of the core. See Table 17 for sample depths and stratigraphy. Scales: whole core diameter = 85 mm; core plug diameter = 20 mm

Table 20. Rock mechanical properties and bulk density for the diamictite, two shales and three sandstones from Barnicarndy 1. Mode of failure is also noted. Samples should fail in shear for an ideal test; where axial splitting occurs, rock strength can be over-estimated. Abbreviations: E, Young's modulus; v, Poisson's ratio. The data in bold (3412) are from a low quality test and sample 3428 is a repeat of that test. Modified from Jarrett et al. (2020)

GSWA no.	*CSIRO no.*	*Stratigraphic unit*	*Rock type*	*Depth (m)*	*Bulk density (g/cc)*	*UCS (MPa)*	*E*	*v*	*Failure*
247924	3413	Grant Group	Compact diamictite	725.00	2.41	55	9.5	0.12	Ax Sp/ Shear
247925	3381	Barnicarndy Fm.	Clean sandstone	1127.00	2.02	17.1	2.8	0.14	Shear
247926	3415	Samphire Marsh Mbr	Compact shale	2269.50	2.58	60.5	5.7	0.07	Ax Sp
247927	**3412**	**Fly Flat Mbr**	**Clean sandstone**	**2316.80**	**2.53**	**140.5**	**26.1**	**0.09**	**Ax Sp**
247927 (repeat)	3428	Fly Flat Mbr	Clean sandstone	2316.80	2.52	239.1	35.2	0.14	Shear
247928	3417	Fly Flat Mbr	Compact shale	2395.70	2.65	84.7	10.1	0.12	Ax Sp
247929	3382	Yapukarninjarra Fm.	Clean sandstone	2530.00	2.45	148.7	25.6	0.14	Shear

Table 21. Ultrasonic velocities calculated from P-wave and S-wave arrivals at about 50% peak strength (axial stress) for the diamictite, sandstones and shales from Barnicarndy 1. Bulk density is corrected for sample deformation to 50% peak stress. Abbreviations: Vp,s, P- and S-wave velocities; E, Young's modulus; v, Poisson's ratio; G, shear modulus; K, bulk modulus. *The data in bold (3412) are from a low quality test and sample 3428 is a repeat of that test. Modified from Jarrett et al. (2020)

GSWA no.	247924	247925	247926	**247927**	247928	247929	247927 (repeat)
CSIRO no.	3413	3381	3415	**3412**	3428	3417	3382
Stratigraphic unit	Grant Group	Barnicarndy Formation	Samphire Marsh Mbr	**Fly Flat Member**	Fly Flat Member	Yapukarninjarra Formation	Fly Flat Member
Rock type	Compact diamictite	Clean sandstone	Compact shale	**Clean sandstone**	Compact shale	Clean sandstone	Clean sandstone
Depth (m)	725.00	1127.00	2269.50	**2316.80**	2395.70	2530.00	2316.80
Axial Stress (MPa)	28.13	8.02	31.75	**73.45**	45.49	68.42	119.08
Bulk Density (g/cm^3)	2.42	2.03	2.60	**2.54**	2.67	2.47	2.54
P-wave velocity Vp (km/s)	3.19	3.53	3.31	**5.21**	3.44	4.76	4.97
S-wave velocity Vs (km/s)	1.86	1.91	1.93	**2.53**	1.94	2.50	2.88
Dynamic Young's Modulus E (GPa)	20.79	19.11	24.08	**43.74**	25.53	40.44	52.46
Dynamic Poisson's Ratio v	0.24	0.29	0.24	**0.35**	0.27	0.31	0.25
Dynamic shear modulus G (GPa)	8.26	7.39	9.69	**16.24**	18.13	35.46	34.80
Dynamic bulk modulus K (GPa)	13.52	15.46	15.56	**47.48**	18.13	35.46	34.80
Vp/Vs	1.72	1.85	1.71	**2.06**	1.77	1.91	1.73
P-wave slowness (us/ft)	95.46	86.39	92.10	**58.47**	88.70	64.02	61.29
S- wave slowness (us/ft)	164.00	159.91	157.88	**120.64**	156.93	121.97	105.98

Table 22. Rock mechanical properties and bulk density for four Grant Group diamictite samples and two Samphire Marsh Member shales from Barnicarndy 1. Abbreviations: E, Young's modulus; v, Poisson's ratio. Mode of failure is also noted. Samples should fail in shear for an ideal test; where axial splitting occurs, rock strength can be over-estimated

CSIRO no.	*GSWA no.*	*Stratigraphic unit*	*Rock type*	*Depth (m)*	*Bulk density (g/cc)*	*UCS (MPa)*	*E*	*v*	*Failure*
3525	250544	Grant Group	compact diamictite	691.00	2.44	57.4	14.3	0.16	Ax Sp/Shear
3527	250545	Grant Group	compact diamictite	745.57	2.46	57.6	108	0.12	Ax Sp/Shear
3529	250546	Grant Group	compact diamictite	799.38	2.46	57.4	6.6	0.09	Ax Sp
3531	250547	Grant Group	compact diamictite	852.69	2.51	48.5	16.7	0.32	Shear
3533	251801	Samphire Marsh Member	compact mudstone	1498.71	2.58	78.1	10.6	0.13	Shear
3535	251802	Samphire Marsh Member	compact mudstone	2098.82	2.68	76.0	9.2	0.12	Shear

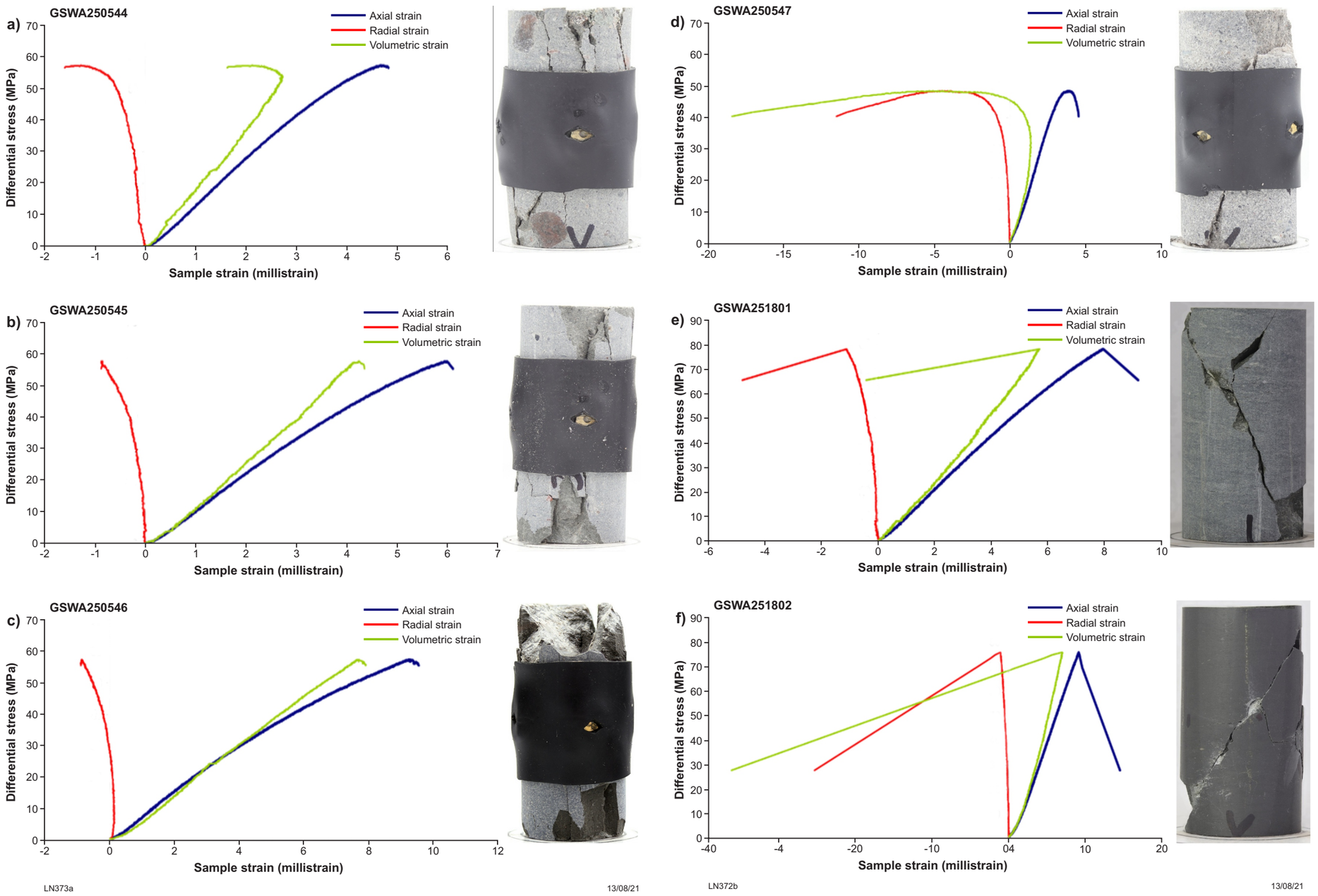

Figure 71. Stress-strain curves for four samples of the Grant Group diamictite and two samples from the Samphire Marsh Member in Barnicarndy 1. After the cut-off point on the curves, strength drops immediately to zero: a) Grant Group GSWA250544 showing a peak UCS just under 60 MPa and dilation only occurring just before failure, with the core plug image showing failure as a mixture of shear and axial splitting that may slightly overestimate rock strength; b) Grant Group GSWA250545 also showing a UCS just under 60 MPa with no dilation before failure and the core plug image showing failure as a mixture of shear and axial splitting that may again slightly overestimate rock strength; c) Grant Group GSWA250546 showing a UCS just under 60 MPa with no dilation occurring before failure and the core plug image showing failure as mainly axial splitting with minor shear that may overestimate rock strength; d) Grant Group GSWA250547 showing a UCS about 50 MPa with significant dilation before failure and the core plug image showing failure in shear indicating the value may be closer to the true UCS; e) Samphire Marsh Member GSWA251801 showing UCS above 70 MPa with no dilation occurring before failure and a core plug image showing failure in shear; f) Samphire Marsh Member GSWA251802 showing a UCS above 70 MPa with no dilation before failure and a core plug image showing failure in shear. Scales: core diameter = 85 mm

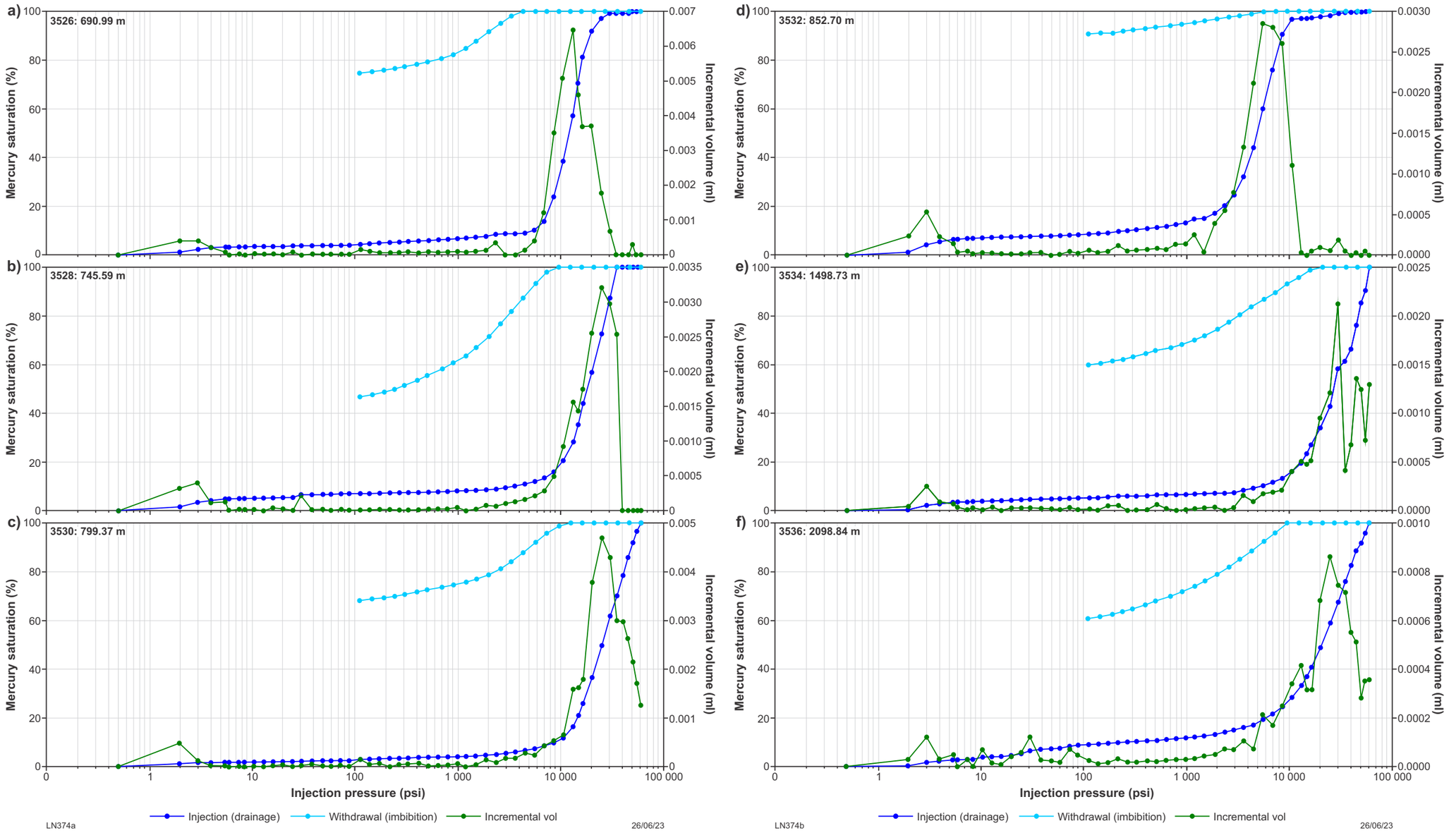

Figure 72. Mercury injection and withdrawal curves for: a) Grant Group diamictite sample 3526 (GSWA 250544) with estimated threshold pressure of 6889 psi; b) Grant Group diamictite sample 3528 (GSWA 250545) with estimated threshold pressure of 8586 psi and full intrusion not completed at the highest pressures; c) Grant Group diamictite sample 3530 (GSWA 250546) with estimated threshold pressure of 10 585 psi and full intrusion not completed at the highest pressures; d) Grant Group diamictite sample 3532 (GSWA 250547) with estimated threshold pressure of 2346 psi; e) Nambeet Formation shale sample 3534 (GSWA 251801) with estimated threshold pressure of 10 587 psi and full intrusion not completed at the highest pressures; f) Nambeet Formation shale sample 3536 (GSWA 251802) with estimated threshold pressure of 6888 psi and full intrusion not completed at the highest pressures

Using the provided *P–T* conditions (Table 23), along with estimated fluid density and gas density, the CH_4-brine interfacial tension can be calculated using the approach of Firoozabadi and Ramey (1988). Inserting these values into industry standard nomograms (e.g. Schowalter, 1979) results in large potential CH_4 column heights for all these samples (Table 24). The results here assume that the in situ system is fully water wet and that there are no changes in contact angle from this initial state.

Using the given *P–T* conditions (Table 23), the CO_2-brine interfacial tension (IFT) can be calculated from the data of Pereira et al. (2016) among many options. There is some variability between research groups on exact values of CO_2 IFT and their variation with temperature and pressure, although a cross-check with the results of Bachu and Bennion (2009) gave similar numbers. Inserting these values into industry standard nomograms results in large potential CO_2 column heights for these samples (Table 24). One should bear in mind that under some of the in situ *P–T* conditions assumed, the CO_2 could be in a gaseous/liquid phase rather than super-critical. One further assumption here is that there is no change in contact angle for the CO_2-brine system.

All these samples are able to seal very large gas columns for both CO_2 and CH_4 under the assumptions used for the given *P–T* conditions. Although the pressure and temperature data are estimates, small variations in these numbers do not significantly affect the seal capacities calculated. For comparisons between laboratory and field measurements, the numbers given refer to the total gas column height the seal could hold back in a static situation. One should also bear in mind the scale issue and consider whether MICP measurements on 1 cm scale samples are fully representative of a seal that covers many square kilometres in area and is potentially tens to hundreds of metres thick. This is always going to be a valid question especially given shale heterogeneity and the potential presence of fractures and faults. Finally, if the situation is dynamic, i.e. the trap is filling faster than it is leaking, then a column height can exceed measured static capillary pressure and associated column height estimations.

Bulk density

The bulk density of Barnicarndy 1 rock samples was measured via helium pycnometry (Grosjean et al., 2020a,b). In total, 197 Barnicarndy 1 samples between 195 and 2679 m were analysed for bulk density. These measured bulk density values are plotted against downhole depth in Figure 73a and a summary of statistical data is presented in Table 25. Full details on each sample and measured values can be found in Appendix 24 (Grosjean et al., 2020a).

Bulk densities are observed to range between 2.50 and 2.88 g/cm^3 with a mean value of 2.69 g/cm^3 (SD = 0.06 g/cm^3). The minimum value of 2.50 g/cm^3 at 2574.2 m is for a sandstone in the Yapukarninjarra Formation. Mineral assemblages derived from XRD analysis show that this sandstone is composed almost exclusively of quartz (97%) and, additionally, hosts the lowest concentration of iron (III) oxide. The bulk density of pure quartz is much higher at 2.65 g/cm^3 but factors such as porosity and degree of cementation have more control on bulk densities than mineral composition (Schön, 2015).

Of all stratigraphic units, the Grant Group displays the highest variability in measured bulk density, with values ranging from 2.52 to 2.88 g/cm^3 and an SD of 0.09 g/cm^3. The Barnicarndy and Nambeet formations display very little density variation, internally and between each formation, with mean values of 2.69 g/cm^3 (SD = 0.04 g/cm^3) and 2.70 g/cm^3 (SD = 0.04 g/cm^3), respectively. Measured density of the undivided pre-Canning basement sedimentary rocks of the Yeneena Basin are on average slightly higher when compared to the other stratigraphic units (>2.7 g/cm^3). This is likely a consequence of their greater depth of burial and low grade metamorphism, and from the presence of calcite and dolomite in these sediments (Schön, 2015), alongside quartz and mica.

Magnetic susceptibility

Magnetic susceptibility measurements were acquired on 142 core samples between 583.5 and 2679.1 m using a Bartington MS3 system equipped with a MS2K sensor. Each magnetic susceptibility value consists of an average of 10 consecutive measurements made across the core. These measured magnetic susceptibility values are plotted against downhole depth in Figure 73b. A summary of statistical data is presented in Table 26. See Appendix 24 for full details on each sample and measured values (Grosjean et al., 2020a).

Magnetic susceptibility corresponds to the ability of a material to be magnetized in an external field and depends upon the mineral composition of the material being diamagnetic, paramagnetic or ferromagnetic. Results greater than 5 x 10^{-3} SI are greatly controlled by the presence of ferromagnetic minerals while paramagnetic minerals have low values around 5 x 10^{-4} SI. Diamagnetic minerals such as quartz, calcite or dolomite have weak, negative readings, about -1 x 10^{-5} SI (Ellwood et al., 1993).

Magnetic susceptibility values in Barnicarndy 1 are either negative or very low ranging from -1.67 to 0.99 x 10^{-3} SI with a mean value of -0.03 x 10^{-3} SI (SD = 0.32 g/cm^3). This is consistent with the well being dominated by diamagnetic to paramagnetic mineral assemblages.

The Grant Group shows the highest variability in measured magnetic susceptibilities with values ranging from -1.48 to 0.99 x 10^{-3} SI. The Barnicarndy and Yapukarninjarra formations consist mostly of diamagnetic minerals with mostly negative values for magnetic susceptibilities. With an average magnetic susceptibility value of 0.1 x 10^{-3} SI, the Nambeet Formation is dominated by paramagnetic minerals.

Table 23. In situ *P–T* conditions estimated for the Grant Group diamictite and Samphire Marsh Member shales in Barnicarndy 1. ρw is the density of water under in situ conditions assuming 50 000 ppm total dissolved solids and ρg is the density of pure CH_4 and CO_2 at the temperatures given. Temperature estimated from 27 °C average surface temperature plus 37 °C/km

CSIRO no.	*GSWA no.*	*Depth (m)*	*Pressure (psi)*	*Temp (°C)*	*ρw (g/cc)*	*ρg CH_4 (g/cc)*	*ρg CO_2 (g/cc)*
3526	250544	690.99	981	53	1.020	0.043	0.159
3528	250545	745.59	1059	55	1.020	0.047	0.176
3530	250546	799.37	1135	57	1.020	0.050	0.193
3532	250547	852.68	1211	59	1.020	0.053	0.210
3534	251801	1498.73	2129	82	1.020	0.086	0.405
3536	251802	2098.84	2981	105	1.020	0.109	0.477

Table 24. Air-mercury capillary threshold pressures for four diamictite samples and two Nambeet Formation shale samples from Barnicarndy 1, with calculated interfacial tensions (IFT) and column heights for pure CH_4 and CO_2 for in situ *P–T* conditions (Table 20). Column heights have been rounded down to the nearest 10 m

CSIRO no.	*GSWA no.*	*Depth (m)*	*Air-Hg Pth (psi)*	*CH_4 IFT (dynes/cm)*	*CO_2 IFT (dynes/cm)*	*CH_4 column height (m)*	*CO_2 column height (m)*
3526	250544	690.99	6889	61.9	43	820	650
3528	250545	745.59	8586	61.2	41	1020	790
3530	250546	799.37	10 585	60.5	39	1250	940
3532	250547	852.68	2346	59.8	38	270	200
3534	251801	1498.73	10 587	53.0	30	1130	970
3536	251802	2098.84	6888	47.7	28	680	670

Table 25. Measured bulk density statistics for samples from Barnicarndy 1

Property	*Stratigraphic unit*	*N*	*Min*	*Max*	*Mean*	*Std Dev*
Bulk density (g/cm^3)	All	197	2.50	2.88	2.69	0.06
	Grant Group	42	2.52	2.88	2.68	0.09
	Barnicarndy Formation	41	2.59	2.80	2.69	0.04
	Nambeet Formation	93	2.61	2.82	2.70	0.04
	Yapukarninjarra Formation	17	2.50	2.75	2.67	0.08
	Undivided Yeneena Basin	4	2.72	2.82	2.77	0.04

N = # of samples, Min = minimum value for set, Max = maximum value for set, Std Dev = standard deviation

Table 26. Measured magnetic susceptibility statistics for samples from the Barnicarndy 1 well

Property	*Stratigraphic unit*	*N*	*Min*	*Max*	*Mean*	*Std Dev*
Magnetic susceptibility (x10^{-3} SI)	All	142	-1.67	0.99	-0.03	0.32
	Grant Group	16	-1.48	0.99	-0.29	0.64
	Barnicarndy Formation	37	-1.67	0.05	-0.19	0.34
	Nambeet Formation	75	-0.08	0.24	0.10	0.08
	Yapukarninjarra Formation	11	-0.10	0.09	-0.03	0.06
	Undivided Yeneena Basin	3	-0.06	0.11	0.04	0.09

N = # of samples, Min = minimum value for set, Max = maximum value for set, Std Dev = standard deviation

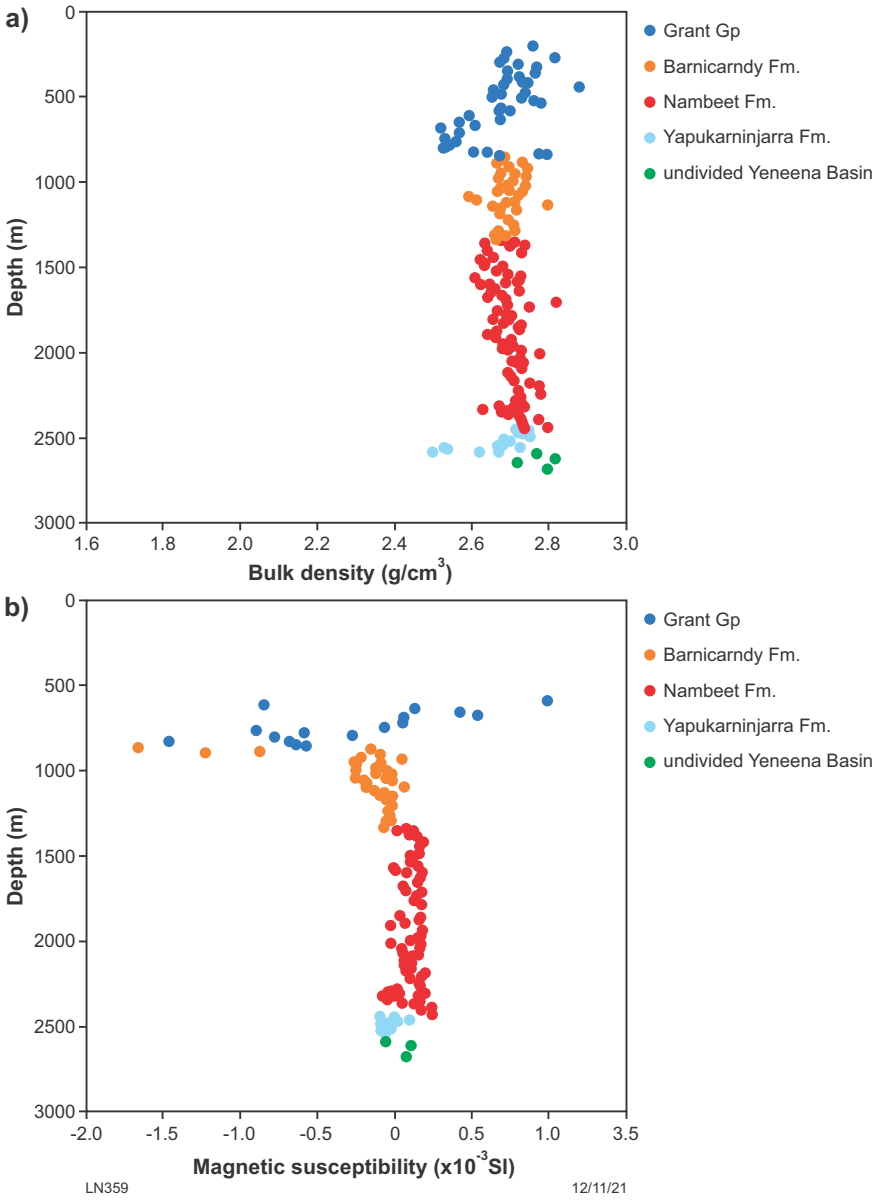

Figure 73. a) Bulk density vs depth; b) magnetic susceptibility vs depth with colour-coded stratigraphy

Synthesis and key geoscientific outcomes

The value in drilling a continuously cored deep stratigraphic well through the entire Barnicarndy Graben succession and the underlying Yeneena Basin is clearly demonstrated by the multiple and wide-ranging geoscientific outcomes that have arisen not only from the seismic and wireline characterizations but also the subsequent post-well analytical program. From the discovery of anomalously high seismic velocities, which will assist in the accurate prognosis of future drilling programs, to discoveries in the Ordovician palynoflora allowing a clearer understanding of land-plant evolution, this fully cored geological section will continue to reveal key contributions to the geological knowledge of the Canning Basin and the Ordovician Period well into the future.

Anomalous seismic velocity

The identification of anomalously high seismic velocities for the Grant Group and Barnicarndy Formation resulted in new insights on the burial history of the western Canning Basin. This also provides data that will allow greater accuracy in future seismic depth predictions in this region. The high seismic velocities corroborate the thermochronology and organic thermal maturity findings indicative of a much deeper burial for the Barnicarndy Graben than is seen currently and a large amount of overlying post-Carboniferous sedimentary section has been eroded. With the depth to pre-Canning Basin basement prognosis 385 m shallower than actual, depths to primary targets risk exceeding project budgets. The new velocity information can now assist in accurate depth prognosis for future drilling programs in the Barnicarndy Graben and possibly the Samphire Graben.

Type sections for new Canning Basin stratigraphic units

The continuous core from Barnicarndy 1 provides the type sections for two new formations within the Canning Basin stratigraphy. The two new formations lie below and above the Nambeet Formation within the Barnicarndy Graben, with the 490 m thick Barnicarndy Formation sitting conformably above the Samphire Marsh Member and the 142 m thick Yapukarninjarra Formation conformably below the Fly Flat Member. The definition cards for these two formations are included here (Appendices 2, 3).

Diverse fossil assemblages

Initial work on Barnicarndy 1 has indicated a rich, diverse macrofossil assemblage, particularly within the Nambeet Formation. The diversity of the macrofossil assemblage identified in the Nambeet Formation of Barnicarndy 1 shows obvious similarities to other faunas seen in the Ordovician of the Canning Basin and further afield in basins across northern Australia, and will therefore provide an extensive dataset for future correlations (Martin et al., 2021b). The accompanying age data provided by CA-IDTIMS geochronology, in Barnicarndy 1 and other Canning Basin wells, will also aid in more precisely tying Canning Basin biozones to the geological timescale.

The Ordovician microfossil assemblages are also significant, providing invaluable insights both into the age of the sedimentary succession in Barnicarndy 1, and more broadly on the development of the Canning Basin. A new species, *Juanognathus*? *denticulatus* (Zhen et al., 2022) and several age-diagnostic taxa were recovered within the diverse conodont assemblage, with the potential to improve the biostratigraphy of this section and correlation to other equivalent-aged units with further sampling and study.

For the pre-Permian palynology, the utility of *A. grootaertii* as an indicator of late Tremadocian–early Floian assemblages is reinforced by the co-occurrence of conodont faunas of the same age in Barnicarndy 1 (Foster et al., 2021). Similarly, the late Tremadocian–early Floian (Early Ordovician) age of *Polygonium canningianum, Micrhystridium infrequens*, and *Lophosphaeridium aequicuspidatum*, which were reported from the Nambeet Formation in Acacia 2 (Foster and Wicander, 2015), is confirmed here. Prior to these studies, these aforementioned species had only been reported from Lower–Middle Ordovician (Willara, Goldwyer and Nita formations) assemblages in the Canning Basin. Finally, the recovery of 'cryptospores' similar to those already reported from equivalent-aged units in Samphire Marsh 1 (Strother and Foster, 2021) and Theia 1 (Foster et al., 2021) is significant, with these spores postulated as representing evidence for the evolution of terrestrial plants.

Geochronology

Fifty bentonite beds were identified on site during the drilling of Barnicarndy 1. Only 10% of the sampled beds yielded euhedral zircons and only two of the four CA-IDTIMS dates match previous geochronology from samples in Olympic 1. This, however, provides a chronostratigraphic marker horizon within the Samphire Marsh Member that can be traced from the Barnicarndy Graben to the Broome Platform.

Detrital zircon geochronology provides constraints on sediment provenance and maximum depositional ages for all the formations encountered in Barnicarndy 1. This assisted in the characterization of the new Barnicarndy and Yapukarninjarra formations.

Thermochronology

Uranium–Thorium/Helium [(U–Th)/He] thermochronology of zircon and apatite (Appendix 12; Danišík, 2021) calculated the thickness of missing section above the various stratigraphic units. The majority of the missing 2–3 km was removed by uplift and erosion of the Barnicarndy Graben since the Permian. This corroborates well with interpretations of maturity based on vitrinite and vitrinite equivalence studies, as well as seismic velocity anomalies (Zhan, 2021).

Chemostratigraphy

Chemostratigraphy over the Barnicarndy 1 cored interval defined six major chemostratigraphic boundaries and nine distinct packages. The unique Ordovician chemostratigraphic signature suggests a differing sediment provenance. The potential for correlation with the global

carbon isotope curves of Argentina and China have been proposed, which leads to the hypothesis that the Yapukarninjarra Formation may extend into the Cambrian.

Geochemical signatures

The biomarker and isotopic signatures from the core extracts in Barnicarndy 1 distinguish between the different organic matter contributions to the Samphire Marsh and Fly Flat members of the Nambeet Formation. These unique organic sources show a higher contribution from bacteria (including cyanobacteria and green sulphur bacteria) in comparison to algal lipids, a feature observed in Ordovician-sourced oils of the Canning Basin.

Thermal maturity

Measured mean maximum vitrinite reflectance (Rv) and vitrinite reflectance-equivalent (Rve) calculated from graptolite data indicate that the sedimentary section in Barnicarndy 1 has reached the oil window at a depth of about 500 m (i.e. Rv >0.55%) in the Grant Group, and the gas window is reached at a depth of about 2000 m (i.e. Rv >1.3%) in the Samphire Marsh Member of the Nambeet Formation.

Hydrogen and helium system

Paleo-hydrogen and -helium systems have been identified by their occurrence in fluid inclusions, measured by FIS studies in Barnicarndy 1 (Appendix 20; Fluid Inclusion Technologies, 2020). These gases, among others are released from core samples during crushing and measured as a millivolt response for individual or a ratio of ionic species from FIS mass spectrometric analysis. Barnicarndy 1 has two main intervals of enhanced hydrogen and one interval of enhanced helium (Fig. 66).

The two main intervals of enhanced hydrogen abundance occur from 827 to 1354 m and from 2180 to 2640 m. The shallow interval is primarily within the Barnicarndy Formation but includes the basal part of the Grant Group whereas the deeper interval includes the basal Samphire Marsh Member, the entire Fly Flat Member and Yapukarninjarra Formation and the weathered part of the Yeneena Basin section. The only interval of high helium is coeval with the deeper hydrogen occurrence. This co-variance of hydrogen and helium near the bottom of the well suggests a common source, possibly related to the radioactive decay of uranium and thorium bearing minerals that produce helium as a daughter product, and can produce hydrogen via radiolysis of water. The nearby Mount Crofton Granite is notably radiogenic (McNaughton and Goellnicht, 1990). The radiation from K-bearing minerals can also facilitate the radiolysis of water to produce hydrogen. The absence of significant helium in the Barnicarndy Formation suggests a redox process of iron oxidation and reduction of water to produce hydrogen in this shallower interval. It also suggests an effective seal within the Nambeet Formation partitioning the helium- and hydrogen-bearing fluids in lower reservoirs from the hydrogen-bearing fluids in the Barnicarndy Formation.

Although the FIS data do not provide quantitative values for helium or hydrogen, they do indicate a previously active system for these rare gases, which has provided the required source, migration pathway and seal, at some time in the past. Additional quantitative and isotopic analysis is required to determine the gas source characterization and timing of emplacement. Petroleum inclusions identified in four sandstone samples in the Barnicarndy Formation also indicate previous hydrocarbon migration. While this site was chosen due to a lack of structural trapping, this may bode well for elsewhere in the Barnicarndy Graben if there is a structural closure.

Carbon sequestration and underground hydrogen storage potential

Although remote, the region contains existing and potential for future large CO_2 emitters. Major mining projects include Telfer, with Haverion being developed to the east, and the likelihood of future developments in the area is high. The Telfer natural gas pipeline is located within 500 m of the Barnicarndy 1 drill site. In addition, the proposed Asian Renewable Energy Hub, to be centred 140 km to the northwest of Barnicarndy 1 (Fig. 74), aims to produce 26 000 megawatts of renewable energy (wind and solar) for the large-scale production of green hydrogen. For these reasons, knowledge of potential targets for both carbon capture and underground storage (CCUS) and underground hydrogen storage in the region are important.

Barnicarndy 1 has two distinctive reservoir-seal pairs that have potential for future sequestration and storage of CO_2 or other gases. The deeper reservoir-seal pair includes a sandstone reservoir section in the Yapukarninjarra Formation, which is sealed in part by the tight sandstones of the Fly Flat Member but primarily by the over 900 m thick mudstone section of the Samphire Marsh Member. The second and most prospective reservoir-seal pair is the Barnicarndy Formation sandstone reservoir section and the overlying Grant Group diamictite seal. The reservoir and seal characteristics of these units are discussed in the routine core and rock properties analysis sections as well as the petrophysical evaluation section.

The Yapukarninjarra Formation reservoir section is 114 m thick from 2471 to 2585 m, with 33 m net porous reservoir for a net to gross of 12.1%. Estimated salinity is approximately 116 000 ppm based on wireline logs. Routine core analysis of seven samples indicates permeability in the range of 0.001 – 40.5 mD (Kair) and a porosity range from 1.0 to 18.4% (Appendix 21). Seal capacity is mainly focused on the Samphire Marsh Member with ultra-low permeameter tests of a sample at 2269.22 m providing a mean permeability over three measurements of 0.00020 mD. A shale sample from the Fly Flat Member at 2395.95 m provided even tighter results by the same method with mean permeability of 0.00013 mD. Even the sandstone sample from the Fly Flat Member at 2316.75 m yielded an ultra-tight permeability of 0.00597 mD. Seal capacity evaluation of two samples from the Samphire Marsh Member indicate the ability to hold CH_4 or CO_2 gas columns in the range of 680–1130 m and 670–970 m, respectively. It is interesting to note the shallower sample at 1498.73 m depth can hold the higher gas column for both CH_4 and CO_2.

Although the reservoir characteristics are quite poor for the Yapukarninjarra–Nambeet reservoir seal pair, the seal component is very good. The depth of this reservoir-seal pair, combined with a tight reservoir and ultra-tight seal, while not optimal for injection, storage or production at this location, may prove to be better elsewhere at shallower depths in the graben.

The Barnicarndy–Grant Group reservoir-seal pair has much better quality reservoir characteristics encompassing the entirety of the Barnicarndy Formation and the lowermost re-worked sandstone interval of the basal Grant Group. This reservoir is 512.0 m thick from 825.0 to 1337.0 m, with a net porous reservoir of 500.8 m, average porosity of 16.5% and net to gross of 98%. Permeability and porosity values from 10 routine core analysis samples over the reservoir interval ranged from 41.5 to 3836.0 mD (Kair) and 15.4 to 24.7% porosity (Appendix 21).

Seal capacity results for three of the Grant Group diamictite samples from the second subset of analyses indicate capillary threshold pressure estimates of about 7000 to about 10 000 psi. These are consistent with results from an air-mercury threshold pressure range of about 6900–8600 psi of one diamictite sample at 725 m in the first subset tested by Jarrett et al. (2020). These threshold pressures equate to significant gas column heights of 820–1250 m for CH_4 and 650–940 m for CO_2.

It should be noted that the diamictite and mudstone samples were not preserved from desiccation before testing, therefore will not provide high confidence results for the evaluation of a regional seal capacity. Loss of in situ pore fluids can make shale stronger and stiffer compared to its subsurface behaviour; as such, the tests here probably represent significant over-estimates of rock strength and stiffness (Young's modulus) compared to an in situ, fully water saturated equivalent material.

A number of factors are required in addition to the downhole petrophysical characteristics of reservoir and seal for successful storage of CO_2 or other gases. The greater than 800 m depth of the reservoir component of the Barnicarndy Formation–Grant Group reservoir-seal pair at the drill site is beneficial, as this is considered the minimum depth for CO_2 storage and sequestration assuming average temperature and pressure conditions (Heinrich et al., 2004). The depth to the top of the reservoir is likely to increase into the depocentre of the graben to the north of Barnicarndy 1, but further seismic and drilling would be required to test this assumption. It is also possible that similar stratigraphic and reservoir-seal potential exists in the Samphire Graben to the north. Additional seismic along the axis of the Barnicarndy Graben and continuing north across the on-trend Samphire Graben, followed by stratigraphic drilling, would help define the gas storage potential of that area.

Sequence stratigraphy

An integrated sequence stratigraphic assessment was completed on the Barnicarndy 1 cored interval from 580 to 2680 m (Appendix 25). Using the third order sequence as the fundamental unit (about 1 Ma), the entire succession is divided into eight sequences based on unit boundaries, gross description, depositional analysis and sequence stratigraphy (Fig. 75). These sub-divisions define the major breaks in sedimentation.

From the oldest to youngest, the basal Canning Basin unconformity marks a first order sequence boundary (about 100 Ma) separating the underlying Yeneena Basin from the Yapukarninjarra Formation. The second sequence boundary lies within the Yapukarninjarra Formation, separating a highstand systems tract (HST) near the base from a transgressive system tract (TST) occupying the upper part of the formation. This boundary has implications for further subdivision of the formation. A transgressive surface of erosion (TSE) defines the boundary between the Yapukarninjarra Formation and the overlying Fly Flat Member of the basal Nambeet Formation. The TST continues up to a marine flooding surface (MFS) within the Fly Flat Member, which demarcates the inflection point into the overlying HST for the upper Fly Flat member.

The third sequence boundary occurs near the top of the Fly Flat Member, overlain by a TST that extends upward to a second MFS within the middle of the Samphire Marsh Member of the Nambeet Formation. The MFS is overlain by a HST, which extends through the upper Samphire Marsh Member and into the Lower Barnicarndy Formation. The fourth sequence boundary separates the lower and upper Barnicarndy Formation. A TST in the upper Barnicarndy Formation terminates at a first order magnitude sequence boundary separating the Ordovician sequence from the Carboniferous–Permian sequence. The sixth and seventh sequence boundaries are tentatively identified within the upper Grant Group, acknowledging the complexities of interpreting sequence stratigraphy within glacigene successions. A final first order sequence boundary marks the contact between the Grant Group succession and the overlying Cenozoic section at 96 m.

Suggested further work relating to this sequence stratigraphic analysis includes additional ichnology studies over the Samphire Marsh Member, additional source rock sampling within this well, a regional sequence stratigraphic study in neighbouring Canning Basin tectonic components and seismic stratigraphic studies.

Structural history

The Barnicarndy Fault, which defines the western margin of the Barnicarndy Graben, is coincident with the more extensive Rudall internal major crustal boundary of Martin et al. (2021a; Fig. 74). In onshore Western Australia this major crustal boundary extends southeast from the coastline at Eighty Mile Beach along the western margins of both the Samphire Graben and Barnicarndy Graben, before transecting the Paleoproterozoic to Mesoproterozoic Rudall Province. It continues southeast beneath the Tabletop Shelf of the Canning Basin and the Officer Basin, to finally merge with the Musgrave south major crustal boundary. In the Barnicarndy Graben region, the Rudall internal major crustal boundary sub-divides the Paterson Orogen into a predominantly copper endowed region to the west and a gold endowed region to the east (Fig. 74). This gold-copper differentiation suggests an intrinsic relationship to basement source composition and migration pathways created by major crustal boundaries and their associated splays.

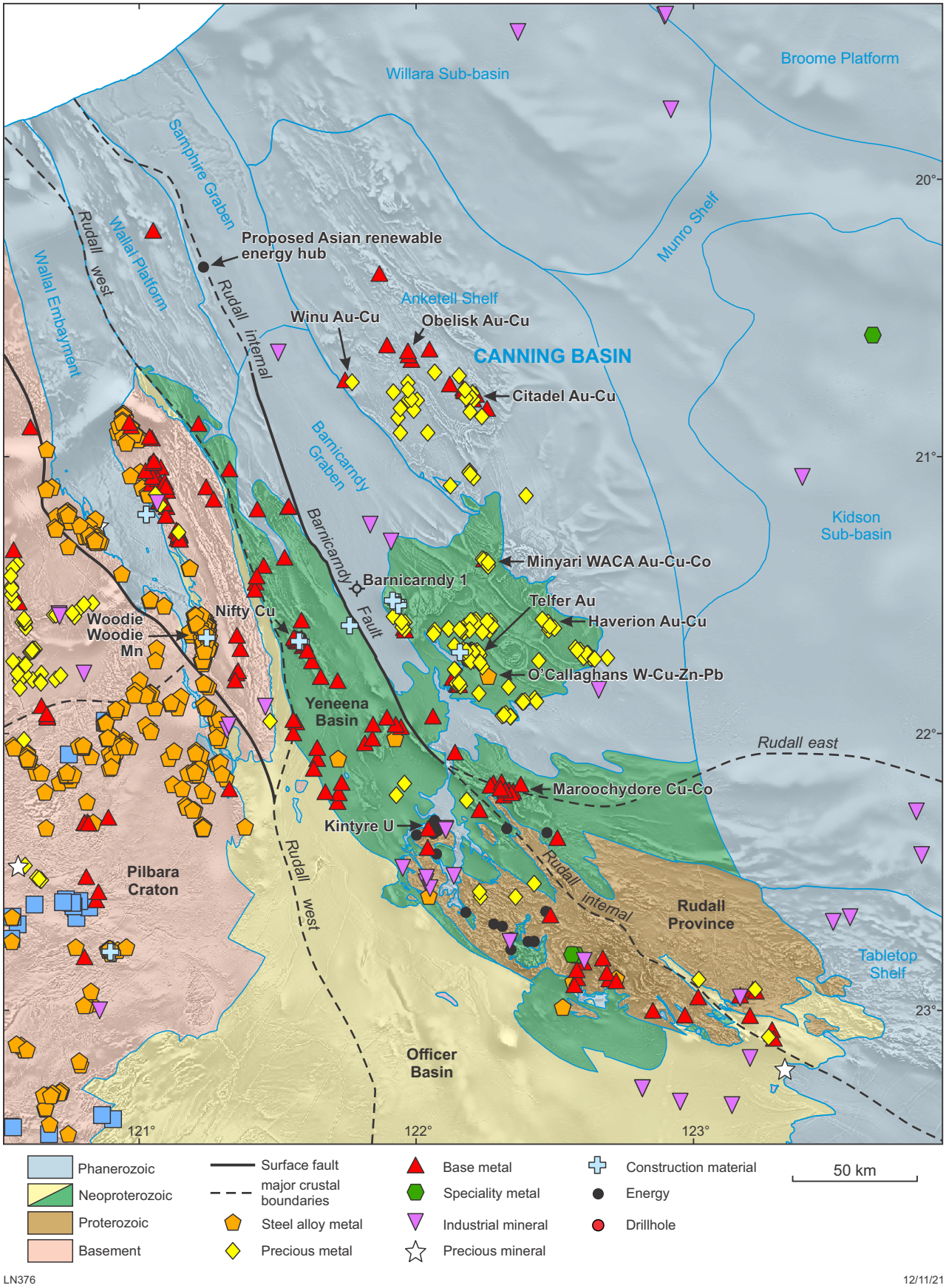

Figure 74. Regional map of part of the Paterson Orogen with MINEDEX mineral occurrences, select mineral deposits, major crustal boundaries and Canning Basin tectonic subdivision

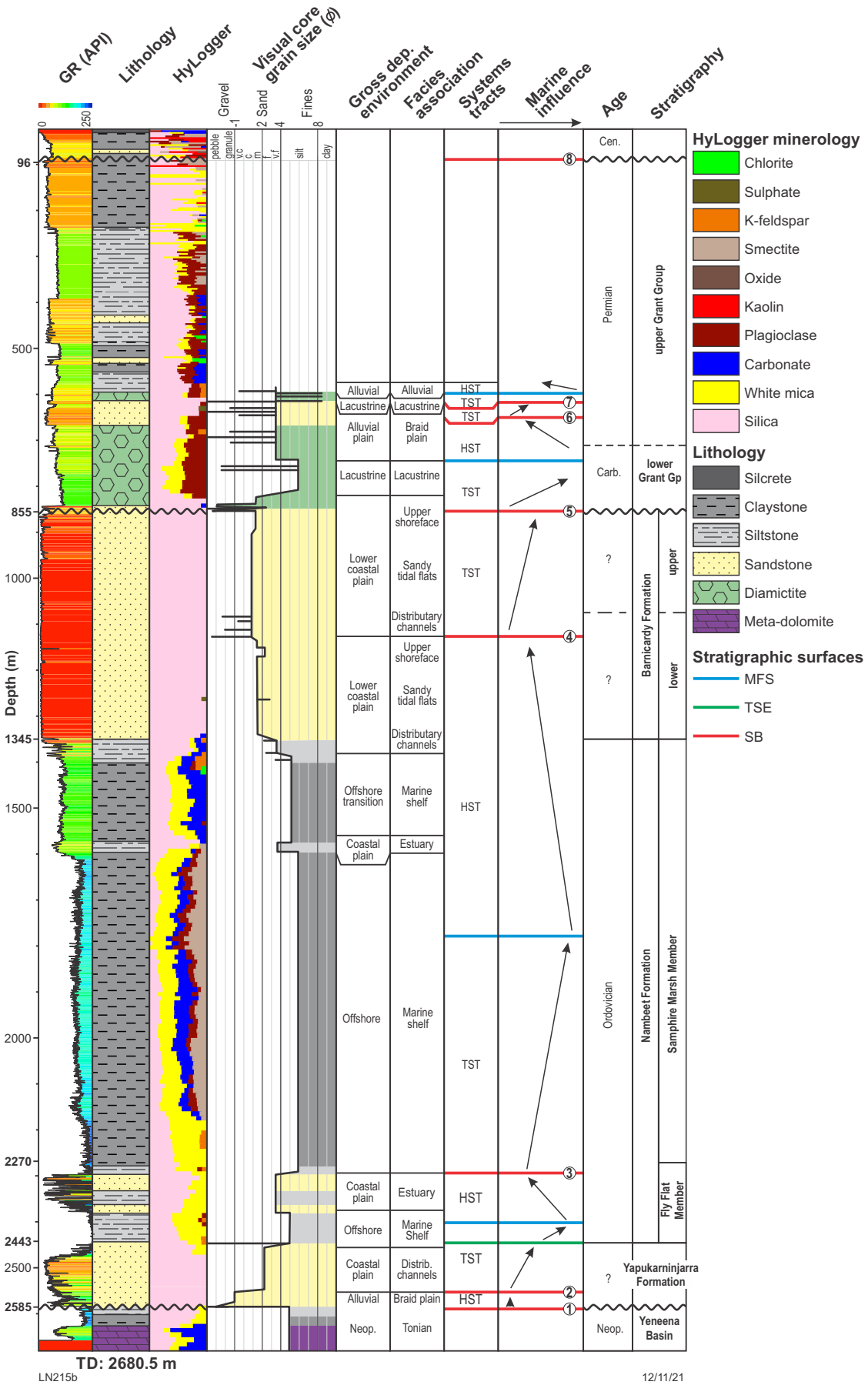

Figure 75. Depositional and sequence stratigraphic analysis including GR, lithology, HyLogger mineralogy, visual core grain size, gross depositional environment, facies associations, system tracts, marine influence, age and stratigraphy (from Appendix 25). Abbreviations: MFS, marine flooding surface; TSE, transgressive surface of erosion; SB, sequence boundary (numbered sequentially); HST, highstand systems tract; TST, transgressive systems tract

The thickness of the Lower to Middle Ordovician section of the Barnicarndy Graben suggests active fault movement driving subsidence early in Canning Basin history. In addition, three lines of evidence, including vitrinite reflectance and vitrinite reflectance equivalence data (Appendix 19; Ranasinghe and Crosdale, 2020), seismic velocity anomalies (Zhan, 2021) and thermochronology (Danišík, 2021), all point to significant post-early Permian uplift and erosion of the Barnicarndy Graben succession. The thermochronology, specifically, suggests that up to 3 km may have been removed, likely related to late fault reactivation. Although the late uplift event is not well dated, it may at least in part be associated with the Upper Triassic Fitzroy Transpression documented elsewhere in the basin. This event is broadly coincident with the extrusion of mafic volcanics in the Sapphire Graben (feeder sills dated at 224.19 ± 2.79 Ma; Mory et al., 2017) and possibly the Triassic volcanics offshore in the Rowley and Bedout sub-basins. This may have implications on paleogeographic reconstructions and the hypothesized triple junction of (MacNeill et al., 2018). Paschke et al. (2018) have proposed this failed orthogonal rifting to the East Gondwana Interior rift was modified by a mid-Permian extensional event. Repeated reactivation and magmatic activity along the Rudall internal major crustal boundary and associated faults has significant implications for continued or renewed migration of deep-seated mineralizing fluids into the Barnicarndy Graben and surrounding terrain during the history of the Canning Basin. Other syn-depositional faults systems, for example the Admiral Bay Fault Zone (Connor, 1990), are specially and genetically connected to major mineral deposits elsewhere in the Canning Basin.

Acknowledgements

Geoscience Australia provided the funding for this stratigraphic drilling program and post well analysis through the Exploring for the Future Program and the Geological Survey of Western Australia also provided funding for post-well analysis through the Exploration Incentive Scheme. Consultation with the Western Desert Lands Aboriginal Corporation provided the following name changes: Waukarlycarly 1 to Barnicarndy 1, Waukarlycarly Embayment to Barnicarndy Graben and West Waukarlycarly Fault to Barnicarndy Fault.

References

Alexander, R, Noble, RA and Kagi, RI 1987, Fossil resin biomarkers and their application in oil to source rock correlation, Gippsland Basin, Australia: The APPEA Journal, v. 27, p. 63–72.

Alavi, SN 2013, Structure, stratigraphy and petroleum prospectivity of the Waukarlycarly Embayment, Canning Basin, Western Australia: Geological Survey of Western Australia, Record 2013/10, 36p.

Allen, KA, Eder, J and Tipps, RD 1971, Final report Canning Basin Anketell seismic survey (projects 277 & 283): West Australian Petroleum Pty Ltd: Geological Survey of Western Australia, Statutory petroleum exploration report S614 A1 (unpublished), 152p., <www.dmirs.wa.gov.au/wapims>.

Anand, RR 2004, Weathering history, landscape evolution and implications for exploration, *in* Regolith landscape evolution across Australia: a compilation of regolith landscape case studies with regolith landscape evolution models *edited by* RR Anand and P de Broekert: Cooperative Research Centre for Landscape Environments and Mineral Exploration (CRC LEME), Perth, Western Australia, p. 2–40.

Antia, J 2020, Petrographic analysis of rotary sidewall cores, Waukarlycarly-1, Canning Basin, Australia: Core Laboratories, Houston, Texas: Geological Survey of Western Australia, Statutory petroleum exploration report G004185 A5 (unpublished), 95p., <www.dmirs.wa.gov.au/wapims>.

Bacchin, M, Wynne, P and Courtney, D 2006, Index of gravity surveys: first edition: Geoscience Australia, Record 2006/001, 440p.

Bachu, S and Bennion, DB 2009, Interfacial tension between CO_2, freshwater and brine in the range of pressure from 2 to 27 MPa, temperature from 20 to 125°C and water salinity from 0 to 334 000 mg·L^{-1}: Journal of Chemical Engineering Data, v. 54, p. 765–775.

Backhouse, J 2020, Waukarlycarly 1: palynology of 7 samples: Geological Survey of Western Australia, Paleontology Report 2020/47, 5p.

Backhouse, J and Mory, AJ 2020, Mid-Carboniferous – Lower Permian palynology and stratigraphy, Canning Basin, Western Australia: Geological Survey of Western Australia, Report 207, 133p.

Bagas, L 2000, Paterson, WA Sheet 3354: Geological Survey of Western Australia, 1:100 000 Geological Series.

Bagas, L 2004, Proterozoic evolution and tectonic setting of the northwest Paterson Orogen, Western Australia: Precambrian Research, v. 128, p. 475–496, doi:10.1016/j.precamres.2003.09.011.

Bagas, L and Nelson, DR 2007, Provenance of Neoproterozoic sedimentary rocks in the northwest Paterson Orogen, Western Australia, *in* Proceedings of the Central Australian Basins Symposium (CABS), Alice Springs, Northern Territory, 16-18 August 2005 *edited by* TJ Munson and GJ Ambrose: Northern Territory Geological Survey, Special Publication, p. 1–10.

Bailey, AHE, Jarrett, AJM, Tenthorey, E and Henson, PA 2021, Understanding present-day stress in the onshore Canning Basin of Western Australia: Australian Journal of Earth Sciences, v. 68, no. 6, p. 818–838, doi:10.1080/08120099.2021.1879265.

Beard, JS 1973, The elucidation of paleodrainage patterns in Western Australian through vegetation mapping: Vegmap Publications, Applecross, Western Australia, Vegetation Survey of Western Australia Occasional Paper 1, 17p.

Boreham, CJ, Edwards, DS, Czado, K, Rollet, N, Wang, L, van der Wielen, S, Champion, D, Blewett, R, Feitz, A and Henson, PA 2021a, Hydrogen in Australian natural gas: occurrences, sources and resources: The APPEA Journal, v. 61, no. 1, p. 163–191, doi:10.1071/AJ20044.

Boreham, CJ, Edwards, DS, Sohn, JH, Palatty, P, Chen, JH and Mory, AJ 2020, Gas systems in the onshore Canning Basin as revealed by gas trapped in fluid inclusions, *in* Exploring for the Future: extended abstracts *edited by* K Czarnota, IC Roach, ST Abbott, MW Haynes, N Kositcin, A Ray and E Slatter: Geoscience Australia.

Boreham, CJ, Sohn, JH, Cox, N, Williams, J, Hong, Z and Kendrick, MA 2021b, Hydrogen and hydrocarbons associated with the Neoarchean Frog's Leg Gold Camp, Yilgarn Craton, Western Australia: Chemical Geology, v. 575, p. 120098, 23p., doi:10.1016/j.chemgeo.2021.120098.

Brocks, JJ, Grosjean, E and Logan, GA 2008, Assessing biomarker syngeneity using branched alkanes with quaternary carbon (BAQCs) and other plastic contaminants: Geochimica et Cosmochimica Acta, v. 72, no. 3, p. 871–888.

Brooke, W 1987, Annual report Throssell Range project E45/1SA 4 December 1985 to 3 December 1986, Western Mining Corporation Limited, Exploration Division: Western Mining Corporation Limited: Geological Survey of Western Australia, Statutory mineral exploration report A19901, <www.dmirs.wa.gov.au/wamex>.

Chemostrat Australia Pty 2019, Heavy mineral, detrital zircon geochronology and elemental analysis of Samphire Marsh-1: Prepared for Quadrant Energy: Geological Survey of Western Australia, Statutory petroleum exploration report G32893 A1 (unpublished), 7p., <www.dmirs.wa.gov.au/wapims>.

Combaz, A and Peniguel, G 1972, Etude palyno-stratigraphique se l'Ordocicien dans quwlques sondages du Bassin de Canning (Australie Occidentale): Bulletin du Centre de Recherches Pau-SNPA, v. 6, p. 121–167.

Connor, AG 1990, Admiral Bay zinc-lead deposit, *in* Geology of the mineral deposits of Australia and Papua New Guinea *edited by* FE Hughes: Australian Institute of Mining and Metallurgy, Monograph 14, p. 1111–1114.

Cox, GM, Halverson, G, Stevenson, RK, Vokaty, M, Poirier, A, Kunzmann, M, Li, Z-X, Denyszyn, SW, Strauss, JV and MacDonald, FA 2016, Continental flood basalt weathering as a trigger for Neoproterozoic Snowball Earth: Earth and Planetary Science Letters, v. 446, p. 89–99, doi:10.1016/j.epsl.2016.04.016.

Czarnota, K, McIntyre, A, Maidment, D and Neumann, N 2007, Revised geodynamic framework for the Neoproterozoic Paterson Orogen: Deformation in the desert, Alice Springs, Northern Territory, 9–13 July 2007: Specialist Group in Tectonics and Structural Geology, Geological Society of Australia, Deformation in the desert, p. 30.

Czarnota, K, Berner, E, Maidment, DW, Meixner, A and Bagas, L 2009, Paterson Area 1:250 000 scale solid geology interpretation and depth to basement model, explanatory notes: Geoscience Australia, Record 2009/16, 89p.

Danišík, M 2021, Thermochronology of Barnicarndy 1 well (Western Australia) – constraints from zircon and apatite (U–Th)/He dating and thermal history modelling: Geological Survey of Western Australia, Statutory petroleum exploration report G004185 A24 (unpublished), 21p., <www.dmirs.wa.gov.au/wapims>.

Dent, LM and Normore, LS 2017, Assessment of thermal maturity using bitumen, graptolite, and bioclast reflectance: Ordovician Nambeet Formation, Canning Basin: Geological Survey of Western Australia, Report 170, 1111p.

Dewhurst, DN, Jones, RM and Raven, DR 2002, Microstructural and petrophysical characterization of the Mudrong Shale: application to top seal risking: Petroleum Geoscience, v. 8, p. 371–383.

Dent, LM, Normore, LS and Martin, SK 2021, Reference section, revised stratigraphy and facies analysis of the Ordovician Nambeet Formation, Canning Basin, Western Australia: Geological Survey of Western Australia, Perth, Report 211, 75p.

Doublier, MP, Gessner, K, Johnson, SP, Kelsey, DE, Haines, PW, Howard, HM, Chopping, R, Smithies, RH, Hickman, AH, Martin, DMcB, Southby, C, Champion, DC, Huston, DL, Calvert, AJ, Gorczyk, W, Kohanpour, F, Moro, P, Costelloe, R, Formin, T, Yuan, H and Kennett, BLN 2020a, Basement interpretation of the Kisdon seismic survey 18GA-KB1 (1:500 000 scale): Geological Survey of Western Australia, non-series map.

Doublier, MP, Johnson, SP, Gessner, KT, Howard, HM, Chopping, R, Smithies, RH, Martin, DMcB, Kelsey, DE, Haines, PW, Hickman, AH, Czarnota, K, Southby, C, Champion, DC, Huston, DL, Calvert, AJ, Kohanpour, F, Moro, P, Costelloe, R, Fomin, T and Kennett, BLN 2020b, Basement architecture from the Pilbara Craton to the Aileron Province: new insights from deep seismic reflection line 18GA-KB1, *in* Exploring for the future: Extended Abstracts *edited by* K Czarnota, IC Roach, S Abbott, M Haynes, N Kositcin, A Ray and E Slatter: Geoscience Australia, Canberra, p. 1–4.

Edwards, DS, Boreham, CJ, Kennard, JM, Chen, J, Grosjean, E, Mory, AJ, Sohn, J and Zumberge, JE 2013, Stable carbon and hydrogen isotopic composition of Paleozoic marine crude oils from the Canning Basin: comparison with other West Australian crude oils, *in* The Sedimentary Basins of Western Australia IV: Proceedings of the West Australian Basins Symposium — Expanding our horizons *edited by* M Keep and SJ Moss: WABS 2013, Perth, Western Australia, 18–21 August 2013: Petroleum Exploration Society of Australia, 32p.

Edwards, DS, Grosjean, E, Boreham, CJ, Sohn, J, Hong, Z, Jinadasa, N, Long, I and Buckler, T 2021, Exploring for the Future: Organic geochemistry analyses on Lower Ordovician cores from Barnicarndy 1, Barnicarndy Graben, Canning Basin, Western Australia: Geoscience Australia, Canberra, Record 2021/25, 19p, doi:10.11636/Record.2021.025.

Edwards, DS, Grosjean, E, Brocks, JJ and van Maldegem, L (editors) 2018, Paleo-reconstruction of the Canning Basin epicontinental seaway using carotenoid-derived biomarkers from crude oils and source rocks: 20th Australian Organic Geochemistry Conference (AOGC 2019): Origins of Oil, Old Organics and Organisms: Program and Abstracts: 3–7 December, 2018: Geoscience Australia, Record 2018/44, 134p.

Edwards, DS, Summons, RE, Kennard, JM, Nicoll, RS, Bradshaw, J, Bradshaw, M, Foster, CB, O'Brien, GW and Zumberge, JE 1997, Geochemical characteristics of Palaeozoic petroleum systems in northwestern Australia: APPEA Journal, v. 37, p. 351–377.

Edwards, DS and Zumberge, JE 2005, The oils of Western Australia II: regional petroleum geochemistry and correlation of crude oils and condensates from Western Australia and Papua New Guinea: Geoscience Australia and GeoMark Research Ltd, 515p., unpublished.

Eggleton, RA 2008, Regolith mineralogy, *in* Regolith science *edited by* KM Scott and CF Pain: CSIRO Publishing, Collingwood, Victoria, p. 45–72.

Ellwood, BB, Borradaile, GJ and Stephenson, A (editors) 1993, Minerals and the magnetic properties of rocks: In: Tarling, D.H. & Hrouda, F. (eds.) The Magnetic Anisotropy of Rocks: Chapman and Hall.

Esteban, L, Kager, S and Monmusson, L 2020, Waukarlycarly Embayment petrophysical testing programme: CSIRO-Energy; Report EP203496: Geological Survey of Western Australia, Statutory petroleum exploration report G004185 A13 (unpublished), 21p., <www.dmirs.wa.gov.au/wapims>.

Firoozabadi, A and Ramey, HJ, Jr 1988, Surface tension of water–hydrocarbon systems at reservoir conditions: Journal of Canadian Petroleum Technology, v. 27, no. 3, article no. PETSOC-88-03-03, doi:10.2118/88-03-03.

Flowers, RM, Ketcham, RA, Shuster, DL and Farley, KA 2009, Apatite (U–Th)/He thermochronometry using a radiation damage accumulation and annealing model: Geochimica et Cosmochimica Acta, v. 73, no. 8, p. 2347–2365, doi:10.1016/j.gca.2009.01.015.

Fluid Inclusion Technologies Inc 2021, A stratigraphic reconstruction of bulk volatile chemistry from fluid inclusions in Barnicarndy-1: Prepared April 19, 2021 for Geoscience Australia: Geological Survey of Western Australia, Statutory petroleum exploration report G004185 A10 (unpublished), 89p., <www.dmirs.wa.gov.au/wapims>.

Folk, RL 1980, Petrology of sedimentary rocks: Hemphill Publishing Company, Austin, Texas, USA, 182p.

Forbes, A, Sullivan, N, Edwards, D and Grosjean, E 2020, Chemostratigraphy of Waukarlycarly-1, Canning Basin, Western Australia: Report CAu50017 prepared for Geoscience Australia: Chemostrat Australia Pty: Geological Survey of Western Australia, Statutory petroleum exploration report G004185 A14 (unpublished), 34p., <www.dmirs.wa.gov.au/wapims>.

Foster, C and Wicander, R 2015, An Early Ordovician orange-walled microphytoplankton assemblage from the Nambeet Formation, Canning Basin, Australia: biostratigraphic and paleogeographic significance: Palynology, v. 40, 379–409.

Foster, CB, Edwards, DS and Long, I 2021, Reconnaissance study of Early Ordovician organic-walled microfossils from Barnicarndy 1, Barnicarndy Graben, Canning Basin, Western Australia: Geoscience Australia, Record 2021/40, 75p., doi:10.11636/record.2021.040.

Fowler, MG, Stasiuk, LD, Hearn, M and Obermajer, M 2004, Evidence for *Gloeocapsomorpha prisca* in Late Devonian source rocks from Southern Alberta, Canada: Organic Geochemistry, v. 35, no. 4, p. 425-441, doi:10.1016/j.orggeochem.2004.01.017.

Fraser, AR 1976, Gravity provinces and their nomenclature: BMR Journal of Australian Geology and Geophysics, v. 1, p. 350–352.

French, KL, Rocher, D, Zumberge, JE and Summons, RE 2015, Assessing the distribution of sedimentary C_{40} carotenoids through time: Geobiology, v. 13, no. 2, p. 139–151, doi:10.1111/gbi.12126.

Galbraith, RF 1988, Graphical display of estimates having differing standard errors: Technometrics, v. 30, no. 3, p. 271–281, doi:10.2307/1270081.

Gardiner, NJ, Maidment, DW, Kirkland, CL, Bodorkos, S, Smithies, RH and Jeon, H 2018, Isotopic insight into the Proterozoic crustal evolution of the Rudall Province, Western Australia: Precambrian Research, v. 313, 31-50., doi:10.1016/j.precamres.2018.05.003.

Goellnicht, NM, Groves, DI and McNaughton, NJ 1991, Late Proterozoic fractionated granitoids of the mineralised Telfer area, Paterson Province, Western Australia: Precambrian Research, v. 51, p. 375-391, doi:10.1016/0301-9268(91)90109-N.

Grosjean, E, Edwards, DS, Boreham, CJ, DiBugnara, D and Buckler, T 2020a, Magnetic susceptibility and bulk density data from Waukarlycarly 1, Canning Basin, Australia: Destructive Analysis Report 2020-007: Geoscience Australia, Record 2020/019, 5p., doi:10.11636/Record.2020.019.

Grosjean, E, Edwards, DS, Hong, Z, Chen, J, Jinadasa, N and Buckler, T 2020b, Rock-Eval pyrolysis data from Barnicarndy 1, Canning Basin, Australia: destructive analysis report 2020-003: Geoscience Australia, Record 2020/06, 9p., doi:10.11636/Record.2020.006.

Grosjean, E, Edwards, DS, Hong, Z, Jinadasa, N and Webster, T 2021, Investigation of potential hydrocarbon contamination sources during the study of Barnicarndy 1: Geoscience Australia, Record 2021/22, 28p., doi:10.11636/Record.2021.022.

Guenthner, WR, Reiners, PW, Ketcham, RA, Nasdala, L and giester, G 2013, Helium diffusion in natural zircon: radiation damage, anisotropy, and the interpretation of zircon (U–Th)/He thermochronology: American Journal of Science, v. 313, no. 3, p. 145–198, doi:10.2475/03.2013.01.

Guppy, DJ, Lindner, AW, Rattigan, JH and Casey, JN 1958, The geology of the Fitzroy Basin, Western Australia: Bureau of Mineral Resources, Geology and Geophysics, Bulletin 36, 136p.

Haines, P, Wingate, M, Maidment, D and Zhan, Y 2018a, Initiation of the Canning Basin: extensional magmatism in the middle Cambrian?, *in* Abstracts *edited by* Australian Geoscience Council: Australian Geoscience Council Convention: Big issues and ideas in geoscience, Adelaide, South Australia, 14–18 October: Australian Geoscience Council, p. 148.

Haines, PW, Wingate, MTD and Kirkland, CL 2013, Detrital zircon U-Pb ages from the Paleozoic of the Canning and Officer Basins, Western Australia: implications for provenance and interbasin connections, *in* The Sedimentary Basins of Western Australia IV: Proceedings of the West Australian Basins Symposium — Expanding our horizons *edited by* M Keep and SJ Moss: WABS 2013, Perth, Western Australia, 18–21 August 2013: Petroleum Exploration Society of Australia, 19p.

Haines, PW, Wingate, MTD, Zhan, Y and Maidment, DW 2018b, Looking beneath the Canning Basin: New insights from geochronology, seismic and potential-field data, *in* GSWA 2018 extended abstracts: promoting the prospectivity of Western Australia: Geological Survey of Western Australia, Record 2018/2, p. 30–33.

Hancock, EA, Green, AA, Huntington, JF, Schodlok, MC and Whitbourn, LB 2013, HyLogger-3: implications of adding thermal-infrared sensing: Geological Survey of Western Australia, Perth, Western Australia, Record 2013/3, 24p.

Hancock, EA, Normore, LS and Wawryk, MJ 2020a, Drillhole Waukarlycarly 1: Hyperspectral logging of core: Geological Survey of Western Australia, HyLogger Record 2020/6, 8p.

Hancock, EA, Normore, LS and Wawryk, MJ 2020b, Drillhole Waukarlycarly 1: Hyperspectral logging of cuttings: Geological Survey of Western Australia, HyLogger Record 2020/07, 6p.

Hannaford, C 2020, Palynological analysis of Waukarlycarly-1, Canning Basin, Western Australia: Geological Survey of Western Australia, Paleontology Report 2020/44, 11p.

Hantschel, T and Kauerauf, AI 2009, Fundamentals of basin and petroleum systems modeling: Springer, Berlin, Heidelberg (Germany), 476p., doi:10.1007/978-3-540-72318-9.

Haynes, DW, Brooke, WJL and Mazzoni, PP 1993, Application of conceptual models for sediment-hosted ore deposits in the discovery of the Nifty copper and adjacent zinc-lead deposits, Yeneena Basin, Western Australia, *in* Mineral deposit modeling: Geological Association of Canada, Canada, Special Paper 40, p. 75–88.

Heinrich, JJ, Herzog, HJ and Reiner, DM 2004, Environmental Assessment of Geologic Storage of CO2: MIT LFEE 2003-002: Massachusetts Institute of Technology, Cambridge, Massachusetts, 8p.

Hocking, RM 1994, Subdivisions of Western Australian Neoproterozoic and Phanerozoic sedimentary basins: Geological Survey of Western Australia, Record 1994/4, 85p.

Hocking, RM, Mory, AJ and Williams, IR 1994, An atlas of Neoproterozoic and Phanerozoic basins of Western Australia, *in* The sedimentary basins of Western Australia: Proceedings of the West Australian Basins Symposium, Perth Western Australia, 14–17 August 1994 *edited by* PG Purcell and RR Purcell: Petroleum Exploration Society of Australia, Perth, p. 21–43.

Hoffmann, CF, Foster, CB, Powell, TG and Summons, RE 1987, Hydrocarbon biomarkers from Ordovician sediments and the fossil alga *Gloeocapsomorpha prisca* Zalessky 1917: Geochimica et Cosmochimica Acta, v. 51, no. 10, p. 2681–2697.

Huang, WY and Meinschein, WG 1979, Sterols as ecological indicators: Geochimica et Cosmochimica Acta, v. 43, no. 5, p. 739–745, <www.sciencedirect.com/science/article/pii/0016703779902576>.

Hunt Oil Company of Australia 1997, Final report, Waukarlycarly seismic survey interpretation: Hunt Oil Company of Australia: Geological Survey of Western Australia, Statutory petroleum exploration report S10316 A5 (unpublished), <www.dmirs.wa.gov.au/wapims>.

Iasky, RP 1990, Officer Basin, *in* Geology and mineral resources of Western Australia *edited by* Geological Survey of Western Australia: Geological Survey of Western Australia, Memoir 3, p. 362–380.

Inoue, M and Ohomi, M 1981, Relation between uniaxial compressive strength and elastic wave velocity of soft rock: Proceedings of the International Symposium on Weak Rock, Tokyo, September 1981.

Jarrett, A, Bailey, AHE, Dewhurst, DN, Esteban, L, Kager, S and Monmusson, L 2020, Exploring for the Future — Waukarlycarly 1 petrophysical testing program data release, Canning Basin, Australia: Geoscience Australia, Record 2020/28, 34p., doi:10.11636/Record.2020.028.

Jarvie, DM 2021, Correlation of T_{max} and measured vitrinite reflectance, viewed 18 June 2021, <www.wildcattechnologies.com/post/grow-your-blog-community>.

Jones, SC 1972, A rapid accurate unsteady state Klinkenberg permeameter: Society of Petroleum Engineers Journal, v. 3535, p. 383–397.

Jourdan, F, Hodges, K, Sell, B, Schaltegger, U, Wingate, MTD, Evins, LZ, Söderlund, U, Haines, PW, Phillips, D and Blenkinsop, T 2014, High-precision dating of the Kalkarindji large igneous province, Australia, and synchrony with the Early-Middle Cambrian (Stage 4-5) extinction: Geology, v. 42, p. 543–546, doi:10.1130/G35434.1.

Kelsey, DE, Lu, Y and Smithies, RH 2022, O'Callaghans Supersuite (P_-OC-g): Geological Survey of Western Australia; WA Geology Online, Explanatory Notes extract, viewed 23 April 2022, <www.dmirs.wa.gov.au/ens>.

Kennard, JM, Jackson, MJ, Romine, KK, Shaw, RD and Southgate, PN 1994, Depositional sequences and associated petroleum systems of the Canning Basin, WA, *in* The sedimentary basins of Western Australia: Proceedings of the West Australian Basins Symposium, Perth Western Australia, 14–17 August 1994 *edited by* PG Purcell and RR Purcell: Petroleum Exploration Society of Australia, Perth, p. 657–676.

Ketcham, RA 2005, Forward and inverse modeling of low-temperature thermochronometry data: Reviews in Mineralogy and Geochemistry, v. 58, no. 1, p. 275–314.

Kitto, PL 1978, Final report on the Barnicarndy coal project: Peko-Wallsend Operations Ltd, Geopeko Division, Western Australia: Geological Survey of Western Australia, Statutory mineral exploration report A35899 (unpublished), <www.dmirs.wa.gov.au/wamex>.

Klinkenberg, LJ 1941, The permeability of porous media to liquids and gases, *in* Drilling and production practice, SOCAR Proceedings 2(2): American Petroleum Institute, p. 200–213.

Koopmans, MP, Schouten, S, Kohnen, ME and Sinninghe Damste, JS 1996, Restricted utility of aryl isoprenoids as indicators for photic zone anoxia: Geochimica et Cosmochimica Acta, v. 60, no. 23, p. 4873–4876, doi:10.3997/2214-4609.201902983.

Kopty, Z 2020, Appendix P – Downhole seismic logging for Geological Survey of Western Australia (GSWA): Full waveform sonic (FWS) and zero offset vertical seismic profile (ZVSP) at the Waukarlycarly drill site, *in* Waukarlycarly 1 basic data well completion report: Geological Survey of Western Australia, Report 206, 26p.

Krapf, CBE 2011, New insights into the regolith of parts of the Gascoyne region: Geological Survey of Western Australia, Record 2011/22, 54p.

Lu, Y, Wingate, MTD, Romano, SS, Mole, Kirkland, CL, Kemp, AIS, Belousova, EA, Smithies, RH, Gessner, K and Johnson, SP 2021, Zircon lutetium–hafnium isotope map of Western Australia: Geological Survey of Western Australia; data layer, <www.dmirs.wa.gov.au/geoview>.

Luo, Q, Fariborz, G, Zhong, N, Wang, Y, Qiu, N, Skovstedd, CB, Suchý, V, Hemmingsen Schovcbo. N., Morga, R, Xu, Y, Hao, J, Liu, A, Wu, J, Cao, W and Min, X 2020, Graptolites as fossil geo-thermometers and source material of hydrocarbons: an overview of four decades of progress: Earth-Science Reviews, v. 200.

MacNeill, M, Marshall, N and McNamara, C 2018, New insights into a major Early-Middle Triassic rift episode in the NW Shelf of Australia, *in* AEGC Extended Abstracts 2018: First Australasian Exploration Geoscience Conference, Sydney, Australia, 18 February 2018, 5p.

Magee, J 2009, Palaeovalley groundwater resources in arid and semi-arid Australia - a literature review: Geoscience Australia, Record 2009/3, 224p.

Maidment, D, Huston, DL, Maas, R, Czarnota, K, Neumann, N, McIntyre, A and Bagas, L 2008, The Nifty-Kintyre-Duke Cu-U-Pb-Zn mineralizing events: Links to the evolution of the Yeneena Basin, northwest Paterson Orogen, *in* GSWA 2008 extended abstracts: promoting the prospectivity of Western Australia: Geological Survey of Western Australia, Record 2008/2, p. 27–29.

Maidment, DW 2005, Paleozoic high-grade metamorphism within the Centralian Superbasin, Harts Range region, central Australia.: Australian National University, Canberra, ACT, PhD thesis (unpublished).

Maidment, DW 2017, Geochronology from the Rudall Province, Western Australia: Implications for the amalgamation of the West and North Australian Cratons: Geological Survey of Western Australia, Report 161, 95p.

Maidment, DW, Huston, DL and Beardsmore, T 2017, Paterson Orogen geology and metallogeny, *in* Australian Ore Deposits *edited by* GN Phillips: Australasian Institute of Mining and Metallurgy, Monograph 32, p. 411–416.

Maidment, DW, Huston, DL and Heamann, L 2010, The age of the Telfer Au-Cu deposit and its relationship with granite emplacement, Paterson Province, Western Australia: Geoscience Australia, Professional Opinion 2010/05, 40p.

Martin, DMcB, Murdie, RE, Cutten, HN, Kelsey, DE, Thomas, CM, Quentin de Gromard, R, Zhan, Y and Haines, PW 2021a, Major crustal boundaries map of Western Australia: Geological Survey of Western Australia; data layer, <www.dmirs.wa.gov.au/geoview>.

Martin, JR, Redfern, J, Horstwood, MSA, Mory, AJ and Williams, BPJ 2019, Detrital zircon age and provenance constraints on late Paleozoic ice-sheet growth and dynamics in Western and Central Australia: Australian Journal of Earth Sciences, v. 66, no. 2, p. 183–207, doi:10.1080/08120099.2019.1531925.

Martin, SK, Allen, HJ, Haines, PW and Phillips, C 2021b, Preliminary paleontological summary of Barnicarndy 1 stratigraphic well, Canning Basin: Geological Survey of Western Australia, Paleontology Report 2021/1, 18p.

McNaughton, NJ and Goellnicht, NM 1990, The age and radiothermal properties of the Mount Crofton Granite, Telfer area, Western Australia: Australian Journal of Earth Sciences, v. 37, p. 103–106.

Mory, AJ 2017, A Paleozoic perspective of Western Australia: Geological Survey of Western Australia, Perth, Western Australia, 58p.

Munnecke, A and Samtleben, C 1996, The formation of micritic limestones and the development of limestone-marl alternation in the Silurian of Gotland, Sweden: Facies, v. 34, p. 159–176.

Nelson, DR 2000, 137655: metasandstone, Telfer West Dome; Geochronology Record 418: Geological Survey of Western Australia, 5p., <www.dmirs.wa.gov.au/geochron>.

Nelson, DR 2001, 137657: metasandstone, Telfer West Dome; Geochronology Record 419: Geological Survey of Western Australia, 4p., <www.dmirs.wa.gov.au/geochron>.

Nelson, DR 2002, 169119: metasandstone, Fandango Prospect; Geochronology Record 91: Geological Survey of Western Australia, 5p., <www.dmirs.wa.gov.au/geochron>.

Normore, L, Haines, PW, Carr, LK, Henson, P, Zhan, Y, Wingate, MTD, Zhen, YY, Lu, Y, Martin, S, Kelsey, D, Allen, H and Fielding, I 2021, Barnicarndy Graben, southern Canning Basin: stratigraphy defined by the Barnicarndy 1 stratigraphic well: The APPEA Journal, v. 61, no. 1, p. 224–235, doi:10.1071/AJ20160.

Normore, LS and Dent, LM 2017a, Olympic 1, Canning Basin: Geological Survey of Western Australia; Digital Core Atlas Series, 212p. <www.dmirs.wa.gov.au/wapims>.

Normore, LS and Dent, LM 2017b, Petroleum source potential of the Ordovician Nambeet Formation, Caning Basin: Evidence from petroleum well Olympic 1: Geological Survey of Western Australia, Report 169, 20p.

Normore, LS and Rapaic, M 2020, Waukarlycarly 1 basic data well completion report: Geological Survey of Western Australia, Report 206, 14p.

Normore, LS, Zhen, YY, Dent, LM, Crowley, JL, Percival, IG and Wingate, MTD 2018, Early Ordovician CA-IDTIMS U–Pb zircon dating and conodont biostratigraphy, Canning Basin, Western Australia: Australian Journal of Earth Sciences, v. 65, p. 61–73, doi:10.1080/08120099.2018.1411292.

Paschke, C, O'Halloran, G, Dempsey, C and Hurren, C 2018, Interpretation of a Permian conjugate basin margin preserved on the outer Northwest Shelf of Australia: ASEG Extended Abstracts, no. 1, p. 1–8.

Paterson, MS 1978, Experimental Rock Deformation: The Brittle Field: Springer-Verlag, New York, 254p.

Percival, J 2015, Co-funded Government – industry exploration drilling program, Lake Waukarlycarly project potash exploration, E45/4273, 4274, 4291, final report: Reward Minerals Ltd: Geological Survey of Western Australia, Statutory mineral exploration report A105255 (unpublished), 16p., <www.dmirs.wa.gov.au/wamex>.

Pereira, L, Chapoy, A, Burgass, R, Oliveira, MB, Coutinho, J and Tohidi, B 2016, Study of the impact of high temperatures and pressures on the equilibrium densities and interfacial tension of the carbon dioxide/water system: Journal Chem Thermodynamics, v. 93, p. 404–415, doi:10.1016/j.jct.2015.05.005.

Peters, KE and Cassa, MR 1994, Applied source rock geochemistry, *in* The petroleum system: from source to trap *edited by* LB Magoon and WG Dow: American Association of Petroleum Geologists, Tulsa, Oklahoma, USA, Memoir 60, p. 93–120.

Peters, KE, Walters, CC and Moldowan, JM 2005, The biomarker guide, volume 2: Cambridge University Press, Cambridge, UK, Biomarkers and isotopes in petroleum systems and Earth history, 1155p.

Pillans, B 2004, Geochronology of the Australian regolith, *in* Regolith landscape evolution across Australia: a compilation of regolith landscape case studies with regolith landscape evolution models *edited by* RR Anand and P de Broekert: Cooperative Research Centre for Landscape Environments and Mineral Exploration (CRC LEME), Perth, Western Australia, p. 41–61.

Pojeta Jr, J and Gilbert-Tomlinson, J 1977, Australian Ordovician pelecypod molluscs: Bureau of Mineral Resources, Geology and Geophysics, Bulletin 174, 64p., 29 pl.

Porter, TM 2017a, Nifty and Maroochydore copper deposits, *in* Australian Ore Deposits *edited by* GN Phillips: Australasian Institute of Mining and Metallurgy, Monograph 32, p. 423–426.

Porter, TM 2017b, Telfer gold–copper deposit, *in* Australian Ore Deposits *edited by* GN Phillips: Australasian Institute of Mining and Metallurgy, Monograph 32, p. 417–422.

Radke, M and Welte, DH 1983, The methylphenanthrene index (MPI): a maturity parameter based on aromatic hydrocarbons: Advances in Organic Geochemistry, p. 504–512.

Rajabi, M, Tingay, M, Heidbach, O, Hillis, R and Reynolds, S 2017, The present-day stress field of Australia: Earth-Science Reviews, v. 168, p. 165–189, doi:10.1016/j.earscirev.2017.04.003.

Ranasinghe, SP and Crosdale, PJ 2020, Report on source rock type, maturation levels and hydrocarbon potential of a suite of samples from Waukarlyarly-1 in the Canning Basin, Western Australia: Report prepared for Geoscience Australia: Geological Survey of Western Australia, Statutory petroleum exploration report G0004185 A4 (unpublished), 20p., <www.dmirs.wa.gov.au/wamex>.

Reeckmann, SA and Mebberson, AJ 1984, Igneous intrusions in the north-west Canning Basin and their impact on oil exploration, *in* The Canning Basin, W.A. *edited by* PG Purcell: Proceedings of the GSA/PESA Canning Basin Symposium, Perth, Western Australia, 27–29 June 1984, p. 389–399.

Rickards, B and Chapman, A 1991, Bendigonian graptolites (Hemichordata) of Victoria: Memoirs of the Museum of Victoria, v. 52, p. 1–135.

Roach, IC, Costelloe, MT and Whitaker, AJ 2010, Previous and concurrent work, *in* Geological and energy implications of the Paterson airborne electromagnetic (AEM) survey, Western Australia *edited by* IC Roach: Geoscience Australia, Record, p. 29–47.

Romero-Sarmiento, MF, Riboulleau, A, Vecoli, M and Versteegh, G 2010, Occurrence of retene in upper Silurian–lower Devonian sediments from North Africa: Origin and implications: Organic Geochemistry, v. 41, no. 3, p. 302–306, doi:10.1016/j.orggeochem.2009.10.003.

Romero-Sarmiento, MF, Riboulleau, A, Vecoli, M and Versteegh, G 2011, Aliphatic and aromatic biomarkers from Gondwanan sediments of Late Ordovician to Early Devonian age: an early terrestrialization approach: Organic Geochemistry, v. 42, no. 6, p. 605–617, doi:10.1016/j.orggeochem.2011.04.005.

Rubenstein, CV, Gerrienne, P, La Puente, GS de, Astini, RA and Steemans, P 2010, Early Middle Ordovician evidence for land plants in Argentina (eastern Gondwana): New Phytologist, v. 188, no. 2, p. 365–369, doi:10.1111/j.1469-8137.2010.03433.x.

Schimmelmann, A, Sessions, AL, Boreham, CJ, Edwards, DS, Logan, GA and Summons, RE 2004, D/H ratios of terrestrial-sourced petroleum systems: Organic Geochemistry, v. 35, no. 10, p. 1169–1195, doi:10.1016/j.orggeochem.2004.05.006.

Schlumberger Limited 1991, Log Interpretation Principles/Applications. (Schlumberger Educational Services: Houston, Texas, USA.).

Schön, JH 2015, Chapter 4 - Density, Physical Properties of Rocks: Fundamentals and Principles of Petrophysics: Elsevier.

Schowalter, TT 1979, Mechanics of secondary hydrocarbon migration and entrapment: AAPG Bulletin, v. 63, no. 5, p. 723–760.

Scrimgeour, IR 2013, Chapter 29: Irindina Province, *in* Geology and mineral resources of the Northern Territory *compiled by* M Ahmad and TJ Munson: Northern Territory Geological Survey, Special Publication, 29:1-29:12.

Sessions, AL 2016, Factors controlling the deuterium contents of sedimentary hydrocarbons: Organic Geochemistry, v. 96, p. 43–64, doi:10.1016/j.orggeochem.2016.02.012.

Sessions, AL, Burgoyne, TW, Schimmelmann, A and Hayes, JM 1999, Fractionation of hydrogen isotopes in lipid biosynthesis: Organic Geochemistry, v. 30, no. 9, p. 1193–1200, doi:10.1016/S0146-6380(99)00094-7.

Sessions, AL, Sylvia, AP, Summons, RE and Hayes, JM 2004, Isotopic exchange of carbon-bound hydrogen over geological timescales: Organic Geochemistry, v. 68, no. 7, p. 1545–1559, doi:10.1016/j.gca.2003.06.004.

Sinninghe Damste, JS, Kenig, F, Koopmans, MP, Koster, J, Schouten, S, Hayes, JM and Leeuw, JW de 1995, Evidence for gammacerane as an indicator of water column stratification: Geochimica et Cosmochimica Acta, v. 59, p. 1895–1900, doi:10.1016/0016-7037(95)00073-9.

Smith, PM and Allen, HJ 2023, Early Ordovician trilobites from Barnicarndy 1 stratigraphic well of the southern Canning Basin, Western Australia: Alcheringa, 58p., published online 07/08/2023, doi:10.1080/03115518.2023.2226194.

Sorensen, MK 2015, Mud-filtrate correction of sonic logs by fluid substitution: Modulus and pore-fluid coupling by pore-filling clay: Technical University of Denmark, Department of Civil Engineering.

Southby, C, Carr, L, Henson, P, Haines, P, Zhan, A, Anderson, J, MacFarlane, S, Formin, T and Costelloe, R 2019, Exploring for the future: Kidson Sub-basin seismic interpretation: ASEG Extended Abstracts, 2019, v. 1, 3p., doi:10.1080/22020586.2019.12073007.

Spaak, G, Edwards, DS, Foster, CB, Pagès, A, Summons, RE, Sherwood, N and Grice, K 2017, Environmental conditions and microbial community structure during the Great Ordovician Biodiversification Event; a multi-disciplinary study from the Canning Basin, Western Australia: Global and Planetary Change, v. 159, p. 93–112, 20p., doi:10.1016/j.gloplacha.2017.10.010.

Strother, PK and Foster, CB 2021, A fossil record of land plant origins from charophyte algae: Science, v. 373, p. 792–796, doi:10.1126/science.abj2927.

Strother, PK, Taylor, WA, Beck, JH and Vecoli, M 2017, Ordovician spore 'thalli' and the evolution of the plant sporophyte: Palynology, v. 41, p. 57–68, doi:10.1080/01916122.2017.1361213.

Taylor, G and Eggleton, RA 2017, Silcrete: an Australian perspective: Australian Journal of Earth Sciences, v. 64, no. 8, p. 987–1016, doi:10.1080/08120099.2017.1318167.

Traves, DM, Casey, JN and Wells, AT (editors) 1956, The geology of the south-western Canning Basin, Western Australia: Bureau of Mineral Resources, Geology and Geophysics, Report 29, 76p.

Tulipani, S, Grice, K, Greenwood, P, Haines, PW, Sauer, P, Schimmelmann, A, Summons, RE, Foster, CB, Bottcher, ME, Playton, T and Schwark, L 2015, Changes of palaeoenvironmental conditions recorded in Late Devonian reef systems from the Canning Basin, WA: A biomarker and stable isotope approach: Gondwana Research, v. 28, no. 4, p. 1500–1515, doi:10.1016/j.gr.2014.10.003.

van Aarssen, B, Alexander, R and Kagi, R 2000, Higher plant biomarkers reflect palaeovegetation changes during Jurassic times: Geochimica et Cosmochimica Acta, v. 64, p. 1417–1424, doi:10.1016/0146-6380(86)90089-6.

van der Graaff, WJE, Crowe, RWA, Bunting, JA and Jackson, MJ 1977, Relict early Cainozoic drainages in arid Western Australia: Zeitschrift Fur Geomorphologie, v. 21, p. 379–400.

Vavra, CL, Kaldi, JG and Sneider, RM 1992, Geological applications of capillary pressure: A review: AAPG Bulletin, v. 76, p. 840–850.

Velseis Processing Pty Ltd 2019, Seismic data processing report: 2018 Kidson Sub-basin deep crustal seismic survey, land 2D: Geological Survey of Western Australia, Statutory petroleum exploration report S003798 A2, 42p., <www.dmirs.wa.gov.au/wapims>.

Volkman, JK 1986, A review of sterol markers for marine and terrigenous organic matter: Organic Geochemistry, v. 9, p. 83–99.

Wade, BP, Kelsey, DE, Hand, M and Barovich, KM 2008, The Musgrave Province: Stitching north, west and south Australia, *in* Assembling Australia: Proterozoic building of a continent *edited by* PA Cawood and RJ Korsch, Precambrian Research v. 166, p. 370–386, doi:10.1016/j.precamres.2007.05.007.

Walker, M 2020, Petrophysical evaluation, Waukarlycarly-1 stratigraphic well, Canning Basin, Western Australia: Walker Petrophysics Pty Ltd: Geological Survey of Western Australia, Statutory petroleum exploration report G004185 A7 (unpublished), 39p., <www.dmirs.wa.gov.au/wapims>.

Walker, M 2021, Petrophysical evaluation Barnicarndy-1 (formerly Waucarlykarly-1) stratigraphic well, Canning Basin, Western Australia: Appendix – Discussion of core electrical properties Barnicarndy Sandstone: Walker Petrophysics Pty Ltd: Geological Survey of Western Australia, Statutory petroleum exploration report G004185 A23 (unpublished), 16p., <www.dmirs.wa.gov.au/wapims>.

Wang, L, Edwards, DS, Bailey, A, Carr, LK, Boreham, CJ, Grosjean, E, Normore, L, Anderson, J, Jarrett, AJM, MacFarlane, S, Southby, C, Carson, C, Khider, K, Henson, P, Haines, P and Walker, M 2021, Petrophysical and geochemical interpretations of well logs from the pre-Carboniferous succession in Barnicarndy 1, Canning Basin, Western Australia: The APPEA Journal, v. 61, no. 1, p. 253–270, doi:10.1071/AJ20038.

Wang, P, Du, Y, Yu, W, Algeo, TJ, Zhou, Q, Xu, Y, Qi, L, Yuan, L and Pan, W 2020, The chemical index of alteration (CIA) as a proxy for climate change during glacial-interglacial transitions in earth history: Earth-Science Reviews, v. 201, article no. 103032, 22p., doi:10.1016/j.earscirev.2019.103032.

Washburn, EW 1921, A note on the method of determining the distribution of pore sizes in a porous material: Proceedings of the National Academy of Sciences of the United States of America, v. 7, p. 115–116.

Wawryk, M 2020, GSRSD XRD Analysis: Geological Survey of Western Australia, Statutory petroleum exploration report G004185 A9 (unpublished), 10p., <www.dmirs.wa.gov.au/wamex>.

Wawryk, MJ and Hancock, EA 2019, Application of rapid benchtop X-ray powder diffractometry for identification and characterization of mineral phases in geological materials: Geological Survey of Western Australia, Record 2019/9, 31p.

Wilson, A and Thrane, L 2020, Waukarlycarly-1 structural and sedimentological analysis of an Acoustic Televiewer borehole image log, onshore Canning Basin, Western Australia; ImageStrat Report DM-20-1: Geological Survey of Western Australia, Statutory petroleum exploration report W006030 A2, 117p., <www.dmirs.wa.gov.au/wapims>.

Wilson, P 2016, Metals X limited, Final Surrender Report for the period 21 April 2015 to 12 October 2016, Final Surrender Report, E45/4114: Geological Survey of Western Australia, Statutory mineral exploration report A110336 (unpublished), 14p., <www.dmirs.wa.gov.au/wamex>.

Wingate, MTD 2007a, 136057: quartz sandstone, Acacia 2; Geochronology Record 655: Geological Survey of Western Australia, 5p., <www.dmirs.wa.gov.au/geochron>.

Wingate, MTD 2007b, 136069: quartz sandstone, Looma 1; Geochronology Record 656: Geological Survey of Western Australia, 5p., <www.dmirs.wa.gov.au/geochron>.

Wingate, MTD 2007c, 184268: quartz sandstone, Gap Spring; Geochronology Record 657: Geological Survey of Western Australia, 5p., <www.dmirs.wa.gov.au/geochron>.

Wingate, MTD 2007d, 184269: quartz sandstone, Carranya Homestead; Geochronology Record 658: Geological Survey of Western Australia, 5p., <www.dmirs.wa.gov.au/geochron>.

Wingate, MTD and Haines, PW 2009a, 135962: sandstone, Samphire Marsh 1; Geochronology Record 777: Geological Survey of Western Australia, 5p., <www.dmirs.wa.gov.au/geochron>.

Wingate, MTD and Haines, PW 2009b, 135963: sandstone, Wilson Cliffs 1; Geochronology Record 778: Geological Survey of Western Australia, 5p., <www.dmirs.wa.gov.au/geochron>.

Wingate, MTD and Haines, PW 2009c, 135964: sandstone, Wilson Cliffs 1; Geochronology Record 779: Geological Survey of Western Australia, 5p., <www.dmirs.wa.gov.au/geochron>.

Wingate, MTD and Haines, PW 2009d, 135965: phyllitic metasandstone, Acacia 2; Geochronology Record 780: Geological Survey of Western Australia, 5p., <www.dmirs.wa.gov.au/geochron>.

Wingate, MTD, Kirkland, CL, Spaggiari, CV and Smithies, RH 2015, U-Pb geochronology of the Madura Province, in Eucla basement stratigraphic drilling results release workshop: extended abstracts edited by CV Spaggiari and RH Smithies: Geological Survey of Western Australia, Record 2015/10, p. 14–16.

Wingate, MTD, Fielding, IOH, Lu, Y, Normore, LS and Haines, PW 2021a, 246756: siltstone, Barnicarndy 1; Geochronology Record 1809: Geological Survey of Western Australia, 8p., <www.dmirs.wa.gov.au/geochron>.

Wingate, MTD, Lu, Y, Fielding, IOH, Dent, LM and Normore, LS 2021b, 226181: sandstone, Olympic 1; Geochronology Record 1828: Geological Survey of Western Australia, <www.dmirs.wa.gov.au/geochron>.

Wingate, MTD, Lu, Y, Fielding, IOH, Dent, LM and Normore, LS 2021c, 226182: sandstone, Olympic 1; Geochronology Record 1829: Geological Survey of Western Australia, <www.dmirs.wa.gov.au/geochron>.

Wingate, MTD, Lu, Y, Fielding, IOH, Normore, LS and Haines, PW 2021d, 237994: siltstone, Barnicarndy 1; Geochronology Record 1739: Geological Survey of Western Australia, 8p., <www.dmirs.wa.gov.au/geochron>.

Wingate, MTD, Lu, Y, Fielding, IOH, Normore, LS and Haines, PW 2021e, 237995: siltstone, Barnicarndy 1; Geochronology Record 1740: Geological Survey of Western Australia, 8p., <www.dmirs.wa.gov.au/geochron>.

Wingate, MTD, Lu, Y, Fielding, IOH, Normore, LS and Haines, PW 2021f, 237996: quartz sandstone, Barnicarndy 1; Geochronology Record 1741: Geological Survey of Western Australia, 6p., <www.dmirs.wa.gov.au/geochron>.

Wingate, MTD, Lu, Y, Fielding, IOH, Normore, LS and Haines, PW 2021g, 237997: siltstone, Barnicarndy 1 1742: Geological Survey of Western Australia, 8p., <www.dmirs.wa.gov.au/geochron>.

Wingate, MTD, Lu, Y, Fielding, IOH, Normore, LS and Haines, PW 2021h, 237998: quartz sandstone, Barnicarndy 1; Geochronology Record 1743: Geological Survey of Western Australia, 8p., <www.dmirs.wa.gov.au/geochron>.

Wingate, MTD, Lu, Y, Fielding, IOH, Normore, LS and Haines, PW 2021i, 246755: quartz sandstone, Barnicarndy 1; Geochronology Record 1736: Geological Survey of Western Australia, 8p., <www.dmirs.wa.gov.au/geochron>.

Wingate, M, Lu, Y, Fielding, IOH, Normore, LS and Haines, PW 2021j, 246757: quartz sandstone, Barnicarndy 1: Geochronology Record 1737: Geological Survey of Western Australia, 8p., <www.dmirs.wa.gov.au/geochron>.

Wingate, MTD, Lu, Y, Fielding, IOH, Normore, LS and Haines, PW 2021k, 246758: sandstone, Barnicarndy 1; Geochronology Record 1738: Geological Survey of Western Australia, 8p., <www.dmirs.wa.gov.au/geochron>.

Wingate, MTD, Lu, Y, Normore, LS and Haines, PW 2021l, 195463: quartz sandstone, Sally May 2; Geochronology Record 1754: Geological Survey of Western Australia, 18p., <www.dmirs.wa.gov.au/geochron>.

Wingate, MTD, Lu, Y, Normore, LS and Haines, PW 2021m, 195464: quartz sandstone, Sally May 2; Geochronology Record 1755: Geological Survey of Western Australia, 17p., <www.dmirs.wa.gov.au/geochron>.

Wingate, MTD, Lu, Y and Haines, PW 2018a, 199446: monzogranite, Samphire Marsh 1; Geochronology Record 1525: Geological Survey of Western Australia, 5p., <www.dmirs.wa.gov.au/geochron>.

Wingate, MTD, Lu, Y and Haines, PW 2018b, 199448: micaceous quartzite, Thangoo 2; Geochronology Record 1527: Geological Survey of Western Australia, 8p., <www.dmirs.wa.gov.au/geochron>.

Wingate, MTD, Lu, Y and Haines, PW 2019a, 199496: metasandstone, Frankenstein 1; Geochronology Record 1562: Geological Survey of Western Australia, 7p., <www.dmirs.wa.gov.au/geochron>.

Wingate, MTD, Lu, Y and Haines, PW 2019b, 199497: metasandstone, Wilson Cliffs 1; Geochronology Record 1563: Geological Survey of Western Australia, 5p., <www.dmirs.wa.gov.au/geochron>.

Wingate, MTD, Lu, Y, Roche, LK and Haines, PW 2019c, 214945: psammitic gneiss, Citadel Project; Geochronology Record 1564: Geological Survey of Western Australia, 8p., <www.dmirs.wa.gov.au/geochron>.

Wingate, MTD, Pirajno, F and Morris, PA 2004, Warakurna large igneous province: A new Mesoproterozoic large igneous province in west-central Australia: Geology, v. 32, no. 2, p. 105–108.

Zachos, JC, Shackleton, NJ, Revenaugh, JS and Pälike, H and Flower, B.P. 2001, Climate response to orbital forcing across the Oligocene-Miocene boundary: Science, v. 292, no. 5515, p. 274–278.

Zhan, Y 2018, A seismic interpretation of the southwestern Canning Basin, Western Australia: Geological Survey of Western Australia, Report 178, 34p.

Zhan, Y 2021, Velocity anomalies and out-of-plane reflections in Barnicarndy 1, Canning Basin: The APPEA Journal, v. 61, p. 271–290, doi:10.1071/AJ20082.

Zhan, Y and Haines, PW 2021, Kidson Sub-basin seismic survey - a panorama of the southern Canning Basin: Geological Survey of Western Australia, Report 216, 28p.

Zhang, L, Huang, D and Liao, Z 1999, High concentration retene and methylretene in Silurian carbonate of Michigan Basin: Chinese Science Bulletin, v. 44, p. 2083–2086.

Zhen, YY, Allen, HJ and Martin, SK 2021, Preliminary conodont studies of Barnicarndy 1 stratigraphic well, Canning Basin: Geological Survey of Western Australia, Paleontology Report 2021/2, 3p., <https://geodocs.dmirs.wa.gov.au/Web/document/600367>.

Zhen, YY, Allen, HJ and Martin, SK 2022, Early Ordovician conodonts from Barnicarndy 1 stratigraphic well of the Southern Canning Basin, Western Australia: Alcheringa, article no. 2017481, 15p., doi:10.1080/03115518.2021.2017481.

Zhen, YY, Nicoll, RS, Normore, LS, Percival, IG, Laurie, JR and Dent, LM 2020, Ordovician conodont biostratigraphy of the Willara Formation in the Canning Basin, Western Australia: Palaeoworld, v. 30, no. 2, p. 249–277, doi:10.1016/j.palwor.2020.06.006.

REPORT
239

BARNICARNDY 1 INTERPRETATIVE WELL COMPLETION REPORT

LS Normore, PW Haines, Y Zhan, MTD Wingate, DS Edwards, Y Lu, SK Martin, E Grosjean, CJ Boreham, L Wang, D Dewhurst, A Bailey, CB Foster, DE Kelsey, HJ Allen, IOH Fielding, M Wawryk, EA Hancock, N De Souza Kovacs, LK Carr and P Henson

Barnicarndy 1 is a stratigraphic drillhole within the Barnicarndy Graben of the southwestern Canning Basin funded by Geoscience Australia's Exploring for the Future initiative and operated by the Geological Survey of Western Australia (GSWA). The project followed the acquisition of the Kidson seismic survey (18GA-KB1) in 2018 providing critical subsurface data for a poorly understood component of the basin imaged by that survey. Drilled in September – November 2019, the hole reached total depth of 2680.53 m (fully cored below 580 m) in low-grade metasedimentary rocks of the Yeneena Basin unconformably overlain by Ordovician and Permo-Carboniferous units of the Canning Basin. The core includes the type sections of two new stratigraphic units, the Yapukarninjarra and Barnicarndy Formations. This 'interpretive' well completion report and its appendices detail the results of post-drilling analysis, funded in part through GSWA's Exploration Incentive Scheme, including biostratigraphy, ichnology, geochronology, thermochronology, petrophysics, chemostratigraphy, petrography, organic and inorganic geochemistry, petroleum system studies, fluid inclusion stratigraphy, sedimentology and sequence stratigraphy of the drillhole.

Further details of geoscience products are available from:

First Floor Counter
Department of Mines, Industry Regulation and Safety
100 Plain Street
EAST PERTH WESTERN AUSTRALIA 6004
Phone: +61 8 9222 3459 Email: publications@dmirs.wa.gov.au
www.dmirs.wa.gov.au/GSWApublications